# Development of a non-invasive method to detect pericellular spatial oxygen gradients using FLIM

Hosny, Neveen Amera

# Development of a non-invasive method to detect pericellular spatial oxygen gradients using FLIM

Neveen Amera Hosny

2011

This thesis is submitted for the

Degree of Doctor of Philosophy

in Medical Engineering

School of Engineering and Material Science,
School of Biology and Chemical Science,
Queen Mary,
Unversity of London

## Declaration

I confirm that the work presented in this thesis is the author's own and that the copyright of this thesis rests with the author and no quotation from it or information derived from is may be published without the prior written consent.

Neveen Hosny

# Acknowledgements

I'm thankful to say we have reached the end of our relationship. There have been many ups and downs during our short lived fling, but alas it was never meant to be, one day I would always have to stop writing and just print you off ready for binding. The experiences has been exhilarating, painful and damn right depressing, but I have gained a wealth of knowledge about new techniques and met a great set of colleagues and friends in the process.

Initially I would like to thank my supervisors Martin Knight and David Lee for obtaining the grant and employing me to conduct this work. The assistance with completing this thesis has been most welcomed and would not have been possible without your help.

I would also like to extend my thanks to the people who provided me with exciting opportunities to test my experiments on their systems. Robin Maytum in the biology department offered the use of absorption spectrometer. Ignacio Hernandez and Bill Gillin in the physics department facilitated the use of their luminescence system. Klaus Suhling at Kings provided the use of their single-photon confocal TCSPC system for comparison studies. Boris Vojnovic provided intellectual stimulation and continued interest in the development of the project, without which all enthusiasm might have been lost, for which I am indented to you.

The progress of the work took place in two places the laboratory and the office. Here two groups of people have kept the bounce in my step and push in my stride! They were the ones that made this PhD entertaining and a big thanks will have to go out to the lab group: Angus Wann, Afshin Anssari-Benam, Kirsten Legerlotz, Hannah Heywood and Lauren Shor. Also the most important group being the 'office boys' without whom life would not have been as interesting or amusing. These righteous people consist of Percy Song, Steffanie Hunk, Fed Christ, Milan Rayamajhi, Osman, 'the boy' Henry Clarke and his treacle Clarise Sarell.

I would like to thank my family Mum, Dad, Shereen and Georgina for always being around and providing me with lost of love and support! I would also like to thank my extended family Pekka and Anna who are always so interested in what is happening and always offer their support and love, Thank you!

Finally and by no means least I will thank Raisa, who without which I would never have endeavoured on this crazy journey or managed to complete it without you constantly being there for my every need. The last mention goes to Indy Croft who is the coolest mini man on the planet and always knows how to cheer you up with a wiggle.

Well that's me signing off and for whoever picks up this thesis 'you're dangerous!'

# Abstract

Extracellular oxygen concentrations affect cellular metabolism and influence tissue function. Detection methods for these extracellular oxygen concentrations currently have poor spatial resolution and are frequently invasive. Fluorescence Lifetime Imaging Microscopy (FLIM) offers a non-invasive method for quantifying local oxygen concentrations. However, existing FLIM methods also show limited spatial resolution >1 μm and low time-resolved accuracy and precision, due to widefield time-gate.

This study describes a new optimised approach using FLIM to quantity extracellular oxygen concentration with high accuracy (±7 μmol/kg) and spatial resolution (≅ 0.3 μm). An oxygen sensitive fluorescent dye, tris(2,2′-bipyridyl)ruthenium(II) chloride hexahydrate $[Ru(bipy)_3]^{+2}$, was excited with a multi-photon laser and fluorescence lifetime was measured using time-correlated single photon counting (TCSPC). The system was fully calibrated with optimised techniques developed for avoiding artefacts associated with photon pile-up and phototoxicity, whilst maximising spatial and temporal resolution. An extended imaging protocol (1800 sec) showed no phototoxic effects on cells at dye concentrations of <0.4 mM. Extracellular spatial oxygen gradients were identified around isolated chondrocytes, seeded in three-dimensional agarose gel. The technique was validated by regulating oxygen cellular consumption and thus confirming that the oxygen gradient was governed by cellular consumption. The technique identified a subpopulation of cells exhibiting statistically significant spatial oxygen gradients at the cell perihery. The subpopulation was shown to be significantly larger in cell diameter correlating with what that expected from chondrocytes in the deep zone. This technique provides an exciting opportunity to non-invasively quantify pericellular spatial oxygen gradients from within three-dimensional cellular constructs without prior manipulation of the cells. Thus by examining cellular metabolisms it will advance our understanding of the optimal cellular environment for tissue engineering and regenerative medicine.

# Table of Contents

## CHAPTER 1 • INTRODUCTION



## CHAPTER 2 • OXYGEN DETECTION TECHNIQUES

# Index of Figures

# Index of Tables

## Publications

**Neveen A. Hosny**, David A. Lee, Martin M. Knight. "Extracellular oxygen concentration mapping with confocal multiphoton laser scanning microscope and TCSPC card" *Proc. SPIE, Vol. 7569, 756932 (2010)*

## Abbreviations

| | |
|---|---|
| AB | AlamarBlue |
| ADC | Analogue to digital converter |
| AFP | Actual focus postion |
| ANOVA | Analysis of variance |
| AOBS | Acoustic-optical beam-splitter |
| AOM | Acoustic optical modulator |
| Atm | Atmosphere |
| ATP | Adenosine-5'-triphosphate |
| BSA | Bovine serum albumin |
| CFD | Constant fraction discriminator |
| CODATA | The committee on data for science and technology |
| CT | Computational tomography |
| DCM | Dichloromethane |
| DMEM | Dulbecco's modified eagle medium |
| DNA | Deoxyribonucleic acid |
| ECM | Extracellular matrix |
| EOM | Electro-optical modulator |
| EPR | Electron paramagnetic resonance |
| FAD | Flavin adenine dinucleotide |
| FBS | Fetal bovine serum |
| FCS | Fluorescence correlation spectroscopy |
| FD | Frequency-domain |
| FITC | Fluorescein isothiocyanate |
| FLIM | Fluorescence lifetime imaging microscopy |
| FOV | Field of view |
| FRET | Fluorescence resonance energy transfer |
| FWHM | Full width half maximum |
| GAG | Glycosaminoglycan |
| GUI | Graphical user interface |
| GVD | Group velocity dispersion |
| HEPES | 4-(2-hydroxyethyl)-1-piperazineethanesulfonic acid |
| IC | Internal conversion |
| IMS | Industrial methylated spirits |
| IRF | Instrument response function |
| ISC | Intersystem crossing |
| IUPAC | International units for physics and chemistry |
| LASER | Light amplification by stimulated emission of radiation |
| LED | Light-emitting diode |
| LMS | Laser scanning microscope |
| MCP | Micro-channel plate |
| MLC | Metal ligand complex |
| MLE | Maximum likelihood estimator |
| MP | Multi-photon |
| MRI | Magnetic resonance imaging |
| NA | Numerical aperture |
| NAD | Nicotinamide adenine dinucleotide |
| NFP | Nominal focus position |
| NIO | near-infrared oximetry |
| NIR | Near infra-red |
| NMR | Nuclear magnetic resonance |
| OPO | Optical parametric oscillator |
| PAH | Polycyclic aromatic hydrocarbons |
| PAM | Photoacoustic microscopy |
| PAT | Photoacoustic tomography |

| | |
|---|---|
| PBA | Pyrenebutyric acid |
| PBS | Phosphate buffered saline |
| PDT | Photodynamic therapy |
| PEG | Poly(ethylene glycol) |
| PET | Positron emission tomography |
| PGA | Programmable gain amplifier |
| PMT | Photomultiplier tube |
| PSF | Point spread function |
| PTFE | Polytetrafluoroethylene |
| RC | Resistor-capacitor |
| REDOX | Oxidation-reduction |
| RF | Radio frequency |
| RNA | Ribonucleic acid |
| ROI | Region of interest |
| ROS | Reactivive oxygen species |
| SHG | Second harmonic generation |
| SNYC | Synchronised count |
| SOP | Standard operating procedure |
| SPCImage | Single photon counting image |
| SPCM | Single photon counting module |
| SPE | Single-photon excitation |
| STZ | Superfical zone |
| SYNC | Synchronisation |
| TAC | Time-to-amplitude converter |
| TCSPC | Time Correlated Single Photon Counting |
| TD | Time-domain |
| TPA | Two-photon absorption |
| TPE | Two-photon excitation |
| TRITC | Tetramethylrhodamine-5-(and 6)-isothiocyanate |
| TTS | Transit time spread |
| UV | Ultra-violet |

# Introduction 1

The maintenance of normal physiological homeostasis in animal tissue is dependent on the delivery of key nutrients and metabolites to the resident cells. Oxygen is required for the efficient generation of adenosine-5'-triphosphate (ATP) via aerobic respiration and for many other cellular processes. The delivery of oxygen to tissues *in-vivo* is achieved primarily via the cardiovascular system and through diffusion across short tissue distances to cells. Some tissues such as articular cartilage are avascular and rely on diffusional delivery of oxygen over distances of up to several millimeters. Alterations in the local oxygen environment can have profound effects on cellular activity, potentially affecting cell viability, metabolic activity and differentiation state. As such, alterations in the effective provision of oxygen to tissue plays a role in a variety of pathological conditions including reperfusion injury, ischemic heart disease and various types of cancer. The appropriate provision of oxygen is also critical for the *ex-vivo* development of neo-tissue for a variety of cell-based tissue engineering therapies.

In cell based therapies oxygen plays an important role for the growth of cells in culture and influences their expansion and differentiation [151]. For example, in cartilage based tissue engineering, changes in oxygen levels have profound effects on chondrocytes affecting phenotype, gene expression, morphology and response and production of cytokines [93]. A major hindrance to the development of three-dimensional cell-based regenerative therapies stems from the delivery and monitoring of oxygen. Due to the restricted size of cell culture constructs (<5 mm dia.) current detection methods use either global consumption rates to define the oxygen usage [126], single point spatial information using non-invasive phosphorescence [104] or invasive probes [51]. Essentially the main drawback of these techniques is the global nature of the measurement and the limited spatial resolution. There is currently a lack of suitable oxygen detection method that can accurately quantify low oxygen concentration and provide non-invasive measurements at high spatial resolution (<500 nm) with anatomical registration.

Accordingly, this thesis will focus on the development of an appropriate oxygen detection system that will be applied in a cellular based tissue engineering context of

anatomical relevance. This chapter provides a greater depth of detail from the above discussion emphasizing the importance of oxygen in cell biology and cell-based therapies. Current oxygen detection technologies will be further reviewed and the selection narrowed based on a set of specified criteria for further investigation. Chondrocytes will be used as the chosen cell model for these tests and detail of their morphology, functionality and structural environment will be reviewed.

## 1.1 Oxygen in biosynthesis

Cell and animal development, maintenance of normal tissue and repair response to tissue injury, rely on the cohesive co-ordination of physiological processes [288], which operates via a highly complex series of pathway signals between extracellular and intracellular compartments in diverse environments [288]. Regulation of this homeostasis requires energy derived from high energy carrying electron molecules i.e. Nicotinamide adenine dinucleotide (NAD), Flavin adenine dinucleotide (FAD), and most importantly ATP [5]. The efficient and effective production of ATP is maintained via aerobic respiration involving oxygen as the final receptor of the electron transport chain. Aerobic respiration is achieved with dimolecular oxygen being converted in a step-wise process through a set of reactive oxygen species (ROS) and finally released as water [5].

The purpose of dioxygen is to facilitate three functions: complete the production of ATP in aerobic respiration, to aid the biosynthesis of various molecules in metabolic pathways and conversion of lipid soluble molecules into water soluble form [138]. Conversion of dioxygen into radicals also provides a host of activation energies with constructive and destructive consequential outcomes for cells [138]. Further discussion will focus on two main biochemical pathways involved in the utilising oxygen for energy production and the implication of oxygen radicals within the cellular environment.

### 1.1.1 Production of energy

Eukaryotic cells use molecular dioxygen ($O_2$) for a wide variety of cellular processes, most notably respiration. At the final stage of a systematic controlled network of pathways aerobic respiration produces cellular energy or ATP via oxygen involvement at the final receptor. The sequence of events that lead to the production of ATP relies on the presence of oxygen or food molecules i.e. sugars, fatty acids and amino acids. Figure 1 displays a summary of respiration and by-product production.

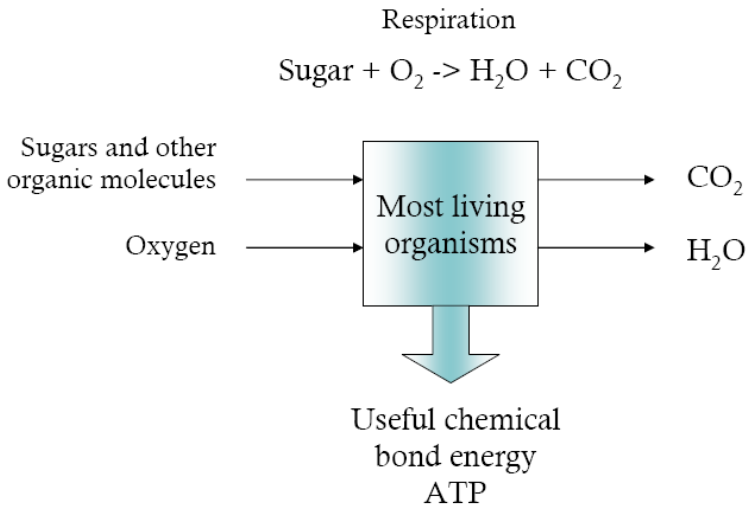


**Figure 1 – Flow diagram identifying the main requirements for most living organisms to create energy that allow cellular respiration and the waste products produced. Adapted from Alberts [5].**

ATPs importance stems from its high energy bond at its phosphate. This creates an active carrier that can supply energy for transport pumps, molecular motors or synthesis of protein, nucleic acid and macromoleculs. Over or under production of ATP can trigger a cascade of events. For example, a $Na^+$- K (sodium-potassium) pump located in the cell membrane is driven by ATP. Its purpose is to maintain osmotic balance by ensuring that the intra and extracellular sodium levels are counterbalanced otherwise the cell will shrink or expand [5]. Osmotic stress can regulate gene expression through biochemical pathways triggering chromosome condensation in the nucleus and leading to reduced production of ribonucleic acid (RNA) and therefore protein production [81]. This effect of ion concentration has been shown to affect proteoglycan production in chondrocytes [297], used in the initial stage of extracellular matrix development, leading to deficient tissue structure and impeding function [120]. This establishes the vital importance ATP control and production has on influencing the function of a cell, and alludes to the key role oxygen plays in the quantity of ATP produced.

There are two forms of energy systems that operate in a cell, one involves the use of oxygen, aerobic, and the other does not, anaerobic [160]. The major difference between the aerobic and anaerobic energy system is the quantity of ATP produced, where completion of the full aerobic pathway produces 32 ATP/glucose whereas anaerobic processes produce 2 ATP/glucose [6]. There are two major metabolic pathways involved in the production of ATP termed, glycolysis and oxidative phosphorylation, as depicted by Figure 2.

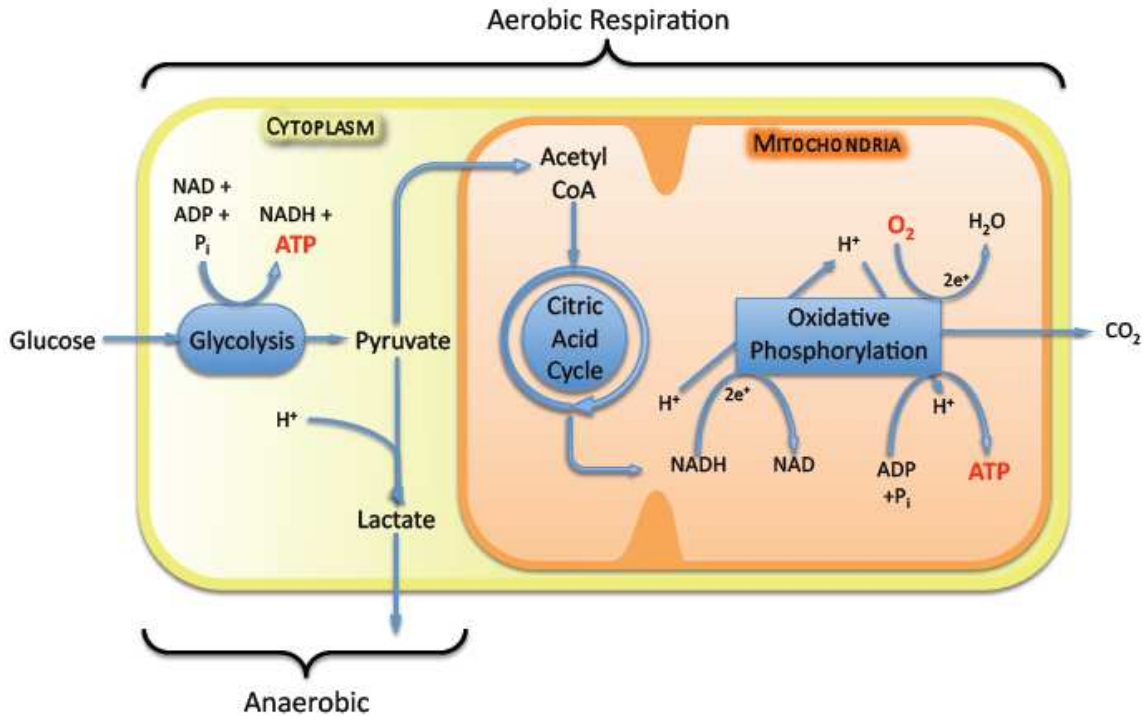


**Figure 2 – A schematic diagram of a cell cytoplasm and mitochondria displays the main cellular biosynthesis pathways involved in respiration and production of energy. Aerobic: Glucose enters the cytoplasm and is converted through glycolysis to pyruvate, enzymes convert it to Acetyl CoA where it enters the citric acid cycle and produces NADH, two high energy electron ($2e^+$) stimulate oxidative phosphorylation through the electron transport chain, driving hydride ions ($H^+$) into the mitochondrial membrane. To stabilise pH level hydride ions are sequestered back, creating ATP through the process. Anaerobic: Glucose enters cytoplasm and is converted through glycolysis to pyruvate and then transformed to lactate with the addition of a hydride ion. Not drawn to scale.**

#### 1.1.1.1 Glycolysis

In the cell cytoplasm glucose is metabolised into pyruvate through glycolysis. Briefly, the mechanism is initiated with two ATP hydrolysis converting glucose into fructose 1,6-bisphosphate, which is split into two glyceraldehyde 3-phosphates. The aldehyde groups are oxidised and phosphorylated into pyruvate producing four ATP and two NADH molecules in the process, replacing the two ATP used in the initial stages [5].

A lack of available oxygen will typically reduce oxidative phosphorylation and trigger the cell to producing ATP anaerobically under these conditions. The redundant pyruvate created at the end of the glycolysis pathway does not enter the mitochondria, but instead stays within the cytosol. As oxidative phosphorylation is not being utilised the $H^+$ ions are not being regulated so in order to maintain the increasing pH levels, $H^+$ are added to pyruvate [190]. This reduces pyruvate to lactate [16-18] and counteracts the effect of acidosis [255].

#### 1.1.1.2 Citric acid cycle

If oxygen is available pyruvate then enters the mitochondrial matrix and is oxidatively decarboxylated by the pyruvate dehydodrgenase complexes to yield acetyl coenzyme A (acetyl CoA) [160], releasing carbon dioxide ($CO_2$) in the process. Acetyl CoA enters the citric acid cycle (Kreb Cycle) where the primary function is to oxidise acetyl groups. In the process high energy electrons in the form of hydride ions (proton, $H^+$), are channelled to high energy carrier molecules $NAD^+$ and FAD to form NADH and $FADH_2$ that are used in oxidative phosphorylation [5].

#### 1.1.1.3 Oxidative phosphorylation

At the inner mitochondrial membrane the high energy electrons delivered from the citric acid cycle pass through the electron transport chain. The electron transport chain is integrated into the inner mitochondrial membrane and consists of three protein complexes I, III, and IV and two mobile carrier molecules [160] coenzyme Q/ubiqinane (UQ) and cytochrome c (Cyt c). Complex II is part of the citric acid cycle, but is assigned to the respiratory chain. In combination with complex I it accepts electrons from NADH or FADH where UQ passes the electrons on to complex III and Cyt c passes it to complex IV [160]. In complex IV (cytochrome c oxidase) dioxygen is bound to two paramagnetic metal ions and reduced in a two-electron step process to peroxide [138]. A further two electrons and four $H^+$ join in another two step process finally producing two $H_2O$ molecules [5]. Complex V is not part of the electron transport chain, but is considered to be part of the respiratory chain for synthesising/hydrolysing ATP [160].

Each complex acts as an electron-transport driven $H^+$ pump [5] effectively pumping $H^+$ into the inter membrane space with each electron triggered complex and establishing a proton gradient across the mitochondrial membrane [160]. This drives the chemiosmotic mechanism of $H^+$ flowing back through the ATP synthase complex, catalyzing the synthesis of ATP from ADP and Pi (in Figure 3) completing the aerobic energy production process.

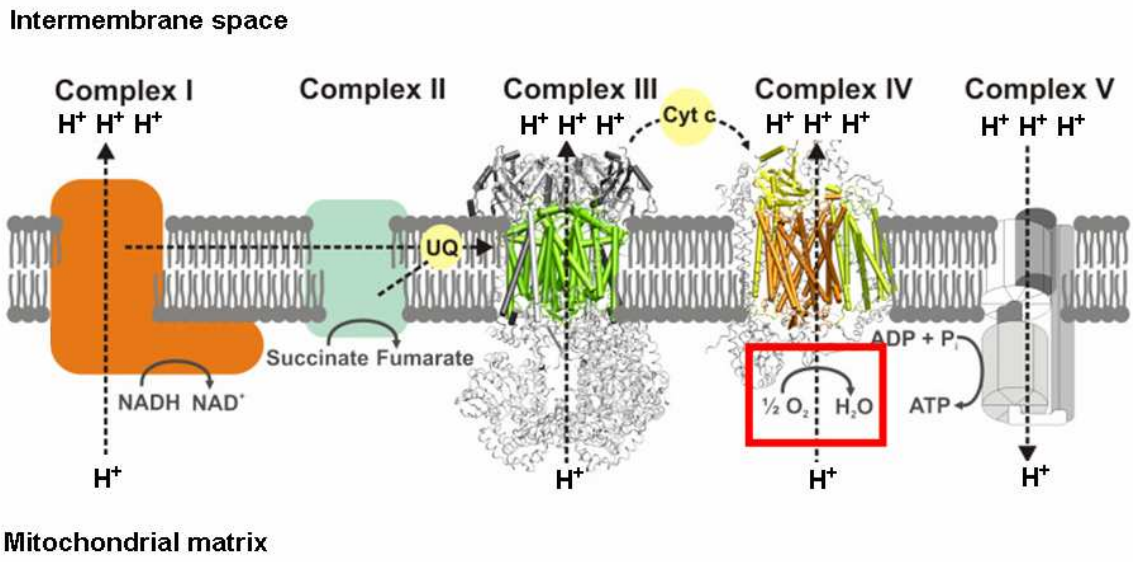


**Figure 3 – Schematic representation of oxidative phosphorylation process involving the electron transport and respiratory chain. Complexes I (NADH dehydrogenase) and II (succinate dehydrogenase) receive electrons from either NADH or $FADH_2$. Electrons are then carried between complexes by the carrier molecules coenzyme Q/ubiquinone (UQ) and cytochrome c (CYC). ATP synthesis by Complex V (ATP synthase) is driven by the proton gradient, and occurs in the mitochondrial matrix. The red box highlight where oxygen is utilised. Adapted from Fonseca [59].**

### 1.1.2 Oxygen and reactive oxygen species

#### 1.1.2.1 Oxygen processing in cellular environment

As discussed in section 1.1.1.3 cytochrome oxidase uses two metal ions to bind oxygen in place during the addition of electrons. If oxygen only obtained one extra electron and was not bound it would form superoxide ($O_2^-$) and become dangerously reactive rapidly taking up additional electrons wherever possible [5]. The addition of further electrons and protons ($H^+$) allows the superoxide conversion to hydrogen peroxide, water + hydroxyl radical and eventually water. This form of biological oxidation is thought to account for 90% of the dioxygen consumed in the biosphere [138]. Even though these radicals are used in the signalling pathways $O_2^-$ cannot pass through the cell membrane, whereas $H_2O_2$ can. The use of hydrogen peroxide is as an oxidant rather than a radical and can be found in human fluids and exhaled breath, although it can also be toxic [247].

So far only the gaining of electrons has been discussed, but through chemical or photochemical stimulation the electron spin in triplet ground state oxygen can undergo conversion to the singlet ground state, as depicted in Figure 4. Triplet oxygen will only react with other radicals, where as singlet oxygen will react rapidly with all electron rich compounds [299]. These variations of triplet oxygen are known as reactive oxygen species (ROS).

The generation of ROS has polarised implications, aiding communication in normal cell signalling pathways that can regulate cellular proliferation [288] and the destructive effects of oxidative stress, which can promote tissue degradation and damage [247]. Further discussion will focus on the importance of oxygen driving signals and the impact of oxygen toxicity.

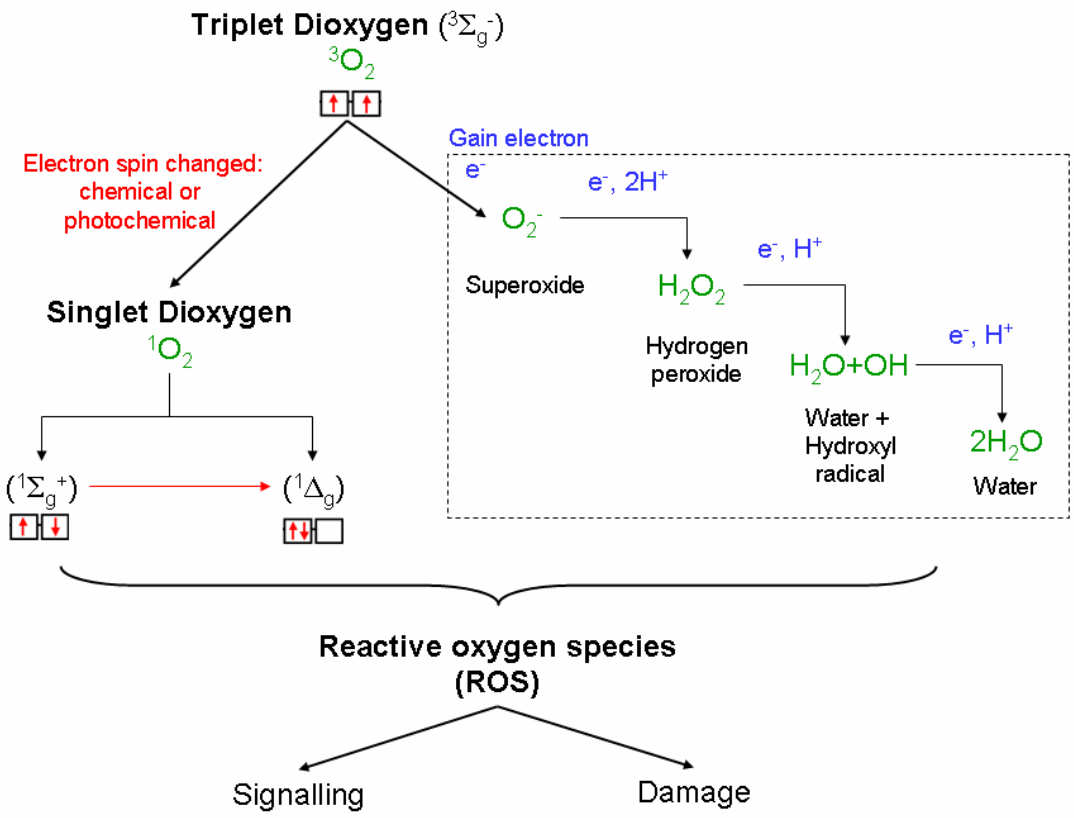


**Figure 4 – Flow diagram describing the conversion of triplet dioxygen into either singlet dioxygen or radical oxygen by electron spin change or gaining an electron, respectively.**

### 1.1.2.2 Oxygen signalling

There are two general mechanisms that can be used to describe the concept behind oxygen and ROS signalling: alteration in intracellular redox state and oxidative modification of proteins [288]. These actions can be used to maintain the cytosol in a strongly 'reduced' condition in comparison to the extracellular matrix or to critical amino acid residues that affect protein structure and function. The effect of these actions can be seen in multiple pathways within the cell, triggering signals from cell surface receptors to the nucleus [288].

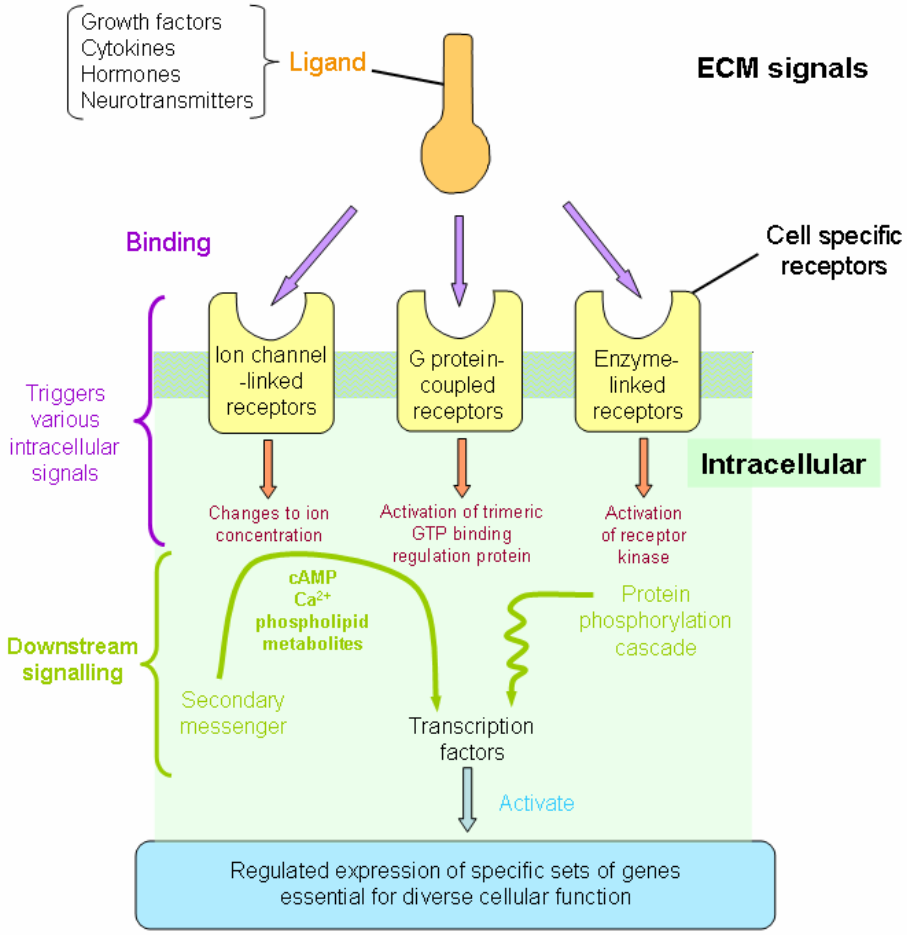


**Figure 5 – Diagrammatic example of cellular events that can be triggered from one event leading to an array of intracellular signals being stimulated by oxygen and oxygen related species. Adapted from Thannickal *et al.* [288].**

The example in Figure 5 displays receptors located at the cell membrane that trigger a variety of intracellular signals. The involvement of ROS is not identified in this diagram as the majority of the time the actual mechanistic pathway are unknown [288], but its influence is key at different stages. For example, the induced ROS production in neuronal cells by glutamates have been shown to be mutually exclusive on the changes in intracellular ion concentrations [263]. There are certain cytokines in non-phagocytic cells, that can stimulate oxidant production and appear to intersect with a host of intracellular pathways involved in growth, cell division, transformation, apoptosis, and senescence [83].

Also, a number of ligands that bind to the G protein-coupled receptors have been shown to generate ROS in different cell systems. Some of these ligands mediate cellular hypertrophy in vascular smooth muscle [253] and in cardiac myocyte [173]. The mechanism behind them is still largely unknown, but it is known that the stimulation of the G protein-RAS extends from the plasma membrane to the mitochondria leading to an increase in ROS generation [316].

ROS are also involved in a protective role killing invading pathogens stimulated by bacteria in leukocytes, but the inability to distinguish between host and pathogen leads to a loss of structural integrity and function of the surrounding connective tissue. ROS have been shown to depolymerise hyaluronan resulting in a loss of viscosity, but the presence of sulphate on glycosaminoglycan (GAG) is thought to protect the molecule [214].

The use of dioxygen in the signalling pathways also has implications with regards to oxygen consumption and has been shown to induce reduction of oxygen levels at the cell surface [123]. So far the discussion on the signalling and protective roles oxygen and oxygen related species facilitate have dominated, but their interactions with the surrounding environment have highlighted the possible detrimental effects ROS can induce and this requires further discussion.

#### 1.1.2.3 Oxidative damage

It is clear that very low levels of ROS can stimulate a host of cellular functions like cell division whereas high levels ROS can induce oxidative stress resulting in oxidative damage and eventually leading to growth arrest, apoptosis or necrosis [98]. Oxidative stress is a mechanism of oxygen toxicity and can result from increased exposure to oxidising gases or from a lowered protection against oxidants, but can occur simultaneously without one relying on the other [247]. The first level of prevention and defence are antioxidants and cell repaired system, respectively. These act to remove or restore damaged cellular components and failure to do so leads to oxidative aging and tissue damage involving proteins, lipids, carbohydrates and nucleic acid [247].

An abundance of oxygen provides the opportunity for ROS to develop. Elevated levels of oxygen (530 mmHg) have been shown to produce changes in hamster testicular tissue structure. Long term exposure at these levels resembled the tissue damaged observed in ionizing radiation and/or the effects of vitamin E deficiency. Similar levels of exposure, in rabbits, also lead to induced visual cell death [71]. The connection between hyperoxia and generation of ROS can be easily linked and causes a catalogue of disturbances in cellular metabolism, where lactate production is increased, mitochondrial morphology is altered, and intracellular ATP is depleted [190].

In cartilage ROS plays a crucial role in the regulation of chondrocyte activity involving cellular activation, proliferation, and matrix remodelling. When antioxidant concentration is reduced or the production of ROS exceeds the capable antioxidant levels “oxidative stress” leads to structural and functional cartilage damage culminating in cell death and matrix degradation [119].

Even though oxidative damage has been shown to have serious implications to cellular viability in other arenas it has been applied advantageously. In the field of cancer therapeutics, oxidative damage has been used extensively with radiotherapy. Essentially radiotherapy detaches electrons from atoms or molecules creating an abundance of free electrons. When cells are surrounded by oxygen it provides an ideal opportunity for ROS generation [38]. Tumor cells become resistant to radiotherapy at oxygen levels less than 10 mmHg. The presence of oxygen is required to create DNA double strand breaks through ROS generation. The potential difference in biological behaviour between acute and chronic hypoxia techniques using non-invasive imaging are required to determine the oxygen levels [38].

This same principle is utilised in photodynamic therapy where photo-excitation of endogenous or exogenous fluorophores generate singlet oxygen by inducing a change in the electron spin of the triple state dioxygen [189]. As this stimulus can be applied intracellularly it creates an extremely specific and targeted technique for cell death in treatment of cancerous cells.

In summary, oxygen concentrations are essentially linked to energy production of ATP, but knowledge of these levels can also provide an insight to the potential signalling and toxicity. The link between oxygen utilisation in the signalling pathway leading to effective cell consumption suggests that the monitoring of extracellular consumption would be more informative, rather than the general approach to attempt to monitor intracellular consumption [68, 71].

Although the importance of oxygen and oxygen related species has been identified, the specific role and mechanism by which they work is not fully understood. Only within the past decade has it been understood that ROS are not only involved in toxic effects on cells and tissue, but are used in signalling pathways to drive cellular function, e.g. proliferation, differentiation, and actin cytoskeleton regulation [288]. For these reasons the role of oxygen and oxygen related species in cell biology is important in diagnostic and therapeutic arenas, including tissue engineering.

## 1.2 Oxygen in regenerative therapies

The cellular functions discussed above are vital to the success of regenerative 3D cell based therapies where expansion, dedifferentiation and protein production are critical for efficacy. Cell-based therapies are designed to utilise the cell's biochemical mechanisms to perform functions that cannot be replicated by surgical interventions or drug deliveries

[232]. It also takes advantage of the cells own ability for cell production and tissue replacement. Cell-based therapies can be applied through two methods, a readily available self proficient surplus of cells as found in blood transfusion of bone marrow transplantation. The other method requires significant manipulation of cells *in vitro* and is generally described as cell and tissue engineering [232].

### 1.2.1 Tissue Engineering

Tissue engineering aims to facilitate the replacement of damaged or defective tissue by substituting donor cells from amplified autologous, allogenic, xenogenic, or syngenic sources [232]. These are typically implanted via a 3D matrix into a variety of tissues such as cartilage, bone, skin, liver, muscle or breast [58]. Cell culture is required for the expansion and structural growth, respectively attained by monolayer or three-dimensional construct. The optimal substrate selection for growth, signalling and function are cell and tissue dependent, i.e. harder based scaffolds are more suitable for bone, but not liver or breast [58]. Further discussions regarding suitable methods of culture and structural material properties will be examined in section 1.7.

In vivo cellular processes are naturally in balance due to the microenvironment communication between metabolic processes and cellular or tissue dynamics. The supporting factors of tissue engineering must deliver uniform nutrient, oxygen and growth factors. Concentrations must be homogenously distributed to approximately 100 μm, within the vicinity of the cell less than this and non-uniformity is expected, which maybe sub-optimal [232]. To resurface sections of cartilage damage it would require an engineered tissue to be grown >5 cm in thickness. Current laboratory techniques are restricted to approximately 5 mm for tissue engineered cellular constructs [286]. To optimally up-scale for cell- and tissue-culture there are several design challenges:

- Provision of tissue/cellular oxygenation [149]
- Delivery and removal of important macromolecules and waste [61]
- Managing the perfusion at physiological rates within a microenvironment [232]

All these issues are important aspects of cell culture, but the focus will be oxygen. The delivery of oxygen is restricted by the solubility and the physiological rate of fluid flow governed by the rate of cellular consumption [232]. If optimal oxygen levels are not maintained in 3D structures gradients can develop where low local concentrations will slow metabolic rates and signalling. In skeletal muscle tissue engineering, the major limiting factor is that myoblasts are unable to proliferate and differentiate further than 150 μm from the nutrient source and oxygen supply [159]. Elevated local oxygen levels will

increase ROS and oxidative stress causing tissue or cellular damage that eventually leads to apotosis, or necrosis as has been shown in chondrocytes [120]. If sufficient supply cannot be maintained or waste products removed from around the cells, the development of tissue will slow or fail completely [35, 36]. Therefore parameters such oxygen concentration and pH must be carefully monitored and controlled [61].

Identification of oxygen consumption rates provides an estimate of the ideal requirements for the cells, but establishing this relationship is complex. The optimum level of oxygen delivery is consumption dependent based on the specific uptake rates of different cell types. For example, in bone-marrow this can vary between 0.7 fmol/cell/h for lymphocytes to 14.4 fmol/cell/h for megakaryocytes [53]. It has even been shown that within the same cell types there are differences in oxygen consumption rates based on the original location of the cells from the native cartilage tissue, as shown in Table 1. Subpopulations have also been noted in cancer cells where current research in clinical oncology is focusing on detecting these subpopulations to determine the effects on prognosis and response to radiotherapy [38]

**Table 1 – Selection of cell types with subpopulations exhibiting different oxygen consumption rates [127]**

| Cell type | Location dependence | Maximum oxygen consumption rates (fmol/cell/h) | Studies |
|---|---|---|---|
| Bovine chondrocytes | Superfical | 3.2 | Heywood et al. [127] |
| | Deep | 6.6 | |
| Avian growth plate cartilage | Prehypertrophic | 37.4 | Haselgrove et al. [117] |
| | Hypertrophic | 93.6 | |
| Porcine intervetebral disk | Annulus fibrousus | 6 | Huang et al. [115] |
| | Nucleus pulposis | 11.5 | |

Table 1 presents the different oxygen consumption rates, but to observe and determine these rates requires the cellular subpopulation to be separately extracted prior to culture [127]. Adding to the complexity it is established that the effective diffusion [298] and the diffusion coefficient [133] of macromolecules and oxygen in three-dimensional supporting structures are influenced by the type of material [176]. It has been shown that the effective diffusion in scaffold materials can also vary greatly [176], e.g. diffusion in the small intestine and urinary bladder submucosa was found to vary between $2.43 \times 10^{-6}$ to $6.61 \times 10^{-6}$ $cm^2/s$ compared with a commercially available synthetic polyethylene based vascular graft, Darcon™ reported to be $46.67 \times 10^{-6}$ $cm^2/s$ [298]. There are even differences between synthetic materials like agarose and aliginate; the diffusion coefficients of oxygen at the same temperature (30°C) and concentration (2% (w/v)) is $2.6 \times 10^{-5}$ $cm^2/s$ and $2 \times 10^{-5}$

$cm^2/s$, respectively, which is about 10% and 30% less than that in pure water [133]. These differences can be due to pore sizes [242] and material charge density/electrical conductivity [103].

Therefore the ability to determine, spatially, concentration changes is an important factor in the assessment of optimal oxygen delivery. This is also time for treating and diagnosing diseases involving avascular tissue, like cancer radiotherapy treatment [39] or the onset of rheumatoid or osteoarthritis cartilage [102]. The general problems of determining these values derive from the capability of monitoring oxygen concentration *in situ*. Measurement of the media surrounding the cells provides a simple and effective means of extracting the global oxygen concentration over time providing a method of determining the consumption rate. As discussed previously, oxygen concentrations are required to be homogenously dissipated at spatial resolutions >100 μm. Therefore, monitoring or measuring techniques should provide the ability to acquire oxygen concentrations at spatial resolutions of <100 μm. In monolayer culture this is easily resolved as cells lay on a flattened surface and are approximately 10-100 μm in diameter and therefore depth is not an issue. The measurement becomes complex when cells are seeded in a three-dimensional matrix requiring a non-invasive technique to avoid penetrating the substrate and damaging the cells or tissue. Further investigation will now focus on the available detection methods for oxygen concentrations in three-dimensional structures.

## 1.3 Oxygen detection techniques

A variety of instruments exist that are capable of detecting oxygen in gas, liquid, and tissue samples. These vary in size from small microelectrodes to large magnetic resonant scanners both capable of *in-vivo* or *in-vitro* investigation. The decision of method and technique rests with its suitability for the intended application. Certain instrumentation is developed for the sole purpose of measuring oxygen, while others are adapted to extract the same relevant information. Some techniques designed to measure oxygen may therefore not be necessarily suitable for the intended application of three-dimensional cell based investigation.

### 1.3.1 Detection methods

Mass spectroscopy requires samples to be vaporised (>300°C) prior to irradiating them with an ionizing beam. This separates and sorts the charged particles according to mass-to-charge ratio and has been used to monitor patients oxygen levels during surgical

operations to maintain optimal anaesthesia [220]. This technique can only be applied to gas and liquid samples and provides no spatial resolution.

Other methods use the number of detected protons to determine the concentration. Nuclear magnetic resonance (NMR) does this by applying an external magnetic field to the sample, that aligns the nuclei spins, whilst a separate radio-frequency pulse sends the nuclei spins out of alignment. The rate of recovery to the original alignment relates to the environment and the produced peak describes the number of protons and therefore the concentration. Unfortunately this does not provide spatial registration or resolution [157]. Another method that uses the same principle, but instead the recovery time is used to produce image contrast between different tissues is called blood oxygen limited diffusion magnetic resonance imaging (BOLD MRI). This method has been used to provide qualitative data that differentiates between oxygenated and deoxygenated blood, but it can only be used on haemoglobin, suffers with sensitivity issues induced by volume and flow and does not provide quantitative information [164].

Instead of using protons some methods work on measuring electrons, such as electron paramagnetic resonance (EPR). It is restricted to chemical species that only exhibit unpaired electrons, by absorbing microwaves within a magnetic field it changes the chemical species spin state. The wider the absorption peak the higher the concentration of oxygen present. Although it does provide quantitative spatially resolved measurements of oxygen there is no spatial registration with regards to the sample [78]. Another method that determines the oxygen levels based on the absorption characteristics of electrons is near-infrared oximety (NIO). This instead uses infra red light, which passes through tissue and is absorbed by blood. Currently it can only be used on haemoglobin and provides no spatial registration or resolution [164]. A summary of these techniques is shown in Table 2.

**Table 2 – Summary of individual oxygen detection instruments**

| Techniques | Method of Measurement | Problems |
|---|---|---|
| Gas chromatography/ Mass Spectrometer | Sorts particles accordingly to a mass-to-charge ratio | Only gas and liquid samples and no spatial resolution |
| Nuclear Magnetic Resonance (NMR) | Area under the peak describes the number of protons and therefore concentration | No spatial registration with regards to sample or resolution |
| Blood oxygen limited diffusion magnetic resonance imaging (BOLD MRI) | This is used qualitatively to differentiate between oxygenated and deoxygenated blood | Only used on haemoglobin, sensitivity issues from flow, not quantitative |
| Electron Paramagentic Resonance (EPR) [78] | The larger the absorption the more oxygen is present i.e. the line is broadened | No spatial registration with regards to sample |
| Near-Infrared Oximetry (NIO) | The absorption characteristics define the oxygen level in haemoglobin. | No spatial registration or resolution and only used on haemoglobin. |

Individually these techniques do not meet the basic requirements of providing spatial resolution or the ability to measure oxygen concentrations without tissue restriction. Specifically designed and combinations of the above methods are available that do facilitate spatial resolution. These techniques can be categorised into two classes of method that are respectively invasive and non-invasive.

### 1.3.2 Invasive detection

Two techniques that embody this method are optical and electrode probes. Individually the probes do not provide location resolved registration of measurement, but can be, and indeed have been, combined with computational tomography (CT) or ultrasound [164] to identify positional information. The optical sensor operates via optical fibre light stimulation of an embedded fluorescent sensor generally contained within a silica gel [101, 102] or sol-gel [103, 104] matrix. Light excites the fluorophore at its specific wavelength and returns the measured emission to a detector. The measured intensity or lifetime is then converted to reflect oxygen pressure or concentration. It has been used to determine oxygen gradients within collagen based tissue engineered matrixes for assessing the release of vascular endothelial growth factor triggered by tissue hypoxia [51]. Unfortunately the scaffold must be penetrated by the optical probe creating an invasive procedure. It has also been used frequently in aquatic biology to determine oxygen depth gradients in sediment [154].

The second probe type consists of two different metal electrodes where one is polarised when oxygen contacts the surface and reduces it to water. The reduction causes an oxidation at the second electrode and creates a current proportional to the concentration of oxygen. Each reaction effectively consumes oxygen in the process, where the rate of electrode oxygen consumption is approximately 0.4 - 5 pmol/h [295]. This might seem insignificant when measuring global consumption of a population of cells, but when compared with the individual cellular consumption rate shown in Table 1 it will have a marked effect. A population of at least 50-100 cells would be required to counteract the consumption rates of the probe. The low level of cellular oxygen consumption highlights the electrode interference, which is avoided with the use of a fluorescent optical probe. However, electrodes have been widely used for monitoring oxygen levels [308] from monolayer cell culture of isolated rat alveolar type II cells [191], to providing transcutaneous oxygen measurement for determining blood oxygen levels [239]. Disadvantages include long-term instability, sterilisation problems, sensor drift, difficulty of adaptation to continuous monitoring, automation for high-throughput measurement, and susceptibility to electrical interferences when used in bioreactors [124, 126]. But the electrodes spatial resolution is superior to the optical probe and can be custom made to approximately 3 μm [106].

### 1.3.3 Non-invasive detection

There are a variety of techniques available that can perform oxygen detection non-invasively such as PET, combinations of previously discussed techniques such as MRI and EPR, and luminescence.

#### 1.3.3.1 Positron emission tomography

Positron emission tomography (PET) can be used to determine oxygen concentrations in tissue by inhalation of oxygen [$^{15}O$] [245]. It requires use of MRI or CT to provide an anatomical image of the physiology upon which PET measurements can be registered. The radioactive material $^{15}O$ has a half-life of 122 sec and in the process of decaying it emit positrons (anti-electrons), which collide with electrons to produce gamma rays. Two gamma rays emit in opposite directions and are captured from sample/subject by the surrounding PET scanner. When oxygen is utilised in a specific area of the tissue hot spots are observed and can be quantified. The main problems associated with this technique tend to be the overestimation of blood oxygen levels, the inability to record measurements from within disorganised vasculature or tissue [245], and it is not a direct measurement of concentration, but rather the activity level of metabolism [16].

#### 1.3.3.2 Combined MRI, NMR and EPR

As discussed previously in section 1.3.1 the MRI, NMR or EPR are individually not suitable for the intended application, but when combined they compensate for lack of suitability. Using MRI and NMR together provides the ability for anatomical registration gained by the MRI scanner, while the NMR specifically measure the concentration of oxygen from a reporter molecule at the location defined by the size of the MRI voxel. This can achieve a spatial resolution of approximately 1-1.25 mm [323], oxygen detection accuracy of 1-3 mmHg and due to the reporter molecules slow excretion from the body, long term repeatable measurements of up to 40 days [157] [323]. The main issue is the effect of flow artefacts on sensitivity [157] and most importantly the limited number of MRI scanners fitted with the ability to perform fluorocarbon NMR [323]. The same lack of availability exists for the combined MRI and EPR systems [163], but again a spatial resolution of approximately 1-1.8 mm is achievable with the production of three-dimensional maps. A reporter molecule is still required for the detection of oxygen and the accuracy is limited to 4-5 mmHg of oxygen [194], therefore it is not as sensitive as the MRI and NMR.

#### 1.3.3.3 Photoacoustic tomography/microscopy

Photoacoustic tomography/microscopy (PAT/PAM) is a hybrid of visible/infrared laser pulses and ultrasound transducers used for excitation and for signal detection, respectively. The combination allows endogenous molecules or contrast agents to absorb light (electromagnetic waves), and undergo a rapid temperature rise that leads to an increase in pressure at the illuminated volume. An ultrasonic emission is generated that can be detected by ultrasound transducers, revealing specific physiological absorption from up to 3 mm in depth, used to form 3D maps [164, 174]. It has been used for blood oxygen mapping and *in-vivo* determination of the size and position of melanoma below the skin [229]. It has more recently been successfully applied to oxygen sensitive dyes providing a penetration of at least 2-3 cm [17]. The lateral and axial spatial resolution is >45 μm and >15 μm, respectively, and currently restricted by the size of the ultrasound transducer. It does provide some of the highest spatial resolution out of all the techniques discussed, but it is not enough to resolve at the individual cell level.

#### 1.3.3.4 Luminescence

The luminescent techniques are all based on microscopes using either wide-field or confocal systems, providing the facility for spatial resolution and location registration. The principles of all the luminescent techniques are essentially the same as the optical sensor,

using an excitation light to stimulate a fluorophore and a detection method to capture the emitted light. The available systems can be divided into the two forms of measured emission, phosphorescent and fluorescent. Another distinction can be made from the type of excitation used, continuous, single-photon or two-photon. Phosphorescent measurement methods tend to be used with porphyrin based dyes, such as Oxyphor R2, as the emitted lifetimes are very long [104]. Long lifetimes hinder the collection of light and restrict the ability of achieving high spatial resolution. Even with the use of a confocal [320] or two-photon [82] system the resolutions are still restricted to 1 μm. These very long lifetimes also provide more time for cellular interactions to influence the measurements [171]. The advantage of fluorescent measurement is the improvement in resolution when using a confocal system (<300 nm) [91] compared with a wide-field microscope [324]. Even so using a higher numerical aperture objective to achieve high spatial resolution restricts the measurement depth that can be achieved. A summary of the techniques discussed is shown in Table 3, with identified parameters of interest.

**Table 3 – Comparison of available oxygen detection techniques**

| | Method | Techniques | Spatial resolution | Acquisition time | Range | Imaging capability | Accuracy | Delivery | Problems |
|---|---|---|---|---|---|---|---|---|---|
| Invasive | Optical sensor | Oyxlab $pO_2$ ™ Oxylite probe. Platium-based fluorophore in a silicone matrix | Estimated >500μm (350-700 μm tip dia.) | <10 sec | 0-60 mmHg | No image, Single point, depth defined by length of probe | 0.7 mmHg; 0.46% $O_2$ | Penetrates tissue / construct | No spatial registration must be used with other techniques, invasive [231]. |
| | | Presens sensor type: PSt1 or TOS7 taper sensor excited fluorophore | Tip size <50-140 μm outer diameter 140-900 μm | <1-15 sec (gas) <2-30 sec (liquid) | 0-375 mmHg (0-50%$O_2$) 0-22 mmHg (0-3%$O_2$) | No image, Single point, depth defined by length of probe | ±0.4% at 20.9% $O_2$ ±0.05% at 0.2% $O_2$ | Penetrates tissue / construct | No spatial registration must be used with other techniques, invasive. Lifetime 5 years [246]. |
| | Electrode probe | Unisense Oxygen probe Clark-type sensor | Estimated >16μm (8-800 μm tip dia.) | < 0.3 sec | 0-760 mmHg | No image, Single point, depth defined by length of probe | 0.3μM; 0.14% $O_2$ | Penetrates tissue / construct | Same as above, but aslso sensor consumes $O_2$ $4x10^{-4}$-$5x10^{-3}$ nmol/ hour. Lifetime 1 year. [295]. |
| Non-invasive | PET | Positron Emission Tomography ionizing radiation | 9.45 mm | 6 sec / frame | 0-760 mmHg | Yes, 3D map | Undefined | Inhalation of [$^{15}O$] – $O_2$ | Overestimates bloody oxygen levels, cannot measure in disorganised vasculature or tissue, ionizing radiation [245]. |
| | MRI + NMR | Fluorocarbon MRI - $^{19}F$, FREDOM | 1-1.25 mm | 2-6.5 min / image | 0-120 mmHg | Yes, long term repeatable measurements up to 40 days | 1-3 mmHg if > 5 mmHg; 0.7-2% $O_2$ | Hexafluorobenzene (HFB) reporter molecule | Lack of systems have this and can suffer from flow artefacts [323]. |
| | | PISTOL - proton imaging of silanes for tissue oxygen levels | Undefined | 3.5 min / image | 0-160 mmHg | Yes, long term repeatable measurements | 3 mmHg; 2% $O_2$ | Hexamethyl-disiloaxane (HMDSO) | Not as sensitive as fluorocarbon based MRI [157]. |

| | Method | Techniques | Spatial resolution | Acquisition time | Range | Imaging capability | Accuracy | Delivery | Problems |
|---|---|---|---|---|---|---|---|---|---|
| Non-invasive | MRI + EPRI | EPRI with MRI and Overhauser enhanced MRI | 1-1.8 mm | 3D EPR scan 8 min | 0-40 mmHg | Yes, 3D map | 4-5 mmHg; 2.6-3.3% $O_2$ | Injection with triarylmethyl | Not in widespread use as requires specialised equipment [163, 194]. |
| | PAM/PAT | Photoacoustic microscopy/ tomography | 45 μm lateral (x-y) 15 μm axial(z) | 160 min 2D image 8x8 mm | Undefined | Yes, up to 3 mm in depth | Undefined | Injection of fluorescent microspheres or dye | Mircospheres (>16 μm) cannot pass through capillaries [322]. Oxygen sensivity dye untested with cells [17]. |
| | Luminescence | Phosphorescence - wide area illumination | 20 - 100 μm | 17 sec range / point | 0-60 mmHg | No, single point; depth 1mm - 800 μm | Undefined | Oxyphor R2 [Pd-meso-tetra(4-carboxyphenyl) porphine] | Restricted resolution and can only produce single point registration [104, 268]. |
| | | Phosphorescence - confocal | 1 μm lateral, 2.4 μm axial | 30-50 ms / point | 0-159 mmHg | Yes with confocal, but only single point O2 measurements | Undefined | Oxyphor R2 | Does not provide oxygen map, but has spatial resolution and registration [241, 320]. |
| | | Phosphorescence - two photon | 1 μm - 2.5 μm | 0.5 ms | 0-159 mmHg | Yes, fluorescence and anatomical image; depth 2.2 mm | ±2.5 mmHg; 1.6% $O_2$ | Oxyphor R2, Phosphorescent probe PtP-C343 | Loss of spatial resolution to increase number of photons collected, low two photon absorption [79, 82, 208]. |
| | | Fluorescence - widefield CCD | 150 μm illumination, but CCD not specified | 20 sec | 0-300 μM | Yes, 2D map | 8 μM; 0.8% $O_2$ | $[Ru(bipy)_3]^{+2}$ | Resolution limited by wide field and accuracy limited time-gating [279, 324]. |
| | | Fluorescence - confocal | Estimated 193 - 240 nm (x100 obj, NA 1.25) | 100-400 sec, 256 x 256 - 512 x 512 | <0.02 - 300 μM | Yes, working distance 180 μm | 2% $O_2$ | $[Ru(bipy)_3]^{+2}$ | Depth of access restricted by working distance of objective lens [91] |

The list in Table 3 provides a large amount of information on the discussed techniques and highlights the variety available. Therefore, to reduce the selection, a criterion based on prior discussions about oxygen in tissue engineering has been used to produce a list of specifications:

- High spatial resolution (<100 μm)
- High accuracy of oxygen concentration (<5 mmHg)
- Non-invasive
- Detection of oxygen in all tissues types
- Capability of registering measurement relevant to a physical location
- Not restricted to surface measurements
- Capability of tissue/construct sample measurement

Applying the above criteria to the techniques discussed in Table 3 and focusing on the spatial resolution limit and oxygen detection capability it reduces the selection of techniques down to the invasive probes (electrode and optical), PAM and all the luminescence techniques. Moving to the next set of specifications the technique must perform non-invasive measurements and have the ability to detect oxygen in all tissue types this excludes the probes and PAM techniques. This leaves only non-invasive luminescent methods that fulfil the required criteria. The advantage of using these methods are the flexibility associated with investigating of other metabolites within the same environment from endogenous or exogenous fluorophores. A more detailed evaluation of luminescence and the mechanism, process of stimulation and measurement follows.

## 1.4 Oxygen detection method based on luminescence

### 1.4.1 Luminescence

Luminescence is the emission of light from any substance and occurs from electronically excited states [170]. The emission of 'cold light' (luminescence) is the response to an input of energy [249]. The type of energy differentiates the types of luminescence that is seen, but luminescence is not associated with thermal or electric energy like incandescent light [249], some examples are shown below:

- Bioluminescence – results from biological process, e.g. light from glow-worms and other organisms like bacteria [249].

- Chemiluminescence – light emitted as a result of (cold) chemical reaction [249]
- Sonoluminescence – compressed sound wave collapse gas bubble to produce a picosecond flash of light [21].
- Triboluminscence – application of mechanical energy to a solid creates an emission of light, e.g. scraping a knife against a hard sugar cube produces a spark [328].
- Radioluminescence – luminous paint contains a compound which glows when radioactive particles interact with it [249].
- Photoluminescence – light produced by illuminating a compound with photons (electromagnetic radiation) [249].

The type of luminescence used in the detection methods previously discussed is photoluminescence and is formally divided into two categories, phosphorescence and fluorescence, dependent on the nature of the excited state [170].

### 1.4.2 Photoluminescence

Photoluminescence is produced when a fluorophore is excited with a stimulating light sending an electron into a high energy state. Once there a decay process occurs where an emission of light is produced upon the high energy electron returning to ground state. In Figure 6 a fluorophore molecule is represented by a simplified Bohr-model, which displays the electron orbital shells surrounding the atom, no vibrational levels are associated with the atom only electron molecules. The location of electron excitation is identified by the Bohr-model the excitation and emission mechanism involved in photoluminescence can be effectively described using a simplified Jablonski diagram.

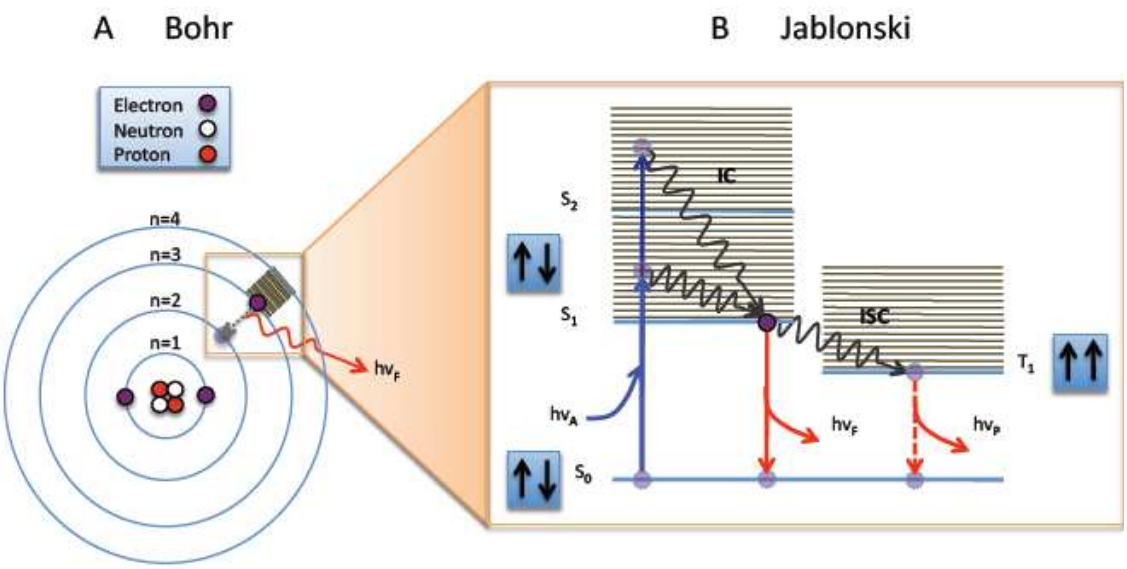


**Figure 6 – Pictorial representation of the mechanism of excitation and emission. A: Simplified Bohr-model of a molecule. B: Simplified Jablonski diagram describing the molecular electronic transitions occurring between the valences of the atom, S0, S1, S2, Sn – singlet states, 0 – denotes ground state, 1,2,n denote excited states, T1 – triplet state. Adapted from Suhling [280] and Lakowsic [171].**

The energy difference between $S_0$ (singlet ground state) and $S_1$ (singlet lowest unoccupied molecular orbit) is too large for thermal stimulation therefore light is required to induce fluorescence [171]. The electrons in the highest occupied molecular orbit can be excited by electromagnetic radiation to an unoccupied molecular orbit [75]. Internal conversion (IC) relaxes the electrons through the vibrational energy levels, via thermal dissipation, to equilibrate to the $S_1$. Fluorescence emission occurs by the activated molecule electron releasing its energy between $S_1$ and $S_0$ [171]. Electrons can also complete an intersystem crossing from $S_1$ to $T_1$ (triplet lowest unoccupied molecular orbit). The difference between singlet and triplet is defined by the orientation of the electron dipole moments, being either anti-parallel or parallel, respectively, as shown by the blue boxes in Figure 6. Transitions from $S_1$ to $T_1$ are termed intersystem crossings (ISC) and undergo forbidden triplet state spin conversion [224], but transition from $T_1$ to $S_0$ takes microseconds rather than pico- or nano-seconds as in fluorescence and is thus termed phosphorescence [171].

Examination of the Jablonski diagram reveals that energy of the emission is typically less than that of absorption, therefore fluorescence typically occurs at lower energies or longer wavelengths, as first observed by Stokes in 1852 [170] and referred to as 'Stokes shift'.

### 1.4.3 Measuring photoluminescence

Fluorescence can be measured using two methods; steady-state i.e. continuous illumination, or time-resolved i.e. pulsed or modulated light. Steady-state is more

commonly used for determining absorption or emission spectra as it ensures that all the fluorophore electrons are in an excited state [171]. Time-resolved measurements use fast detectors to record the decaying intensity over time. This measurement can provide the fluorophore lifetime or rotation, which can be used to describe the interaction of the fluorophore within its environment.

#### 1.4.3.1 Steady-state

Intensity can be used to determine absorption and emission spectra of fluorophores, by measuring the population of electrons in the high energy state [171]. This allows intensity contrast to create luminescent images through population activation, but quantitative measurements are difficult to achieve between samples and either require some form of added reference dye for cellular measurements or strict environmental controls [171].

#### 1.4.3.2 Time-resolved

Time-resolved measurements are decays with time and can be used to determine lifetime (intensity) and anisotropy (polarization). Intensity decays describes the fluorophore interaction with the environment; rotational decay describes the shape and flexibility of macromolecules [171]. The rotational decay is not relevant to the information required and shall not be discussed further. Lifetime provides an added layer of information about the local environment [100] that is independent of probe concentration, autofluorescence, cellular volume changes, and fading due to probe photobleaching [284]. Also it is unaffected by equipment instabilities such as drifts in lamp intensity and inner filter effects, which are major limitations of intensity based sensing [20].

The lifetime decay extracts information about how the fluorophore is affected by the environment, to enable measurement of the refractive index, viscosity, pH, ion concentration in-situ without disturbing the cells [281]. Another advantage of lifetime over intensity is the ability to spectrally determine the difference between dyes with the overlapping or identical spectral profiles [281]. The disadvantages compared with steady-state are associated with the complexity of analysing the data and the expense of the equipment [281]. Time-resolved lifetime decay measurements can traditionally be categorised into two main excitation methods:

- Time-domain: Pulsed light shorter than the decay of fluorophore lifetime
- Frequency- domain: Intensity modulated light

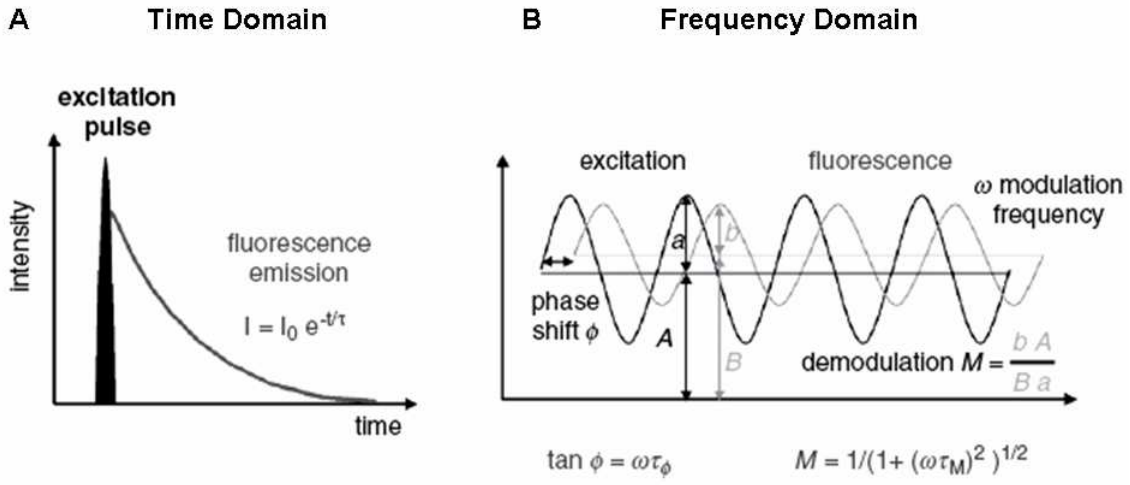


**Figure 7 – Two time-resolved methods available for the detection of lifetime. A: Uses time domain to measure the exponentially decaying fluorophore with time after an excitation pulse. B: Frequency domain measures the phase shift in the frequency modulation between the excitation and fluorescence waveforms [280].**

*Time-domain (TD)*

TD uses pulsed excitation sources shorter than the lifetime of the fluorophore to stimulate electrons and a detector records the emission in set time windows to provide a decaying response [256]. The emission process is random and each fluorophore has the same probability of emitting resulting in an exponential response $I = I_0 e^{-t/\tau}$ [171], as shown in Figure 7A.

*Frequency-domain (FD)*

The FD operates by exciting the fluorophore through an intensity modulated light source that can be continuous or pulsed [100]. The modulation frequency of the emitted emission is compared with the excitation frequency. The time-delay between the excitation and emission wavelength is measured as a phase shift angle $\tan\phi = \omega\tau_\phi$ [281]. The difference in peak-to-peak height between the excitation and decreased emission signal also provide another independent measure of lifetime $M = 1/(1+(\omega\tau_m)^2)^{1/2}$, as shown in Figure 7B [171].

*TD vs FD*

The TD and FD are related by Fourier Transformation with equivalent results [281]. The TD provides easy visualisation of the decaying fluorophore and has a less complex analysis than the FD. Although FD is seen to be easier to implement for long lifetime dyes as the equipment is simpler because there is no need for a pulsed laser. Also

there is no restriction to the rate of excitation as with TD, which requires the decay to complete before being re-excited. However, the signal-to-noise ratio has been shown to be higher for TD than for FD [281] this feature suggests that TD would be more suitable to low level emission rates.

#### 1.4.3.3 Rate of Decay

Lifetime is the product of many events occurring through the process of excitation and emission. The same processes are seen in both lifetime and intensity, except lifetime provides a higher sensitivity to the environmental changes. There are inherent components that combine to produce the final measurements, which consist of a list of rate parameters for each involved process. These describe the interaction of the light with the fluorophore and the cascade of pathways that can occur. These processes have been discussed in section 1.4.2, but the mechanisms are shown in Table 4.

**Table 4 – Identifies the various forms of donor emission, associated rate constants, and the interaction with a quencher. Adapted from Demas [64] and O'Connor and Phillips [224].**

| | |
|---|---|
| $D + hv \xrightarrow{I_a} {}^{*1}D$ | Absorption |
| ${}^{*1}D \xrightarrow{k_r} D + hv$ | Radiative rate of emission |
| ${}^{*1}D \xrightarrow{k_{ic}} D$ | Internal conversion |
| ${}^{*1}D \xrightarrow{k_{isc}} {}^{*3}D$ | Intersystem crossing |
| ${}^{*1}D \xrightarrow{k_d} product$ | Disassociation/decomposition |
| ${}^{*1}D + Q \xrightarrow{k_{2a}} D + Q + product$ | Product formation |
| ${}^{*1}D + Q \xrightarrow{k_{2b}} D^{\pm} + Q^{\pm}$ | Oxidised and reduced form |
| ${}^{*1}D + Q \xrightarrow{k_{2b}} D + {}^{*}Q$ | Donor ground state-quencher excited |

The donor ($D$) represents a fluorophore being excited by light ($hv$) where the rate of absorption ($I_a$) creates a singlet state excited donor (${}^{*1}D$) [224]. From here the methods of deactivation follow those outlined in the Jablonski diagram in Figure 6. The radiative rate of emission ($k_r$) from the excited donor returns the donor back to ground state and produces an emission of light [64]. The internal conversion ($k_{ic}$), intersystem crossing ($k_{ics}$) rate constants are described as the rate constant for intramolecular excited state deactivation and referred to as $k_q$ [64], as shown by Eq. 1. The combined non-radiative rate processes is termed $k_{nr}$ [280], as shown by Eq. 2,

**Eq. 1** $$k_q = k_{ic} + k_{ics}$$

**Eq. 2** $$k_{nr} = k_q + k_d + k_2[Q]$$

**Eq. 3**
$$k_2 = k_{2a} + k_{2b} + k_{2c}$$

where, $k_d$ is the rate of decomposition, and $k_2$ is the sum of all the bimolecular rate constants for all bimolecular excited state deactivations [64]. The bimolecular rate constant is quencher dependent and describes by how the quencher interacts with the fluorophore within that environment. Typical quenchers are oxygen, halogens, heavy metal ions, and a variety of organic molecules [28].

These non-radiative pathways reduce the probability of photon emission and the fluorescence quantum yield ($\Phi_F$) is used to describe the probability that an excited molecule will emit [64]. Substances with the largest quantum yields, approaching unity, display the brightest emission [170, 280], in terms of fluorophore fluorescence the higher the quantum yield the more efficient the measurement process [121]. It is the number of emitted photons (fluorescence) relative to the number of absorbed photons [170], and can be thought of as a ratio [280], as shown in Eq. 4,

**Eq. 4**
$$\Phi_F = \frac{k_r}{k_r + k_q + k_d + k_2[Q]}$$

**Eq. 5**
$$\Phi_F = k_r \tau$$

The quantum yield is related to the average time an electron remains in the excited state prior to returning to ground state, described as the fluorescence lifetime (τ) [280] [121], by equation Eq. 5. The lifetime determines the available time for the fluorophore to interact with or diffuse within its environment [170] and is therefore defined as the inverse of the sum of the rate parameters for all depopulation processes [280], as shown by Eq. 6.

**Eq. 6**
$$\tau = \frac{1}{k_r + k_q + k_d + k_2[Q]}$$

When a fluorophore within an environment has no quenching influences ([Q]= 0) the lifetime can be described by $\tau_0$ and is equal to Eq. 7.

**Eq. 7**
$$\tau_0 = \frac{1}{k_r + k_q + k_d} = \frac{1}{k_r + k_{nr}}$$

Substituting Eq. 7 into Eq. 6 provides Eq. 8

**Eq. 8**
$$\frac{1}{\tau} = \frac{1}{\tau_0} + k_2[Q]$$

Multiplying Eq. 8 by $\tau_0$ provides the familiar form of Eq. 9

**Eq. 9**
$$\frac{\tau_0}{\tau} = 1 + \tau_0 \cdot k_2[Q]$$

By substituting the Stern-Volmer quenching constant $K_{SV} = k_2\tau_0$ into Eq. 9 it provides the well establish Stern-Volmer equation [64, 171, 224, 281]:

**Eq. 10**
$$\frac{\tau_0}{\tau} = 1 + K_{SV}[Q]$$

The Stern-Volmer constant is used to describe the relationship of bimolecular quenching between fluorophore and quencher. Measurement of lifetime with and without quencher at increasing concentrations describes whether the type of quenching involved is static, dynamic or a combination of both [171]. By identifying these factors the type of interaction can be determined from graphical plots where deviations from linearity describe some form of restriction in the quenching process. Whereas no correlation would be described as static, a dynamic relationship would be shown as linear [171]. These influences are dependent on the type of chosen oxygen dye and the environment it is found in.

In summary, photoluminescence was chosen as the option for oxygen detection and shown that there are two methods for measuring the luminescence. Steady-state measures the average intensity produced after continuous illumination, whereas a more suitable option is time-resolved. Time-resolved avoids the environmental susceptibilities associated with intensity measurements and time-domain provides a simple interface that will allow a wider variety of users to access in the future. There are a host of events that occur after excitation, but they are all dictated by the type of fluorophore and the environment it finds itself.

## 1.5 Oxygen sensitive dyes

Small molecules, like oxygen, naturally act as quenchers of fluorescence [170]. Some fluorophores are particularly sensitive and fall into two main categories; polycyclic aromatic hydrocarbons and organometallic compounds.

### 1.5.1 Polycyclic aromatic hydrocarbons (PAH)

Pyrene and pyrene derivatives are types of PAHs [11] and have been used as intracellular oxygen sensors [252]. Pyrenebyutic acid has been applied to rat liver cells for intracellular measurement of oxygen concentrations [301]. A number of factors make them an unsuitable option as an oxygen sensitive dye. For example the emission overlaps with autofluorescence within the cellular environment, poor chemical- and photo-stability, increased likelihood of photodamage from excitation wavelength in the UV range [143],

limited sensitivity in the physiological range [241], and quenching caused by reactive oxygen species [14, 251]

### 1.5.2 Organometallic compounds

The other main group consisting of organometallic compounds are classified into two categories; the metalloporphyrins group, which consists of Platinum ($Pt^{2+}$), Palladium ($Pd^{2+}$), and Zinc ($Zn^{2+}$) [11] and the transition metal polypyridyl complex group that includes Ruthenium ($Ru^{2+}$), Rhenium ($Re^{+}$) Osmium ($Os^{3+}$), and Iridium ($Ir^{3+}$) [11]. This group shows strong luminescence with long lifetimes and are frequently used as probes for optical oxygen sensors [11].

#### 1.5.2.1 Metalloporphyrins

Porphyrins are phosphorescent and exhibit lifetimes in the order of hundreds of microseconds allowing for the use of cheaper technologies such as LED [11]. But they are susceptible to photobleaching due to inherent poor photostability [11] and can be sensitive to pH and temperature [143]. Platinum based hybrid matrix bound sensors have been developed to measure the pH and partial pressure of oxygen simultaneously, but they still suffer from temperature sensitivity and can be susceptible to dye leaching [260]. Platinum based sensors have also been embedded into polymer matrixes and used in real-time multi-well plate measurements for metabolic investigation [211]. These types of matrix bound platinum sensors have also been used to determine surface oxygen gradients from *in vitro* explants of cartilage tissue [149].

Palladium based sensors, like the commercially available Oxyphor R2 [74], have provided researchers with the ability to intravenously inject diluted solutions, along with a visualisation dye, and measure single point oxygen measurements along *in vivo* arteriole networks [79, 320], or the arteriolar walls of rat skeletal muscle [267] and have been used in comparative analysis to determine the oxygen consumption rate of chondrocyte cells in agarose and collagen gels [104]. All measurements have only been able to provide single point oxygen measurements, but have achieved them from within the tissue depth.

#### 1.5.2.2 Transition metal ligand complexes (MLC)

The MLC groups contain a metal centre and one or more organic ligands. These MLCs display mixed singlet-triplet states and intermediate lifetimes ranging from 400 ns to several microseconds [11]. One of the most established complexes is ruthenium (II) and has been widely used as a probe for oxygen sensing, due to the high specificity and sensitivity to oxygen. Its popularity lies in the linear response to oxygen concentration in

homogeneous solution [11], the large Stokes shift creating a robust photochemical [318], high photostability [46, 225] and high fluorescence quantum yield [143]. The long lifetime and red emission (frequency) avoids interference from autofluorescence components. The lifetime has also been shown to be insensitive to pH, and ion concentrations [91, 324]. Ruthenium(II) complexes have been used extensively for the detection of oxygen and the quantification of oxygen concentrations *in-vitro* [324] and *in-vivo* [137, 208] and will be the focus of further discussion.

## 1.6 Ruthenium(II) complexes

The first example of luminescence arising from the charge transfer transition in tris-2,2'-bipyridine-ruthenium(II) ($[Ru(bipy)_3]^{2+}$) was in 1959 by Paris *et al.* [233]. Over the past 50 years ruthenium(II) complexes have been extensively reviewed with continued interest arising from a combination of chemical stability, redox properties, excited state reactivity, luminescence emission and excited state lifetime [144]. The emitting- and excited-states can be extremely sensitive to variations in the metal, coordinating ligands and local environment [66]. This has lead to the development of several hundred derivatives with multiple applications [144]. Used initially as a method for solar energy conversion [226] they have been involved in a variety of research from solid-state light-emitting [85] or electro-luminescent [272] devices, to biological sensors [91] or molecular probes [139], but more consistently as a model compound to study excited-state charge transfer [171]. Although the photophysics is still disputed [124] to enable the efficient application of ruthenium(II) the luminescence properties that dictate the excitation and emission states require understanding [66]. As a simple example tris-2,2'-bipyridine-ruthenium(II) complex consists of a single ruthenium metal centre, with six surrounding nitrogens, that pair three sets of aromatic rings holding 10 carbons and 8 hydrogen's, as shown in Figure 8.

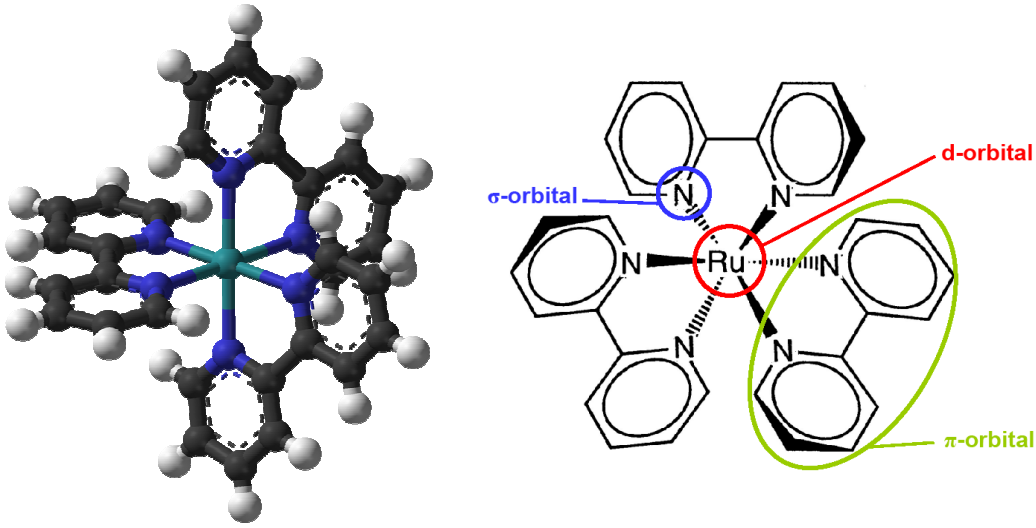


**Figure 8 – Chemical structured layout of $[Ru(bipy)_3]^{2+}$ in 3D and 2D. Left: Three dimensional structural model of $[Ru(bipy)_3]^{2+}$ [114]; Metal centre is ruthenium (green), six nitrogen (blue), 30 carbon (black), and 24 hydrogen (white). Right: Two dimensional structure of $[Ru(bipy)_3]^{2+}$ with denote orbitals, adapted from Damrauer [60].**

The ruthenium metal is a $d^6$ orbital system [144] that splits in the presence of the organic polypyrindine ligands into two $d^3$ systems. These two systems possess σ -orbitals localised on the nitrogen atoms and π donor- and π* acceptor-orbital delocalised on the aromatic rings as depicted in Figure 8 [144]. Other forms of ruthenium(II) complex tend to have either additional ligands on the bipyridyl ring or a different set of ligands added to the metal complex. Excitation of ruthenium(II) cations leads the electrons to initially delocalise from the metal, and localise on one of the 3 bipyridyl ligands. From here it relaxes back to the lowest excited triplet state [99].

### 1.6.1 Applications of the ruthenium(II) complex

The symmetrical structure shown in Figure 8 has allowed for anisotropy studies with the addition of an extra single ligand [171]. Ruthenium(II) complexes have been shown to bind to DNA and to be used as a sensitive tool for probing DNA structure [188]. It is one of the most widely used [254] and efficient photosensitizers [217] stemming from its ability to generate singlet oxygen [68]. This has lead to its application in photo-induced cleavage of DNA [99] where it has been applied as a combination approach, with porphyrin, to enable photodynamic therapy [63]. It appears to induce few DNA interstrand crosslinks, but protein-DNA crosslinks are shown to be induced by the complexes [23]. The addition of peptides to ruthenium have produced a membrane permeable probe to provide intra-cellular measurements [221].

### 1.6.2 Ruthenium(II) use with oxygen

Ruthenium(II) complexes have been applied in a variety of applications for the detection of oxygen. The main options available are to embed the dye in some form of permeable gel or matrix, immobilise the complex inside beads, directly coat or fuse the dye to a 3D tissue engineering structure, or allow the dye to be dissolved in solution.

#### 1.6.2.1 Embedded

Ruthenium(II) complexes have been absorbed into silica gel and embedded with a silicone-rubber membrane. This has allowed the application of this method in many situations, including commercial systems utilising 96 multi-well plates [313]. A similar kind of system has also been used for long term cell culture, to continuously monitoring the dissolved oxygen in a perfused bioreactor without causing cellular toxicity [86]. It can also be sealed on to a coverslip and has been applied to *in vivo* situations for monitoring oxygenation changes in brain tissue during ischemia and reperfusion [152]. The same type of system has been applied to measurement of transcutaneous oxygen partial pressure relating to the microcirculation under the skin [277]. These types of biofilm have many applications, including combined imaging of bacteria and oxygen [167], *in vivo* visualisation of rat intestinal microvascular network [137] and hand-held optical sensor for skin [315].

#### 1.6.2.2 Beads

An alternative option to embedding ruthenium(II) complexes in silicon matrix is to immobilise them in beads. Lipobeads, a phospholipids-coated polystyrene particle, have been used as a protective vehicle for ruthenium(II) for intracellular measurements of macrophages [142]. This avoids interactions with cellular components although it has only tested this method on monolayer samples and previous methods that use similar principles succumb to aggregation [143]. Layer-by-layer electrostatic nanosensors have been applied to ruthenium(II) encapsulation [321], but no cellular tests were completed. This method has also been combined to produce a dual sensor using oxygen and glucose within a nanoengineered alginate sphere via electrostatic mediated precipitation [41]. No cellular tests were completed and the oxygen measurements showed a second-order Stern-Volmer relationship. One study tested ruthenium(II) coated nanobeads with cells and managed to measure cellular oxygen consumption extracellularly, but in this case the beads were attached to the cell surface. Huge standard deviations can be seen in the measurements along with dye photobleaching because intensity measurements had been used [166]. It maybe presumed that any cellular surface attachment would cause downstream signalling

from the positive charge carried by ruthenium(II) as well as focused generation of ROS at the cell surface, likely to permeate the membrane.

#### 1.6.2.3 Coating

Another option directly coats [187] or fuses [3] the ruthenium with the tissue engineered hydrogel scaffolds, via layer by layer technology or gelled together during the scaffold production process. Coating the ruthenium(II) on to the hydrogels is achieved by soaking and washing in repetitive cycles. The main issue described was the non-uniformity of dye distribution [187]. This created problems due to the intensity based measurements being used. The authors stated that very few dead cells were noted, but no confirmation of viability was provided. The process of gelling ruthenium(II) during the scaffold production process showed good viability, but only global concentrations changes were reported without any spatial information and a two-site Stern-Volmer model was required to described the intensity based oxygen concentrations [3].

#### 1.6.2.4 In solution

In solution ruthenium(II) complexes have been used for intracellular measurements of oxygen in macrophages [91], although it was found that a reduction was seen in the sensitivity once the dye had penetrated the cellular membrane [143]. It has also been tested intracellularly on adenocarcinoma, human epithelial cells [279, 324], but recently it has been shown that these intracellular measurements suffer from a lack of understanding how the internal components influence the recorded measurements. In order to tackle this problem the group resorted to using EPR oximetry to characterise the correct oxygen concentrations in parallel with the fluorescence lifetime measurements, in the hope that some complex mathematical model could be used to extract the relevant information [278]. Ruthenium(II) in solution has also been applied to bioreactor flow chambers during the culture of mouse myoblasts. This technique was hoped to aid future designs of flow chambers by quantifying changes in oxygen concentration, based on cellular density, consumption and flow rate [202]. The previous specification listed in 1.3.3.4 established ruthenium(II) processing must be met by the required criteria of the intended application, as shown in Table 5.

**Table 5 – Summary of the available methods for utilising ruthenium(II) and the requirements for the intended application**

| Criteria | Ruthenium(II) | | | |
|---|---|---|---|---|
| | Embedded in matrix | Bead | In scaffold | Solution |
| 3D measurements | | ⊗ | ⊗ | ⊗ |
| Extracellular | ⊗ | | ⊗ | |
| Ability to diffuse/flow | | ⊗ | | ⊗ |
| High spatial resolution | | ⊗ | | ⊗ |
| Simple linear Stern-Volmer relationship | | | | ⊗ |
| **Total** | **1** | **3** | **2** | **4** |

This summary Table 5 has identified ruthenium(II) in solution as the most viable option. Even though 'extracellular' has not been ticked the dye does remains in the extracellular domain for several hours prior to penetrating the cell membrane. With the detection method and fluorophore identified it only remains for the cellular model to be investigated.

## 1.7 Cartilage model system

During normal activity a normal human hip or knee joint can withstand loads of up to 10 times the normal body weight or maintain function for up to 9 decades [57]. Once the joint components become damaged or degraded it is apparent that normal function will suffer. This is compounded by the limited self repair capacity of articular cartilage that defines the interest in tissue engineering intervention. Oxygen in the reparative process has been shown to be vital to the structure and function of the produced engineered tissue.

Cartilage tissue is an opaque translucent tissue, which is ideal for use on illumination based instruments and minimises the possibility of tissue absorption. The use of chondrocytes for the cell model means that a transparent engineered construct can be used without structures for cell attachment, which is generally required for most cells.

The following discussion will focus on the natural structure and composition of cartilage, chondrocytes function, oxygen delivery, chondrocyte metabolism and the problems associated with articular cartilage repair. These problems can be alleviated though tissue engineering, which will be described along with the implications of changes to oxygen environmental concentration and the impact on engineered tissue development.

### 1.7.1 The structure of cartilage

Diathrodial joints are enclosed within a strong fibrous capsule [57] and are externally supported by surrounding ligaments, tendons, and muscle [215], as shown in Figure 9. The synovium secretes a metabolically active lubricating liquid, termed synovial fluid, filling the capsule [57]. The articular cartilage is a hyaline cartilage that lines the subchondiral bone [9, 307]. The combination of the synovial fluid and the articular cartilage creates a near frictionless bearing system during locomotion [57].

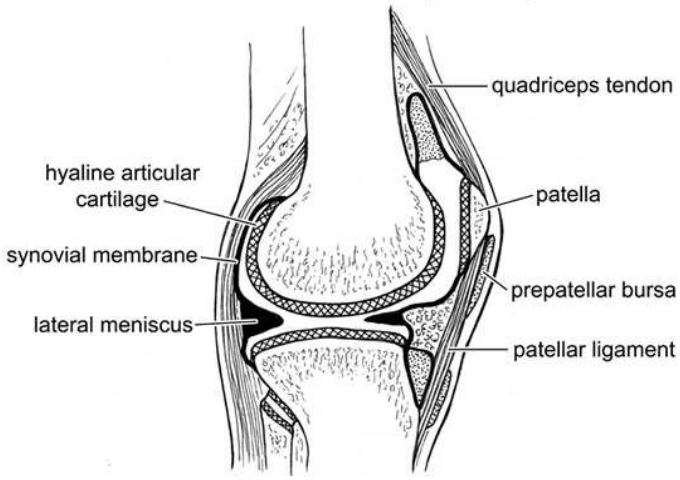


**Figure 9 – Example of a diathrodial joint, displaying the lateral view of a knee. The anatomical composition identifies the location of the tendon, ligament, articular cartilage, synovial membrane and menisci. As it is a knee joint the patella is also featured [289].**

The cartilage and bone interface consists of three components; cancellous bone, subchondral bone and articular cartilage, as shown in Figure 10 [289]. Articular cartilage uses a single cell type, the chondrocyte, to maintain the surrounding extracellular matrix.

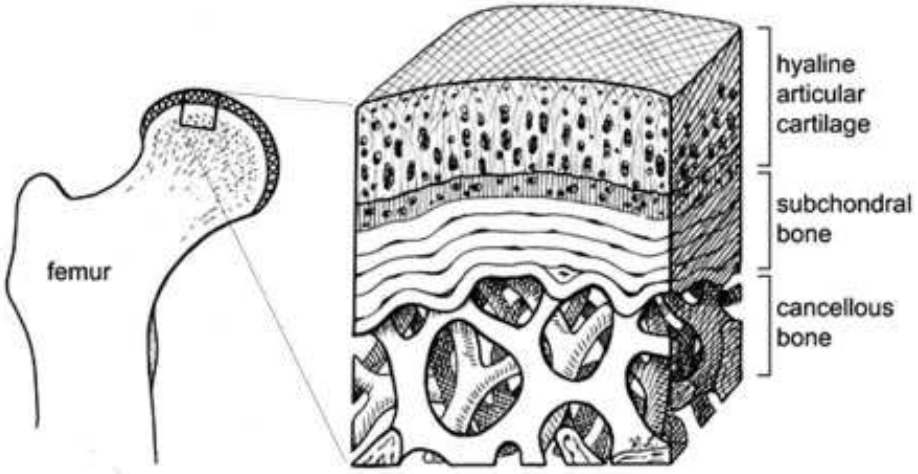


**Figure 10 – Hyaline articular cartilage and bone interface of a normal joint. Example a femoral head on the left with a zoomed in section exhibiting on the right of the cartilage bone interface: articular cartilage, subcondral bone, and cancellous bone [289].**

Articular cartilage can be described by three uncalcified superficial (10-20%), intermediate (40-60%) and deep (30-40%) zones and one calcified zone [43], as shown in Figure 11. These zones are defined by chondrocyte morphology and ECM composition and organisation.

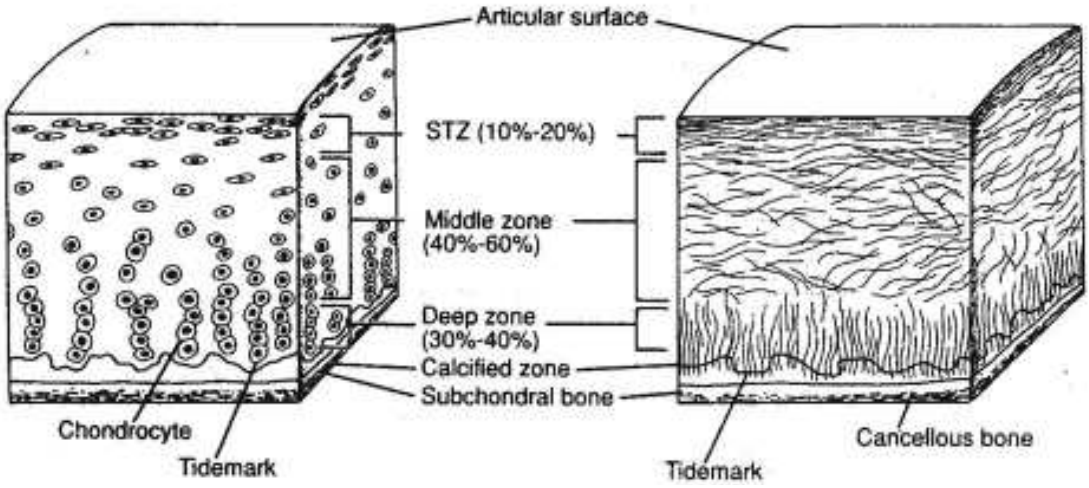


**Figure 11 – Cross-section of articular cartilage with zones percentages and locations displayed, Left: Section show phenotype and morphology of chondrocytes, Right: section show orientation of collagen fibres. Zonal areas are identified as superficial (STZ), middle, deep, and calcified. The start of the calcified zone is identified by the tidemark and ends at the subchondrial and cancellous bone [43].**

#### 1.7.1.1 Chondrocytes

Chondrocytes occupy only 2-10% of the total volume of articular cartilage [9, 185, 216, 243, 294]. The cells are morphologically ellipsoidal and vary in size dependent on species and location within articular cartilage [185]. The cell size can vary in the human knee from 10-14 μm between cells from superficial and deep zones [135]. At the surface chondrocytes appear flattend and closely packed [243]. In the intermediate zone the cells are rounder [9] and occupy less matrix volume [243], but in the deep zone cells are sparsely distributed, form vertical columns and have a large round morphology [9]. Beyond the tidemark, viable large chondrocyte cells with enlarge lacuna occupy the calcified zone [227, 276]. This zone is formed of mineralised cartilage that adjoin the subchondral bone [9, 294]. Chondrocytes here express a hypertrophic phenotype, synthesize collagen type X and can calcify the ECM [243].

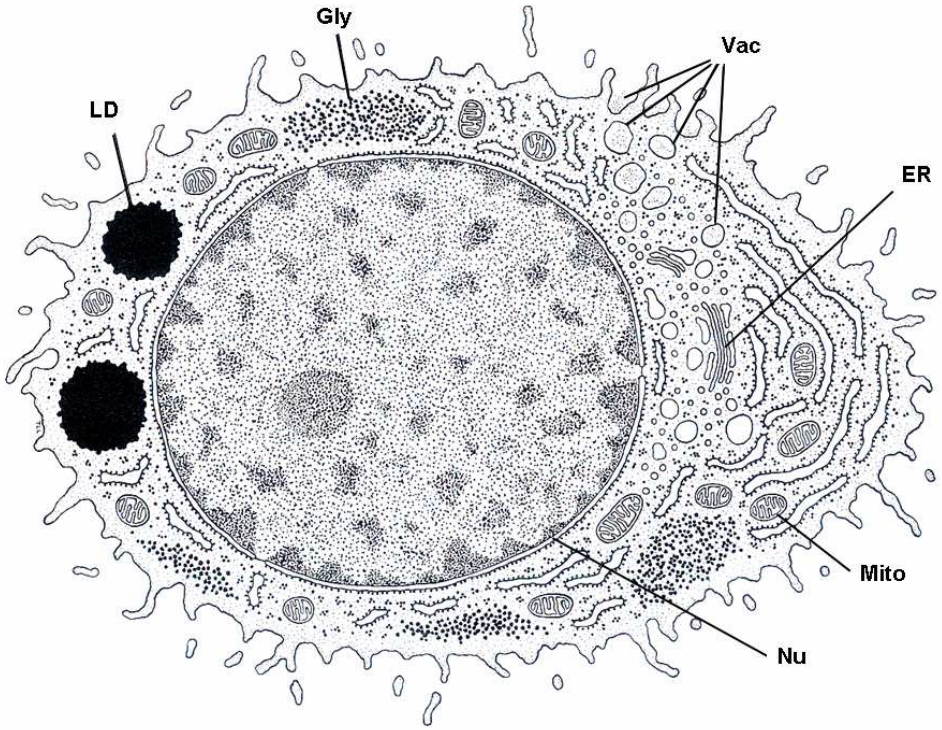


**Figure 12 – Drawing of a chondrocytes internal structure. The abbreviations are: LD lipid droplet, Gly glycogen granules, VAC vacuoles, ER endoplasmic reticulum, Mito mitochondria, and Nu nucleus [181].**

#### 1.7.1.2 The ECM

The ECM is opaque in appearance and provides a fibre-reinforced gel like structure in which the chondrocytes reside [216, 294]. It also functions to provide important signals to the cells [162] regarding the surrounding environment. The ECM is mainly composed of collagen type II (wet weight 15-22%), proteoglycan aggrecan (wet weight 4-7%), and water (wet weight 60-85%) [57, 61, 216], as shown in Figure 13. These main components provide tensile strength, resistance to compression and reside in the voids facilitating convection of essential nutrients, respectively. The minor components within the ECM only account for less than 5% [57], but their function is vital for the meshing of the ECM structure. These include: link protein, hyaluronan, biglycan, collagen type I, V, VI, IX, XI, decorin, fibromodulin, perlican, thrombospondin and cartilage oligomeric matrix protein [57].

In the superficial zone collagen fibres are thin and form tightly packed horizontal leaves [136] that lie parallel to the articulating surface [294]. As the collagen fibres transcend the organisation becomes more disorganised, oblique and the fibrils become larger [243, 294]. In the deep zone the collagen fibres are arranged in vertical columns perpendicular to the surface mimicking the chondrocyte orientation [294]. The collagen fibres pass the tidemark and are anchored vertically into place by the calcified zone [136], providing a strong anchoring system to the subcondral bone [57].

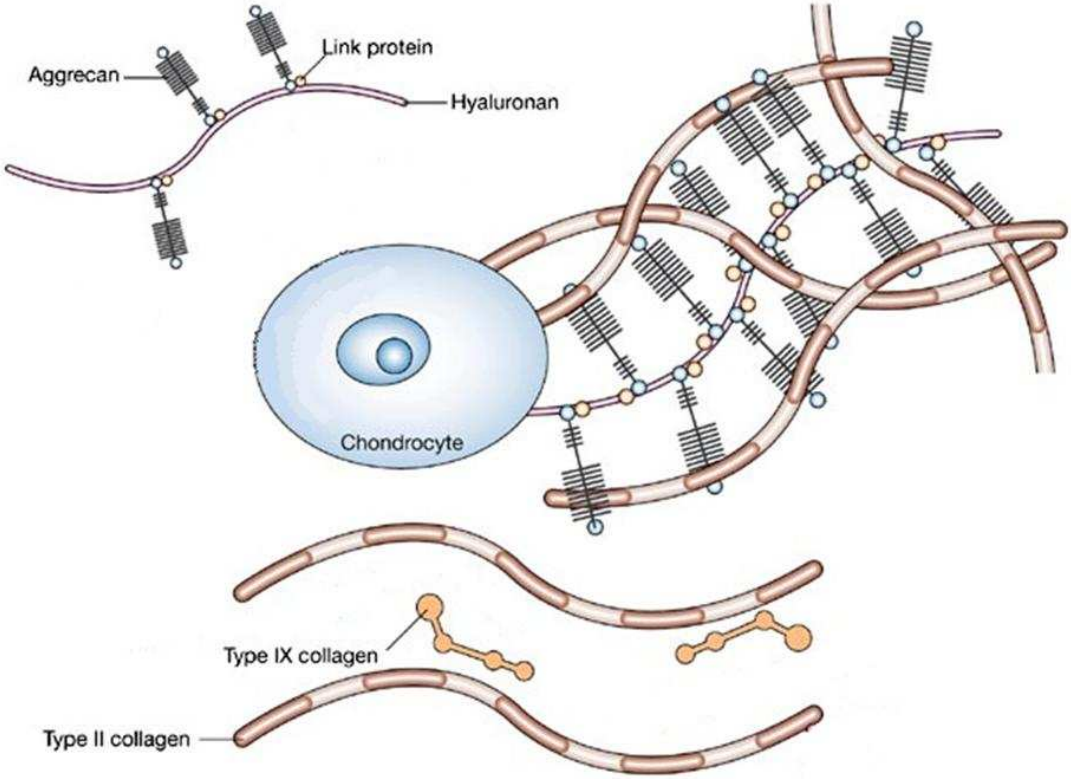


**Figure 13 – Chondrocyte surrounded by extracellular matrix components including aggrecan, hyaluronan, Type II and IX collagen [52].**

The zonal characteristics of the articular cartilage have been summarised in Table 6. Sub-divisions of the ECM have also been defined on the basis of proximity to the chondrocyte. Immediately surrounding the cells is a pericellular matrix, followed by a territorial matrix and a interterritorial matrix [244].

**Table 6– Articular cartilage zonal effects on chondrocyte, phenotype and density, and ECM, orientation and organisation.**

| Zones | Chondrocytes | | Collagen (ECM) | | Cartilage % |
|---|---|---|---|---|---|
| | Phenotype | Density | Orientation | Organisation | |
| Superficial | Flattened ellipsoid | High | Parallel | Horizontal, thin | 10-20 |
| Intermediate | Rounder | Medium | Oblique | Less organised, thicker | 40-60 |
| Deep | Larger, round | Sparse, Vertical columns | Perpendicular to surface | Vertical columns | 30-40 |
| Calcified | Large, round | - | Perpendicular thick fibres | Vertical columns | 3-8 |

From Table 6 it is apparent that the articular cartilage is a highly organised structure whose specific role is to aid locomotion of joints by minimising friction and translating shear stress through to the underlying bone. However, in order to maintain this structure chondrocytes require sufficient nutrients and oxygen delivery.

### 1.7.2 Cartilage oxygen delivery

In mature articular cartilage the delivery of oxygen to the tissue is generally considered to be from arterial blood supply surrounding the synovial capsule [182]. Oxygen and nutrients diffuse through the synovium into the synovial fluid and to the articulating surface [190], as shown in Figure 14. This delivery is aided by convection, stimulated through joint movement [102, 210, 243, 325]. Nutrients and oxygen are required to diffuse through the full depth of the cartilage. The cartilage thickness can vary dependent on anatomical location, age, and species. With age the thickness tends to decrease [4] and in human knees it can be >2 mm, while in rabbit of the same joint it can be <0.5 mm [325]. These parameters also define the oxygen concentration at the articulating surface, which is also affected by disease states. The difference between normal and a variety of joint disease states in human can be 6.5%-9% [107] to 1%-10.3% [290], respectively.

It is estimated that the oxygen concentration in the deep zones is likely to be <1% $O_2$ [271]. However, as shown earlier in Table 1, recent studies between the subpopulation of chondrocyte cells have shown that the superficial cells consume oxygen at a lower rate than the deep cells. Only invasive methods or computationally modelled based on global consumption rates of chondrocytes have been used to determine the actual concentrations [262, 271, 325]. These low levels of oxygen in cartilage would be considered hypoxic for most other cells, but is referred to as normoxia for chondrocytes [101, 210].

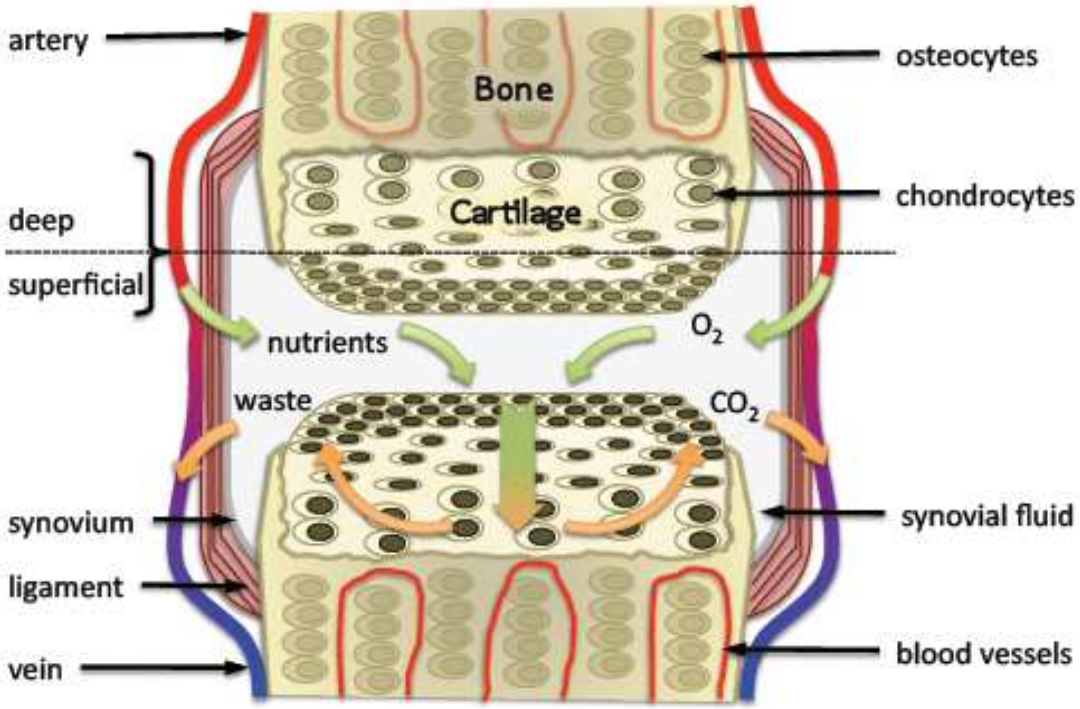


**Figure 14 – Schematic representation of oxygen delivery from blood supply to cartilage surface and through to the deep zone.**

In immature cartilage blood vessels supply nutrients direct to the deep layer, unhindered due to the incomplete development of the subchondral plate [199]. Once the tissue has reached maturity and has a fully developed calcified zone nutrient delivery is not supported by the subchondral vessels [55], even though a few small blood vessels do reach beyond the subchondral bone [136], as shown in Figure 15. It has been shown *in vivo* by Ogata *et al.* [228] that in adult rabbits hydrogen gas was not taken up from the subchondral bone into the cartilage, demonstrating that diffusion of dissolved gases, like oxygen, should not be able to reach cartilage from the subchondral bone. However a conflicting study, examining the concentration of glycosaminoglycan (GAG) in articular cartilage, used intravenous injection of gadolinium ($Gd(DTPA)^{2-}$) and noted that the contrast agent appeared to penetrate both from the articulating surface and the cartilage bone interface [24]. The experiment was performed *in vivo* on adult human subjects and suggests that unhindered diffusion is possible from the subchondral bone. Whether the negative charge of $Gd(DTPA)^{2-}$ influences this process is unclear, but it cannot be attributed to the disease state as all subjects were normal volunteers.

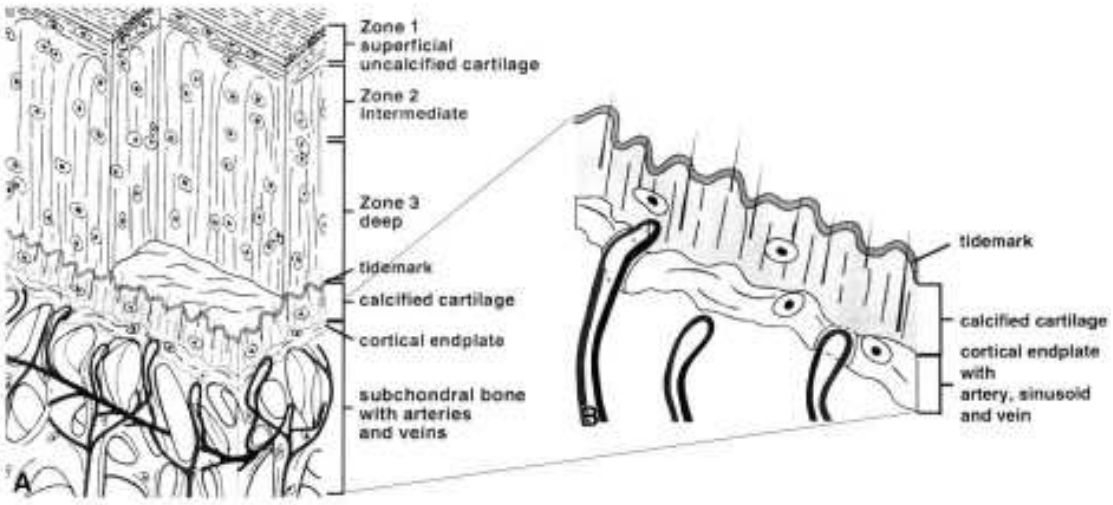


**Figure 15 – A pictorial representation of a proximal bone display a cut through section of articular cartilage, which defines the cartilage zones and shows the interface with the subchondral bone. A zoomed in section between the tidemark and subchondral bone show how the arteries and veins sometime reach into the calcified cartilage. Adapted from Imhof *et al.* [136].**

Many studies assume that there is no transfer of oxygen from the subchondral bone suggesting that cartilage restrictions to oxygen delivery and the greater density of superficial cells will inevitably lead to the development of an oxygen gradient [101, 102, 119, 179, 210, 216, 294, 307, 325] that would influence cellular metabolism. However, computational models have been used to explore the possibility of the cartilage being provided with up to 50% of its supply from the subchondral bone. These models suggest that the gradient would be more gradual and reduce slightly across the centre of the cartilage tissue [325].

### 1.7.3 Cartilage metabolism

It had generally been assumed that at the surface superficial cells utilised oxidative phosphorylation for energy and the decrease in oxygen with depth was accompanied by a shift in their metabolism to glycolysis [190]. However, the recent understanding that deeper cells consume oxygen at a higher rate than superficial cells contradicts the general consensus of an oxygen gradient. The importance of understanding chondrocytes surrounding oxygen consumption or the possibility of gradient development is now fundamental to creating accurate computationally models and the productive progress of tissue engineering.

### 1.7.4 The role of oxygen in cartilage metabolism

The oxygen gradients in constructs are determined by a number of factors including: cell density and distribution, diffusion/convention rate and the oxygen consumption rate of the cells [190]. The diffusion rate of oxygen is dependent on the

construct architecture and the diffusion coefficient or effective diffusivity of oxygen in the matrix [190] as previously outlined in section 1.2.1.

The oxygen consumption can be affected by methods of culture and can, in turn, induce differences in matrix development. In monolayer, cells are exposed to a uniform oxygen concentration, unlike cells within a three-dimensional construct [190]. Even so Pettersen *et al.* [238] showed that oxygen gradients developed from human breast cancer cells across the depth of a monolayer flask (1.6 mm) using a microelectrode, which increased over consecutive days. Heywood *et al.* [130] showed that gradients developed in a 3D alginate system impacted cellular viability and induced the development of necrotic areas at the centre. As cellular density increased the cellular viability at the centre of the construct decreased. Guaccio *et al.* [104] measured the oxygen concentrations non-invasively in two 3D tissue engineered constructs, agarose and collagen. In agarose constructs oxygen levels reduced to zero after a depth of 1.2 cm in 24 h, but this was not observed in collagen based constructs. This effect was also reported by Kellner *et al.* [149] who compared, non-invasively, the development of oxygen gradients in explanted cartilage and 3D polymer-based constructs. They found that in the centre of the artificial construct oxygen levels dropped to zero, whereas the explants reached a minimum of 20 mmHg.

The effect that oxygen concentration has on chondrocytes is varied. Chondrocytes seeded in monolayer and 3D systems have been examined by many researchers who have assessed the implications of specific oxygen environments on cellular function. For example, Femer *et al.* [80] investigated porcine chondrocytes cultured at 20% oxygen compared with 5% and 1% oxygen. An increase in the production of proteoglycan, collagen and hyaluronan was seen in the cells cultured at 5%, whereas a decrease production in the same components were seen when cells were cultured at 1% oxygen. The material properties of cartilage were also examined at 20% oxygen, with a reduced stiffness after 3 days. When cells were transferred to a 1% oxygen environment no change was seen, but at 5% oxygen the stiffness returned to the same levels reported prior to incubation at 20%. Permeability was found to increase at 20% and return to normal at 5%. This suggested that diffusion would be affected, but only at 1% oxygen was the diffusion rate of dextran in the superficial zone lowered; no effect was seen in the other zones. Murphy *et al.* [218] also found 5% oxygen provided optimal culture conditions of chondrocytes. Oxygen concentration profiles are also affected by alterations in cellular metabolic rates induced by the addition of serum or growth factors, which can lead to lower oxygen within the tissue [325].

### 1.7.5 Cartilage damage

Chondrocytes are responsible the production and maintenance of the extracellular matrix (ECM) and are critical to its maintenance [9, 185, 190]. Chondrocytes experience changes in hydrostatic pressure from joint articulation, which aids modulation of metabolic activity [294] by removing waste and replenishing essential cell nutrients, oxygen and ions. Problems occur when joints are immobilised or have reduced loading causing static pressure that restricts vital cellular components and impede the rate of ECM synthesis [185]. With age, alterations to the cartilage metabolism also lead to degeneration of the articulating surface [294] with limited intrinsic capacity for repair [307]. These issues can accelerate through injury, such as blunt trauma or chondral fracture, as shown in Figure 16 [294] or via disease, such as osteoarthritis [307] or rheumatoid arthritis. Treatment options vary from the removal of an affected tissue and replacement with donor or autologous graft [307], to total replacement of an entire joint in extreme circumstances [190].

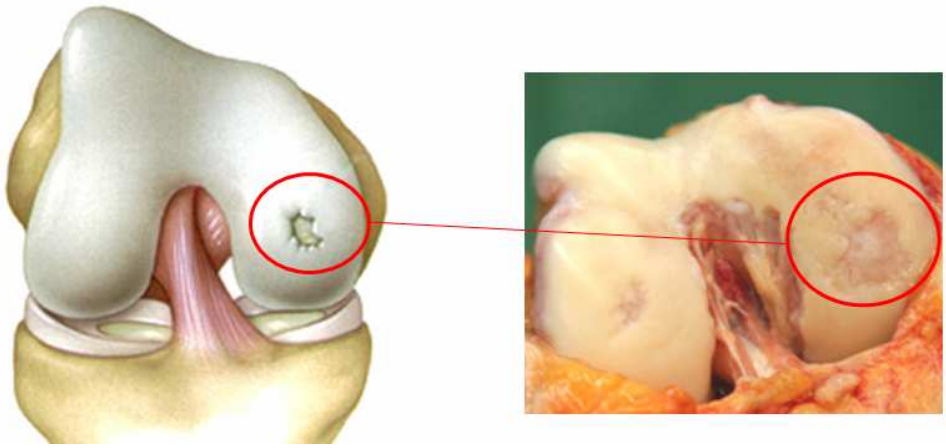

**Figure 16 – Posterior view of open knee joint with articular cartilage surface damage, Left: cartoon diagram depicting damage highlighted by red circle, Right: Real open knee surgery showing cartilage damage in red circle [153].**

### 1.7.6 Cartilage tissue engineering

Most cartilage repair techniques are aimed at local trauma rather than osteoarthritis. Few surgical protocols have yielded satisfactory results for the treatments and repair of blunt trauma or chondral fracture [293]. Full function is rarely restored back to its native normal state [293] due to the invasive surgery, donor site morbidity, and risk of immunogenic response or pathogenic transfer for allogenic approaches [190]. To address inadequate self repair of cartilage, caused by injury or disease [112], the implantation of an engineered tissue composed of autologous chondrocytes has proven successful. The main difficulty with autologous cell-based tissue engineering strategies is the small number of human chondrocytes that can be harvested [162, 190]. The procedure involves surgery to

extract healthy chondrocytes from an undamaged area with rapid cellular expansion using monolayer cell culture. Chondrocytes are reverted back to their rounded phenotype through three-dimensional cellular culture. Surgery takes place once an adequate number of cells has been established. A periosteal flap is sewed to the surface of the defective site and harvested cells are re-implanted under the flap, as shown in Figure 17.

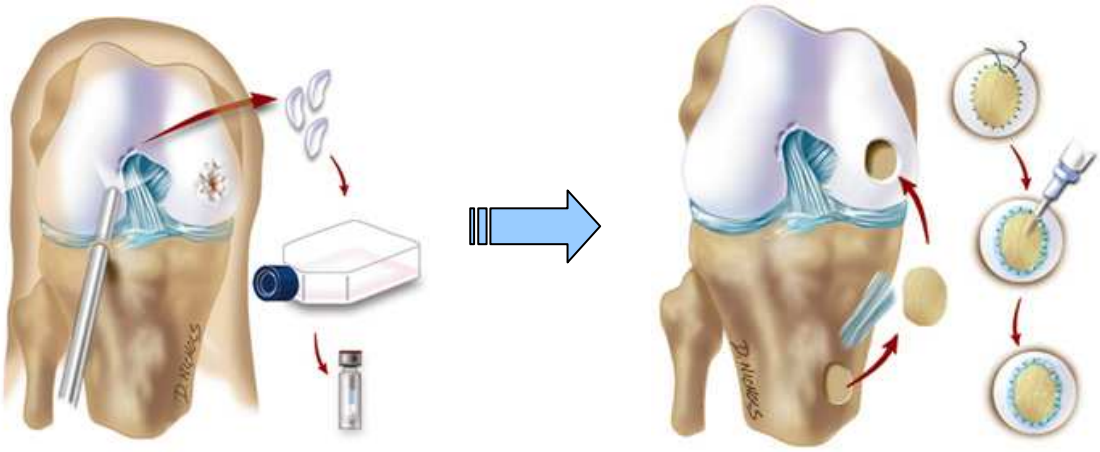

**Figure 17 - Autologous chondrocyte implantation, Left: Extraction of healthy cell for expanding in monolayer then transferring to bioreactors to retain phenotype and harvesting, Right: Stitching of peristeal flap and injection of harvested chondrocytes [153].**

The types of cell culture techniques used for chondrocyte tissue engineering strategies are monolayer (2D), static three-dimensional (3D) and bioreactor cultures [185].

#### 1.7.6.1 Monolayer cell culture

Monolayer culture is a basic approach for chondrocyte propagation. It is economical, technically simple and allows the rapid culture of large numbers of cells [185]. However, after being passaged [185] chondrocyte cells loose their rounded shape [190] and become fibroblast-like, losing their ability to secrete proteoglycans, and change collagen synthesis from type II to type I [185]. This loss of phenotype can result in the creation of inferior cartilage tissue [190]. Therefore, serial monolayer culture of chondrocytes is not representative of native cartilage because it lacks the cell-matrix interactions that chondrocytes possess *in vivo* [185]. This maybe overcome through transfer of cells to a three-dimensional system.

#### 1.7.6.2 3D static cell culture

The imperative behind culturing chondrocytes in a three-dimensional system is to provide an environment that is a more realistic representation of native cartilage to stabilise phenotype for subsequent applications [185]. Three-dimensional static systems use a host of different material scaffolds to provide cellular structural support. The chemical nature of

these scaffolds is polymer-based and is derived from proteins, carbohydrates or is artificially generated, as listed in Table 7.

**Table 7 – Different chemical classes of matrix [134]**

| | Chemical Nature | | |
|---|---|---|---|
| | Protein-based polymers | Carbohydrate-based polymers | Artificial polymers |
| Compositions | Fibrin<br>Collagen<br>Gelatine | Polylactic acid<br>Polygycolic acid<br>Hyaluronan<br>Agarose<br>Alginate<br>Chitosan | Dacron (polyethylene terephthalates)<br>Teflon (polytetrafluoroethylene)<br>Carbon fibers<br>Polyesterurethane<br>Polybutyric acid<br>Polyethylmethacrylate<br>Hydroxyapatite |

Each material has advantages and disadvantages for cartilage tissue engineering applications. For example, it is known that agarose encourages cellular production of collagen type II, but lacks suitable mechanical properties to provide the biomechanical requirements for joint movement [44, 134, 185]. Other materials such as poly(ethylene glycol) (PEG) hydrogels have been designed to better match the mechanical properties of cartilage, and support viability and matrix synthesis. Static culture does not facilitate all aspects of cartilage requirements. External forces that naturally act on native cartilage require implementation, which can be achieved by using bioreactors that are also designed to enhance nutrient delivery.

#### 1.7.6.3 3D Bioreactor cell culture

Bioreactors are designed to support the delivery of nutrients, while maintaining appropriate culture conditions. Bioreactors may also simulate the biofluidic or mechanical environment *in vivo*. The temperature, pH, nutrients, and oxygen levels can all be controlled [185] via the re-circulating fluid in an attempt to stimulate the fluid flow seen with joint movement in native cartilage. More advanced systems also incorporate changes in hydrostatic pressure or facilitate compression. This replicates the impact frequency of walking and provides a natural uniform mixing process of nutrients and oxygen as seen in joint convection [61, 286]. This type of stimulation aims to aid direction of growth for cells, collagen matrix and provide important signalling for tissue development [175]. This controlled stimulated environment for cartilage tissue engineering promotes chondrogenesis, ECM synthesis and tissue formation, supplying better oxygenation and nutrition than static culture systems [185].

**Table 8 – Currently used cell culturing methods and the associated advantages and disadvantages**

| | | Advantages | Disadvantages |
|---|---|---|---|
| Culturing methods | Monolayer | - Economical<br>- Technically simple [185]<br>- High cellular proliferation [185] | - Uniform delivery of oxygen and nutrients<br>- De-differentiation – fibroblast-like [40, 185]<br>- Loss of cell phenotype [190]<br>- Loss of ability for proteoglycans secretion [185]<br>- Collagen synthesis from type II to I [185]<br>- No mechanical loading or stimuli |
| | 3D static | - Provides simple environment for investigating 3D cellular development Round phenotype retained [185]<br>- Technically simple<br>- Correct matrix production [264]<br>- Non-uniform nutrient and $O_2$ [190] | - No mechanical loading or stimuli<br>- Delivery problems for $O_2$, nutrients and removal of waste once matrix developed [61, 149]<br>- Lacks ability of proliferation |
| | 3D bioreactor | - Hydrostatic pressure as in cartilage [61]<br>- Replicates natural uniform mixing [61, 286]<br>- Round phenotype retained [42]<br>- Correct matrix production [304]<br>- Control of pH, $O_2$, temperature, pressure, nutrient supply, waste removal, biostimulation [61, 190, 192] | - Complex setup and control system<br>- Complex fluid flow and cellular interaction<br>- Lacks ability of proliferation |

A summary of the advantages and disadvantages are provided in Table 8. It highlights how the disadvantages of each technique are compensated by the advantages of the others. This shows the reliance and importance of each culturing method and why they must be used in combination to provide expansion (monolayer), cellular investigation (3D static), and bio-stimulation (3D bioreactors).

Bioreactors show the greatest potential in replicating the native cartilage environment, but monitoring of biological parameters and knowledge of oxygen gradient development are required for optimum control of the closed loop systems. Before optimising bioreactor control systems a thorough understanding of oxygen spatial profile from chondrocyte seeded constructs must be obtained to truly model the progression of gradient development. This requires a simpler system to build the knowledge of chondrocyte oxygen consumption in a spatial context. By understanding how cellular consumption and gradients develop a more robust model for bioreactor cell culture can be established.

As stated earlier static cell culture is an ideal option for investigating cellular processes due to its simplicity compared with bioreactors and it avoids the dedifferentiation effects seen in monolayer. To minimise the influences of the construct composition a neutral carbohydrate based polymer, agarose is a simple readily available technology that

has minimal diffusional constraints for oxygen, supports the synthesis of matrix components, and encourages deposition of collagen type II [44, 185]. Agarose gel culture was one of the first three-dimensional culture techniques developed [185], but poor biodegradability limits its use as a matrix for cartilage repair studies *in vivo*. However, agarose gel has been used in many basic *in-vitro* studies studying physiological activities of chondrocytes [134] it is therefore an ideal simplified model for investigating the development of chondrocytes oxygen gradients.

In summary, cartilage is an avascular system with limited cell repair. Its simple opaque environment is ideal for use in a luminescence setup. It has been shown that oxygen influences chondrocyte development in tissue engineering associated with cellular viability, maintenance and structure of the ECM. A static 3D agarose system has been chosen for its simplicity to be used as the cell seeded construct.

## 1.8 Aims and Objectives

The aim of the project is to detect and quantify the presence of cellular induced spatial oxygen concentration gradients within a 3D tissue engineered agarose construct using a time-resolved time-domain lifetime detection method to measure an oxygen sensitive ruthenium(II) complex. The objectives are to:

- Examine available a time-resolved time-domain techniques with a selection of ruthenium(II) complexes in order to determine a suitable technique and fluorophore.
- Combine the chosen optimised time-domain technique and characterised ruthenium(II) complex to assess data acquisition, phototoxicity and image processing.
- Measure oxygen concentrations in a three-dimensional agarose construct seeded with chondrocytes using the calibrated system.
- Confirm that the measured oxygen gradient can truly be attributed to cellular oxygen consumption through inhibition and upregulation of cellular respiration.

# 2 Oxygen detection techniques

## 2.1 Introduction

The previous chapter determined time resolved time-domain fluorescence as the option most likely to fulfil prerequisite requirements. This chapter will be broken down into four parts: examination of ruthenium(II) complexes, testing of possible time-domain techniques, adaptation of selected time-domain technique and quantification of cytotoxicity induced by selected dyes on cells. By the end of this chapter a ruthenium(II) dye and preferred method for measuring lifetime will be chosen to take forward for future experiments.

## 2.2 Ruthenium(II) complexes characterisation

### 2.2.1 Spectral properties

In these experiments the excitation and emission peak of the ruthenium(II) complexes requires determination to ensure efficient stimulation of the fluorophores. The excitation wavelength for $[Ru(dpp)_3]^{2+}$ was indicated by commercial documentation [270] as 455 nm, but no information was provided on the excitation of $[Ru(bipy)_3]^{2+}$ and $[Ru(phen)_3]^{2+}$. There are discrepancies in the published literature as to the correct values to use. For excitation and emission of $[Ru(bipy)_3]^{2+}$ water and PBS, Gerritsen *et al.* [91] used 488 nm and >520 nm, respectively, while Sud *et al.* [279] used 460 nm and >600 nm, respectively. For the excitation and emission of $[Ru(phen)_3]^{2+}$ in water and sol-gel, Dobrucki *et al.* [72], used an excitation of 457 nm, respectively, whilst Campbell *et al.* [45] used 488 nm and >586 nm, respectively.

### 2.2.1.1 Materials

Tris(2,2′-bipyridyl)ruthenium(II) chloride hexahydrate, $[Ru(bipy)_3]^{2+}$, tris(1,10-phenanthroline)ruthenium(II) chloride, $[Ru(phen)_3]^{2+}$, and tris(4,7-diphenyl-1,10-phenanthronline)ruthenium(II) dicholoride, $[Ru(dpp)_3]^{2+}$, were purchased from Sigma-Aldrich (MW: 748.62 g/l, 712.59 g/l, 1169.17 g/l) (224758, 343714, 76886, Sigma-Aldrich, UK). Stock solutions (10 g/l) were created for each dye with deionised water for $[Ru(bipy)_3]^{2+}$ and $[Ru(phen)_3]^{2+}$, whilst $[Ru(dpp)_3]^{2+}$ was dissolved initially with ethanol and then further diluted with deionised water, in accordance with the manufacturers instructions [270].

The chemical structures of all three dyes are shown schematically in Figure 18. The commonality in all the dyes is the metal centred ruthenium(II) complex and the radiating six ligands attached to nitrogen (N). From here the dyes vary, the two main differences being the structures attached to the nitrogen, which come in the form of either pyridyl or phenanthroline. The last dye $[Ru(dpp)_3]^{2+}$ has a phenyl attached to the back of phenathroline.

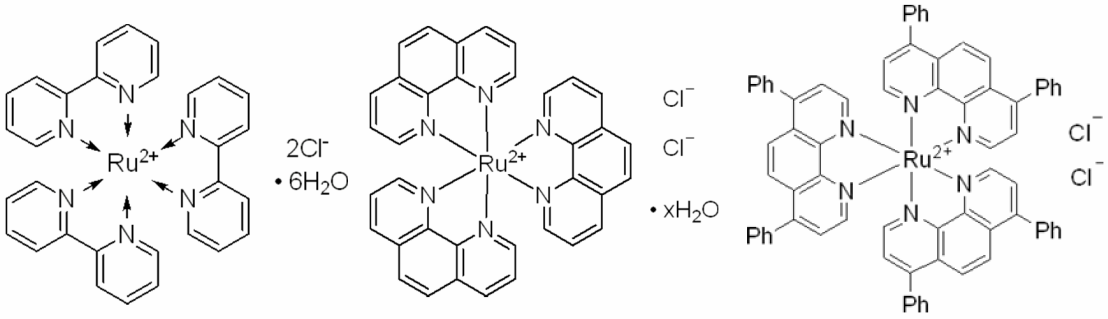


**Figure 18 – A schematic diagram of the chemical structures of ruthenium(II) complexes, Left: $[Ru(bipy)_3]^{2+}$, Middle: $[Ru(phen)_3]^{2+}$, Right: $[Ru(dpp)_3]^{2+}$ [270]. Ru – ruthenium, N – nitrogen, Ph – phenyl, Cl – chloride, $H_2O$ – water.**

### 2.2.1.2 Method

To determine the spectral properties, 2 µl of each dye stock solution was diluted (10 mg/l) with phosphate buffer (pH 8) and dispensed into standard cuvettes with opposing polished windows. Each cuvette was, in turn, placed into a fluorimeter (SLM II, Aminco-Bowman, USA) to acquire excitation and emission spectra. The light was directed through the cuvettes polished window and the transmission measured with a detector, as shown in Figure 19.

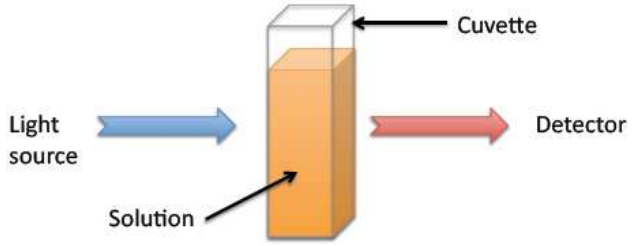


**Figure 19 - Orientation of standard cuvette with opposite polished windows holding a ruthenium sample to obtain excitation and emission spectra on a fluorimeter.**

Each previous study used different types and methodologies with various results. Therefore the current study followed a three stage process repeated for each dye: First, to identify approximately the emission peak, the dye was excited at 455 nm (4 nm bandwidth) and emission intensity was recorded from 550 to 700 nm with a 1 nm bandwidth. Secondly, to confirm the true excitation peak the excitation range was then scanned from 350 to 550 nm with 1 nm bandwidth, while maintaining the emission detection constant at the peak value with a 4 nm bandwidth. Finally, the emission spectrum was re-recorded at the maximum excitation peak to confirm the maximum emission peak.

#### 2.2.1.3 Results: Ruthenium dyes display near identical spectral peaks

The excitation and emission spectra of ruthenium(II) complexes diluted in phosphate buffer (pH 8, 1:1000), are shown in Figure 20, at ambient temperature. The ruthenium spectrum shows a maximum peak excitation for all three dyes at 468 nm. Emission peaks for $[Ru(bipy)_3]^{2+}$, $[Ru(dpp)_3]^{2+}$, and $[Ru(phen)_3]^{2+}$ were only slightly different, at 607 nm, 616 nm, and 592 nm, respectively. Comparing all three dyes, a series of almost identical minor peaks are visible in the excitation spectrum highlighting the commonality between these three ruthenium complexes. Although the peaks display the same position in wavelength the magnitudes of the normalised intensities vary.

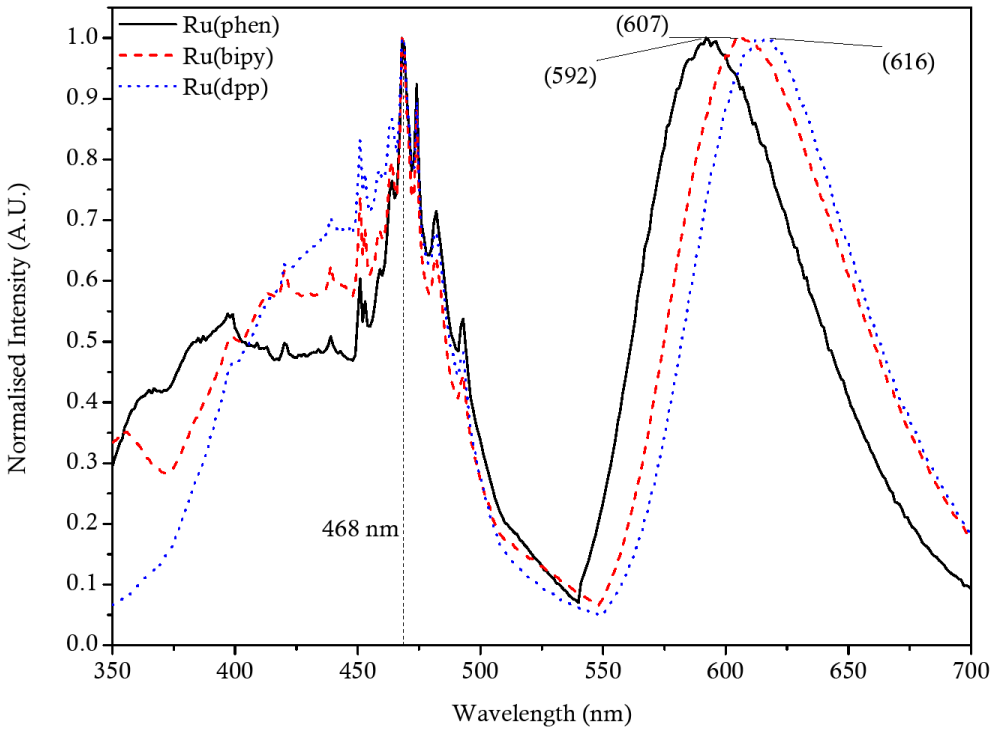


**Figure 20 - Excitation and emission spectra of $[Ru(bipy)_3]^{2+}$, $[Ru(dpp)_3]^{2+}$, and $[Ru(phen)_3]^{2+}$ in aqueous buffer PBS. Intensities have been normalised to the maximum values.**

#### 2.2.1.4 Discussion

In each dye the central chemical component is the ruthenium metal. This commonality between the three dyes is displayed in the spectra for excitation and emission. The maximum peak excitation for all three is 468 nm and the difference between the peak emissions is <20 nm. Although the excitation peaks appear at the same wavelength the magnitudes of the normalised intensities vary. This can be attributed to adjoined ligands affecting the transitions and interactions of the electrons. The excitation spectra of the $[Ru(dpp)_3]^{2+}$ showed a slight discrepancy with the commercial documentation, which stated the excitation peak was 455 nm in 0.1 M of phosphate [270]. This could be related to the sensitivity of the equipment, the filter bandwidths used by the company and the solvent effect and dye concentration. No commercial information was available for the excitation or emission wavelengths of $[Ru(bipy)_3]^{2+}$ and $[Ru(phen)_3]^{2+}$, but papers have been published also showing discrepancy between experimental results, as discussed in section 2.2.1. This confirms the need to obtain first hand spectra prior to conducting experiments to ensure optimum parameters are used.

### 2.2.2 Self-quenching

Self-quenching is defined by International Units for Physics and Chemistry (IUPAC) as the "Quenching of an excited atom or molecular entity by interaction with

another atom or molecular entity of the same species in the ground state."[200]. This effect occurs at high dye concentrations when two identical dye molecules are in close proximity and due to intermolecular interaction, quench the fluorescence just as in fluorescence resonance energy transfer (FRET) [171]. Increasing the distance between these molecules by reducing the concentration, will reduce the level of interaction and therefore increase the intensity [327]. However, the mechanism behind self-quenching is not completely understood even though the process has been known since the late 19$^{th}$ century. It was proposed that as fluorescence only occurred from single molecules (monomers) it was aggregation of these molecules that caused the self-quenching [110]. Even though this is partially true it is seen as a combination of dimerisation of the dye, energy transfer to non-fluorescent dimers, and collisional quenching interactions between dye monomers [110]. The self-quenching effect has previously been shown in optical probe design where ruthenium was embedded into silicone [154]. So as to avoid this effect it was found that lower concentrations (>0.2 mM) were required than would normally be possible in solution [183]. The effect of self-quenching has also lead others to utilise it for looking at single molecular protein folding [327], determine changes in cell volume [110]. A direct comparison of incrementing fluorophore concentrations would provide a means of determining maximum concentration limits due to self-quenching.

#### 2.2.2.1 Methods

For each of the three ruthenium dyes, as listed in section 2.2.1.1, a doubling serial dilution of 1 μM – 14 mM was created from stock solutions (10 g/l) and pipetted into a 96-well microplate (BD Falcon™, Sigma-Aldrich, UK) at a volume of 50 μl per well. The fluorimeter (FLUOstar OPTIMA, BMG LABTECH, GmbH) provided 50 illumination cycles to each well and averaged the intensity. Excitation and emission filters were set to 485 nm and 610±10 nm, respectively. The 'gain adjustment' was set to 1600.

#### 2.2.2.2 Results: $[Ru(bipy)_3]^{2+}$ and $[Ru(phen)_3]^{2+}$ experience decreased intensities at concentrations >7 mM

The concentration dependence of fluorescence intensity for three ruthenium complexes in aqueous solution are shown in Figure 21; all measured at ambient temperature. $[Ru(bipy)_3]^{2+}$ displays a notably higher fluorescence emission at the same concentration as $[Ru(phen)_3]^{2+}$ and $[Ru(dpp)_3]^{2+}$. A linear relationship ($R^2$ >0.95) exists between increasing dye concentration and emitted intensity at concentrations approximately below 7, 8.5, 1.6 mM for $[Ru(phen)_3]^{2+}$ $[Ru(bipy)_3]^{2+}$, and $[Ru(dpp)_3]^{2+}$, respectively. Above these concentration the linear relationship that exists with intensity

starts to deviate and in two of the cases begins to decrease at 7 mM for $[Ru(phen)_3]^{2+}$ and $[Ru(bipy)_3]^{2+}$.

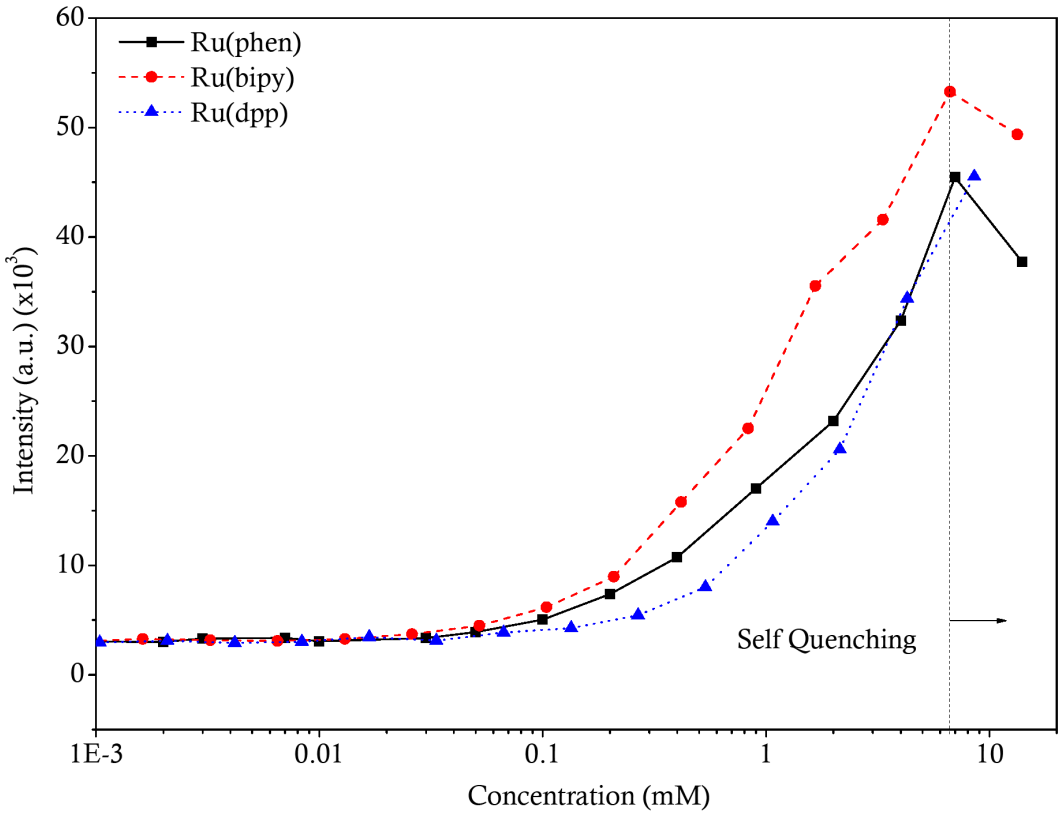


**Figure 21 - Effect of concentration on fluorescence emission intensity in aqueous solution for $[Ru(bipy)_3]^{2+}$, $[Ru(dpp)_3]^{2+}$, and $[Ru(phen)_3]^{2+}$ data plotted on a semi-log scale.**

#### 2.2.2.3 Discussion

An investigation was conducted to determine the limit where dye concentration induced self-quenching. It was identified that two of the dyes, $[Ru(bipy)_3]^{2+}$ and $[Ru(phen)_3]^{2+}$ intensity decreased at concentrations >7 mM. As the only changes in the solutions are the concentration it can therefore be attributed to self-quenching.

### 2.2.3 Conclusions from section 2.2

In conclusion, the peak excitation and emission wavelength for all dyes were determined as 468 nm with peak emission wavelengths of 592, 607, 616 nm for $[Ru(phen)_3]^{2+}$, $[Ru(bipy)_3]^{2+}$ and $[Ru(dpp)_3]^{2+}$, respectively.

The maximum fluorophore concentration in solution should be < 7 mM to avoid affects induced by self quenching.

## 2.3 Time-resolved time-domain systems

### 2.3.1 Introduction

After light excitation of a fluorophore the emission intensity decays over time. To determine the rate at which this occurs, i.e. the fluorescence lifetime, a variety of time resolved time-domain techniques can be used. There are four possible time domain methods that exist:

- Time-gating
- Time correlated single photon counting (TCSPC)
- Streak camera
- Upconversion

Time-gating/pulse-sampling requires the decay to be broken down into discrete time intervals where the intensity is captured, as shown in Figure 22. This allows compartmentalisation and therefore the ability for fast decay accumulation to be dealt with using simple electronic equipment. To create the discrete intervals detectors are either left on and electrical pluses measured on a sampling oscilloscope, or the detector sections the decay by turning on and off during the correct time period [171]. Either way electronic noise is independently added to each detected pulse. The size of the gates is dependent on the type of decay or accuracy required, which provides the flexibility of using long lifetime dyes. Generally the same sized gates are used for mono-exponential decays [19]. However, with more complex multi-exponential decays the shorter gates are used at the beginning enabling the short lifetime to be deciphered from the long lifetime [90].

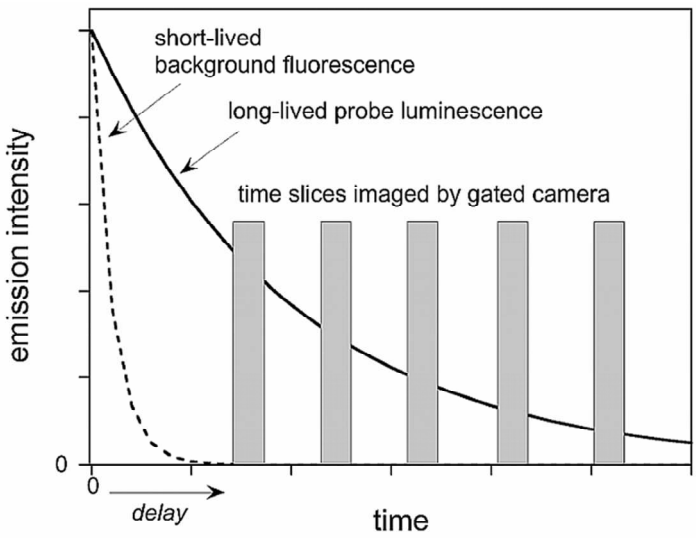


**Figure 22 – Acquisition of fluorescence decay using time-gating technique. The gated sections that are recorded are shown in by the grey boxes and are position after the background fluorescence. The accumulated intensities in these grey boxes are used to derive the lifetime decay [36].**

TCSPC is in some ways similar to time gating, as photons are sequestered into time channels, but it is the method of registering the photons that differs. TCSPC actually detects each photon, by converting it to a digital count. The electronic effects from the equipment do not interfere with each photon detected and this ensures it has the best photon accuracy [27]. The arrival time of each count is then correlated to a time channel. Over time the photons build to produce a histogram that represents the lifetime decay, as shown in Figure 23. The resulting signal to noise ratio is better than that of all other techniques, it has a dynamic range of up to 65536, but the time range is limited to 2 μs due to restrictions in the electronics [27].

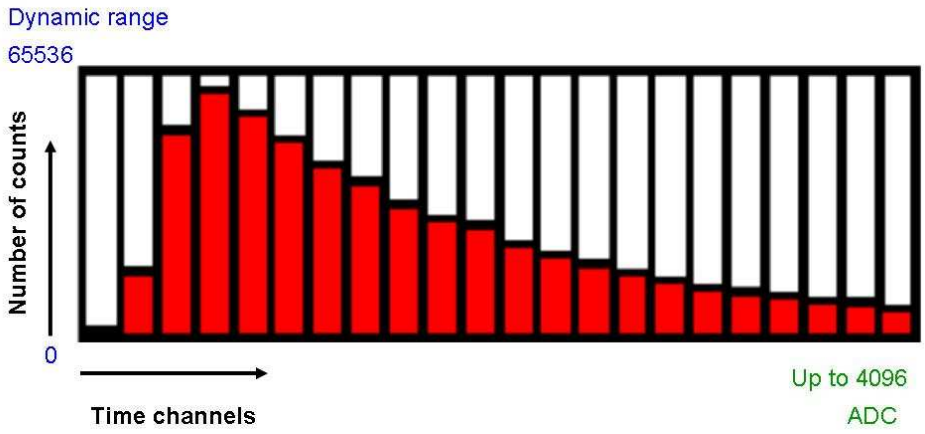


**Figure 23 – Photon collection acquisition of counts into assigned time channels. Height of the time channels is designated by the dynamic range and the number of time channels is assigned by the selecting an appropriate ADC. Adapted from Becker&Hickl [27].**

The streak camera is a specific type of camera that can provide information about the photon arrival time, its position in space, and the intensity. The camera can be used to determine the wavelength of the arriving photons that can provide important information about the environment of the fluorophore [109]. This is achieved by fluorescence passing through a slit and being focused on to a photocathode with a lens. The light is converted into electrons proportional to the intensity, as shown in Figure 24. The electrons are then accelerated and deflected as they pass between sweep electrodes so that they arrive in slightly different vertical positions. As the electrons pass through a micro-channel plate (MCP) they are multiplied and impact a phosphor screen where they are converted back to light, producing an image [171]. The streak camera not only provides the arrival time of photons, but also the location in space and intensity. It also has the best instrument response function (IRF), which is of less importance in the current study as dyes are transistion-metal ligands that have long lifetimes. The objective is to detect small changes in oxygen concentration and thus sensitivity is vital photon counting streak cameras are available, but with a poor S/N and low dynamic range (1000), it rules out the use of a streak camera.

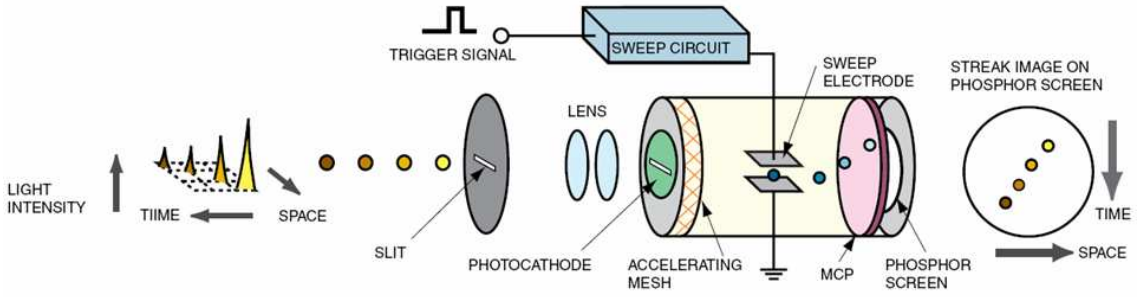


**Figure 24 – Schematic diagram of principle operation of streak camera. On the left it shows light entering the slit at different intensities and being focused down to the photocathode. The converted electrons are accelerated through the mesh and deflected by the sweep electrodes to different locations on the micro-channel plate (MCP) where they are multiplied upon hitting the phosphor screen to produce an image related to space, time and intensity [109].**

Upconversion is similar to time gating except that a laser pulse is used to gate the intensity decay instead of a detector or oscilloscope. The laser beam is split and one beam is directed to the sample while the other path is looped to create a time delay, as shown in Figure 25. The emission from the sample rejoins the delayed laser beam and is directed through an upconversion crystal. Only when the incident photons overlap will the crystal produce any photons [224]. Utilising a laser with a femto- or pico-second repetition rate the decay is gated and intensities recorded at those intervals allowing the full decay to be calculated [171]. Upconversion provides the best time resolution, but needs an extremely complex setup requiring constant realignment for any wavelength adjustment and for ensuring the delay and sample beam hit the crystal at the same point. In addition this approach has the shortest time range of 1-2 ns [171], which restricts the choice of dye to short lifetime time decays. The expected sensitivity to oxygen change would be limited making it unsuitable at low concentrations of oxygen.

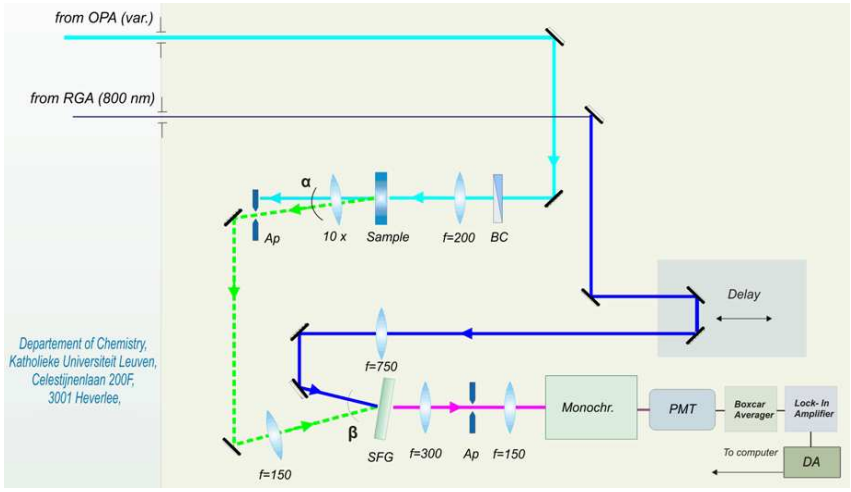


**Figure 25 – Schematic layout of fluorescence upconversion detection system. Output from an Ti:sapphire laser seeds a regenerative amplifier (RGA) this is split into two parts where one pumped an optical parametric generator (OPA) and was sent through to the sample and then to the crystal joined by the original but delayed RGA laser light. This goes onto a monochromator and is recorded on a PMT [148].**

Each of the four techniques has inherent advantages and disadvantages as summarised in Table 9. Using this summary it is possible to identify two techniques that would be unsuitable for the intended application, namely the streak camera and upconversion. The advantage of time-gating is the ability to cope with the long decays due to the high dynamic range. TCSPC has the best photon timing accuracy, which provides precise lifetime decays allowing low oxygen levels to be distinguished.

**Table 9 – Summary of the variety of time-domain techniques looking at the pros and cons.**

| TECHNIQUES | METHOD | ADVANTAGES | DISADVANTAGES |
|---|---|---|---|
| *Time-gate/ pulse sampling* | Intensity measured at discrete time points | • Best speed in accumulating signal<br>• Highest time range and dynamic range | • Loss of signal outsite time gate<br>• Unknown noise level of each data point |
| *Time Correlated Single Photon Counting (TCSPC)* | Each photon is correlated with a time point | • Best photon accuracy<br>• High dynamic range | • Limited time range 2μs |
| *Streak Camera* | Photoelectron dispersion provides time, space and intensity | • Best IRF | • Poor S/N ratio<br>• Low dynamic range |
| *Upconversion* | Similar to time gating but intensity decay is gated by laser pulse | • Best time resolution | • Worst complexity<br>• Lowest time range 1-2ns |

The following experiments will investigate three ruthenium dyes $[Ru(bipy)_3]^{2+}$, $[Ru(phen)_3]^{2+}$ and $[Ru(dpp)_3]^{2+}$, diluted in solution, with lifetime measured using instruments that facilitate time-gating, pulse sampling and TCSPC to acquire time resolved measurements. A comparison will be conducted between the efficiency of the dyes in solution and the ability of the techniques in measuring lifetime based on suitability of use with long lifetime dyes. The final step will determine a suitable technique for adaptation, with the foresight of applying it to a 3D cellular system, whilst maintaining accurately detected lifetimes with a stable and reliable system.

#### 2.3.1.1 Sample preparation

Stock solutions of the three ruthenium dyes ($[Ru(bipy)_3]^{2+}$, $[Ru(phen)_3]^{2+}$ and $[Ru(dpp)_3]^{2+}$) were diluted to concentrations of 16.1 μM with deionised filtered water for ambient samples in atmosphere. Low oxygen samples consisted of 16.1 μM ruthenium dye and 100 mM $Na_2SO_3$. Filter deionzed water with $Na_2SO_3$, but without ruthenium dye, was used as a control.

### 2.3.2 Time gating system

The fluorimeter (FLUOstar OPTIMA, BMG LABTECH, GmbH) operates using a high-energy xenon flash lamp that excites individual wells via a liquid light guide. The returning emission is captured through a separate light guide and directed to a photomultiplier tube (PMT). Controlled filter wheels select the desired excitation and emission wavelengths over the spectral range of 240-740 nm. Operating the system requires time resolved measurement script files to be written, containing information on the excitation routine and gate settings, which work in conjunction with standard files that contain filter setting and well plate layout.

#### 2.3.2.1 Methods

Stock solutions were prepared, with and without $Na_2SO_3$, as described above. Three replicates of each dye and each control were dispensed into the 96-well microplate (BD Falcon™, Sigma-Aldrich, UK) with 100 μl/well. To minimise evaporation and maintain low oxygen environment a plastic adhesive seal was positioned over the wells, as in previous studies [126]. The excitation filter was set to 485 nm and the emission to 610±10 nm, the gain was adjusted to 2200. The intensity decay profiles were created using the multi-chromatics and set with an integration period of 10 μs, which was implemented every 10 μs over the time range 0-60 μs.

#### 2.3.2.2 Data analysis

Replicate measurements were averaged and displayed as the centre point for each gate measurement in the time decay. The control sample (deionized water) was also averaged and subtracted from each ruthenium decay interval, to remove background noise. The form of time-gate analysis is dependent on the type of gating applied. The simplest method for mono-exponential decays uses two evenly sized gates as shown in Figure 26 and performs Eq. 11 and Eq. 12 below to derive the lifetime and amplitude [19], assuming no noise,

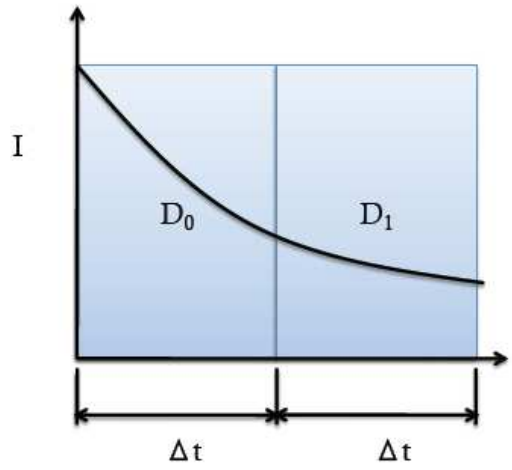


**Figure 26 – Lifetime decay analysis using time-gating with equally spaced separate gates. Abbreviations: *I* is intensity, $D_0$ *and* $D_1$ are gates 1 and 2, $\Delta t$ is the gate width. Adapted from Ballew *et al.* [19].**

**Eq. 11**
$$\tau = \frac{-\Delta t}{\ln\left(D_1/D_0\right)}$$

**Eq. 12**
$$A = \frac{D_0}{\tau\left(1 - D_1/D_0\right)}$$

where, $\Delta t$ is the gate width, $D_0$ and $D_1$ are the measured intensities of the 1st and 2nd gates, $\tau$ is the lifetime and $A$ is the amplitude. This same method can be used for multiple gates of even widths although to calculate $D_0$ and $D_1$ the intervals must be combined by using Eq. 13 and Eq. 14,

**Eq. 13**
$$D_0 = \sum_{j=1}^{N/2} d_j$$

**Eq. 14**
$$D_1 = \sum_{j=N/2+1}^{N} d_j$$

where, N is the number of intervals and $d_j$ is the interval number [19]. For the fluorimeter measurements only the first six gates were used for calculating the lifetime and amplitude.

### 2.3.2.3 Results

Figure 27 shows a semi-logarithmic intensity decay with time for a time gate system for $[Ru(bipy)_3]^{2+}$, $[Ru(dpp)_3]^{2+}$ and $[Ru(phen)_3]^{2+}$ at atmosphere (Atm) and lower oxygen ($Na_2SO_3$) in aqueous solution; at ambient temperature. The lifetimes were calculated from Figure 27 by combining Eq. 13 and Eq. 14 with equations Eq. 11. The measured values for $[Ru(bipy)_3]^{2+}$, $[Ru(dpp)_3]^{2+}$ and $[Ru(phen)_3]^{2+}$ in $Na_2SO_3$ were 6477 ns, 6540 ns, and 6507 ns, while in Atm it was 6429 ns, 6571 ns, and 6468 ns, respectively, as shown in Figure 27.

All the lifetimes are very similar at atmospheric and low oxygen conditions with the largest difference being 142 ns.

The broken lines joining the data points signify the non-continuous measurement of data. The points on the graph describe the centre of the gating block, the bar represents the size of the gate (10 μs) and the decays abruptly end after 70 μs. An initial flat period is visible for all the dyes spanning the first 20 μs of the decay. The intensities are higher for $[Ru(bipy)_3]^{2+}$ and $[Ru(phen)_3]^{2+}$ in $Na_2SO_3$ than in atmosphere, but the intensities for $[Ru(dpp)_3]^{2+}$ are the reverse and 6 times lower than for the other dyes. The last data point is missing for each lower intensity decay measurement of each dye due to the point being equal to zero. A mono-exponential decay should appear linear on a semi-log plot, but as the decay evolves past the plateau the line diverges from linearity at the same points in time. The measured $Na_2SO_3$ and deionised solution was the same as the blank samples indicating that the addition of $Na_2SO_3$ did not produce any fluorescent components (data not shown).

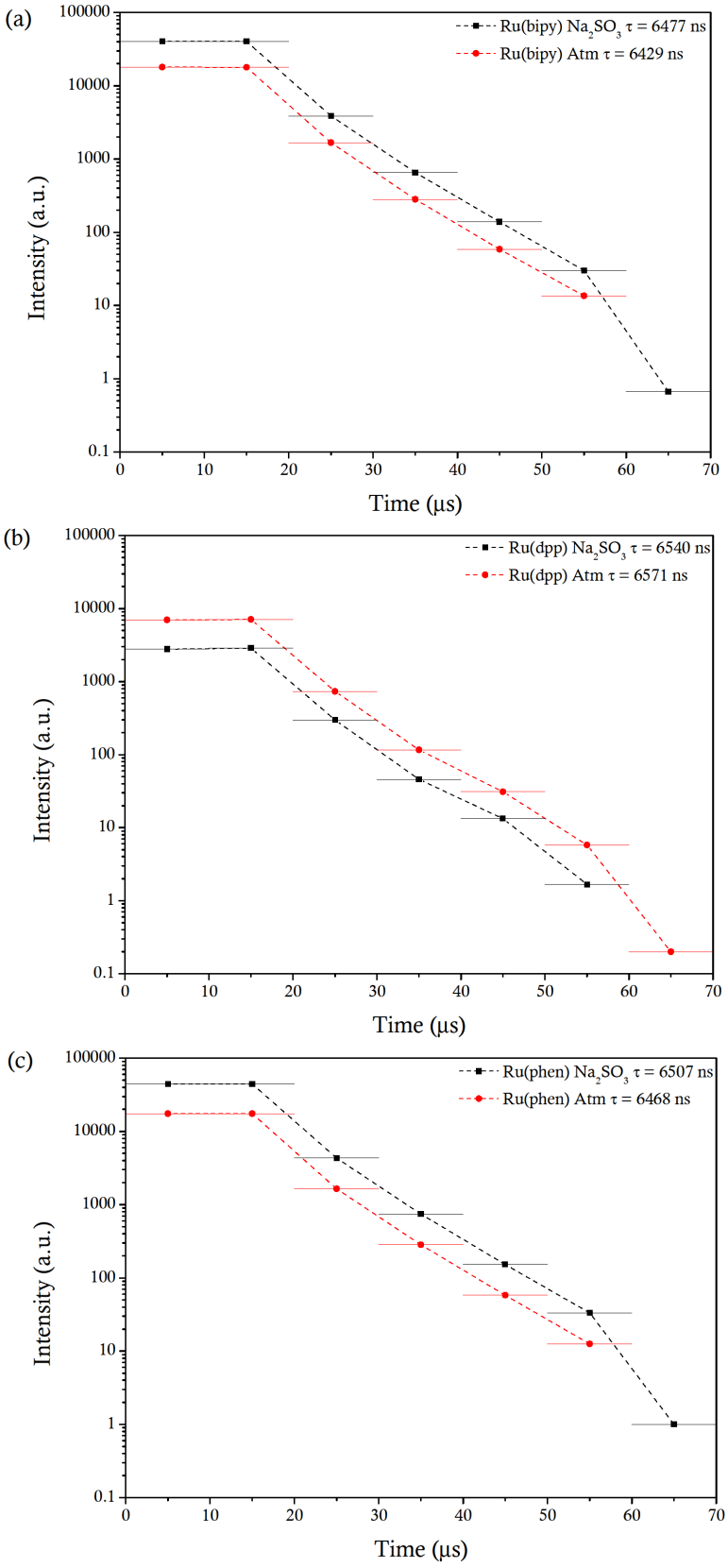


**Figure 27 – Semi-logarithmic decays of intensity during time for ruthenium dyes (a) $[Ru(bipy)_3]^{2+}$ τ = 6477 ns and 6429 ns, (b) $[Ru(dpp)_3]^{2+}$ τ = 6540 ns and 6571 ns, (c) $[Ru(phen)_3]^{2+}$ τ = 6507 ns and 6468 ns, in solutions with $Na_2SO_3$ and in atmosphere, respectively, on a fluorimeter with time-gating.**

#### 2.3.2.4 Discussion

The fluorimeter captures fluorescence after illuminating each well with a liquid light guide (optical fibres) and provides global measurements with no spatial resolution. The restriction of excitation filter meant that maximum excitations were not utilised, minimising efficient signal to noise. The fluorimeter used in these experiments had the facility to produce time-resolved measurements, but the main drawback was the in-built safety mechanism used to protect the PMT. It worked by blocking the excitation light reaching the PMT for the first 10 μs, producing a plateau effect at the start of the decay as seen in Figure 27.

The fluorimeter was unable to record the initial section of the decay and therefore determining if any secondary short lifetime components were present or whether sample contamination had interfered with the results was not possible. It can be estimated that 96.8% of an exponential decay would have completed after 5τ [19], i.e. if lifetime (τ is 1/e of maxium at 37%) was 1000 ns the decay would have virtually completed in 5 μs. However, the earliest time point recorded on the fluorimeter was 10 μs. Hence the results, in Figure 27, where the decay continues and abruptly stops at 70 μs, can not be associated with any ruthenium dye. These apparent decays are more likely associated the tail end excitation flash of the Xenon lamp or from capacitor discharging. The restriction in this technique is highlighted by the lack of response between changes in oxygen and dye type, depicted by the minimum lifetimes of >6 μs.

As the decays complete a divergence from linearity was seen at the same point in all graphs indicating the presence of systematic error. Each gate was separately excited so that the intensities measured are from different excitation flashes. If the excitation power varies during the excitation sequence, a different intensity will be produced. If there are two gates and two passes of excitation then efficiency of the method is halved [284]. This effect was minimised by averaging multiple excitations, however at the same time it induces photbleaching of the fluorophore.

The single advantage of the system was the possibility of acquiring data from multiple samples during one acquisition. A more appropriate system to test would have been the PHERAstar (BMG LABTECH GmbH) microplate reader, which is designed to record and display fluorescence decays, however this is still only capable of global measurements. Recently fluorimeters have been developed that are now capable of recording real-time lifetimes and monolayer cell images, but they still lack the capability of 3D investigation into tissue or constructs.

### 2.3.3 Time-Resolved Luminescence System

A high energy Nd:YAG solid state laser (Surelite™ I, Continuum®, USA) was pumped by a optical parameteric oscillator (OPO) (Panther®, Continuum®, USA) creating a pulse repetition rate of 10 Hz and excitation wavelength range of 410-700 nm. Emission was detected with a PMT (S-20, Hamamatsu Photonics, Japan) that gave a flat response between 400-750 nm. A spectrometer (Triax 550, Jobin Yvon HORIBA, France & USA) was centred around 550 nm using 1200 grooves/mm grating, to detect the signal and display it on a 500 MHz oscilloscope (Waverunner-2, LT372, LeCroy, USA) in real-time. The detected signal was associated to the photon intensity and recorded as a voltage. The voltage signal was triggered when the photocurrent rise time reached a preset threshold, over time building a decay that can be saved and analysed.

#### 2.3.3.1 Methods

Dye stock solutions, with and without $Na_2SO_3$, were prepared as described in section 2.3.1.1 and 2 ml of each pipetted into individual cuvettes and sealed with PTFE caps. Ambient samples were equilibrated in atmosphere. Cuvettes were placed on a raised platform, as shown in Figure 28, and the polished windows were aligned, with excitation light entering perpendicular to the window face and emission exiting the adjoining face to hit the detector, as shown in Figure 29. The excitation of the laser was set to 468 nm and a high pass emission filter at 570 nm for $[Ru(phen)_3]^{2+}$ and 590 nm for $[Ru(dpp)_3]^{2+}$ and $[Ru(bipy)_3]^{2+}$, respectively, placed in front of the detector to block excitation laser light.

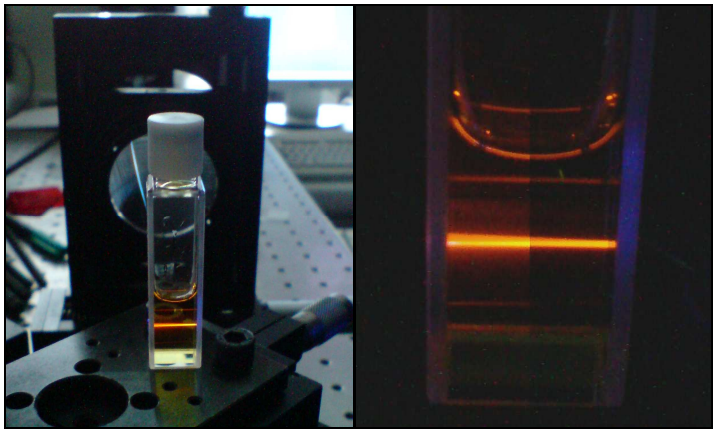

**Figure 28 – Sealed PTFE cuvette with ruthenium(II) complex diluted in deionised $H_2O$. Left: Laser excitation at 468 nm and fluorescent orange emission displayed as line, Right: Zoomed in of emission.**

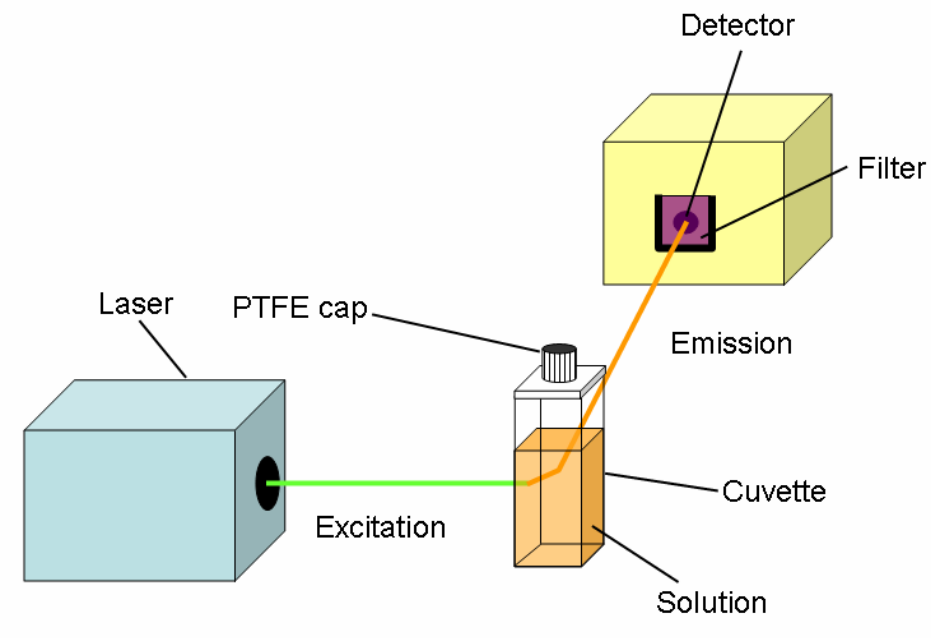


**Figure 29 – Schematic diagram show excitation and emission path of light beam. Excitation exits from laser hit optical window of curvette and reflects the emission light at 45° to the opposing window exiting at right-angles from the following window. The emission hits the filter high pass filter to exclude any excitation light and enters the detector.**

Measurements were recorded on the oscilloscope as a function of time triggered by the optical parametric oscillator, with 256 decays averaged per lifetime profile. Lifetimes and backgrounds were measured with different time bases depending on the length of the decays varying between 0.2-2 ns and slits were set to 1000 μm.

### 2.3.3.2 Data analysis

Measurements were repeated with different time bases, 1, 0.5 and 0.2 ns depending on the length of decay. The background noise was measured with the same time bases. Files were imported into Origin statistical software. Background noise was subtracted from decays with the appropriate time base. Intensity versus time was plotted on a semi-log scale and lifetimes was determined using least square fit analysis with Eq. 15,

**Eq. 15**
$$y = y_0 + A\exp\left(-t/\tau\right)$$

where, $A$ is the amplitude, $t$ is the time point, $y_0$ is the offset and $\tau$ is the lifetime. The model was fitted after the initial peak and before the increase of noise at the end of the decay, as shown in Figure 30.

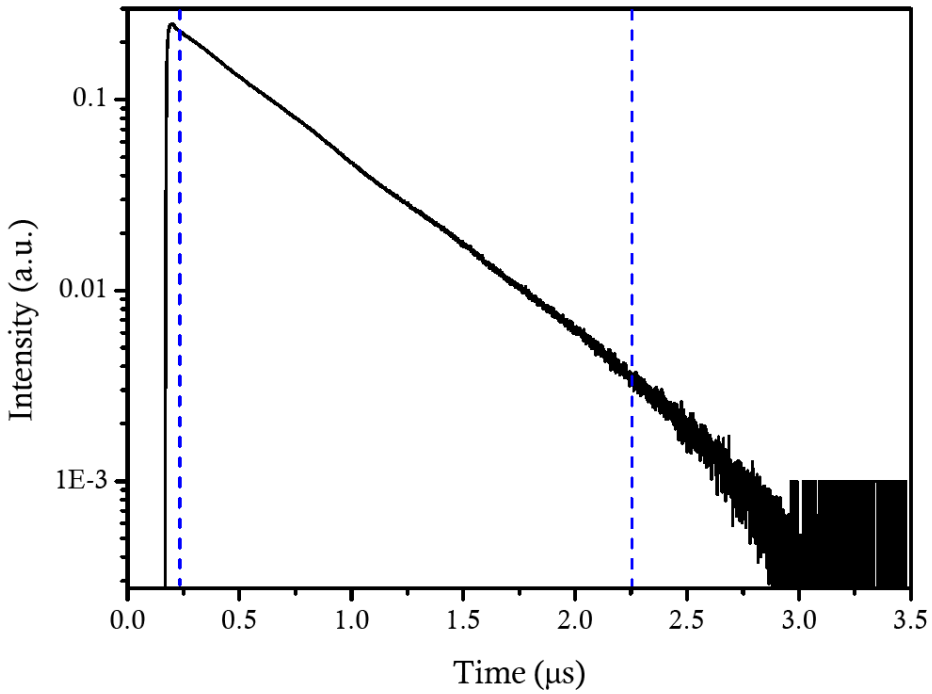


**Figure 30 – Intensity decay with time of $[Ru(bipy)_3]^{2+}$ in water. The models are fitted between the blue dashed lines displayed on the graph.**

### 2.3.3.3 Results

The intensity decay over time using pulse sampling for $[Ru(bipy)_3]^{2+}$, $[Ru(dpp)_3]^{2+}$ and $[Ru(phen)_3]^{2+}$ at atmospheric (Atm) and in $Na_2SO_3$ solution, are shown in Figure 31. The lifetimes measured for $[Ru(bipy)_3]^{2+}$, $[Ru(dpp)_3]^{2+}$ and $[Ru(phen)_3]^{2+}$ in $Na_2SO_3$ were 554 ns, 2573 ns, and 871 ns, while in atmosphere they were 380 ns, 767 ns, and 448 ns, respectively. The mono-exponential model fitted to the decay showed an adjusted $R^2$>0.99 for all decays. The decays shows slight sinusoidal effects in the logarithmic plot, especially for $[Ru(phen)_3]^{2+}$ in Figure 31c. The longest decay completes by 10 μs for $[Ru(dpp)_3]^{2+}$ $Na_2SO_3$, 2.5 times longer than $[Ru(dpp)_3]^{2+}$ in atmospheric oxygen. The peak intensity for both decays in $[Ru(bipy)_3]^{2+}$ and $[Ru(phen)_3]^{2+}$ experiments are similar at around 0.1, but for both $[Ru(dpp)_3]^{2+}$ samples, the peak intensities appear 3 time lower. The lifetimes in the presence of $Na_2SO_3$ have substantially longer lifetimes than in atmosphere indicating that oxygen is quenching the fluorescence as expected for these dyes. The instrument response function of the spectrometer was measured and gave a pulse width of 10 ns at FWHM this defines the limits of the time resolution in analogue systems [27].

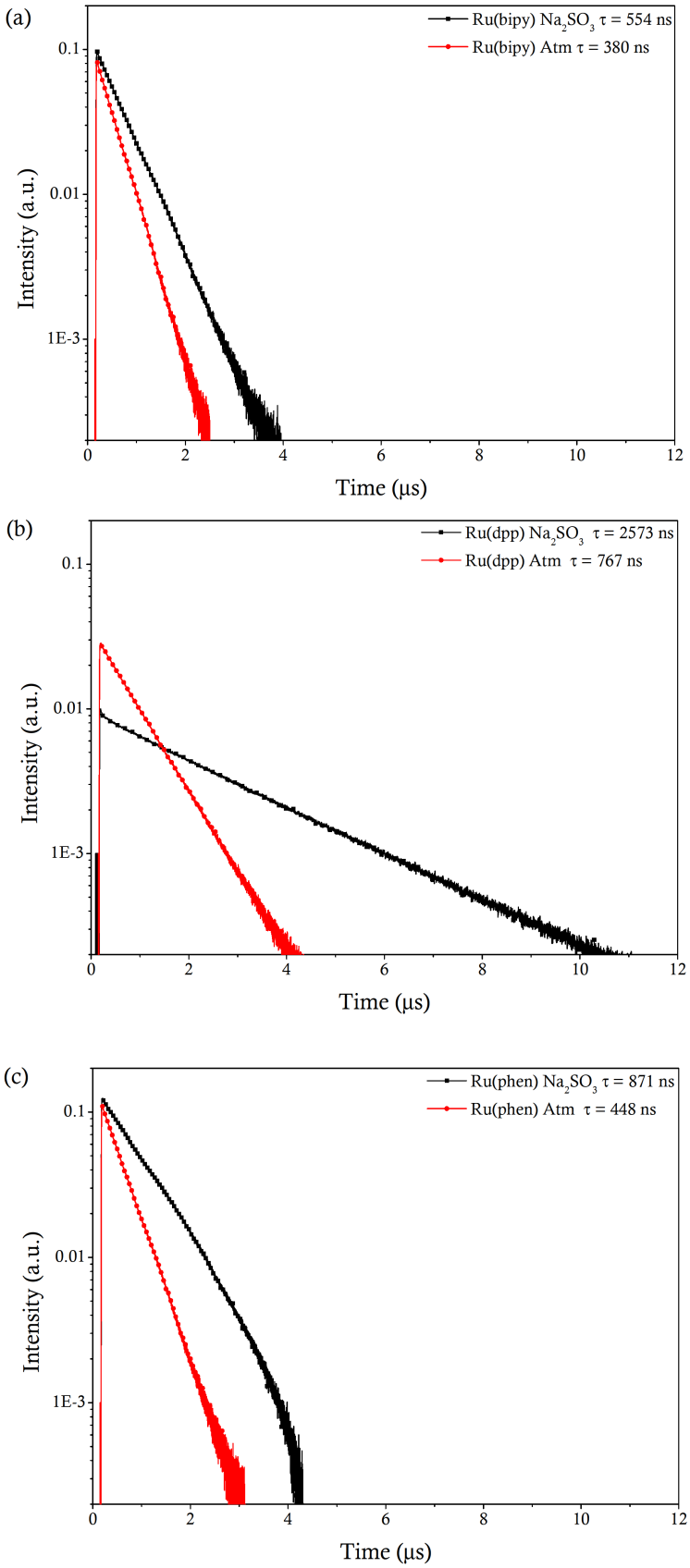


**Figure 31 – Semi-logarithmic decays of intensity during time for (a) $[Ru(bipy)_3]^{2+}$ τ = 554 ns and 380 ns, (b) $[Ru(dpp)_3]^{2+}$ τ = 2573 ns and 767 ns and (c) $[Ru(phen)_3]^{2+}$ τ = 871 ns and 448 ns, displayed in a solution of $Na_2SO_3$ and at atmosphere, respectively, using a time-resolved luminescence system pulsed sampling at room temperature.**

### 2.3.3.4 Discussion

It took <30 seconds to acquire a full lifetime decay. The lifetimes for the $Na_2SO_3$ samples were longer than in atmosphere. This showed that the lack of oxygen reduced the level of quenching hence a longer lifetime was apparent. The measured IRF of the spectrometer showed a FWHM of 10 ns. This introduces a possible error of ±10 ns to the accuracy of the photon timing [27] affecting validity and error of the derived lifetime.

In Figure 31c the decay appears to have a slight sinusoidal variation. Observing the weighted residuals of Figure 31 in Figure 32 it clearly shows that these sinusoidal variations are displayed in (a) $[Ru(bipy)_3]^{2+}$ and (c) $[Ru(phen)_3]^{2+}$. The effect could be associated to the charging and discharging of the RC circuit originating in the detection system, which includes the detector, cabling, and coupling impendence of the oscilloscope. The effect of charging and discharging during acquisition induces the shape of photocurrent pulse to be 'normal' during charging and 'broader' during discharge, increasing the measured intensity and pulse width during discharge [122]. These effects from the RC circuit can be minimised by the number of time points collected (in these experiments exceeds 10,000 during 4 μs) reducing effects arising from photocurrent broadening during detection and improves the time resolution. As a form of photon discrimination over noise using the 'leading edge' as the actual timing of each photon which is affected by amplitude jitter.

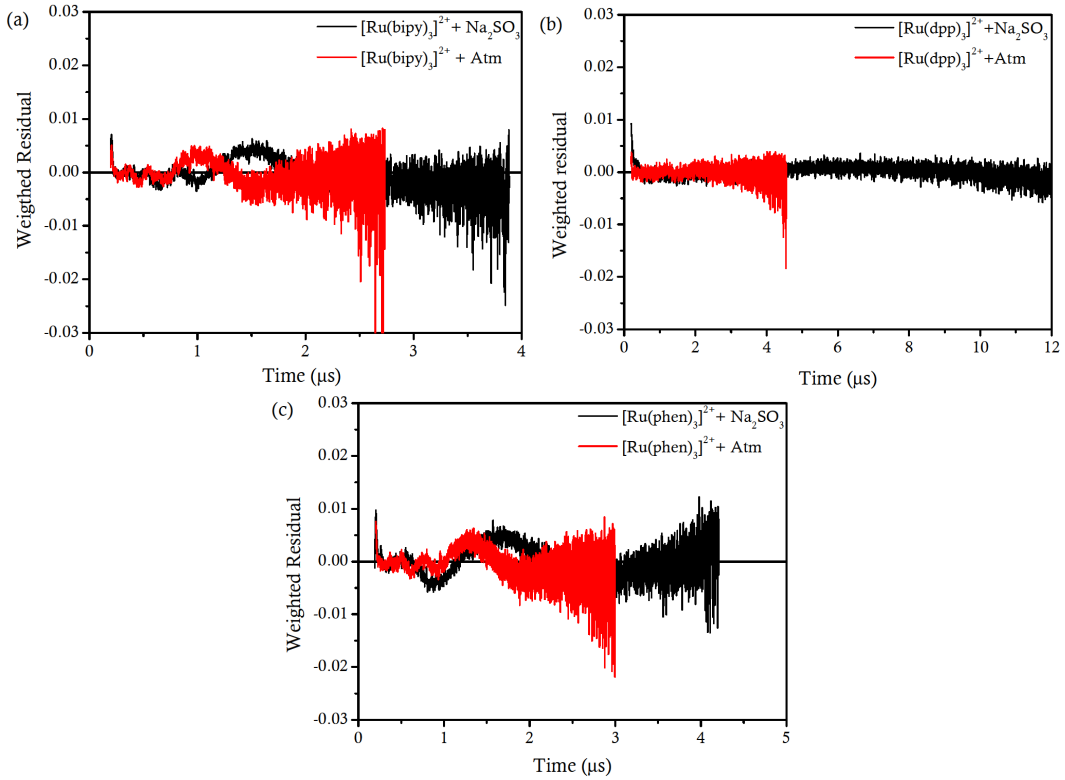


**Figure 32 – Weighted residual of fit and experimental data for (a) $[Ru(bipy)_3]^{2+}$, (b) $[Ru(dpp)_3]^{2+}$ and (c) $[Ru(phen)_3]^{2+}$ in $Na_2SO_3$ (black lines) and at atmosphere (red lines).**

The low peak intensity for $[Ru(dpp)_3]^{2+}$ is either due to concentration or laser power. The concentrations for all the dyes are the same, but in this case the measurement had to be repeated due to other exponential components appearing. Only ruthenium and water are present therefore the other components could have arisen from two populations, dissolved and undissolved ruthenium. As no extra components are seen in these decays, it can be assumed that the concentration was correct therefore it must derive from the laser. The laser power was maintained at the same level for each experiment, but when examining the second set of measurements the peak power had large variations present for consecutive pulses. The laser emission was dependent on previous user settings, the warm up period for the laser and the re-positioning of the cuvette. It highlighted the unreliability of the laser system and the effects on acquired lifetime magnitudes and hence the method.

The luminescence system acquired the full lifetime decay without restriction and provided an instant display of the decay in real-time with the flexibility of a tuneable laser. Unfortunately the disadvantages associated with this technique for future application are marked. The photoluminescence system was very temperamental, requiring realignment for the start of each days experiment. The system was unable to resolve positional excitation through the cuvette, which would be inappropriate for determining gradient measurements. Image acquisition was not possible because spatial information was not acquired due to the type of optical setup. Only solid powders and liquid measurements were possible due to the long path length between sample and detector. If a 3D cell system were used the diffraction and absorption would diffuse the exiting emission so much that it would be difficult to distinguish the low signal over the background noise. The use of 'leading edge' discrimination for time resolved measurements affected the peak height and width of the detected photon caused by the RC circuit. This would affect the overall registration of the photon arrival time and therefore the precision and accuracy of the derived lifetime.

### 2.3.4 Single-Photon Confocal LSM

A pulsed diode laser with variable repetition rate (PLP-10 470, Hamamatsu Photonics, Japan) provided single photon excitation at 467 nm with a 90 ps pulse duration, and pulse repetition between 100 MHz-1 Hz. The laser was connected to an inverted scanning confocal microscope (SP2 DM IRE2, Leica Microsystems Ltd., UK). The emitted photons were detected and counted using a time-correlated single photon counting (TCSPC) card (SPC830, Becker & Hickl, Gmbh) and cooled photomultiplier detector (PMC100-01, Becker & Hickl, Gmbh). The lifetime decays were displayed on a 3 GHz, Pentium IV, 1GB RAM computer.

### 2.3.4.1 Methods

Each dye solution was prepared with and without $Na_2SO_3$ as previously described in section 2.3.1.1. Slide encapsulation was used to minimise effects from evaporation. For each sample 50 µl of solution was pipetted into single cavity (15 mm dia.) microscope slides (76 x 26 mm, MNK-140-010A, Fisher Scientific, UK), as shown schematically in Figure 33. The cavity was enclosed by sliding over a rectangular cover slip (24 x 40 mm, thickness 170 µm, 631-1333, VWR, UK), whilst ensuring no air bubbles were present. Silicone adhesive was applied and cured for 1.5 h to seal the edge of the coverslip creating a liquid tight barrier. Slides were mounted and visualised using a Leica x63 (1.4 NA) oil immersion objective lens.

Experimental setup involved 467 nm excitation and used a pulse picked repetition rate at 500 kHz. The repetition rate was confirmed by the photon detector and synchronised (SNYC) count in the FLIM software. Optimisation of TCSPC acquisition was conducted through a trial and error procedure. FLIM acquisition times were 300 sec and used 256 time channels on the analogue to digital converter (ADC).

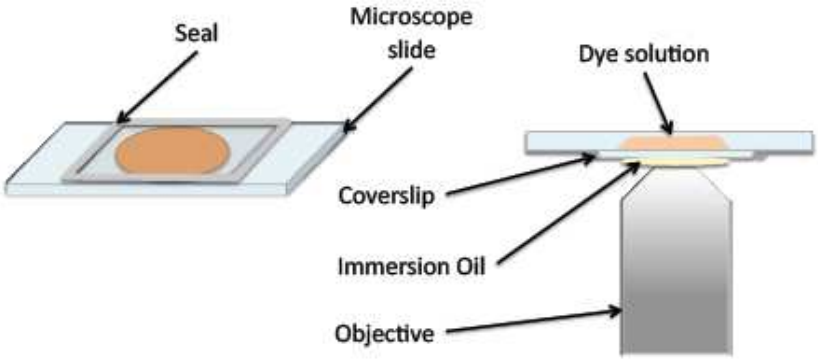


**Figure 33 – Sample set-up for confocal microscope, Left: Microscope slide with cavity holding ruthenium dye sealed with a cover slip and silicone adhesive to create slide encapsulation. Right: Orientation of the encapsulated slide and microscope objective for measuring photon decay with time.**

### 2.3.4.2 Data analysis

Due to the low noise level attributed to this method no extra manipulation of the data was necessary. Fitting the model to determine lifetime used the same software and equation as for luminescence system in section 2.3.3.2.

### 2.3.4.3 Results

The measured semi-logarithmic decays using TCSPC after excitation of $[Ru(bipy)_3]^{2+}$ , $[Ru(dpp)_3]^{2+}$ and $[Ru(phen)_3]^{2+}$ in aqueous solution are shown in Figure 34. The resulting measured lifetimes for $[Ru(bipy)_3]^{2+}$, $[Ru(dpp)_3]^{2+}$, and $[Ru(phen)_3]^{2+}$ in

$Na_2SO_3$ were 539 ns, 363 ns, and 249 ns, while in atm they were 395 ns, 1064 ns, and 440 ns, respectively. The TCSPC time range was restricted to 2 μs therefore the full decay was not recorded or visible. All decay profiles exhibited anomalise at the start, before the excitation, and at end of the decay. All the decays appear noisy indicated by the low level of counts collected apart from $[Ru(phen)_3]^{2+}$. For $[Ru(bipy)_3]^{2+}$ in Atm and $Na_2SO_3$, and $[Ru(phen)_3]^{2+}$ in Atm, the adjusted $R^2$ fits of mono-exponential decays were >0.99, but in Figure 34c $[Ru(phen)_3]^{2+}$ in $Na_2SO_3$ shows a non-linearity on a log-scale at the start of the decay. This indicates that another component is present and is confirmed by the low lifetime and the poor fit of a mono-exponential model with an adjusted $R^2 = 0.97$, where as a bi-exponential model produces an adjusted $R^2 = 0.99$. The decay response for $[Ru(dpp)_3]^{2+}$ appears almost flat with very little sign of any exponential decay present. The $[Ru(dpp)_3]^{2+}$ $Na_2SO_3$ sample has a lifetime almost three times shorter than in atmosphere, while both $[Ru(dpp)_3]^{2+}$ samples have very low count levels, at least 8 times less photons in the peak count than the other two dyes.

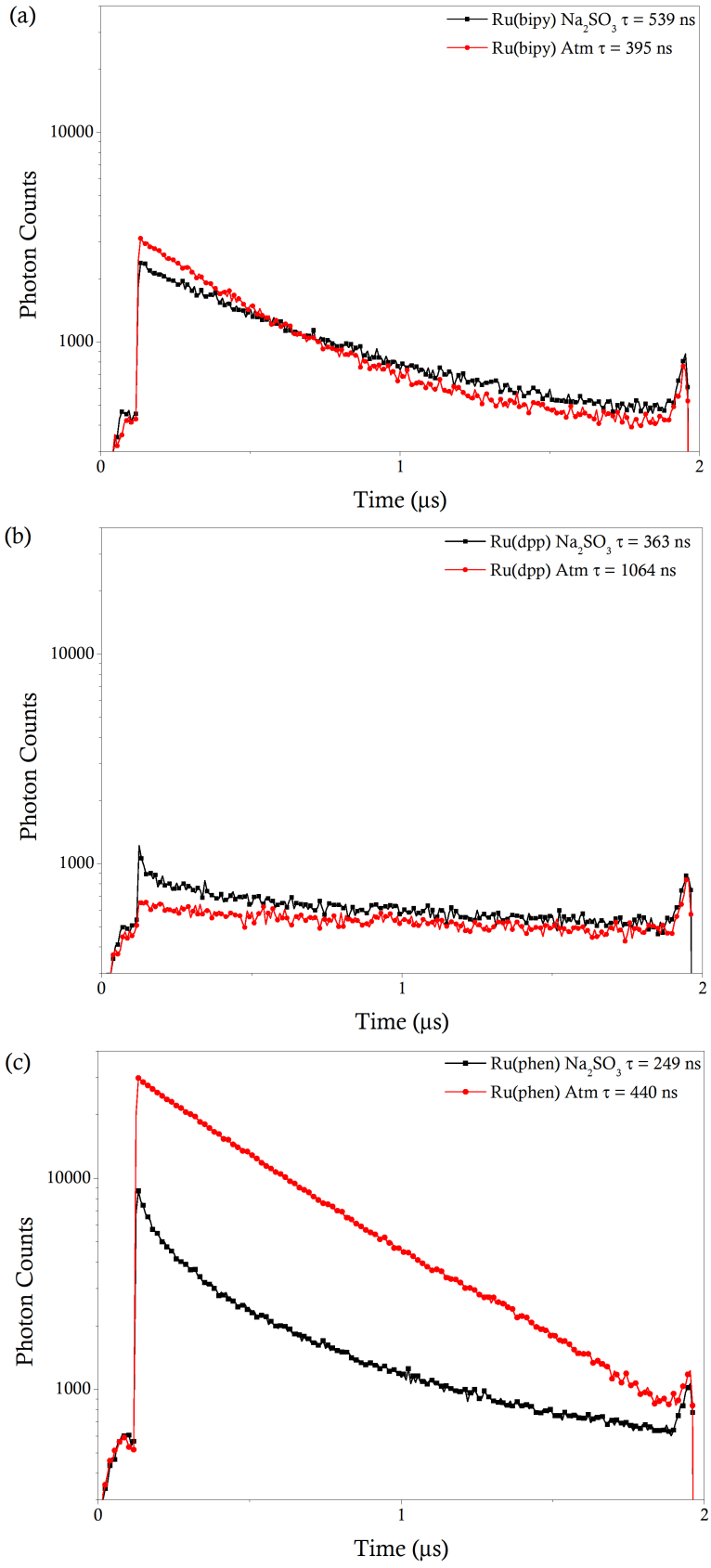


**Figure 34 – Semi-logarithmic decay of intensity during time for (a) $[Ru(bipy)_3]^{2+}$ τ = 539 ns and 395 ns, (b) $[Ru(dpp)_3]^{2+}$ τ = 363 ns and 1064 ns and (c) $[Ru(phen)_3]^{2+}$ τ = 249 ns and 440 ns, in solution with $Na_2SO_3$ and at atmosphere using a single-photon Confocal LSM and TCSPC system at ambient temperature.**

#### 2.3.4.4 Discussion

The decays all appear noisy except for $[Ru(phen)_3]^{2+}$ this indicates a low level of collected counts compared with background for the other decays. Every dye in Figure 34 shows a anomalies at the start and end of the decay. As all three dyes exhibited this it must derive from a systematic error in the system; false triggering of the SYNC and incorrect offset parameters of the TAC would lead to the effects, facilitating an increased background noise. The flat response from $[Ru(dpp)_3]^{2+}$ can only derive from two issues, low concentration or too short a collection time. The collection time was the same for all dyes therefore the issue must arise from the concentration. As the prepared concentrations are the same for each dye and the experiment environments are equal it rules out evaporation, leaving dissociation. This suggests that the dye is not dissolving or precipitates out of solution when competing with another substance that has a better affinity in water, such as $Na_2SO_3$.

The single-photon confocal LSM lacked optimisation for the FLIM set-up files this led to remnants of previous lifetime profiles accumulating at the beginning and ends of the decays. The system was only able to excite at 467 nm, which was adequate for this dye, but would be restrictive if using other fluorophores or for looking at other metabolites. The confocal facilitates the application of cellular samples providing high spatial resolution in the x-y axis, and creating sectioning in the z-axis as well as spatial registration. The use of single photon confocal restricts the excitation to <700 nm where the 'background' absorption limits the penetration depth due to tissue absorption [302] and can induce photo-damage.

### 2.3.5 Conclusion from section 2.3

Three techniques were tested to determine the time-domain suitability of obtaining lifetime decays for ruthenium(II) complexes. Assessment was based on technique utilisation, lifetime collection, and potential for investigating 3D cellular constructs.

The current fluorimeter was not capable of accurately acquiring lifetime, but other systems exist where it would be possible. Unfortunately these systems still rely on wide-field illumination, restricting the level of tissue/construct penetration and spatial resolution that is required. As summaried in Table 10 the fluorimeter in combination with time-gating was a suitable technique for multiple global intensity measurements during one acquisition, but not for multi- and bi-exponential decays, short lifetimes or spatial measurements.

The advantage of the luminescence system is the tunability in excitation and the flexibility of adjusting any part of the system. At the same time to achieve the required

spatial resolution a total system overhaul would be required. The pulse sampling was prone to interference from laser power and RC circuit effects in the cabling influencing the lifetime magnitude and decay, respectively. The time-resolved luminescence systems is excellent for acquiring long lifetime decays in liquid or solid samples, but is an inappropriate method for tissue or cellular measurements and is susceptible to timing errors induced by variations in laser power, RC circuit effects and IRF.

The advantage of using the TCSPC was that these timing problems were removed. Confocal setup also provides the high spatial resolution required in the x-y axis and sectioning in the z-axis. The only drawback was the laser as it could only excite at 467 nm, restricting investigation into other metabolites and increases the probability of photo-damage through the sample. This restricts the imaging/exposure time to the sample and reduces the depth of penetration. The confocal offers high spatial resolution and the ability for investigating cellular samples. If optimised the TCSPC has the potential to provide accurate and sensitive lifetime measurements for ruthenium(II) complexes. This system requires adaptation to provide variable wavelength excitation and a deeper penetration into tissue/construct.

**Table 10 – Summary of the advantages and disadvantage of the three time resolved time-domain systems investigated.**

| TECHNIQUES | ADVANTAGES | DISADVANTAGES |
|---|---|---|
| Fluorimeter | - Multiple samples measured simultaneously | - Initial decay profile not recorded<br>- Restricted excitation and emission wavelength<br>- Only provided global measurements/no spatial information |
| Time-resolved luminescence system | - Flexibility of a tuneable laser<br>- Provides full decay profiles | - Time-gate affected by laser power variation and RC circuit<br>- Unable to use on tissue or cellular samples |
| Single-Photon Confocal LSM | - Used on tissue or cellular samples<br>- High spatial resolution | - Restricted laser excitation<br>- Depth measurements not possible<br>- Collection of entire lifetime decay not possible |

If an optimised setup file was used the only variation to this system would be a multi-photon laser to increase penetration depth, while minimising photo-damage to the surrounding area and gain the flexibility of a tunable laser.

## 2.4 MP Confocal TCSPC time-resolved system

### 2.4.1 Introduction

The addition of a multi-photon laser to a confocal microscope is not a new concept, neither is its combination with TCSPC lifetime detection. This is already a well established technique that is at the forefront of lifetime technology for detection of autofluorescent components and distinction between wavelengths with multiple detectors [158, 168]. It has been used for the detection of rapidly decaying lifetimes, but due to the repetition rate of approximately 80 MHz the available time ranges are restricted to a maximum of 12.5 ns or less. With the addition of a pulse picker the tunability of wavelength is maintained, but with the added gain of variable repetition rates. This form of setup is less often used and tends to be incorporated with time-gated systems [284] because of its ability to rapidly collect fluorescent emission.

### 2.4.2 Equipment

A multi-photon 80 MHz tuneable laser (Mai Tai-Sapphire, Spectra Physics, UK) provided excitation (ex 700 - 990 nm, pulse width 50 - 150 fs) to an inverted scanning confocal microscope (SP2 DM IRE2, Leica Microsystems Ltd., UK). The pulse picker (Model 3980, Newport Spectra-Physics, UK) was capable of reducing the pulse repetition rate from 8 MHz down to single shot, controlled via a pulse selector (Model 3986, Newport Spectra-Physics, UK). The excitation pulse triggered a photon counter (PHD-400N, Becker&Hickl GmbH, Germany) used to determine the start of a decay, while emitted photons were captured using a time-correlated single photon counting (TCSPC) card (SP830, Beckle&Hickl GmbH, Germany) and PMT detector (PMH-100, Becker&Hickl GmbH, Germany). An optimised FLIM set-up file was provided by Leica for photon detection at a repetition rate of 500 kHz.

#### 2.4.2.1 Optical light path

The excitation light exits the Mai-Tai laser by means of a periscope mirror. To utilise the adjustable repetition rate (8 MHz to single shot) the light is directed through the pulse picker where the pulse selector is used to adjust the repetition rate before it exits. For the 80 MHz repetition rate an optional light path is used, the flip-mirror is engaged prior to the pulse picker and diverted around it using two further mirrors perpendicular to each other. A second flip-mirror acts to realign the laser beam to continue along the original light path.

A beam splitter reflects a small percentage of the beam to a photon counter to synchronise the TCSPC module, while the rest continues to the electro-optical modulator (EOM), remotely controlled via the Leica software. Upon exiting the EOM the light continues to another periscope mirror adjusting the height of the beam to reach an opening on top of the SP2 Leica system. The beam travels into the confocal eventually reaching the objective and is focused at the sample. The return emission is detected in a PMT via the objective where the photon emission is converted to counts by the TCSPC module.

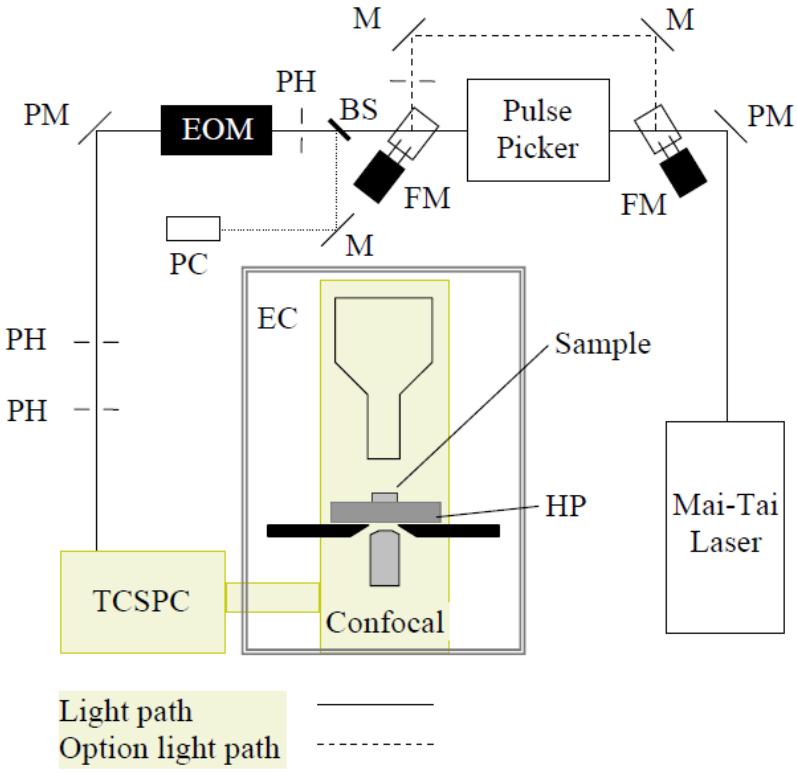


**Figure 35 – Schematic representation of optical light path of FLIM system layout from laser to confocal and TCSPC. Abbreviations: PM – periscope mirror, FM – Flip mirror, M – Mirror, BS – Beam splitter, PC – Photon counter, PH – Pinhole, EOM – electro-optical modulator, TCSPC – Time correlate single photon counting module, EC – Environmental chamber, HP – Heating plate.**

### 2.4.3 Methods

The sample preparation for ambient and low oxygen was carried out as in section 2.3.1.1. The laser excitation and pulse picked repetition rate was set to 880 nm and 500 kHz, respectively. The pinhole was fully open (600 µm) and the beam expander was set to "1" removing the lens and over filling the back objective plane to provide maximum illumination for sample excitation and detection. An SP700 filter blocked laser light reaching the detector at wavelengths >700 nm. The Electrical Optical Modulator (EOM) controlled the laser power and the gain was set to 65% with an offset of 47%. Photons were

collected until the maximum dynamic range was reached (65535/time channel) or 100 sec collection time had elapsed.

### 2.4.4 Results

Figure 36 shows the mono-exponential photon decay against time for $[Ru(bipy)_3]^{2+}$, $[Ru(dpp)_3]^{2+}$ and $[Ru(phen)_3]^{2+}$ at ambient temperature, in atmosphere (Atm) and in $Na_2SO_3$. The lifetimes measured for $[Ru(bipy)_3]^{2+}$, $[Ru(dpp)_3]^{2+}$ and $[Ru(phen)_3]^{2+}$ in $Na_2SO_3$ were 556 ns, 150 ns and 806 ns, while in Atm they were 360 ns, 890 ns and 656 ns respectively. All the dyes exhibit a rapid decline of counts at the end of the time period. The decay for $[Ru(bipy)_3]^{2+}$ and $[Ru(phen)_3]^{2+}$ in Atm solution attain the maximum dynamic range before the set collection times. In the $Na_2SO_3$ samples maximum dynamic range had not been fulfilled before the collection time had elapsed and this gave lower photon peak counts. All dyes show a mono-exponential decay, except for $[Ru(dpp)_3]^{2+}$ in $Na_2SO_3$ where the decay appears very noisy.

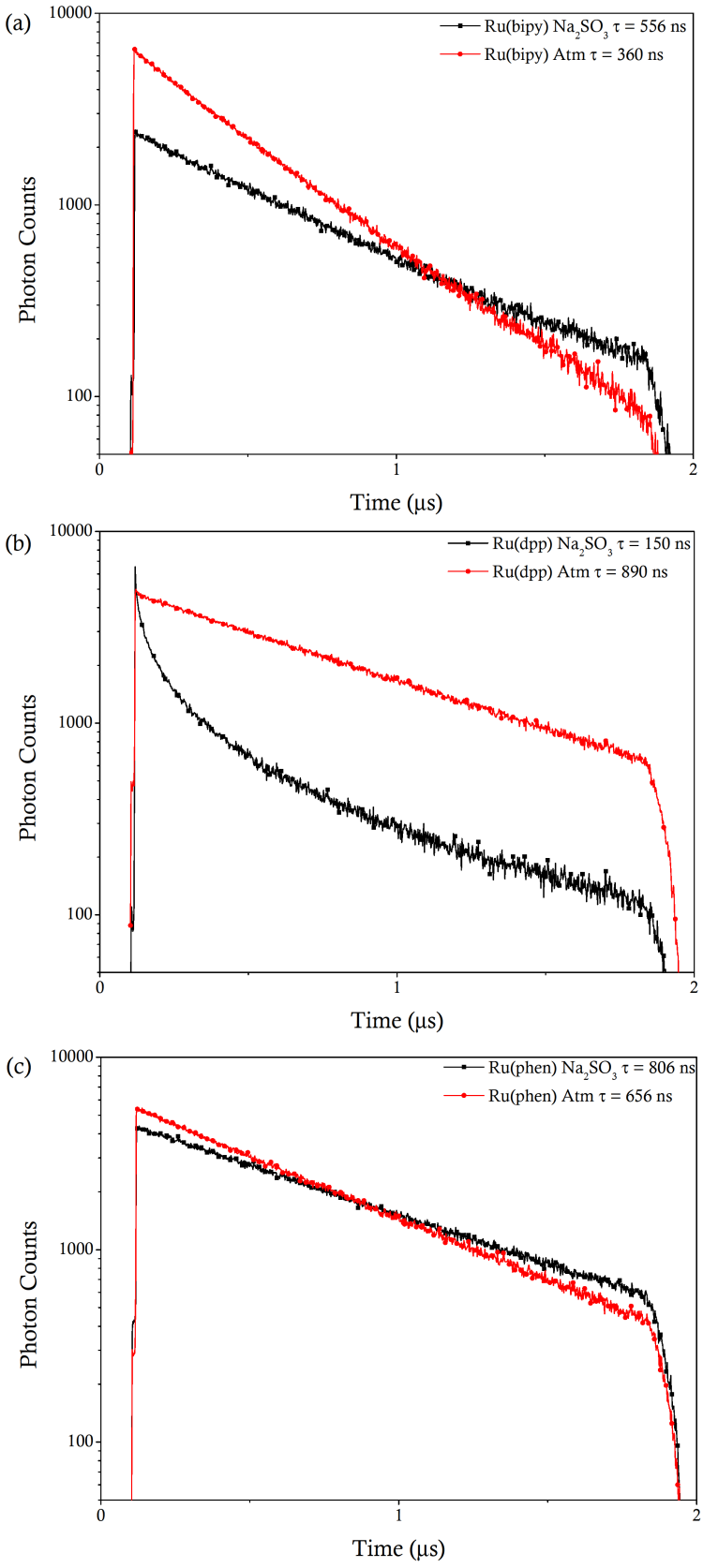


**Figure 36 – Semi-logarithmic decay of intensity during time for (a) $[Ru(bipy)_3]^{2+}$ τ = 556 ns and 360 ns, (b) $[Ru(dpp)_3]^{2+}$ τ = 150 ns and 890 ns and (c) $[Ru(phen)_3]^{2+}$ τ = 806 ns and 656 ns, in solution with $Na_2SO_3$ and at atmosphere using a two-photon Confocal LSM at ambient temperatures.**

### 2.4.5 Discussion

The single photon confocal TCSPC has been adapted by changing the laser and incorporating a pulse picker. This dealt with the issue of flexibility for excitation of other metabolites at different wavelengths, increased the potential penetration depth, while reducing the effects of photo-damage in the out of focus regions. The two photon confocal LSM uses a tunable IR laser (700-900 nm) that can penetrate tissue; as tissue is optically transparent above 700 nm [158]. The incorporation of an optimised FLIM setup file has vastly improved the acquired data, reduced artificial pulsing and produced less noisy decays, but reoccurring problems still arose for $[Ru(dpp)_3]^{2+}$ $Na_2SO_3$ samples as seen in all previous experiments.

There are great similarities between measured and published data as seen in Table 11, but in some cases it is lacking and the greyed out boxes signify poor data. A direct comparison of lifetime decays for $[Ru(dpp)_3]^{2+}$ in solution is near impossible as others have only described it dissolved in an organic solvent [46] or embedded in a matrix [18]. It has proven to be difficult to measure in aqueous solution due to its poor solubility and would therefore be an inappropriate dye to take further for cellular investigation; it is also 400 times more expensive that the other ruthenium(II) complexes tested.

Similar problems were seen for $[Ru(phen)_3]^{2+}$, where the majority of papers describe intensity based measurements and very few showed lifetime results. Liebsch *et al.* [184] did show $[Ru(phen)_3]^{2+}$ at zero oxygen has a lifetime of 880 ns, which is similar for both photoluminescence and two-photon systems. Discrepancies between the published and measured results can be attributed to the non-zero oxygen levels used in current experiments.

$[Ru(bipy)_3]^{2+}$ was well documented for the detection of oxygen in aqueous solution, which was shown by the abundance of measurements reported. The table shows that published and measured data for $[Ru(bipy)_3]^{2+}$ in atmosphere are very similar where the variation <35 ns and span of lifetimes is between 360-395 ns. The measurements for $[Ru(bipy)_3]^{2+}$+$Na_2SO_3$ are near identical for measured data with a difference of <17 ns. Generally the $Na_2SO_3$ values are lower than the published results, but they are compared with zero oxygen measurements and the use of $Na_2SO_3$ cannot be relied upon to completely remove all oxygen from the sample unless monitored.

The photoluminescence system used a PTFE sealed cuvette restricting the oxygen from entering, but the two-photon system used a silicon sealed slide, which has a high permeability to oxygen, but restricts evaporation. This shows the need for an air-tight

sealable chamber to be developed for future experiments that can be mounted onto a microscope stage.

**Table 11 - Lifetime decays in nanoseconds for three ruthenium (II) complexes in aqueous solution at atmosphere and $Na_2SO_3$. Values obtained using three different systems and compared to values reported in previous studies**

| OXYGEN LEVEL | Atm (ns) | | | $Na_2SO_3$ (ns) | | |
|---|---|---|---|---|---|---|
| TECHNIQUES | Ru(bipy) | Ru(dpp) | Ru(phen) | Ru(bipy) | Ru(dpp) | Ru(phen) |
| Luminescence system | 380 | 767 | 448 | 554 | 2573 | 871 |
| Single-Photon Confocal LSM | 395 | 1084 | 440 | 539 | 363 | 249 |
| Two-Photon Confocal LSM | 360 | 809 | 656 | 556 | 150 | 806 |
| Van Houten[300] | | | | 580 *⊕ | | |
| Morris [212] | 393 | 2300 ° | | 600 * | 5300 ° | |
| Castellano [49] | 360± 4 | | | | | |
| Mulazzani [217] | | | | 610 * | | |
| Zhong [324] | 381 □ | | | 610 *□ | | |
| Liebsch [184] | | | | | | 880 * |
| Casper [47] | | | | 630 *⊕ | | |
| Demas [68] | | | | 765 *⊗ | 5340 *⊗ | 313 *⊗ |

* Refers to measurements made at $\tau_0$ i.e. zero oxygen

□ Samples were measured in phosphate buffer solution

° Samples measured in ethylene glycol

⊗ Samples measured in methanol

⊕ Sample measured at 25°C

### 2.4.6 Conclusion from section 2.4

The adapted system has fulfilled all the required specifications outlined at the beginning of the project in Chapter 1 and has shown good correlation with published data for $[Ru(bipy)_3]^{2+}$ in Atm and $Na_2SO_3$. Once again the problems previously seen with $[Ru(dpp)_3]^{2+}$ in aqueous solution have arisen leading to the conclusion that it is not an appropriate dye for aqueous cellular experiments. This leaves two possible ruthenium(II) complexes that have the potential for detecting oxygen in aqueous solution. Both have similar atmospheric lifetimes, but at low oxygen $[Ru(phen)_3]^{2+}$ is longer, which means more sensitive to change in oxygen levels. Before a final decision is reached suitability of using the dyes with cells should be determined.

## 2.5 Cytotoxicity of ruthenium (II) on cells

### 2.5.1 Introduction

As described in Chapter 1 there are a host of ruthenium (II) complexes used in a variety of application, for example, inhibition of cancer cell growth by interstrand crosslinking to DNA [132] or used in photodynamic therapy (PDT) to non-invasively irradiated cells by production of radicals [180]. One of the largest interests in ruthenium(II) complexes derives from its ability to inflict cell death by restricting DNA repair/replication and the production of radicals from light stimulation. It is therefore important to ascertain whether incubation of with cells ruthenium(II) complex will induce cell death or affect cellular metabolism.

It would be expected that as the concentration and exposure times of the dyes increase there would be a reduction of cell growth, therefore a viability assay is required to assess cytotoxic effects from the dyes. AlamarBlue® (AB) provides a measure of cellular metabolic activity by detecting the level of oxidation during respiration. AB has been shown to be more sensitive than the (3-[4,5-dimethylthiazol-2-yl]-2,5-diphenyl tetrazolium bromide) MTT assay and is relatively inexpensive [111]. AB incorporates a colourimetric REDOX indicator so that a reduction causes the REDOX indicator to change from blue to red. Continued metabolism reduces the environment (changes to red), while inhibition of metabolism maintains an oxidised environment (stays blue), but only the reduced form is excited and measured [62]. The vehicle of measurement is a multi-well plate system that can be loaded onto a fluorimeter allowing rapid assessment of multiple samples simultaneously.

Optimisation of AB was necessary before continuing with further experiments as the standard density or incubation period is cell and microwell plate dependent. A 96 well plate with nine cell densities ranging from 391-100,000 cells/cm$^2$ were incubated from 0-74 hours and emission recorded 10 times over a 48 hour period. The data suggested that the optimum cell seeding density for chondrocyte cells was 25,000 cells/cm$^2$ during an incubation period of 48 hours (data shown in Appendix A).

### 2.5.2 Materials and Methods

#### 2.5.2.1 Chemicals

The oxygen sensitive dyes used were Tris(2,2′-bipyridyl)ruthenium(II) chloride hexahydrate $[Ru(bipy)_3]^{2+}$ (224758), and tris(1,10-phenanthroline)ruthenium(II) chloride $[Ru(phen)_3]^{2+}$ (343714) (Sigma-Aldrich, UK); 10 mM stock solutions were created with

deionised water. The cell culture media used was Dulbecco's Modified Eagle Medium (DMEM) (D6429) supplemented with 3.8 g/l HEPES (H0887), 80.6 U/ml penicillin and 80.6 mg/l streptomycin (P4333), 0.12 g/l L-ascorbic acid (A0278), 1% L-glutamine (G7513), and 16% (v/v) fetal bovine serum (FBS) (F7524) (Sigma-Aldrich, UK). Enzyme digestion used Pronase 700 units/ml (P8811) and Collagenase 100 unit/ml (C7657) purchased from Sigma-Aldrich, UK. The viability assay was AlamarBlue® (DAL1025, Invitrogen, UK).

#### 2.5.2.2 Chondrocyte isolation

Chondrocyte isolation followed a well established protocol as used in many previous studies [54, 130]. Cartilage was dissected from the proximal surface of bovine metacarpal-phangel joints of adult steers. Initially joints were cleaned and soaked in 70% Industrial Strength Methanol (IMS) for five minutes prior to dissection. Joints were opened under sterile conditions and sections of cartilage were removed using a scalpel and transferred to media filled 35 mm Petri dishes for each joint. Once all cartilage had been removed from the joint the cartilage fragments were finely diced.

Tissue from each joint (n=3) was sequentially digested, 37°C, with pronase and collagenase enzymes for one and 14 hours, respectively. The digested solutions were sieved through a 70 μm nylon cell strainer (BD falcon), washed three times with DMEM+16%FBS, pooled together, and resuspended in 30 ml fresh DMEM+16%FBS. Once re-suspended in media (DMEM+16% FBS) a haemocytometer was used to determine the number of cells. The cells were seeded in four 96 well plates at a density of 25,000 cells/cm$^2$ and incubated for 48 hours to allow cell attachment.

#### 2.5.2.3 AlamarBlue™ assay preparation

The AlamarBlue® reagent was filtered and diluted in media to produce a 10% (v/v) solution. As a control a small quantity was removed and autoclaved, providing a fully reduced form of AlamarBlue®. The reduced solution was equilibrated at 37°C in a multi-well plate and transferred to the fluorimeter. The reduced form of alamarBlue® was tested with the gain adjustment to ensure the PMT would not saturate during the actual experiment and the value was recorded.

#### 2.5.2.4 Cytotoxicity experiment

To minimise sample photo-degradation the experiment was conducted without lights in the sterile hoods and all pots containing dye and alamarBlue® were wrapped in sliver foil. Six serial dilutions from ruthenium stock solutions were created with media at

concentrations between 5 mM and 156.25 μM. After the cells had been incubated for 48h the media was replaced with each ruthenium dilution and control.

Four multiwell plates were prepared representing cells with different exposure times with dye for 10min, 20min, 40min, and 24h. To aid temperature stability water was pipetted surrounding the periphery of the wells. Plates were immediately transferred to the incubator after applying dye to the cells. Once the exposure times had elapsed, dyes and control solution were removed, replaced with media and incubation was continued until all time points had been completed. At the final time point media was removed from all the plates and replaced with the pre-prepared diluted alamarBlue® in DMEM+16%FBS solution. A control measurement was recorded for each plate to ensure no anomalies were present and all plates were then incubated for a further 48 h and the final measurement was recorded to determine levels of reduction.

### 2.5.3 Data analysis

Background measurements were taken from water, averaged and subtracted from all values. Excel files were exported to OriginPro scientific software where intensity values of replicates were averaged and percentage of cell metabolism calculated using Eq. 16,

**Eq. 16**
$$G_I = \frac{\mathrm{I}_T}{\mathrm{I}_{UT}} \times 100$$

where, $\mathrm{I}_T$ is the fluorescence intensity of treated cells (ruthenium dye added), $\mathrm{I}_{UT}$ fluorescence intensity of untreated cells (negative control), $G_I$ is percentage of metabolic activity, used as a measure of cellular viability.

### 2.5.4 Results

Figure 37 and Figure 38, display the chondrocytes metabolism with increasing dye concentration and exposure. Cells exposed to $[Ru(bipy)_3]^{2+}$ maintain metabolic activity above 80% for all exposure times at concentration <2.5 mM. For $[Ru(phen)_3]^{2+}$ if exposure times are ≤40 min metabolic activity is maintained at 80% for all concentrations <2.5 mM, but at longer exposure times metabolic activity drops below 80% at concentrations >1 mM.

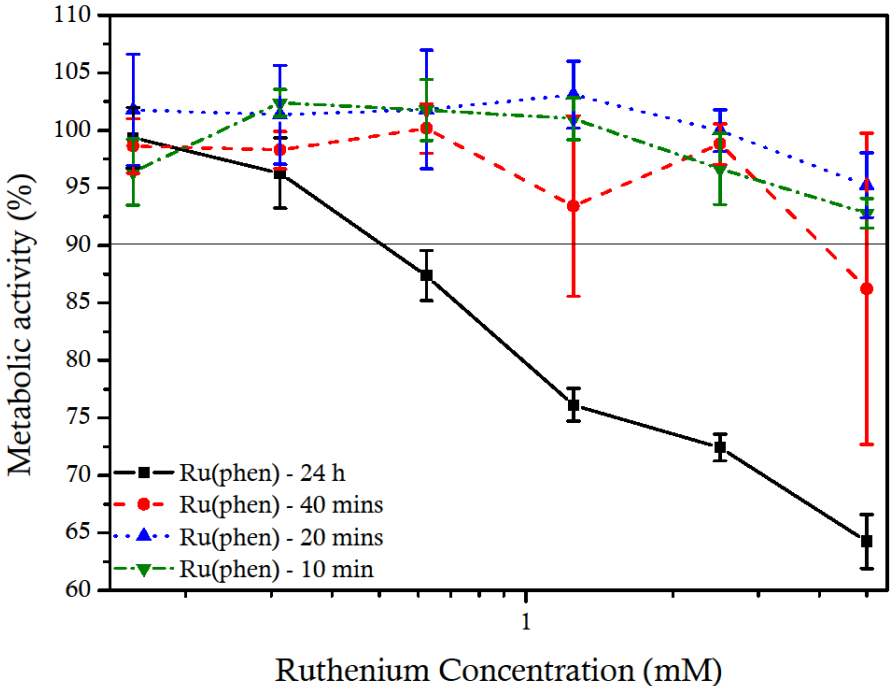


**Figure 37– The effect of concentration and exposure of $[Ru(phen)_3]^{2+}$ on cell metabolic activity, data points represent mean values with error bars representing standard error (n=3).**

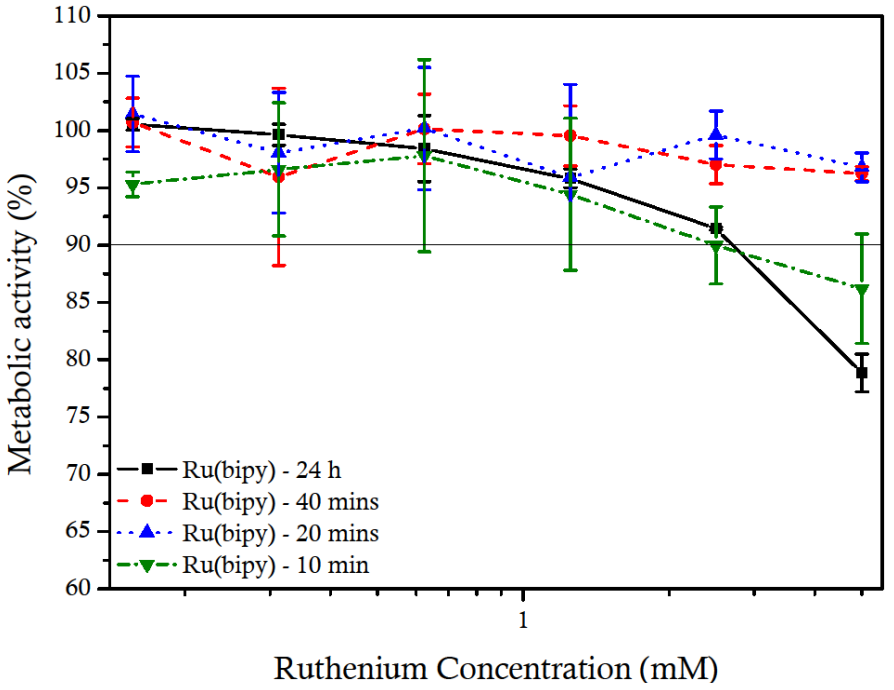


**Figure 38 – The effect of concentration and exposure of $[Ru(bipy)_3]^{2+}$ on cell growth. Data points represent mean values with error bars representing standard error (n=3).**

### 2.5.5 Discussion

Ideally maintaining cellular viability above 90% is the optimal option for cell culturing purposes. At low concentration of $[Ru(bipy)_3]^{2+}$ and $[Ru(phen)_3]^{2+}$ <2.5 mM and exposure times <40 mins cells maintain more than 90% of the metabolic activity of non-

exposed cells. As ruthenium(II) complexes and Calcien AM are of similar molecular weight the time required to diffuse through an agarose construct would be expected to take at least 2h before the sample could be tested. Plus the additional time of illumination suggests only the 24h exposure time can be considered in order to remove any risk of cytotoxicity. Applying this restriction means $[Ru(bipy)_3]^{2+}$ can be applied in cellular measurements up to a concentrations of 2.5 mM. However with $[Ru(phen)_3]^{2+}$ the onset of cytotoxcity is apparent at concentrations as low as 0.5 mM. This was also found by Dobrucki [72] who showed that $[Ru(phen)_3]^{2+}$ did not pass through intact biological membranes, or cause measurable photo-damage to plasma membranes at concentrations of <0.2mM. In order to maintain flexibility the more suitable option for oxygen sensitive dye would be $[Ru(bipy)_3]^{2+}$.

Dobrucki [72] also mentioned the effects from phototoxicity where he found that at extracellular concentrations of <0.2 mM, and after 120 illuminations using 457 nm light, a detectable amount of both complexes accumulated at the plasma membranes. The loss of membrane integrity was suggested to occur via a mechanism that may involve the generation of singlet oxygen species [72]. However, this was suggested to be dependent on dye concentration and the number of illuminations. It highlights that phototoxicity is another aspect that requires further investigation once an established experimental protocol has been completed.

### 2.5.6 Conclusion from section 2.5

It has been shown that $[Ru(bipy)_3]^{2+}$ poses the least cytotoxic risk to chondrocytes provided exposure times and concentrations are maintained at less that 24 h and 2.5 mM. Although the effect of illuminating the dye still requires investigation, it is not possible to test this until a full imaging protocol has been determined.

## 2.6 Air-tight sample chamber

During current experiments it has become apparent that a more appropriate method for transporting dye solution, restricting evaporation and maintenance of low oxygen atmospheres is required for further investigations. These are issues that need to be considered when designing a suitable vessel, but restriction to the design derives from the intended FLIM system, involving a heated confocal microscope. The specifications are:

- Coverslip required for contact with objective
- Temperature must be maintained at 37°C inside chamber
- Chamber must be sealable and maintain low oxygen environment

- Material must be sterilised via autoclave
- Withstand temperature from 4°C to >126°C
- Not degrade, rust or corrode
- Unreactive to oil, aqueous solutions, salts, proteins and methanol

There are a wide variety of materials available for the body of the chamber at our disposal, but the field can be narrow by observing what is already used in the biological field. Traditionally surgical stainless steel uses austenitic 316L due to its high resistance to corrosion, ability to endure sterilisation processing and its high strength material [195]. Its hardness does require specialist tools to machine, but its resistance to corrosion makes it an ideal option for cellular interaction. The other necessary component is the interaction between the body of the chamber and the coverslip. This requires a form of seal that prevents gas permeability.

There are a large variety of seals available, but they are dependent on the type of pressure, temperature, chemical interaction, and permeability of the intended application. One of the lowest gas permeable materials is Butyl based isobutylene-isoprene that are used in high pressure and vacuum systems, although they should not be used in conjunction with mineral oil [305]. This makes it an inappropriate option due to the use of oil on the objective lens. The other option is a fluoroelastomer such as Viton®. This material can withstand severe chemical conditions, high temperature range (-30 to 250°C) [305] and is routinely used in high vacuum systems by Swagelok.

The material properties of both body and seal chosen, the design of the chamber had to be small enough to locate on a microscope stage inside a heating plate, whilst maintaining enough clearance for objective lens to reach the coverslip. The final design is shown in Appendix A and the finished product is displayed below in Figure 39; Six chambers were manufactured.

**Figure 39 – Final manufactured air-tight sample chamber composed of a stainless steel 316L body and Viton® 'o'ring seal. Left: exploded side view of chamber, Right: view of o-ring embedded with in stainless steel body.**

## 2.7 Summary

- Single photon excitation spectra for ruthenium(II) complexes showed that all complexes displared a maximum excitation peak of 468 nm and emission peak of 592 nm, 607 nm and 616 nm for $[Ru(phen)_3]^{2+}$, $[Ru(bipy)_3]^{2+}$ and $[Ru(dpp)_3]^{2+}$, respectively.
- $[Ru(bipy)_3]^{2+}$ was chosen for continued experiments while the two excluded dyes $[Ru(dpp)_3]^{2+}$ and $[Ru(phen)_3]^{2+}$ were shown to be unsuitable for aqueous solutions and induced cytotoxic effects at concentrations >1 mM reducing viability to <80% at exposures of 24h, respectively.
- Assesment of the time-resolved time-domain techniques identified an adapted two-photon TCSPC confocal could meet the required specification with the addition of the pulse picker.

# 3 Calibration of the FLIM system

## 3.1 Introduction

The previous chapter identified the selected oxygen sensitive fluorophore and lifetime detection system as $[Ru(bipy)_3]^{2+}$ and the confocal laser scanning microscope with multi-photon laser excitation and time correlated single photon counting (TCSPC) system, respectively. The laboratory setup and schematic layout of the equipment is displayed below in Figure 40.

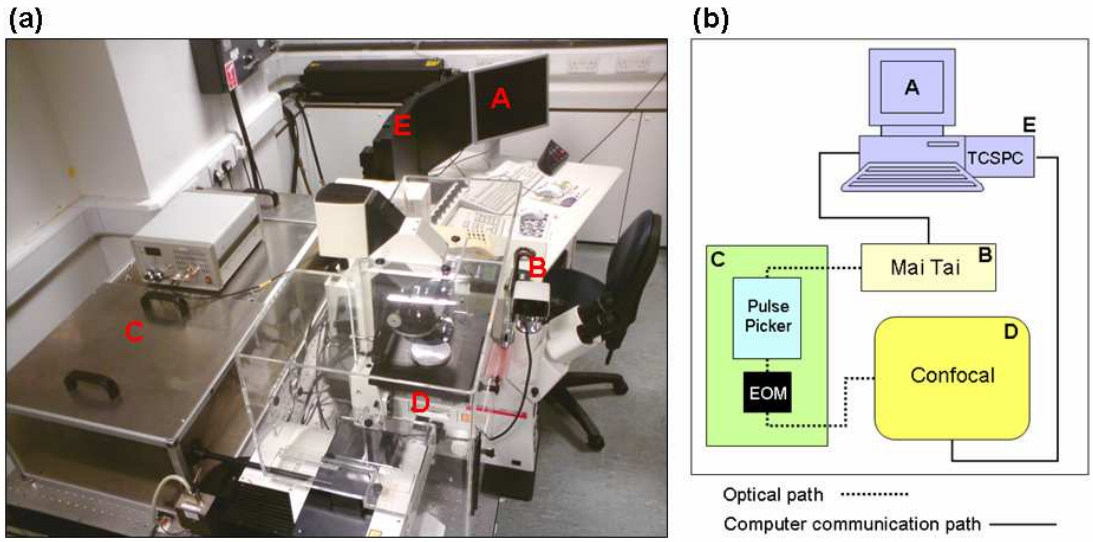


**Figure 40 – The laboratory equipment setup identifies the layout of the FLIM system displayed (a) photographically and (b) schematically. The automated computer (A) control of the confocal and the MP laser (B) drives the operation and data acquisition process. The Mai Tai (B) delivers laser light into the metal safety enclosure (C) containing the pulse picker and EOM. The adjusted pulsed beam exits the enclosure and is directed to the confocal microscope contained within an environmental chamber (D). The lifetime setup and data collection is controlled from the TCSPC (E) module located within the computer and communicates with the confocal.**

This chapter focuses on the issues pertaining to the combination of a fluorescent dye operating at the limits of a relatively rapid detection system. Identifying these complex issues that arise from this unique situation will be achieved by providing a fundamental

understanding of each component. This knowledge base will highlight areas prone to problems and by strategically placing strict controls will resolve and ensure minimum variability or reasons for inducing error. The initial stages of this PhD were involved in the specification and installation of the FLIM system for use with the selected oxygen sensitive fluorophore. This chapter separately investigates the components of this FLIM system: the multiphoton laser, the confocal microscope and the TCSPC module. The experimental calibration will identify set parameters suitable for creating a protocol for future experiments. The standard operating procedure for the alignment and realignment of switching the laser repetition rate between 80 MHz and single-shot is described in Appendix C.

## 3.2 Multi-photon Laser: Two-photon excitation (TPE)

### 3.2.1 Introduction

The theory of two-photon excitation was first described by Maria Goppert-Mayer in 1931 [8], she predicted that an atom or molecule could simultaneously absorb or emit two photons in a single quantised event [197]. It wasn't until 30 years later in 1963 that Kaiser and Garret [146] obtained the technology and were able to confirm the theory. In 1990 the invention of two-photon fluorescence microscopy based on the nonlinear excitation of fluorophores, led to the development of 3D imaging technology, as described by Denk *et al.* [69]. The development of two-photon microscopy removed many issues associated with single-photon excitation (SPE) microscopes. Unlike in SPE, TPE could penetrate deeper within the tissue only exciting at the focal point. This technology has been considered a revolution for biological imaging due to its ability to:

- Reduce photo-damage and allow long term monitoring of living specimens [158]
- Image turbid specimens with sub-micrometer axial resolution of a few hundred nanometers [26]
- Allow high-sensitivity imaging by eliminating the contamination of fluorescent signal from excitation light [284]
- Initiate photochemical reaction within a sub-femtoliter volume inside cells and tissues [69]

SPE excites the specimen throughout the sample, as shown in Figure 41 (continuous beam path) photo-bleaching occurs on a time-averaged excitation intensity, regardless of axial position [69]. The TPE occurs only at the focal point, as shown in Figure 41 (spot), photo-bleaching is dependent on the time-averaged square of the excitation

intensity. Outside of the focal point the TPE reduces quadratically minimising possible photobleaching and providing naturally occurring optical sectioning without the requirement for of pinhole [69].

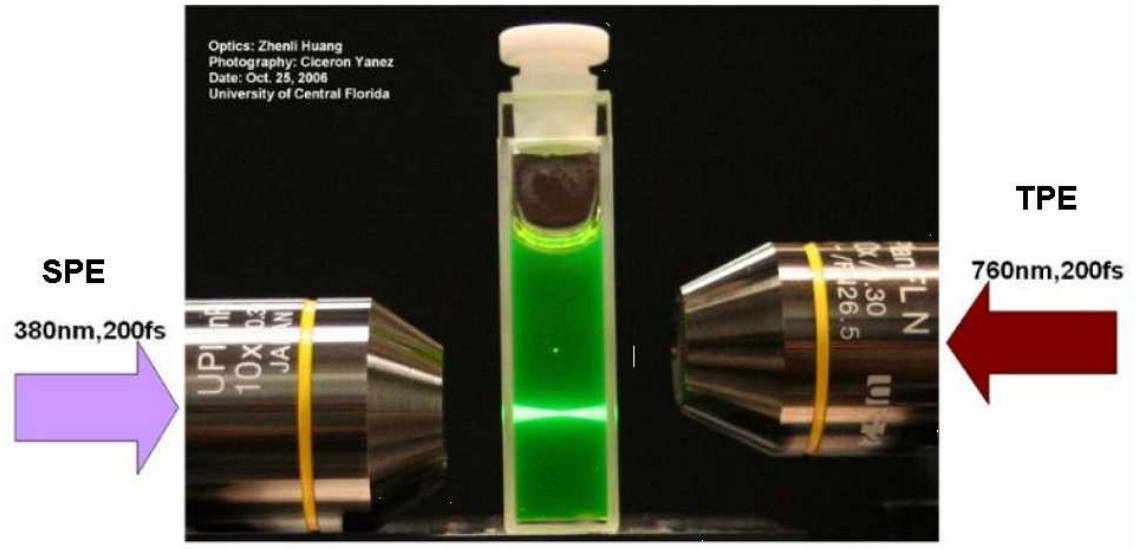


**Figure 41 – Image displaying comparison of TPE (dot) and SPE (cone shape) in a fluorescein sample excited at 380 nm and 760 nm for SPE and TPE, respectively [319].**

The difference between the SP and TP excitation process is diagrammatically shown in Figure 42. In single photon excitation the electrons are excited into the higher energy state ($S_2$) with a single photon, the electrons undergo an internal conversion through vibrational and heat transition, before reaching the lowest high energy state ($S_1$) and reducing to ground state ($S_0$) via fluorescence. In two photon excitation the simultaneous collision of two photons is required within $10^{-15}$-$10^{-16}$s [171] to create enough energy to force an electron into a higher energy state ($S_2$). This is achieved using a femto- or pico-second pulsed laser that emit photons at the same wavelength or two lasers of different wavelengths combined to produce the same excitation energy [274]. Once the electrons attain the higher energy state ($S_2$), the transition process to the ground state ($S_0$) is identical to SPE. Multi-photon excitation is essentially the same as TPE except more than two photons at less energy are required to reach the higher energy state. The setup used in these experiments is designed to measure TP events therefore MP events will not be further discussed.

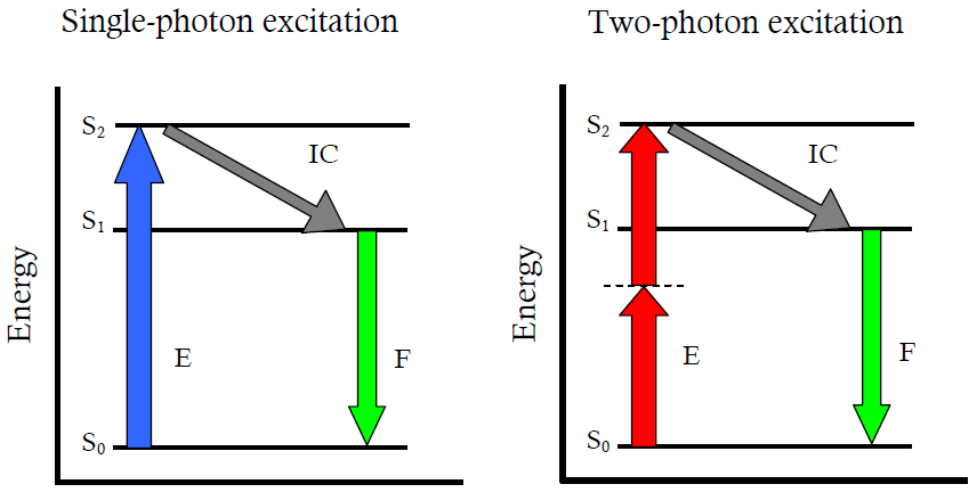


**Figure 42 – Simplified Jablonski diagram displays the electron excitation pathway for SPE and TPE. Left: SPE uses one photon to excite the electron into the higher energy state $S_2$ where internal conversion occurs to the lowest high energy state $S_1$ and fluorescence emission occurs. Right: TPE uses two photons with half the energy to excite the electron into the higher energy state $S_2$ where internal conversion occurs to the lowest high energy state $S_1$ and fluorescence emission occurs. Abbreviations: $S_0$ – ground state, $S_1$ – lowest high energy state, $S_2$ – highest high energy state, E - excitation, IC – internal conversion, F – fluorescence. Adapted from So *et al.* [274].**

TPE is provided by high peak power femto- or pico-second pulses delivered through an objective lens [27]. TPE uses near-infrared laser light (700-1100 nm), which takes advantage of tissues naturally occurring optical window thus avoiding absorption [158]. The major absorbing components of tissue are shown in Figure 43, with regards to chondrocytes in agarose only the water absorption needs to be considered in this situation. This lack of absorption reduces the possibility of photodamage to the surrounding tissue [284], and the likelihood of signal attenuation [26], as shown in Figure 44. This avoids the need to compensate with increased laser power for deeper penetration, but the light is absorbed at the focal point leading to possible photobleaching or damage. However this is minimised with the use of a femto-second laser that reduces the pulse width and exposure time at the focal point [158].

A large variety of methods exist for the production of femto-second excitation sources these experiments used a Mai Tai™ from Newport Spectra-Physics. A more comprehensive understanding is outlined in the following section.

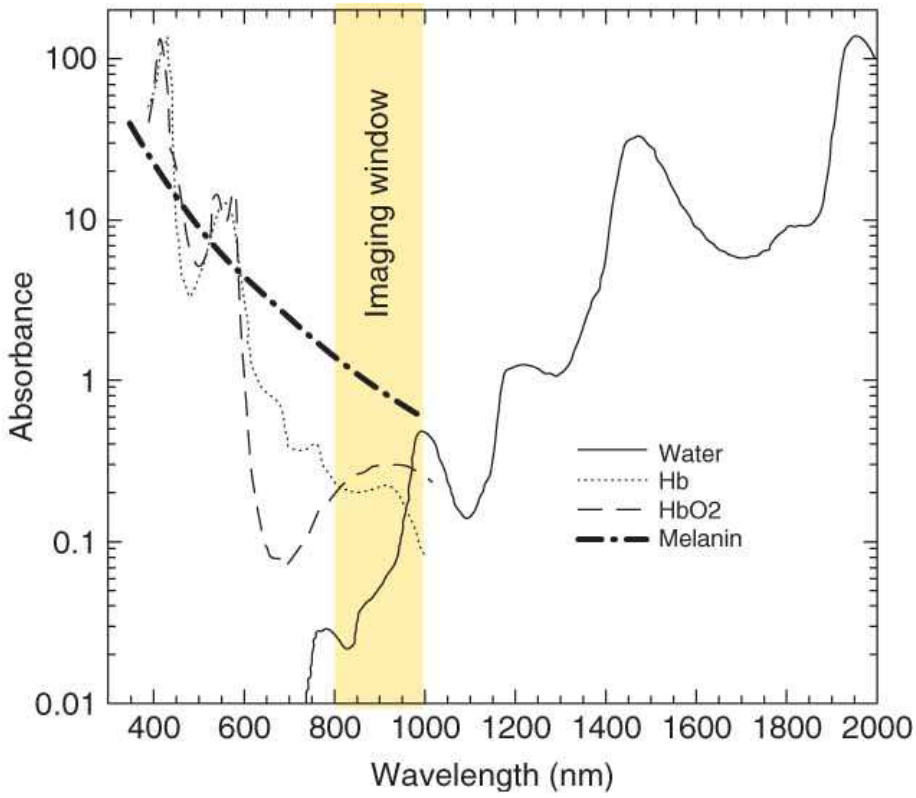


**Figure 43 – Absorbance spectra of water (line), dehaemoglobin (dotted line) oxyheamoglobin (dashed line), and melanin (dash-dot line) across wavelength range from 500 to 2000 nm. The highest optical transmittance window is shown between 800-1000 nm [10], but generally 700-1100nm is considered the optical window as not all tissue has melanin.**

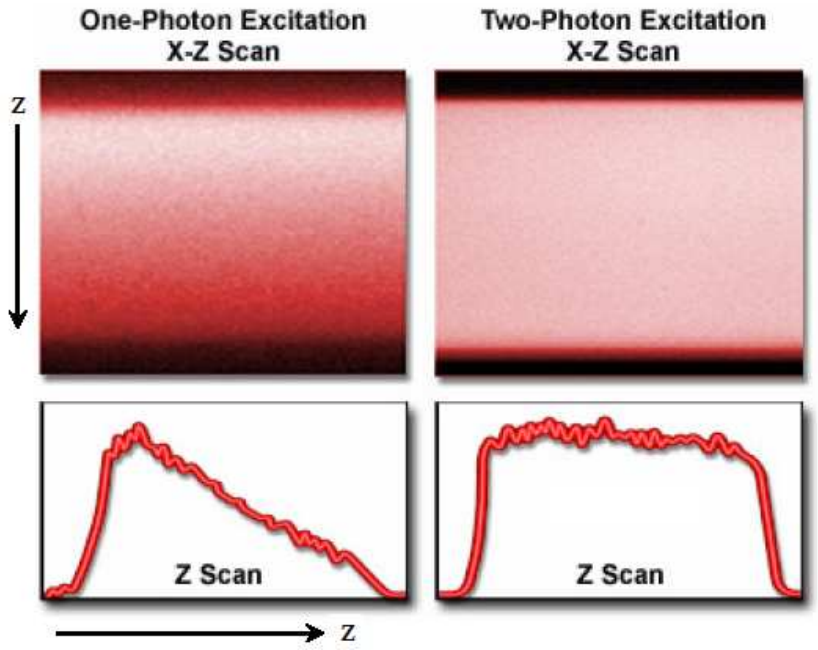


**Figure 44 – Scanned images in the X-Z plane (above) showing the attenuation signal in the z-axis when using of single/one-photon excitation compared to two-photon excitation profile plots in the z-axis. The resulting intensities are shown below. Adapted from Piston *et al.* [240].**

### 3.2.2 Mai Tai™ Sapphire two-photon excitation laser

The Mai Tai™ laser (Ti:Sapphire, Newport Spectra-Physics, UK) is a self contained unit with computer controlled excitation tuning between 710-990 nm. It produces a <100 fs pulse width at a repetition rate of 80 MHz. Cryo-cooling is required with most MP systems, but instead this system maintains diode temperature at <32°C using aqua-cooling [275]. A TP laser is built-up of multiple excitation modules that each stimulate the other; all use the same stimulation method.

The process of excitation consists of a light source, e.g. lamp, electrical power supply or another laser, 'stimulating' a gain medium made from fluid or solid material. The composition of the gain medium determines the emission wavelength and whether it emits continuous or pulsed light. Emission from the gain medium is amplified by a resonator cavity consisting of one highly and one partially reflecting mirror, as shown in Figure 45 [198].

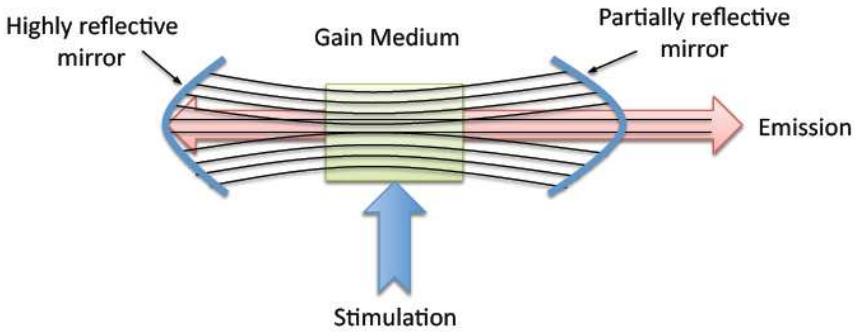


**Figure 45 – Excitation mechanisms is used to stimulate a gain medium and the emitted fluorescence is amplified between two reflective mirrors. Adapted from McConnell [198].**

The Mai Tai™ laser is composed of an electrical power supply (240 V) that stimulates a semi-conductor laser, which emits light at 808 nm. The 808 nm excitation light stimulates a neodymium-doped yttrium orthovanadate ($Nd:YVO_4$) gain medium to generate the strongest laser transition in the $Nd:YVO_4$. This creates a diode-pumped solid-state laser [275] with an emission at 1064 nm [234]. Second harmonic generation is then created by a non-linear crystal, which doubles the frequency and energy producing emission at half the wavelength at 532 nm [234, 236].

The 532 nm emission is directed to a Ti:sapphire crystal, which absorbs in the green spectrum. Ti:sapphire refers to the sapphire ($Al_2O_3$) crystal that is doped with titanium ions [234]. The length of the cavity determines the time between each generated pulse. Within the cavity an AOM generates a periodic loss using regenerative modelocking [275], whereby the longitudinal modes constructively and destructively interfere at points in the cavity to create an in phase 'locked' single circulating pulse [198], as shown by Figure 46.

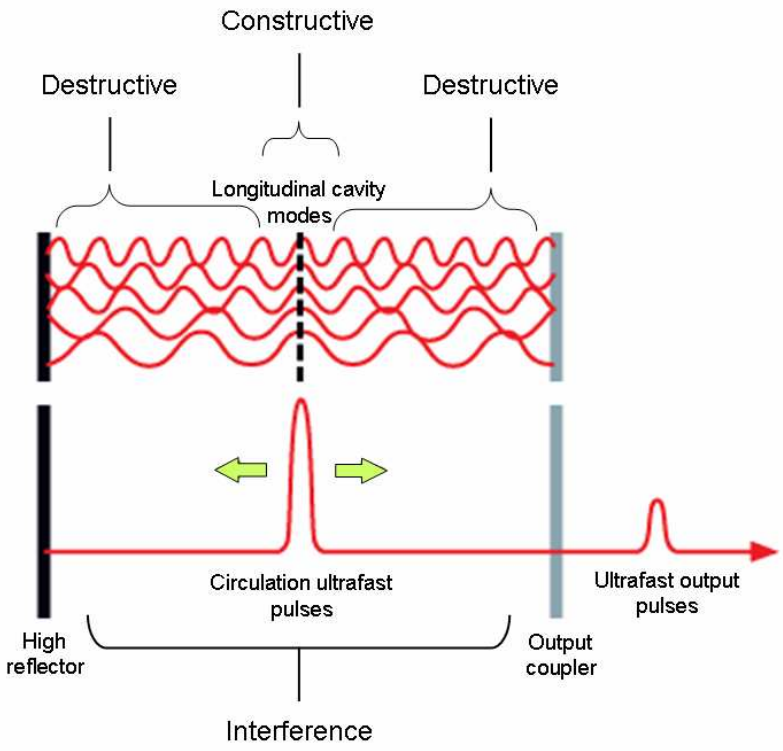


**Figure 46 – Schematic demonstrating longitudinal cavity modes locked in place by constructive and destructive interference. In the process an ultrafast pulse is created circulating the cavity at the speed of light and producing an output pulse via the output coupler. Adapted from Kruger *et al.* [165]**

The AOM signal must be synchronised to the timing of the pulse period to allow the pulse to pass through the AOM with minimal loss. The AOM can be adjusted to ensure this synchronisation is maintained via a feedback loop triggered from exiting pulses [275]. This mode-locks the pulse train and produces 'ultrashort' pulses <100 fs [205, 275]. In the Ti:sapphire cavity it takes 12.5 ns therefore producing a repetition rate frequency of 80 MHz [275].

A pulse travelling through any material is susceptible to a frequency dependent refraction due to the refractive index of the material [204]. A shorter pulse has a larger bandwidth [198] and is therefore composed of many frequencies which would each experience a slightly different index of refraction when entering a material [204]. The difference in refraction creates a time separation between the frequencies corresponding to a velocity difference defined at group velocity dispersion (GVD). If the lower frequencies lead entering the material it is considered positively chirped and so travel faster than higher frequencies. This changes the temporal shape of the pulse by broadening, if it was negatively chirped it would narrow the pulse [275].

Due to the non-uniform power distribution density of the beam profile it introduces an intensity-dependent refractive index at high intensity. This is caused by the non-linear effect of the Ti:sapphire crystal (lasing rod). Higher refractive indexes are induced at the centre causing a Kerr lens self-focusing effect, which changes the beam geometry [205].

Pulse broadening in the Mai Tai does not occur from the AOM, but is due to a combination of group velocity dispersion (GVD) and nonlinear effect in the Ti:sapphire lasing rod [275]. This broadening can reduce the peak power exiting the laser and impact the excitation efficiency. An increase in the average power is then required to produce the same level of fluorophore excitation [97].

These problems are avoided by using negative GVD chirp compensator to rebalance the pulse using a two-prism configuration [275], as shown in Figure 47. Located between the prisms sequence is a tuning slit for wavelength selection of spectral components [275]. The corrected pulse returns back through the Ti:sapphire crystal and exits producing a 80 MHz repetition rate, <100 fs pulse width, and tuning range of 710-990 nm, as shown in Figure 47.

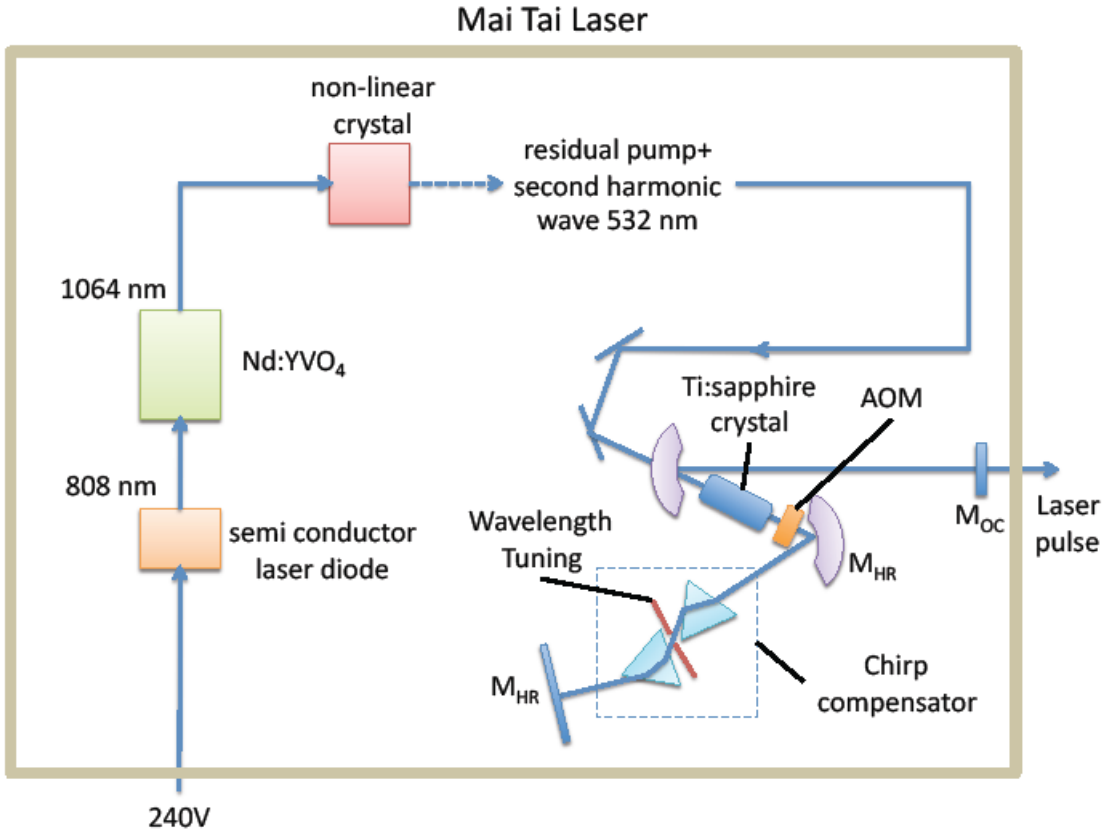


**Figure 47 – Block diagram represents the component parts that compose the Mai Tai laser. 240V power supply provides energy for the laser diode and produces an 808 m, emission that then excites a Nd:$YVO_4$ crystal and emits a 1064 m, wavelength that enters a non-linear crystal. [204, 234, 275].**

### 3.2.3 Control of laser power and repetition rate

Exiting the Mai Tai, the laser beam is diverted to the input port of the pulse picker (Model 3980, Newport Spectra-Physics, UK), as shown in Figure 40. The beam is focused to a narrow waist and a pulse stretcher is used to minimize the peak power to avoid

damaging the AOM crystal [275]. A pulse selector (Model 3986, Newport Spectra-Physics, UK) adjusts the repetition rate by sending an electrical signal to the AOM. A 10W burst, equivalent to 390 MHz RF energy, is generated creating an acoustic wave across the crystal inducing bifringence [275]. The frequency of the bursts can be varied from 10 to 8000 cavity periods this provides a selection of 16 dividing ratios. The acoustic wave interacts with the optical wave (laser beam) and diffracts the propagating beam, as shown in Figure 48. Only the 0 and ±1 order of diffraction are emitted from the pulse picker and the rest are blocked with an aperture [275]. A high level of discrimination between selected pulses and adjacent pulses [234, 275] is achieved by using the Kerr effect to control the refractive index of the crystal material and diffracts the beam by about 3°. The selected frequency exits the pulse picker and pass through a beam splitter, which diverts a small percentage of the beam to the photon counter, synchronizing the excitation pulse with the TCSPC module, the rest continuous to the laser modulator.

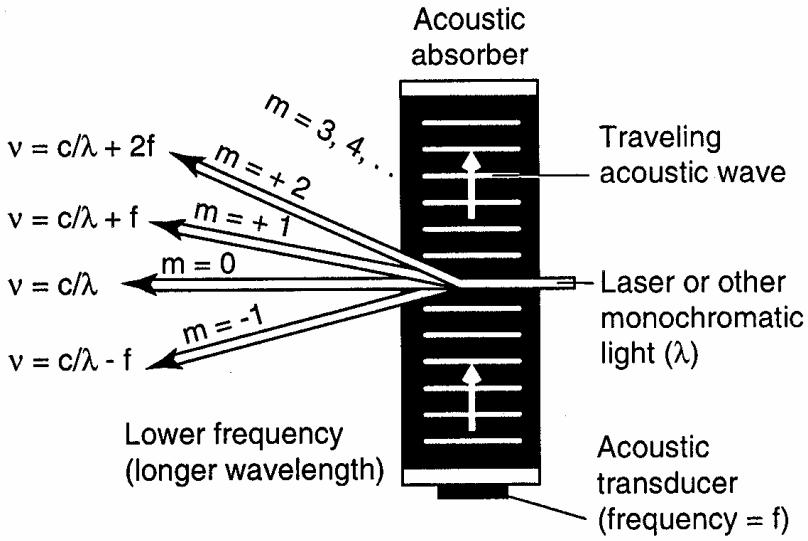


**Figure 48 – Schematic diagram of laser beam passing through crystal and diffracting due to the applied RF pulse producing an acoustic wave. Only the where m=0 and ±1 order does light exits the pulse picker while the rest is blocked by an aperture [275]. Abbreviations: v is the velocity of the acoustic wave, c is the speed of light, f is the acoustic frequency, λ is the wavelength of the incident light, m is the order of diffraction.**

Inside the laser modulator (LM 0202 IR KD*P High Power, Linos, Germany) an EOM crystal is held. It is powered and controlled by a digital pulse amplifier (LIV20, Linos, Germany). The setup uses the Pockel effect to control the refractive index of the crystal with the use of an electric field [205]. This effectively rotates the incident beams polarisation as a function of the applied external field [204]. It is linearly dependent and can modulate the intensity by acting as a voltage-controlled waveplate [236]. Modulation of the intensity is achieved via two polarizers before and after the EOM crystal, as shown in Figure 49. The first polarizer creates vertical polarised light while the second is

positioned with a 90° rotation. This second polarizer will only allow light through at this rotation. Varying the applied voltage 'EOM gain' allows quick changes of the refractive index of the crystal and diffracts the vertically polarised light modulation of the laser beam intensity. An offset voltage, 'EOM offset', is applied for maximum extinction this shifts the intensity curve over the voltage. To go from the minimum to the maximum transmission (<90%) [234] the applied voltage must induce a phase change of π. The adjustment of the EOM gain and offset are controlled from the Leica software. After exiting the EOM the beam enters the Leica SP2 confocal microscope. Information on the confocal will follow in the preceding section 3.3, the focus will now turn to TPE of $[Ru(bipy)_3]^{2+}$.

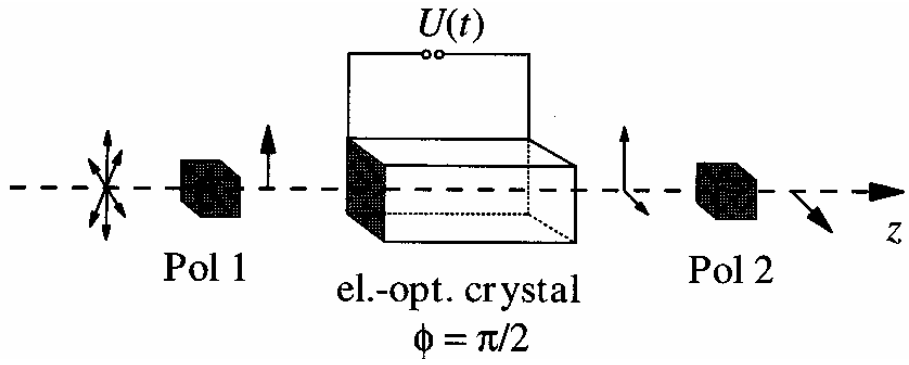


**Figure 49 – Diagram represents the operation of an EOM in controlling the intensity of the laser beam using the Pockel effect. Circularly polarised light enter the first polarizer (Pol 1) and is vertically polarised prior to entering the electro-optical crystal. The applied voltage adjusts the rotation of light and exits to the second polarizer (Pol 2) controlling the intensity [204]. Symbols: U(t) is the applied voltage, ϕ is the polarisation.**

### 3.2.4 Two-photon excitation of $[Ru(bipy)_3]^{2+}$

The process of TPE was discussed in section 3.2.1. The purpose now is to identify the peak TPA of $[Ru(bipy)_3]^{2+}$, which differs from single or continuous excitation. In SPE the fluorophore can be directly excited in the visible spectrum displaying the relationship between incident intensity emission and wavelength. The probability of two-photon excitation occurring relies on the quadratic dependence of the intensity and the cross-sectional area of the fluorophore. Prior knowledge of the one photon cross-section does not always aid quantitative prediction of the two-photon cross-section [70].

It is possible to compare single-photon and two-photon excitation using a simple calculation. Assume the emission wavelength ($\lambda_{em}$) is unrelated and generally shorter than the excitation wavelength $\lambda_{ex}$, which provides $\lambda_{ex} = \gamma\lambda_{em}$, where γ is a constant and must be <1. As two-photon absorption requires simultaneous absorption of two photons at half the energy, the excitation wavelength can be rewritten as $\lambda_{ex} = 2\gamma\lambda_{em}$ [70]. Therefore, if the single photon (SP) excitation and emission peak of $[Ru(bipy)_3]^{2+}$ in water is 468 nm and 608 nm, respectively, it would provide a $\gamma = 0.769$ and the estimated TP excitation as 936

nm. This method has been shown by Xu and Webb [317] to be a reasonable approximation for many dyes, but other researchers have used alternative two photon excitation peaks for $[Ru(bipy)_3]^{2+}$ namely Castellano *et al.* who used 880 nm [48]. This discrepancy arises due to the selection rule for two photon absorption [274]. This relates to TPA transitions only occurring at even-parity transitions between ground and excited state, unlike signal photon absorption based on opposite-parity transition [193], which is what this equation is based on.

Only a small fraction of photons are absorbed in the two-photon process and the response is laser power dependent this makes direct measurement of the cross-section difficult [317]. Instead fluorophores with known two-photon cross-sections and fluorescence quantum efficiencies are compared, but still require knowledge of the applied laser power. The response of TPA cross-sections to the measured incident power allows an estimation of the probability for two photons to be absorbed within a single excitation pulse. This provides an approximation on the possibility of sample saturation and the expected emission rate. The laser power at the sample will be measured to determine the influence over the expected TPA. The power measurements will be applied to theoretical calculations and will incorporate TPA measurements taken from other researchers.

#### 3.2.4.1 Laser power at the sample

The power at the sample was measured using an optical power meter (model 1830-C, Newport Physics, UK) and a low-power semiconductor photodetector (818-IR/CM, Newport Physics, UK), with an additional neutron density filter, which was mounted on the microscope stage. The detected power was adjusted from 730-950 nm in steps of 10 nm in tandem with the laser excitation wavelength, so as to utilise the bandpass filter incorporated into the power meter. The 'offset' and 'gain' of the EOM was adjusted and noted at each set point to maintain maximum delivered laser power. The background light in the room was measured with the detector at the sample and subtracted from the measured laser power values.

Once the power measurements were completed the intensities at the corresponding wavelengths were measured using the TP confocal microscope. A 40 µl (0.412 mM) sample of $[Ru(bipy)_3]^{2+}$ in deionised water at ambient temperature was deposited on a coverslip (no. 1.5, 22x32 mm) (Cat. No. 631-0134, VWR Ltd., UK) and mounted on an x63 (NA 1.4) oil immersion objective lens (506192, HCX PL APO, Leica Microsystems Ltd., GmbH). The maximum intensity was located at 780 nm by traversing through the wavelengths and the PMT gain and offset were adjusted to ensure saturation did not occur. The mean intensity was measured across 550-670 nm, using the same excitation

wavelength in the power measurements at repetition rates of 500 kHz and 8 MHz. The Leica parameter settings were, line average 2, frame average 3, 512x512 image format (voxel size: 0.46503 μm), beam expander 1, and SP700 filter.

The mean intensity at a repetition rate of 500 kHz (Figure 50 left) mimics the rise and falls of the power with matching peaks at 780 nm and 800 nm. The mean intensity at a 8 MHz repetition rate also mimics the power at the sample, but to a slightly greater extent than at 500 kHz (Figure 50 right). The average power at the sample is 14 times greater using the laser repetition rate at 8 MHz than at 500 kHz. This is expected as the pulse rate is 16 times faster. Even though the power has increased by a magnitude of 14 the intensity has only increased by a magnitude of 6.25.

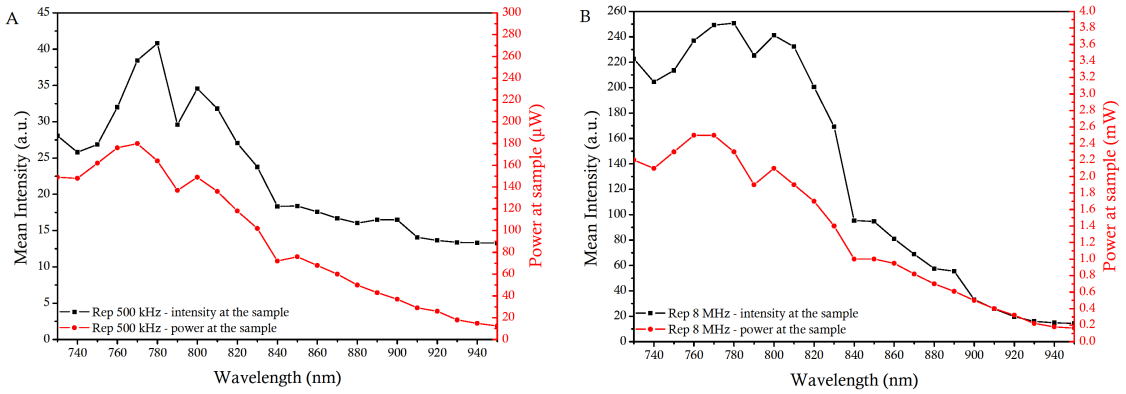


**Figure 50 – Influence of wavelength on intensity and power at the microscope stage with a, A: 500 kHz and, B: 8MHz repetition rate. Intensity (black line squares) measurements at incrementing wavelengths of $[Ru(bipy)_3]^{2+}$ at a concentration of 0.412 mM. Power (red line circles) at the sample was measured with a meter at incrementing wavelengths.**

Observing the response of $[Ru(bipy)_3]^{2+}$ to the change in wavelength and laser power it is difficult to separate what is the main influencing factor. Using these power measurements it is possible to estimate the number of photons absorbed and the expected emission rate that can be attained from each repetition based on TPA measured taken by other researchers.

### 3.2.4.2 Estimated emission rate based on TPA

Applying the power measurements and the TPA values of Nag *et al.* [219] and Castellano *et al.* [48]. Denk *et al.* [69] equation allows an estimate for the number of absorbed photons at both repetition rates. The number of absorbed photons is dependent on the pulse duration, repetition rate, average incident laser power, and the NA of the objective lens [69].

**Eq. 17**

$$n_a \approx \frac{{p_0}^2 \cdot \delta}{\tau_p \cdot {f_p}^2} \left( \frac{NA^2}{2 \cdot \hbar \cdot c \cdot \lambda} \right)^2$$

The number of absorbed photon, $n_a$, is equivalent to, $p_0$ the average measured incident laser power (W), $\delta$ the two photon absorption cross-section ($cm^4$ s/photon) ($1x10^{-50}$ = 1 GM), $\tau_p$ the pulse duration (100 fs), $fp$ the repetition rate (500 kHz and 8 MHz), $NA$ the numerical aperture (NA=1.4), $\hbar$ the Planck's constant ($6.626068x10^{-34}$ $m^2$ kg/s), c the speed of light (299792458 m/s) [204] and λ the excitation wavelength (730-950 nm). Using the values obtained for $n_a$ the photon emission can be estimated from multiplying it by the repetition rate; in order to avoid saturation values, $n_a$ should be <1.

The TPA spectra for $[Ru(bipy)_3]^{2+}$ in dicheoromethane (DCM) has been taken from Nag *et al.* [219] who measured the absorption with a femto-second Ti:sapphire laser with a reduced repetition rate of 500 Hz. The two photon absorption cross-section of $[Ru(bipy)_3]^{2+}$ in water at 880 nm was measured by Castellano *et al.* [49]; using a 90 fs pulse duration and 80 kHz laser repetition rate. Both studies used Rhodamine in methanol as the reference sample. Assuming that TPA continues to decrease, an asymmetric double sigmoidal fit was used to extrapolate the data and cover the full range of wavelengths. The TPA spectra peaks at 785 nm with a cross-section of 211 GM, but the two-photon absorption spectra does not overlap with the single-photon spectra. If the assumed response of the TPA was to continue decreasing Castellano *et al.* [49] measurement would produce the same response for $[Ru(bipy)_3]^{2+}$ as Nag *et al.* [219].

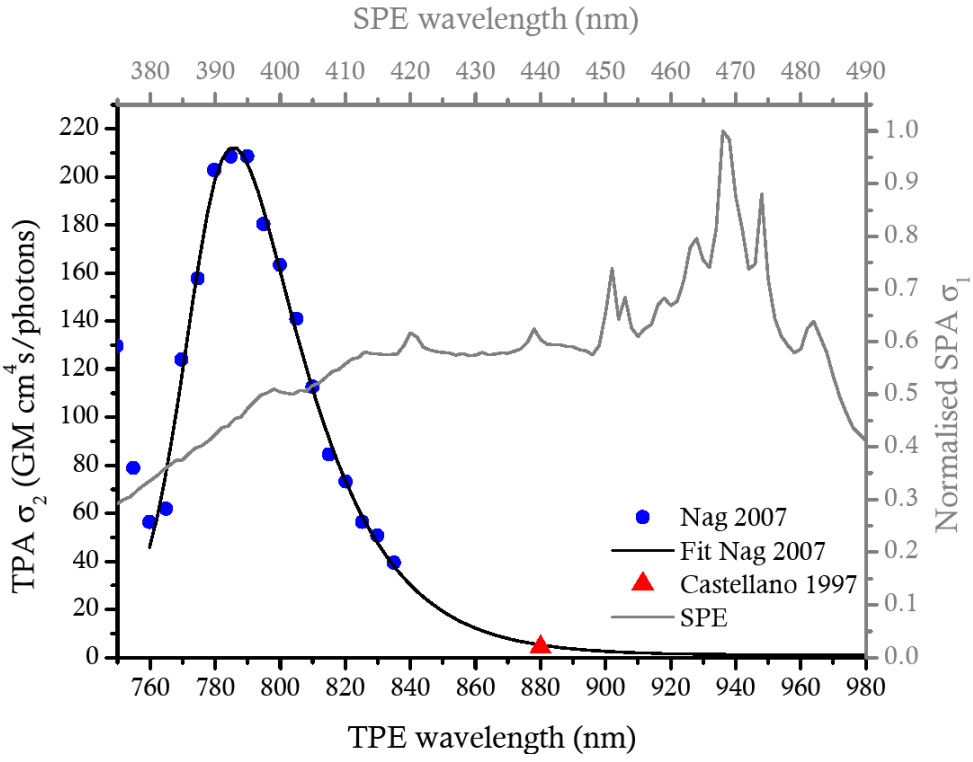


**Figure 51 – Two- and single-photon absorption spectra of $[Ru(bipy)_3]^{2+}$ in water. TPA data extracted from Nag et al. [219] (blue circles) with a fitted line (black line) extended to 980 nm and Castellano et al. [49] (red triangle) data point plotted. SPA data taken using a fluorimeter described in Chapter 2.**

Using the TPA from Nag *et al.* [219] and Eq. 17 the probability that $[Ru(bipy)_3]^{2+}$ would simultaneously absorb two photons during a single pulse period at a repetition rate of 500 kHz and 8 MHz has been estimated in Figure 52. The response at both repetition rates is near identical, only the magnitudes of the number of absorbed and emitted photons differ. Three peaks can be identified for all measurements at 780, 800, and 850 nm. At a repetition rate of 500 kHz the probability of $n_a$ is <0.1 this determines limited ability for sample saturation. The maximum estimated emission of photons is only 2000 photons/s, consisting of 0.4% of the collection rate. At a repetition rate of 8 MHz the probability of $n_a$ occurring is >1 and so at these laser power levels saturation of the fluorophore will be induced. This is also apparent in the estimated emission (right y-axis), which is 200 times greater than the rate of excitation.

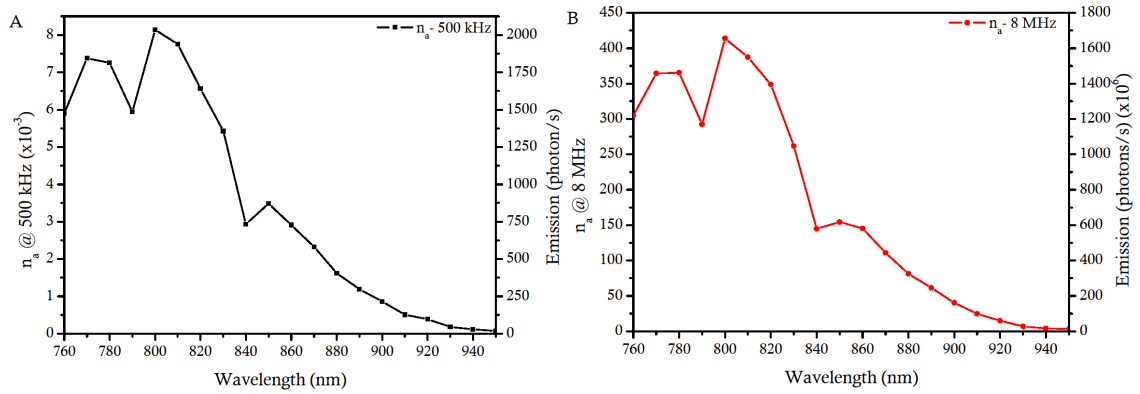


**Figure 52 – Left y-axis probability of two photon simultaneously being absorbed by a $[Ru(bipy)_3]^{2+}$ fluorophore in one excitation cycle and right y-axis represents the rate of photon emission for and at incrementing wavelengths [69, 70]. A: Laser repetition rate 500 kHz (black squares) B: Laser repetition rate 8 MHz (red circles).**

### 3.2.4.3 Discussion

The absorption rates of the TPE cross-section rely heavily on the spatial and temporal coherence of the excitation light [7]. The relationship between the fluorescence power and excitation power is essential for TPE cross-section measurements. [70]. Therefore to determine the number of absorbed photons, saturation, and emission rate, data from Nag *et al.* [219] was used to provide an accurate measurement of the TPA cross-section. Applying these values into Eq. 17 provided the probability of two photons being absorbed during a single excitation cycle. This showed that using the 8 MHz repetition rate at full power would induce saturation of the fluorophore and most probably lead to photobleaching [235]. By contrast, using the 500 kHz repetition rate there would be no chance of inducing saturation at the maximum power, but the estimation suggests there could be a problem with achieving high emission rates at the maximum power. Comparing the estimated emission (Figure 52) to the measured intensity (Figure 50) shows very similar

responses except the peak intensity is at 780 nm instead of 800 nm in the estimated emission.

The two-photon absorption cross-section can be theoretical determined from prior knowledge of single photon transition rates. The two-photon absorption (TPA) cross-section represents the transition from ground state to excited state and is measured in units of $cm^4s$/photon [70]. The simultaneous absorption of two photons requires the 'first' photon to excite the molecule to a virtual intermediate state and a 'second' to excited to the final state, as shown in Figure 53.

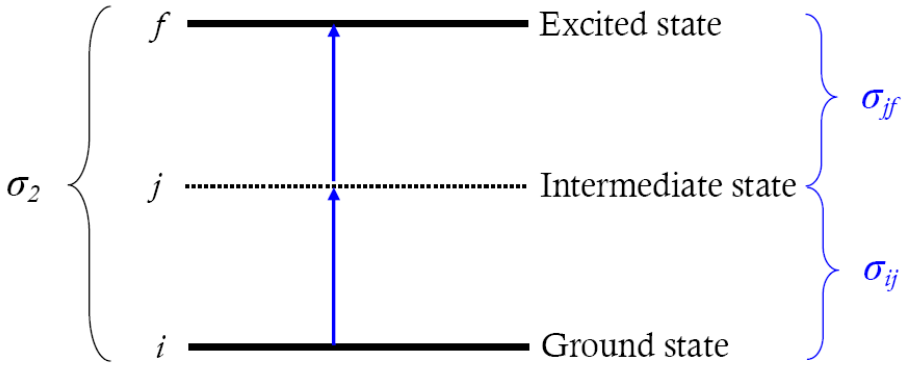


**Figure 53 – Schematic representation of the approximated two photon absorption cross-section using a single intermediate state. The first single photon cross-section $\sigma_{ij}$ represents photon transition from ground state *i*, to intermediate state *j*, and the second single photon cross-section $\sigma_{jf}$ represents a photon transition from intermediate state *j*, to excited state *f*. The complete two photon cross-section represents the combination of single photon cross-sections and the intermediate state lifetime not represented in this diagram. Adapted from Xu *et al.* [70].**

Although all excitation states contribute to this intermediate state, an approximation can improve the reliability of the estimation. The two-photon absorption cross-section $\sigma_2$ can be obtained from [70]:

**Eq. 18**
$$\sigma_2 = \sigma_{ij} \cdot \sigma_{jf} \cdot \tau_j$$

where, $\sigma_{ij}$ and $\sigma_{jf}$ represent the one-photon absorption cross-sections and $\tau_j$ is the intermediate-state lifetime, which determines the time scale for simultaneous photon arrival. It can be estimated as [70]:

**Eq. 19**
$$\tau_j \approx \frac{1}{\Delta\omega} = \frac{1}{|\omega_{ij} - \omega|}$$

where, $\omega_{ij}$ is the transition frequency, and $\omega$ is the incident photon frequency. Applying Eq. 18 and Eq. 19 to $[Ru(bipy)_3]^{2+}$ provides an approximation of the two-photon absorption cross-section. The intermediate and final state energies are assumed to be close to that of an electronic transition ($\omega_{if}$) in the visible frequency range. The transition energy between ground state and metal-to-ligand charge transfer (excited state) has been

determined by Heully *et. al* [124] as 18,242 $cm^{-1}$. The TPA was calculated using the incident photon frequency of 780 nm and 880 nm, based on peak TPA of Nag *et al.* [219] and Castellano *et al.* [48], respectively. Converting all values into frequencies requires use of the equations below [204]:

**Eq. 20**

$$\nu = \frac{c}{\lambda} \qquad \nu = \tilde{\nu} \cdot c$$

where, $\nu$ is the frequency ($s^{-1}$), $\lambda$ wavelength (nm), $c$ speed of light (2.9979x$10^{10}$ cm/s), and $\tilde{\nu}$ is the wave number ($cm^{-1}$) [204]. This provides $\omega_{ij}$ = 5.47x$10^{14}$ $s^{-1}$, $\omega_{780}$ = 3.844x$10^{14}$ $s^{-1}$ and $\omega_{880}$ = 3.407x$10^{14}$ $s^{-1}$ inserting these values into Eq. 19 establishes $\tau_{j780}$ and $\tau_{j880}$ as 6.153x$10^{-15}$ s and 4.85x$10^{-15}$s, respectively. The single photon absorption, $\sigma_{ij}$ and $\sigma_{jf}$, can be related to the extinction coefficient $\varepsilon$ ($M^{-1}$ $cm^{-1}$) and calculated from Eq. 21 below [204]:

$$\varepsilon(\lambda) = \sigma(\lambda)\frac{N_L}{\ln 10} \cong \sigma(\lambda) \cdot 2.6154 \times 10^{20}$$

**Eq. 21**

$$\therefore \sigma(\lambda) = \frac{\varepsilon(\lambda)}{2.6154 \times 10^{20}}$$

where, $N_L$ is Loschmidt's number (6.0221367x$10^{23}$, $mol^{-1}$). Miedlar *et al.* [206] measured the extinction coefficient of $[Ru(bipy)_3]^{2+}$ in water at an absorption maximum of 450 nm as 9000 $M^{-1}$ $cm^{-1}$. Inputting this value into Eq. 21 provides an approximation of the SPA cross-section as 3.44x$10^{-17}$ $cm^2$, which is in good agreement with Tarnovsky *et al.*[285] who measured the SPA for $[Ru(bipy)_3]^{2+}$ at an excitation of 400 nm $\sigma_{400}$= 2.3x$10^{-17}$ $cm^2$. Combining the derived values of Eq. 21 and Eq. 19 with Eq. 18 delivers the TPA cross-section at an excitation wavelength of 780 nm and 880 nm as approximately 7.285x$10^{-48}$ $cm^4$s/photon and 5.743x$10^{-48}$ $cm^4$s/photon, which is within the range of possible values quoted by Xu *et al.* [70] for TPA cross-sections of fluorophores.

The theoretical principle for estimating TPA as described by Xu [70] over estimated the TPA values (728 GM at 780nm, 574 GM at 880 nm) measured by Nag *et al.* [219] by 3.6 times (at 780 nm) and Castellano *et al.* [49] by 2 orders of magnitude (at 880 nm). The errors in these calculations relate to the estimated values for the lifetime state ($\tau_j$) where as in reality they tend to be slower [70] i.e. $[Ru(bipy)_3]^{2+}$ is a trans-metal-ligand where there are variable excitation states that can also enter into triplet states [124]. For complex molecular excitation states the theoretical estimation of TPA is an inappropriate model to use.

Although the TPA of Nag *et al.* [219] appears shifted compared with the SPA peak, another peak exists further in the UV at approximately 300 nm, which is 2.8 times higher

than the peak emission at 468 nm. The left shifted peak in Figure 51 could actually be a right shifted peak originating from 300 nm and could explain the difference between the TPA data for Nag *et al.* [219] and the theoretical results.

### 3.2.5 Conclusion

At a repetition rate of 500 kHz and using maximum power it is estimated that the probability of two photons being absorbed by $[Ru(bipy)_3]^{2+}$ during one excitation cycle is <0.1. Where as, for an 8 MHz repetition rate huge saturation will occur most probably leading to fluorophore photobleaching. The TPA peak of $[Ru(bipy)_3]^{2+}$ exists at 785 nm and does not mimic the SPA spectra. The theoretical model is not able to describe the real intermediate lifetime state and is therefore not appropriate for the more complex molecular excitation states of $[Ru(bipy)_3]^{2+}$. An TPE of 780 nm will be used for all subsequent excitations of $[Ru(bipy)_3]^{2+}$ described in this thesis.

## 3.3 Confocal Laser Scanning Microscope

### 3.3.1 Introduction

Fluorescent microscopes were invented in 1904 and fluorescently labelled anti-bodies appeared in 1941, but the realisation that anti-bodies could be raised to normal proteins was not understood until the 70s where the merger of the microscope and fluorescent labels soon accelerated [13]. By 1984, it was understood that thick samples gave rise to a uniform glow from out-of-focus sections and many researchers had resorted to studying thin and flat cells in an attempt to resolve fine structure. But the single limitation derived from the microscope itself and there was a great demand for improvements to be found.

The confocal microscope was first invented in 1955 by Minsky, but the term ‘confocal’ was first used by Brakenhoff and others in 1979. It described an illumination confined to a diffraction-limited spot in a specimen and the detector confined by an aperture optically conjugated to the focused spot [13]. At the plane of focus the fluorescence from a point object will fall with distance. This occurs according to the inverse fourth-power producing an “optical sectioning” effect where the out-of-focus blur was almost completely removed [236]. Brakenhoff *et al.* [37] could only produce a single point on a specimen at any one time and required the entire specimen and support stage to be moved in a raster fashion. White *et al* [309] used a polygon mirror that rotated and a refractive telescopic relay to create the raster scanning across a sample, but it suffered with

noise generated from beam scanning and triggering and chromatic aberrations, respectively. The improvement came with the replacement of the polygon mirror with a pair of oscillating galvanometer mirrors and Amos *et al.* [12] designed an arrangement of concave mirrors to substitute the refractive telescope relay.

This was the complete confocal point-scanning system, which until now is still manufactured by Bio-Rad [12]. Other major companies have since copied or adapted this confocal point scanning system, which is now seen in the majority of biological laboratories, but the setup and acquisition process are slightly different. This same system was later used, by Denk, Strickler and Webb in 1990 [69], to prove the basis for two-photon induced fluorescence imaging. The operation and layout of the MP laser combined with the confocal will now be discussed.

### 3.3.2 The inverted SP2 Leica confocal microscope

A multi-photon laser only excites at the point of interception with a rapid reduction of excitation from the focal point. All photon emission originates from this femto-litre excitation volume, removing the need for an aperture to exclude out-of-focus blur. As shown in Figure 54 the excitation light (700-990 nm) is diverted via a beam splitter and focus with an objective lens to provide point excitation per pixel. The point excitation raster scans across the field of view and the returning emission passes back through the objective lens and beam splitter (<700nm) to the PMT where the software compiles a pixelated image.

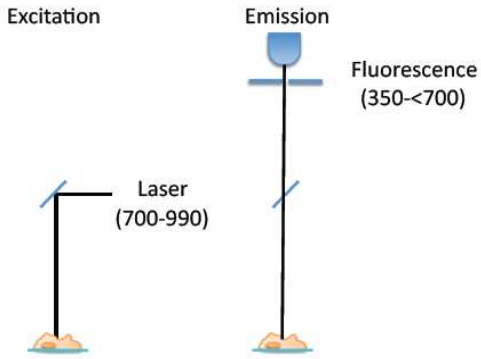


**Figure 54 – Pictorial representation of excitation and emission pathway for laser light in confocal. The pulsed excitation laser is reflected via a beam splitter on to the sample and the emission from the pulse returns only passing through the beam splitter at wavelength <700nm. The light then hits the PMT detector and is converted to a digital signal displayed on the Leica software.**

The confocal system used in these experiments is an inverted Leica SP2 confocal microscope (DM IRE2, Leica Microsystems Ltd., UK). Traditionally a Leica microscope sends the excitation beam through an acousto-optical beam-splitter (AOBS), which operates similarly to an AOM. This allows up to 8 laser lines to be directed at any one time

into the crystal and the propagating acoustic waves diffract the different wavelengths of light. It can be used to spectrally combine or separate light at specific wavelengths [236]. In an IR set-up, as with two-photon laser excitation, this ABOS is not required as the laser is tunable. Instead the light enters an IR beam splitter (SP700) and is diverted to the sample, as shown in Figure 55, via a beam expander. Before the beam enters the objective lens it passes though a k-scanner module and a scan lens. The objective lens focuses the beam to a point on the sample and the k-scanning module raster scans the sample using the galvanometer mirrors. The emission is captured back through the objective, scan lens, k-scanning module, and beam expander. Emission light <700 nm passes through the SP700 beam splitter and enters the pinhole optics that focuses the beam on to the back of the pinhole. In IR mode the pinhole is left fully open (600μm) and the beam passes unrestricted to the collimating lens. Some researchers have reduced the size of the pinhole to improve resolution on fine detailed structure, but this balance must not come at the cost of reducing the intensity [70, 89]. The collimated beam hits the side of a prism and is dissipated into a spectral array of wavelengths directed to a PMT. Mirrors either side of the PMT select the required wavelength, while reflecting the rest of the wavelengths to PMTs located either side, as shown in Figure 55. In the current system only PMT 1 & 2 are installed, but it is possible to have up to four PMTs. Based on the low level of emission discussed in section 3.2.4.3 the pinhole was fully open to maximise light collection and only PMT 1 was utilised for $[Ru(bipy)_3]^{2+}$ experiments.

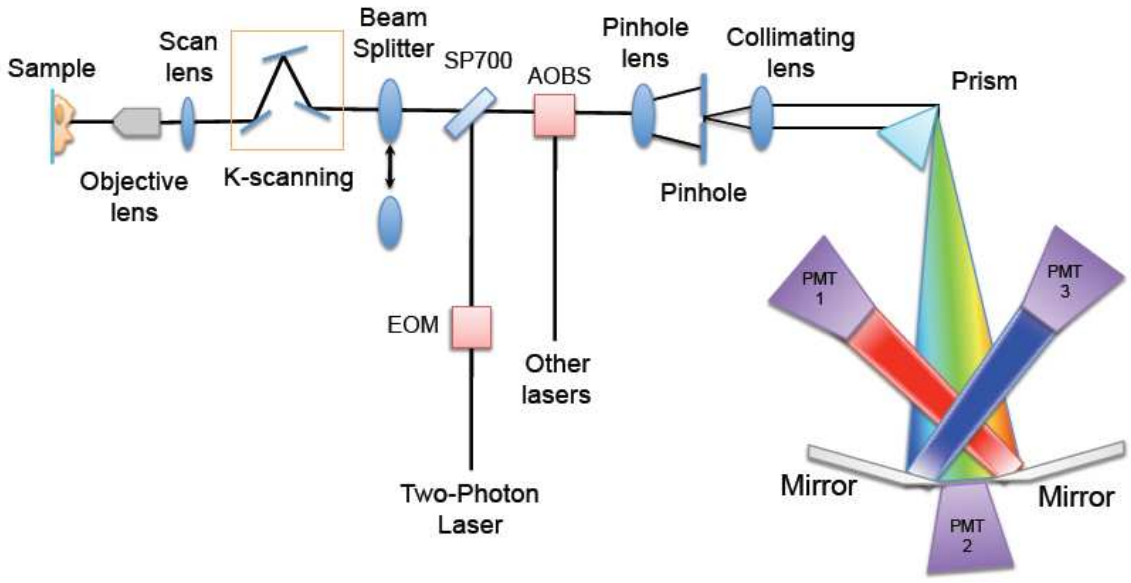


**Figure 55 – Internal optical path of the Leica SP2 confocal from laser to sample and return path to PMT. Adapted from Rietdorf and Paweley [236]. Abberviations: EOM – electro-optical modulator, ABOS – acousto optical beam splitter, PMT – photomultiplier tube.**

With the pinhole fully open and the addition of realigning the optical beam the setup is now susceptible to variation unlike a purely commercialised system. This has

effectively rendered the microscope setup similar to an open optical system. It is therefore important to confirm the actual resolution and asses any misalignment of the laser system, which can be determined from the point spread function.

### 3.3.3 Establishing point spread function (PSF)

The point spread function (PSF) describes the spatial variation in intensity around an infinitely small point source. A Fourier Transform of this point describes the spatial frequency of the diffracted light and is termed the Airy pattern; the cross-section is the Airy disc [236], as shown in Figure 56 A and B, respectively. The cross-section of the airy disc is determind as the diameter of the first dark ring ($d_{ariy}$) that is created when the light waves destructively interfere and is defined by:

**Eq. 22**

$$d_{airy} = \frac{1.22 \cdot \lambda}{\eta \sin \alpha} = \frac{1.22 \cdot \lambda}{NA}$$

where, λ is the wavelength of light, α is the angle of the objective, η is the refractive index, and NA is the numerical aperture of the objective lens. The PSF can be influenced by the optical properties of the system, the NA of the objective lens and optical aberrations. In a two-photon system the PSF is directly related to the localised focal volume of TP absorption [73]. The PSF defines the resolution of the microscope which is the minimum separation at which two point objects can be separately resolved (Figure 56 C-E) [236].

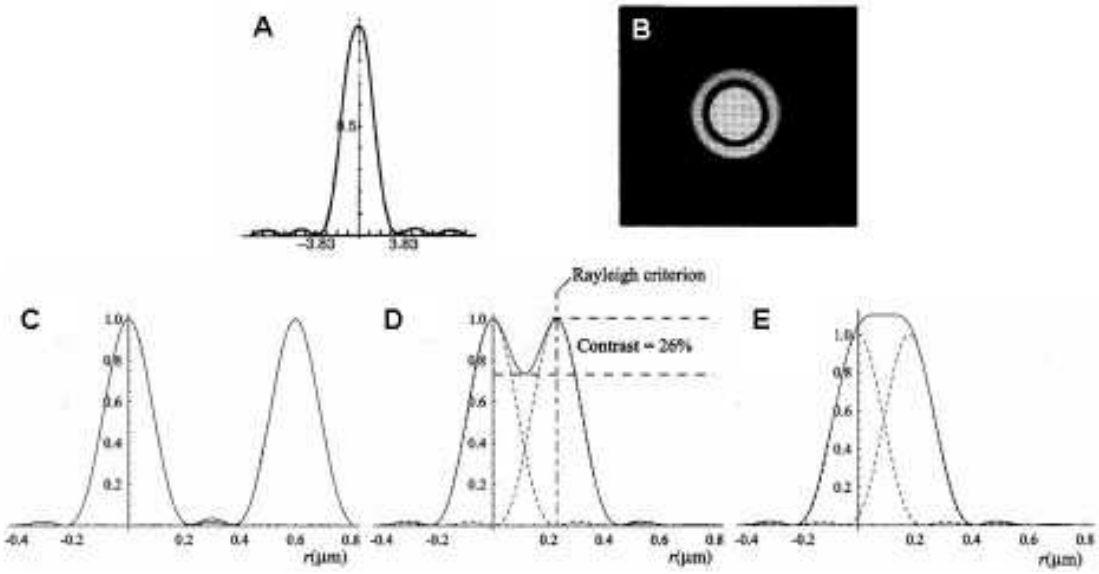


**Figure 56 – Graphical diagram discriminating two point objects at varying distances and a point object airy disc cross-section in an optical system. A: Cross-sectional profile of single point object airy disc, B: Fourier transform of single point object spatial frequency displayed as airy disc pattern, C: Point objects are well separated, D: Point objects separated by Rayleigh criteria providing 26.4% contrast and E: Point objects separated by cut-off distance using Sparrow criteria, no contrast point objects are unresolved. Adapted from Pawley *et al.* [236].**

Determining where that point occurs can be some what ambiguous. According to the Rayleigh criterion two point objects are resolved when the first minimum of one Airy disc is aligned with the central maximum of the second Airy disc [70], as shown in Figure 56 D. Thus the limit of resolution is given by half the diameter of the first airy ring [236], i.e. Eq. 23.

**Eq. 23**

$$r_{airy} = 0.61\frac{\lambda}{NA}$$

However in some cases it is still possible to resolve the two point-like objects beyond the Rayleigh limit, so the development of the Sparrow criterion was seen as an improvement on this [203]. The sparrow criteria states that the dip that exists between two point-like objects coming together can no longer be resolved when the combined maxima of the two Airy discs start to become one, i.e. there is no contrast between them. The Sparrow resolution is defined as a cut-off distance at and below the existence of zero contrast, where as, the Rayleigh resolution describes the level of separation between the points at which 26.8% contrast is achieved [70].

Determining the spatial resolution of a system can be difficult, but an approximation can be achieved by oversampling a subresolution spherical bead [70]. This provides a conjugation of the bead and point spread function (PSF). Measuring the full width half maximum (FWHM) and accounting for the size of the bead will confirm the maximum pixel size that should be used to avoid a loss of structural information about the specimen [236].

#### 3.3.3.1 Methodology

PS-Speck™ Microscope Point Source kit (P7220, Invitrogen, UK) was purchased from molecular probes. PS-Speck™ contains 4 different coloured fluorescent microspheres each with a diameter of 175±5 nm to enable sub-resolution point source calibration. The protocol was based on a combination of standard protocol supplied with kit and the instructed protocol outlined by Grauw *et al.* [70]. The PS-Speck™ kit was stored at 4°C and the suspension density of the microspheres was ~$3x10^9$ beads/ml. A circle was drawn with a permanent pen in the centre of a coverslip (no. 1.5, 22x32 mm) (Cat. No. 631-0134, VWR Ltd., UK). 8 µl of green fluorescent microsphere (ex 505/em 515) suspension was dispensed on to the reverse of the coverslip in the centre of the circle. The coverslip was then left uncovered for 2h to allow the solution to evaporate. Once the sample had dried mounting media, supplied with the kit, was applied to the beads. A small circular coverslip (ϕ 22 mm, Cat. No. 631-0159, VWR Ltd., UK) was positioned on the mounting media and

the sample was positioned on to an x63 oil immersion objective (NA 1.4) lens (11506192, HCX PL APO, Leica Microsystems Ltd., GmbH).

The pulse picked TP laser was set to a repetition rate of 8 MHz and the excitation was set to either 780 nm or 800 nm. The emission was captured over 400-700 nm, scan speed 400 Hz, line average 2, frame average 4, and the beam expander was set to 1 to overfill the backfocal plane of the objective. The marked circle on the coverslip was located using the eye piece then the objective lens was traversed in the z-axis until emission was seen from the beads. The pinhole was fully open (600 μm), image format set to 256 x 256, and the zoom adjusted reducing the image size to 12 μm x 12 μm. A set of beads were selected and the zoom increased to the maximum providing an image size of 7.4 x 7.4 μm. A 25 image z-stack was taken starting below and ending above the bead, the resulting voxel size was 29 x 29 x 90 nm. The completed image sets are shown below in Figure 57.

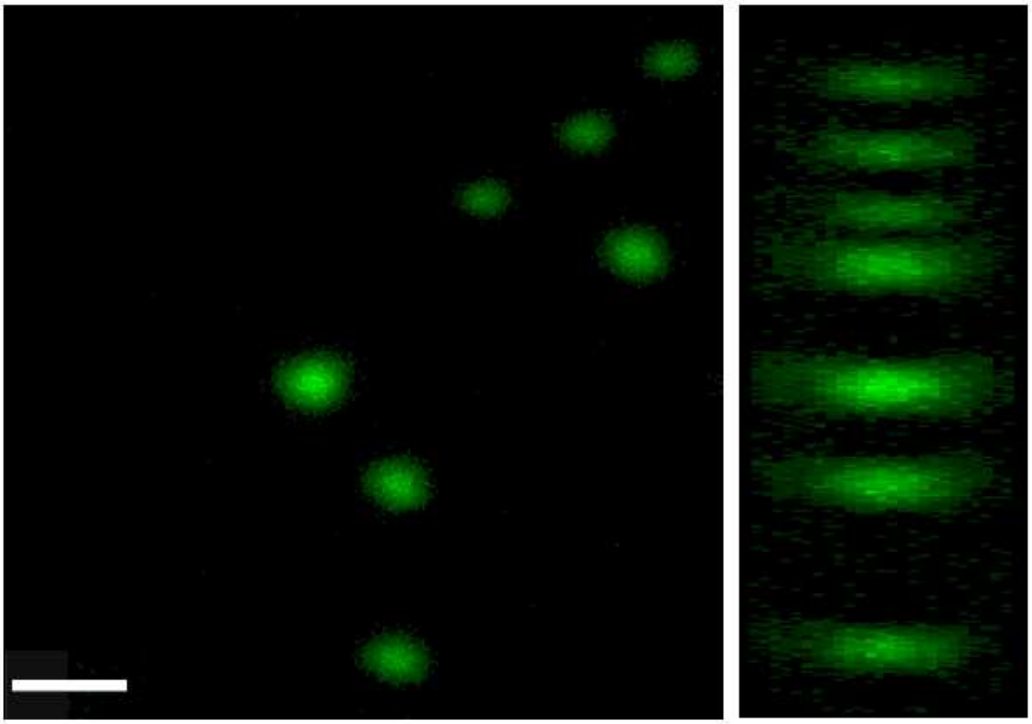

**Figure 57 – 3D image stack of green fluorescent beads taken on a TP confocal using an x63 (NA 1.4) oil immersion objective lens. Average intensity projection in X-Y axis (left) and X-Z axis (right). Scale bar represents 1.5 μm.**

### 3.3.3.2 Data Analysis

The stacked series of images were analysed in Leica confocal software (Version 2.61, LCS Lite, Leica Microsystems, GmbH) using the quantification tools: profile and stack profile. The axial point spread data was obtained from the stack profile by drawing a region of interest (ROI) in the centre a bead and exporting the produced graph. The data

points were imported into Origin software (OriginPro 8 SR0, OriginLab Corporation, USA) and fitted with a Gaussian model to provide the axial full width at half maximum (FWHM) data.

To obtain the lateral data the profile tool was used to draw two lines in the x- and y-axis across the same fluorescent bead. The data points were exported, plotted, and fitted in the same manner as for the axial data using the Gaussian model in OriginPro. This process was repeated for both excitation rates. The image of the bead is an optical transfer function, meaning that it is a combination of the PSF and the object. By subtracting the dimensions of the bead from the image the remaining distance can be determined as the PSF.

#### 3.3.3.3 Results

A zoomed fluorescent bead and its intensity line profile in the x- and y-axis at an excitation of 780 and 800 nm is displayed in Figure 58. The shape of the distribution is Gaussian and both x-y axis overlap well although the data does appear noisy, but symmetrical. The calculated FWHM for the x- and y-axis at an excitation of 780 nm and 800 nm was 272.9 nm and 253.6 nm, and 195.3 nm and 270.7 nm, respectively; taking into account the size of the bead. Figure 59 is an average projection of the z-stacked images in the x-z axis of the same fluorescent bead. The line profile through the z-axis has a asymmetric Gaussian distribution, noticeable in both image and graph. The determined axial FWHM was 836.1 nm and 831 nm for 780 nm and 800 nm, respectively, taking into account the bead size. All Gaussian fits produced an adjusted $R^2$ >0.98. The resulting FWHM values are give in Table 12.

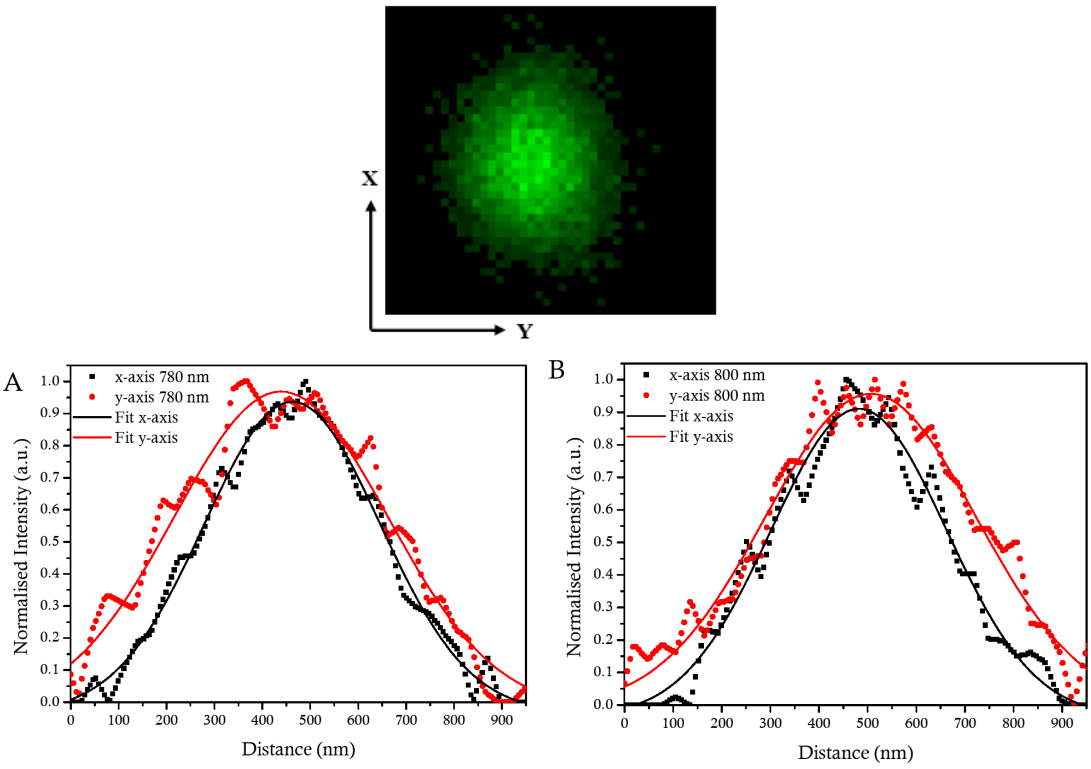


**Figure 58 – Normalised intensity image and profile of fluorescent beads, diameter 175 nm, in x- and y-axis using excitation of 780 and 800 nm. Top: Oversampled image of fluorescent bead in x-y axis at excitation 780 nm, Bottom: Line profile of lateral x-axis (black squares) and y-axis (red cicrles) point spread of fluorescent bead at excitation wavelength A: 780 nm and B: 800 nm.**

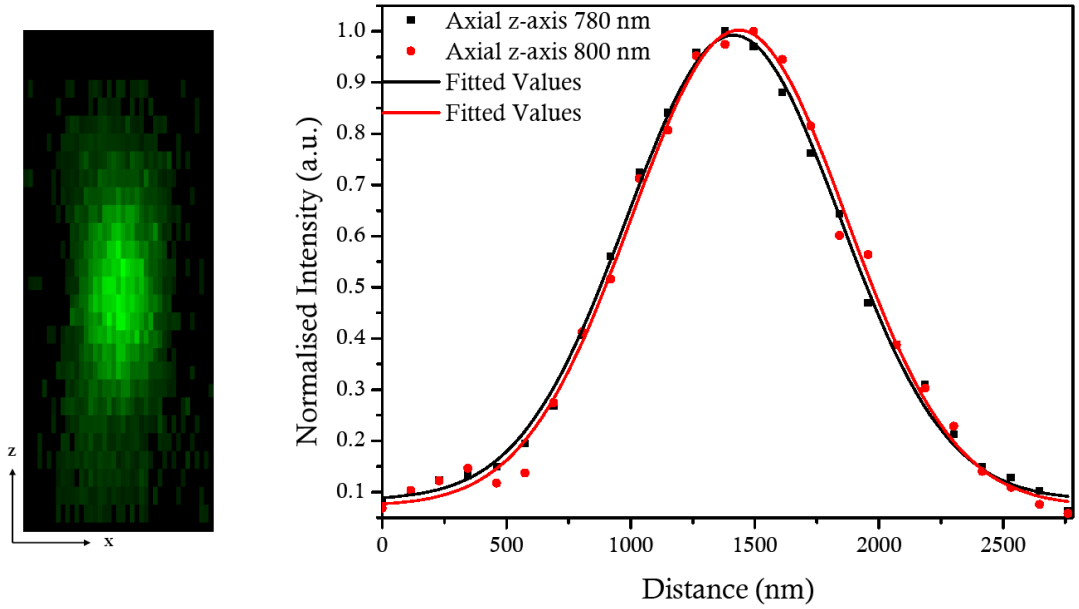


**Figure 59 – X-Z stacked average intensity and normalised intensity profile of fluorescent beads, diameter 175 nm, at excitation 780 and 800 nm. Left: 25 stacked images in z-x axis at 780 nm, Right: Stack plot of the fluorescent bead through the axial direction at excitation of 780 (black squares) and 800 nm (red circles) with Gaussian fits to both represented by the fitted line.**

#### 3.3.3.4 Discussion

Experiment evaluation of the PSF was conducted to establish the resolution of the optical pulse picked TP confocal system. A comparison was also conducted between two excitation wavelengths at 780 and 800 nm to determine possible influences of laser pointing stability drift. The axial resolution is three times larger than the lateral resolution, which compares well with Brakenhoff *et at.* who also showed triple increase of the axial dimensions compared with lateral [37].

The point spread function at FWHM can also be theoretical estimated using established equations [35]. The assumptions are that no light is absorbed or scattered, and the object is independent of position in the field of view [70]. This allows experimental results to be compared with theory, establishing if the resolution has been compromised by distortions from misaligned or refractive index mismatch. The equations below describe the x-y axis (Eq. 24) and z axis (Eq. 25) resolution for a point object in a two-photon microscope [70].

**Eq. 24**
$$r_{x,y} \approx \frac{0.7 \cdot \lambda_{em}}{NA}$$

**Eq. 25**
$$r_z \approx \frac{2.3 \cdot \lambda_{em} \cdot \eta}{NA^2}$$

Where, $r$ is the resolution and the subscript text describes the x, y, z axis, $\lambda_{em}$ is the emission wavelength, $\eta$ is the refractive index of the specimen, and $NA$ is the numerical aperture of the objective lens ( $NA = \eta \sin \alpha$ ).

The table shows the experimental FWHM Gaussian fits for an averaged x-y axis and z-axis from Figure 58 and Figure 59 with the bead sized subtracted to provide the experimental PSF. The theoretical calculations use Eq. 24 and Eq. 25 to calculate the lateral and axial axis, respectively. The theoretical computations were based on the emission wavelength of the green fluorescent beads as $\lambda_{em}$ = 515 nm, a NA = 1.4 and η is the refractive index of the sample which is assumed to be 1.333 (water at 20ºC).

**Table 12 – Comparison of experimental and theoretical PSF in the lateral and axial directions at 780 and 800 nm excitation.**

| | Lateral (nm) | | | Axial (nm) |
|---|---|---|---|---|
| Experimental | x | y | average | z-axis |
| 780 nm | 272.9 | 253.6 | 263.3±9.7 (3%) | 836.1 |
| 800 nm | 195.3 | 270.7 | 233±37.7 (16%) | 831 |
| Theoretical (nm) | 257.5 | | | 805.58 |

At 780 nm excitation, the x-y lateral measurements compare well with the theoretical result showing only a +2% difference in the measure FWHM. The 800 nm excitation exhibits a 5 times greater error (-9.5%) in FWHM of the lateral axis compared with 780 nm. This discrepancy could be due to the distortion arising form a slight broadening of the pulse width with the longer wavelength or from drift of the laser pointing stability as it changes wavelength. The Mai Tai information states that there is a shift of 30 μrads/100 nm when tuning across the range 780-920 nm [275]. It is more likely to arise from the pointing stability causing a change of alignment affecting one axis more than the other, rather than broadening which would affect both x and y axis.

Axial measurements show an increase of 3.7% and 3.2% in the FWHM for 780 and 800 nm excitation, respectively, compared with the theoretical calculations. The discrepancy for both excitations could occur due to refractive index mismatch between the mounting media (water) and immersion oil, which is equivalent to 1.333 at 20°C and 1.518 (Type N, Leica Microsystems Ltd., GmbH), respectively. The mismatch between the sample and immersion fluid results in an incorrect scaling along the optical axis [303]. An approximation of this mismatch can be calculated between the nominal (apparent) focus position (NFP) and the actual focus position (AFP) using the low-NA approximation derived by Hell [118]:

**Eq. 26**
$$AFP = NFP \times \eta_1 / \eta_2$$

where, $\eta_1$ and $\eta_2$ are the refractive index of the immersion fluid and sample. This calculates a scaling factor as $\eta_1/\eta_2 = 1.139$ the measured axial scaling factor at 780 nm and 800 nm is 1.03 for both. This suggests that the assumed refractive index of the mounting media as water is incorrect and exactly matched that of glycerol, which is known to have a refractive index of 1.474 at 20˚C [118].

In a two-photon system a form of wide-field detection is employed by using a fully open pinhole making it insensitive to chromatic effects and other aberration in the detection paths [70]. The PSFs optical response is affected by aberrations or properties of the excitation path [70]. This confirms that any discrepancies seen between experimental and theoretical resolution are most likely due to misalignment.

This effectively means that with each wavelength shift the laser alignment should be checked to confirm the excitation is evenly distributed across the image or only use the aligned wavelength, which has been visually checked. Measuring the PSF has also confirmed the resolution of the system as laterally 263.25± 3% nm and axial 836 nm when using 780 nm excitation this compares well with the theoretically calculated values and

confirms that the protocol outlined in the appendix produces excellent alignment of the system.

### 3.3.4 Confocal raster scanning speed

Measuring $[Ru(bipy)_3]^{2+}$ in deionised water on the Leica requires the laser to scan across the sample to create an image by exciting each pixel in-turn, raster scanning. There are four speeds 200 Hz, 400 Hz, 800 Hz, and 1000 Hz available, which describes the number of lines scanned/sec. The higher the number the faster the image is scanned, but this can incur a penalty for shorter laser dwell time per pixel. Normally the confocal operates a default setting of 400 Hz for continuous or high repetition lasers. The consequences of using a laser at a slow repetition rate needs to be assessed. The effect of an incorrect scan speed could impact the quality of the image and introduce aliasing phase effects.

The sample setup was used as in section 3.2.4.1. The laser repetition rate was set to 500 kHz and TPE intensity images were captured across an excitation wavelength range of 710-870 nm, with 20 nm increments; the PMT was set between 550-670 nm. The parameter settings were 512x512 image format, 200-800 Hz line scan speed, beam expander 1, and SP700 filter.

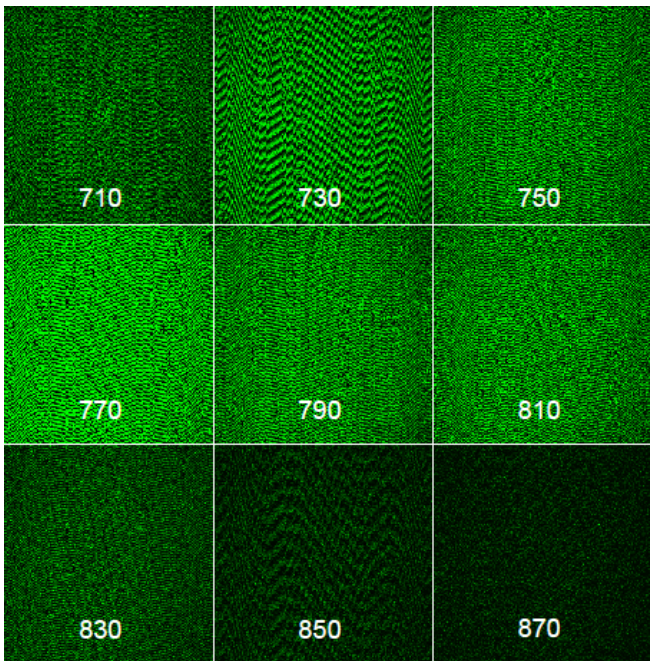


**Figure 60 – Leica intensity images of $[Ru(bipy)_3]^{2+}$ in water at a concentration of 0.412 mM imaged across the excitation wavelength range from 710 – 870 nm in increments of 20 nm with a repetition rate of 500 kHz and line scan of 400 Hz.**

The intensity images of $[Ru(bipy)_3]^{2+}$ in water at a concentration of 0.412 mM with incrementing excitation wavelengths between 710-870 nm, are shown in Figure 60. The

images initially appear dim then increase in brightness peaking at 770 nm and then decreasing from 830 nm onwards. Each image shows some level of distortion with 730nm and 850 nm expressing the worst aliasing effects. The geometric distortions appear to be caused from a shift of phase between the laser scanning speed and the image processing. Using the 400 Hz scan speed the glavomirrors have 2.5 msec to scan one line and with a 512x512 image provides a dwell time of 4.88 μs per pixel. The excitation pulse is <100 fs and the duration between pulse is 2 μs. This only allows each pixel to be excited twice before moving to the next pixel. Increasing to 800 Hz increases the distortions where as reducing the scan rate to 200 Hz removes the geometric distortions. The other option would be to reduce the number of pixels/scan line, which would also remove this effect.

### 3.3.5 Conclusion

The excitation wavelength does affect the PSF, but this can be corrected by re-aligning the laser. As the beam is not visible in the IR range re-alignment could prove problematic at higher wavelengths. At an excitation of 780 nm the lateral and axial resolution has been measured as 263 nm and 836 nm, respectively, which agrees well with theory suggesting the laser has been well aligned.

Slower scan speed or lower size image format is required when raster scanning with a low repetition rate laser.

## 3.4 Time-Correlated Single Photon Counting (TCSPC)

### 3.4.1 Introduction

Fluorimetery measurements using phase and modulation where first introduced in 1926 by Gaviola providing the ability to perform fluorescence decay measurements [155]. By 1949, Norrish and Porter had extended the experimental time-domain from millisecond to microsecond and from then on the advancement in technology accelerated. It was not until 1957 that reasonably accurate determination of fluorescence lifetime was possible due to the introduction of pulsed excitation sources [155]. Unfortunately, during this period and up until the early 80s acquisition times remained slow, limited by electronic response and low repetition light sources that could only facilitate one-dimensional lifetime decay acquisitions [27]. It was not until the combination of transistors on a single chip, increased pulse repetition, and laser power that the full potential of this technique was realised. In 1993, Becker & Hickl was founded and introduced a fast TAC/ADC conversion that created a TCSPC system 100 times faster than any existing device. It also related acquired photons to spatial coordinates and wavelengths, creating a multidimensional TCSPC

system [29]. There are only a few companies that produce time domain time-correlated single photon counting systems, but the principles are the same.

The component parts used in this TCSPC system consist of a photo-multiplier tube (PMT) detector (PMH-100, Becker&Hickl GmbH, Germany) and a TCSPC module (SP830, Becker&Hickl GmbH, Germany). The internal components that create the TCSPC module are composed of a number of architectural blocks mounted onto a single board, as shown in Figure 61, and located inside a computer. Each has an individual function and purpose involved in detection, quantification, digitization, and collation of photons relating to arrival times.

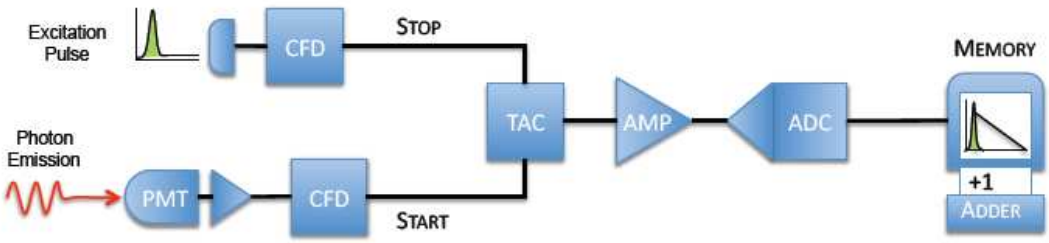


**Figure 61 – Architectural schematic representation of a classic TCSPC system with, photomultiplier tube (PMT) detector, constant fractional discriminator (CFD), time to analogue converter (TAC), Bias Amplifier, analogue to digital converter (ADC), and data memory, adapted from Becker [27].**

A breakdown of each architectural block will be explained below; describing the function and combined operation involved to produce TCSPC lifetime decays. Following this explanation, further sections will investigate variable parameters and issues related to optimisation and control for future experiments.

### 3.4.2 TCSPC module

#### 3.4.2.1 Photomultiplier Tube (PMT) Detector

The role of the PMT is to detect photons from fluorescing samples and relay them to the TCSPC module where the constant fractional discrimination (CFD) continues processing the information. The construction of a PMT incorporates a glass envelope housing a photocathode, several dynodes and an anode maintained in a high vacuum, it is especially good in a low level light situation. As shown in Figure 62 the photon strikes the photocathode. The negative electric field of the photocathode and the positive electric potential of the dynode accelerate the electron to the dynode surface. Upon collision with the surface several electrons are emitted and traverse along the PMT. The electrons amplify as they collide with other dynodes finally produce $10^6$ to $10^8$ electrons [27]. The large positively charged electrode surface used by the anode attracts the accumulated electrons

and upon collision a current pulse indicates the arrival of a photon. As a photon arrives at the photocathode it enters at different trajectories causing a spread of arrival times at the 1st dynode. The distribution of these times is termed the transit time spread (TTS) for the PMT. It is wavelength-dependent and affects the timing accuracy of the arriving photon, therefore limiting the time resolution of the TCSPC [170].

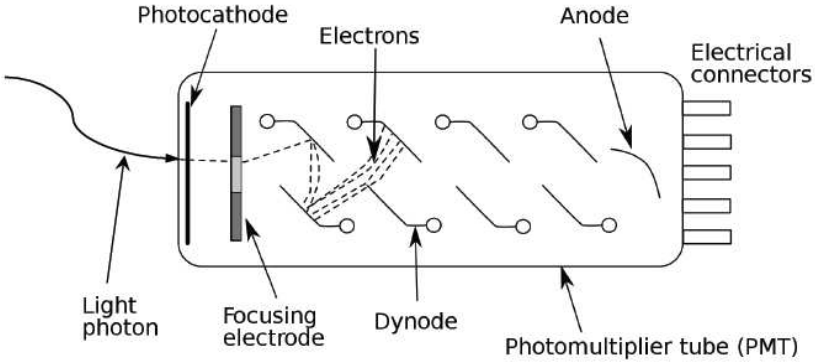


**Figure 62 – Schematic diagram of a photon entering a photomultiplier tube, incrementing the electron gain and producing a current pulse to indicate the arrival of a photon. Adapted from Eberhardt *et al.* [76].**

In order to synchronize the arriving photons in a specific time channel each sweep of the time range must be triggered at the same rate. The laser has a continuous train of excitation pulses with set repetition rates and is therefore an ideal method for synchronizing the TCSPC module. The excitation pulses are detected with a photon counter (PHD-400N, Becker&Hickl GmbH, Germany) that uses a fast PiN photodiode, powered by the detector controller (DCC-100 Becker&Hickl GmbH, Germany) to generate a synchronizing signal [27].

#### 3.4.2.2 Constant Fractional Discriminator (CFD)

A detected signal at the PMT can consist of background noise or photons of differing amplitudes. The objective is to only detect photons and determine accurate arrival times. A constant threshold ensures that only signals above a certain amplitude will trigger and discriminate noise from photons. The technique is termed, 'Leading edge', as shown in Figure 64, but varying pulse amplitudes introduced timing jitter caused by the pulse rise time.

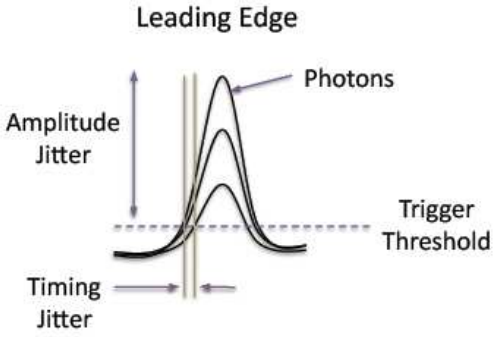


**Figure 63 - Leading edge constant threshold to detect arriving photons is affected by amplitude jitter that manifests a timing jitter [27].**

The development of CFD was to correct for the errors in photon timing. Instead the input pulse is divided into two fractions where a delay is applied to one and the other is inverted. The last step adds them back together producing a zero crossing point independent of pulse height, as shown in Figure 64. The CFD is used for both the reference excitation and detected emission pulse. The detected photon is sent as a zero point signal to the time-to-analogue converter.

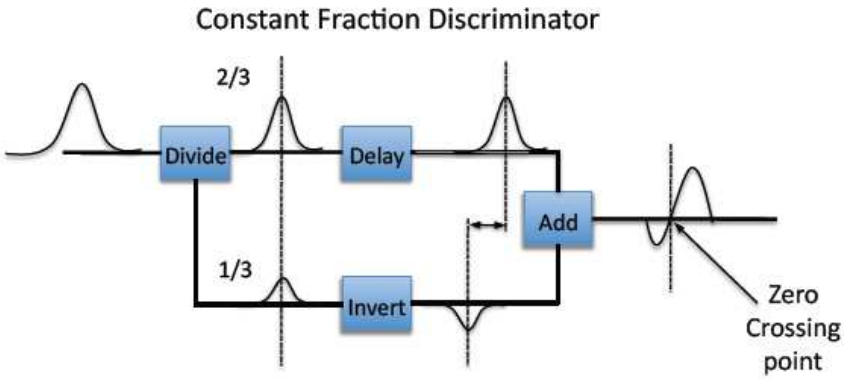


**Figure 64 –Constant fractional discrimination block diagram describing the process or determining the zero cross point for timing of photon arrival [170].**

### 3.4.2.3 Time to Analogue Converter (TAC)

The TAC relates the arrival time of the emitted photon to an analogue voltage that can be later digitised. The zero point signal sent from the CFD 'starts' the TAC capacitor charging until a 'stop' signal is received from the reference excitation pulse and the capacitor stops charging [155], as shown in Figure 65. About 10 ns after the TAC has stopped the ADC is started and the digital processing of the current photon is initiated. The TAC then begins discharging, but the ADC keeps the TAC in a reset state until it is ready to accept the next photon. Once the TAC has returned to its original state and the output amplifiers have resettled the TAC is ready to accept the next photon [27]. The period after

the ‘stop’ signal is termed the TAC ‘dead time’ and increases based on the length of time between ‘start’ and ‘stop’ signal. The system dead time for the detection of a photon is the combination of the TAC ‘dead time’ and the ‘start’ – ‘stop’ time [27].

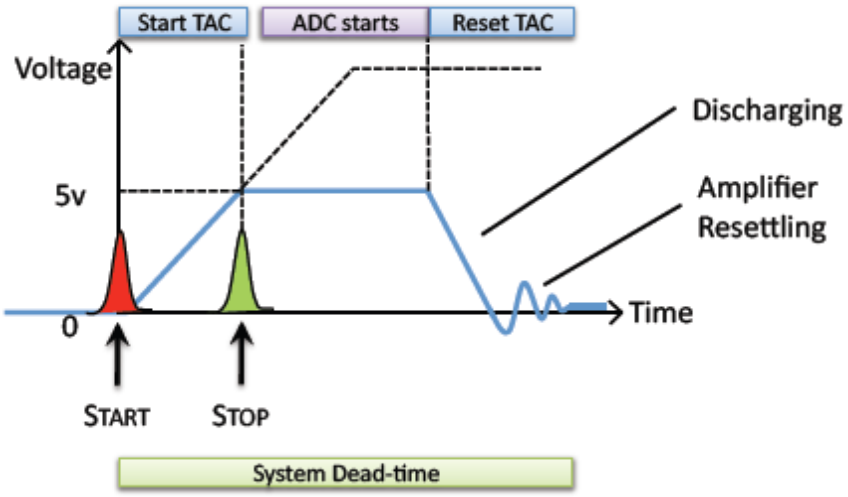


**Figure 65 – A representative diagram of the TAC associating the arrival time of a photon to an analogue signal. This uses a capacitor that ramps the charge at the ‘start’ signal, a photon arriving, and ‘stops’ charge with the arrival of the excitation signal. The voltage is converted for later manipulation to a digital log of the photon arrival time. Adapted from Becker and Pawley [27, 236].**

By adjusting the ‘TAC range’ the gradient of the ramp is adjusted allowing time range changes, based on excitation cycle. A programmable gain amplifier (PGA) is used to vary the ‘TAC gain’, which can magnify the recording interval, but is only really used when the range cannot be reduced any more [27]. The ‘TAC offset’ is used to adjust the position of the ramp on the voltage axis and therefore the position of the decay in the time window. There is also a window discriminator that blocks the processing of any events outside the time range window.

#### 3.4.2.4 Analogue to Digital Convertor (ADC)

The analogue voltage signal from the TAC signal is converted by the ADC to a digital word that represents the photon detection time. The word is then addressed to a memory location and stored in a channel according to the time in the signal period [27]. The SP830 can use up to a maximum of 4098 ADC time channels, but can be reduced dependent on the required time resolution. The memory locates the ADC data words to the associated time channels creating a histogram, as shown in Figure 66. This continues until the collection time has completed or the maximum limit of the memory location has been attained at 65535 counts per channel [27].

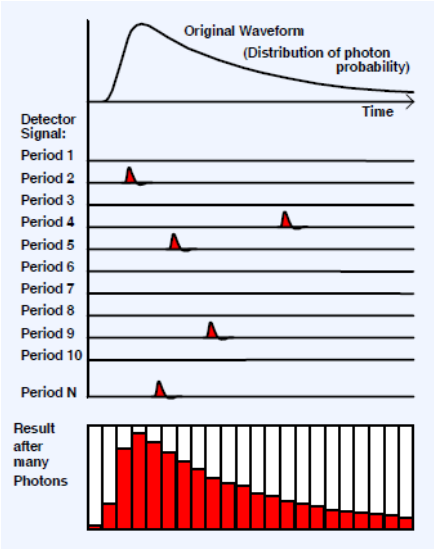


**Figure 66 – Pictorial representation describing the logging of photons per excitation cycle and conversion from detected pulses to the digital conversion in to time channels to build lifetime decay [27].**

### 3.4.3 Multi-dimensional photon distribution

So far the discussion has concentrated on single decay acquisition, the main difference between the TCSPC module and previous systems is not only the speed, due to all the components located on one printed circuit board, but also the correlation of information. Normally the photon distribution is recorded as a function of time, but it can also be associated with spatial location and registration with an intensity image, sequential time resolution, wavelength, or externally triggered with a delivery or motor system, as shown in Figure 67. The calibration of this system will concentrate on the single decay acquisition process, a closer examination of image processing and image registration will be conducted in later chapters.

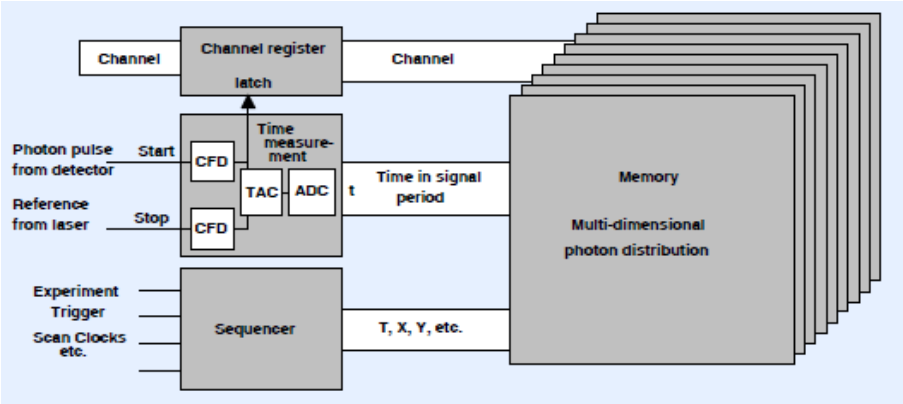


**Figure 67 – Schematic diagram of the TCSPC module and the time correlated photon distribution assigned to memory. The extra parameters that are also recorded via triggers, sync scans, and clocks to provide spatial registration and external sequencing [27].**

### 3.4.4 Instrument response function (IRF)

The recorded decay response after excitation is not a true representation of fluorescence lifetime. Deriving the true lifetime of a fluorophore initially requires the measurement of the IRF. The reason for this is that the recorded decay is a convolution of the IRF and the true lifetime [224]. Therefore to derive the true lifetime the IRF must be measured and deconvoluted from the decay especially when dealing with short lifetime decays [236]. When measuring the IRF it is also a good opportunity to optimise the TCSPC set-up otherwise later changes, which affect the width of the IRF can lead to erroneous results [31]. In the TCSPC system this only needs to occur once after the threshold has been set, it is then saved and recalled for each analysis of the decay. The IRF is the fastest response of the detector to a signal. The best method for recording the IRF uses a scattering medium or a mirror, but using a NIR laser the spectral response of the PMT detector head will be limited to the visible wavelength range [27]. By recording the response from a second harmonic generating (SHG) sample a signal faster than the response of the detector is produced [27]. The measured IRF can suffer from contaminating fluorescence interfering with the detected signal, but a SHG signal it so strong that it does not pose a problem. A false secondary peak can sometimes appear if the sample is not covered arising from backward transmittance of the SHG sample reflecting off the condenser lens or other mirrors [27].

#### 3.4.4.1 Method

The second harmonic sample was made from reconstituted powdered Urea (U5378, Sigma-Aldrich, UK). A bijou tube with 480 mg/ml of Urea was dissolved in deionized water and 40 µl of Urea solution was then pipetted on to a coverslip (thickness 1.5, 22x32 mm) (Cat. No. 631-0134, VWR Ltd., UK). The sample was allowed to dry out over a 2h period and mounted on to a x63 oil immersion objective (NA 1.4) lens (506192, HCX PL APO, Leica Microsystems Ltd., GmbH). The microscope was focused onto the SHG sample and laser excitation set to 780 nm with a repetition rate of 80 MHz using the SP700 filter. The TCSPC module (SP830, Becker&Hickl, GmbH) was set to a collection time of 100 sec, ADC 1024, Gain 4, and time range of 50 ns. TCSPC files .sdt were converted to ASCII files and exported to Origin software (OriginPro 8 SR0, OriginLab Corporation, USA) and a Gaussian model fitted to the peak.

#### 3.4.4.2 Results: Instrument response function can be affected by CFD threshold

The time base used was 50 ps and the IRF completed within the first 5 ns. An uncorrected IRF had a CFD threshold or ‘lower limit’ set to zero and the corrected IRF

was set to -80.39 mV, as shown in Figure 68 A and B, respectively. The uncorrected graph (left) has an extra pulse after the IRF, an increased peak before the main response, and an increased background level from 10 to 35 photons/channel. A Gaussian model was fitted to the peaks of both graphs and the FWHM for uncorrected and corrected was 189.3 ps and 196.2 ps, respectively, adjusted $R^2$ >0.99.

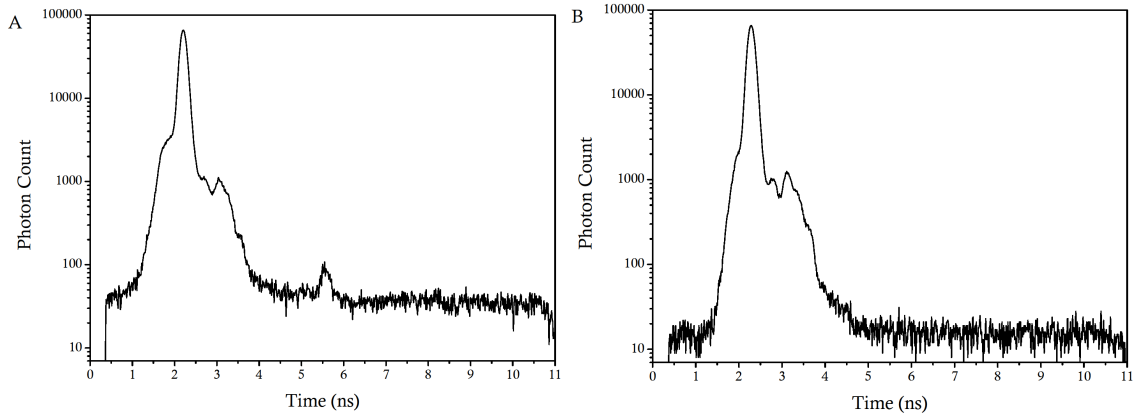


**Figure 68 – Instrument response function of a SHG sample measured on a NIR FLIM system and plotted on a semi-logarithmic graph. A: Sample with CFD threshold set to zero, B: Sample has corrected CFD threshold set to -80.39 mV to reduce background and afterpulsing.**

#### 3.4.4.3 Discussion

The IRF describes the response of a detector in a TCSPC system. It is preferred to use a SHG sample with NIR lasers to avoid spectral wavelength limitations of the detector and to provide a strong signal that can minimise any contaminating fluorescence. Adjusting the threshold and zero cross levels can affect the shape and width of the IRF. This is shown in Figure 68B where the CFD threshold or 'lower limit' is adjusted to suppress afterpulsing and background noise. There is a change of 6.9 ps in the FWHM of the IRF and a reduction in background noise by 25 photons/channel. The values measured for the FWHM of the IRF is comparable with published information for the photomultipler tube PMH-100 in a simple TCSPC setup ~180 ps [30].

Normally, in short lifetime decays the IRF would be deconvoluted from the lifetime decay, but if it is assumed that the $[Ru(bipy)_3]^{2+}$ decay would complete by 2250 ns (5τ) then the IRF would only contribute to $8x10^{-6}$% of the decay. Therefore the level of convolution is very low and can be excluded [75] by determining the lifetime decay after the IRF. This also avoids fitting error induced from scattering that only occur at the beginning of the decay. No deconvolution of the IRF from the $[Ru(bipy)_3]^{2+}$ decay is required.

### 3.4.5 Background noise detection

It is not possible to view the background noise level in the ruthenium decays measured using the TCSPC, because the lifetime has not completed within the limited time

range of the TAC (2 μs). Therefore, when fitting an exponential model to the data the offset ($y_0$) is not able to asses where this occurs. One way of dealing with this is to measure the background levels in the room and subtract or restrict the decay fitting to account for it. This was the general practice in older systems where the background level was subtracted from the decay [224]. Different contributions of possible room noise were evaluated for increments collection periods to determine a relationship.

#### 3.4.5.1 Method

A short decaying media sample was used to determine the room background level. Media was mounted on to a coverslip on the objective lens, the laser excitation was set to 780 nm with repetition rate of 500 kHz. The TCSPC module (SP830, Becker&Hickl, GmbH) was set to an ADC 1024, Gain 1, a count increment of 10, a time range of 2 μs and collection times of 10, 100, 200, 400 sec. The collection timings were applied to three different room environments, total darkness, one monitor on, one monitor on and door open; each measurement was repeated three times. As the 'total darkness' setting would be the standard environment that would be worked in an 800 sec measurement was also taken.

All files were converted to ASCII and imported into Origin software (OriginPro 8 SR0, OriginLab Corporation, USA). Data sets were divided by 10 to remove the effect of the 'count increment'. The measured background was averaged between the 'lower limit' of the TAC and after the emission signal generated from the sample, as highlighted by the dashed lines in Figure 69. Replicate measurements were averaged and standard errors and linear fits plotted for each environment exposure.

#### 3.4.5.2 Results: Background noise has a linear relationship with time

A media sample with short decaying lifetime was used to maximise the number of channels for background counts. The time range for the measurements were 2 μs and counts in channels were averaged from just after the SHG signal and before the end of the time range between 189.15 and 1698.45 ns, as shown in Figure 69. The average and standard error of average counts/channel are calculated for replicate measurements (n=3) and plotted for incrementing collection times for increasing background light environments.

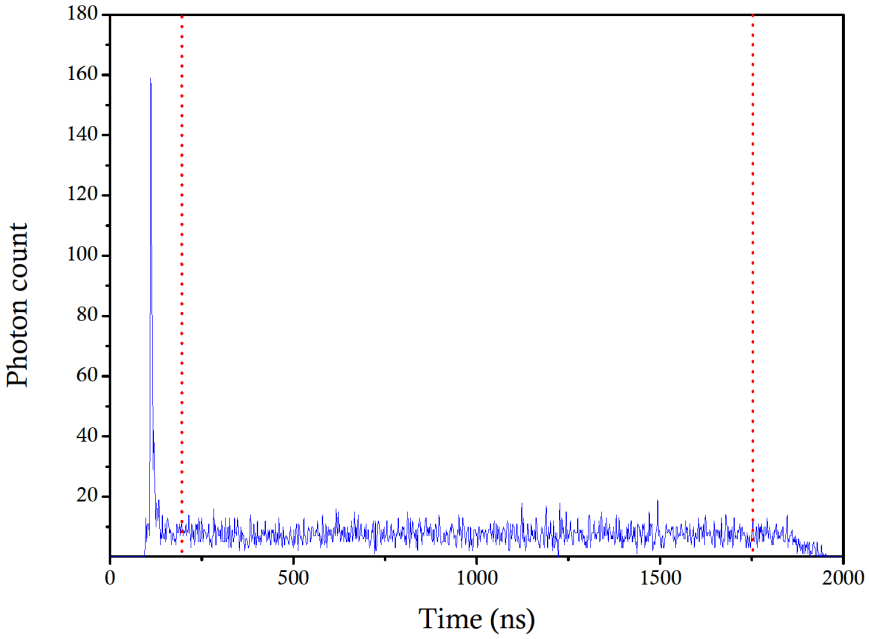


**Figure 69 – The media sample was excited at 780 nm with a repetition rate of 500 kHz and collection rate of 800 sec in a blackout room. Background noise was averaged between the red lines (dashed) for varying levels of room light and repeated (n=3).**

Linear fits were made for each background environment and extended to span the graph, as shown in Figure 70. There is a significant ($p<0.01$) positive linear relationship between the collection time and the average counts/channel for each background environment. The 'blacked out room' (black squares) had the lowest gradient, and 'one monitor on' and 'one monitor and an open door' gradient increased by 37.7% and 65.8%, respectively. The 'blacked out room' contributed to an increase of 1 count per channel/100 sec collection time, where as 'the open door and monitor on' increased the number of counts per channel by 1.5 counts/100 sec collection time.

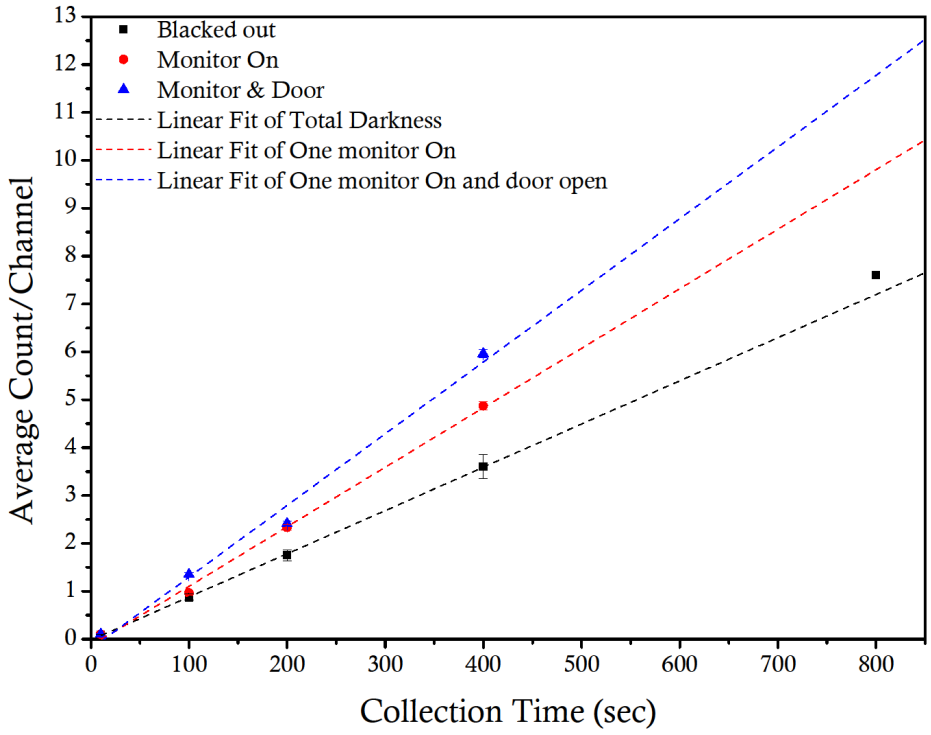


**Figure 70 – The average photon count per channel was collected for incrementing time period from 10-800 sec and with increasing exposures of background light. Three different background noise situations were investigated, a room in total darkness (black square), monitor on in the same room (red circle), and the door open and one monitor on in the same room (blue triangle). Values represent means with error bars indicating SEM for n=3 replicate measures. Linear fits of each background noise environment was performed, adjusted $R^2$>0.98.**

#### 3.4.5.3 Discussion

As expected, increasing levels of background light contributed to a higher accumulation of photon counts/channel. The relationship of accumulating counts within the same environment was positively linear indicating a constant incrementing noise. The shorter the collection time, the lower the background count. The gradient of each environment is only relevant for an ADC of 1024 and time window of 2 μs (500 kHz rep. rate), but the graph can be adapted for other channel widths. These graphs would not be transferable to other systems as the background light is specific to each room, but the graphs do provide a quick reference guide for identifying background noise levels.

### 3.4.6 Lifetime decay fitting

The environmental aspects of running the TCSPC have been explored and now an investigation into operating the TCSPC for acquiring lifetime shall be undertaken. Different models can be used to determine the lifetime of a decaying fluorophore, but the models are based on the physics behind molecular emission. If a dye is excited by an infinitely sharp pulse a population of fluorophores will be excited. The population of electrons in this

excited state will decay at a rate of emission plus non-radiative decay with respect to time [224].

**Eq. 27**
$$\frac{dn(t)}{dt} = -\left(k_r + k_{nr}\right) \cdot n\left(t\right)$$

The above Eq. 27 refers to an exponential decay where $k_r$ is the radiative emission, $k_{nr}$ is the non-radiative emission, and $n(t)$ is the number of excited molecules at time $t$ following excitation [171]. In Chapter 1 (section 1.4) it was discussed that the sum of the radiative and non-radiative rates that depopulate the excited state were equal to the inverse of the fluorescence decay time (lifetime, τ) [75], as shown in Eq. 28.

**Eq. 28**
$$\tau = \frac{1}{k_r + k_{nr}}$$

As each fluorophore has the same probability of emitting for a given period and it is a random event the decay of an excited state population is exponential [171]. Integrating Eq. 27 gives,

**Eq. 29**
$$n\left(t\right) = n_0 \exp^{\left(-t/\tau\right)}$$

where, $n_0$ is the number of excited molecules at time zero. Generally, it is not the number of excited molecules that are observed, more the fluorescence intensity, or when using TCSPC the photon counts that are recorded. However both are proportional to $n(t)$. Therefore, the lifetime can be determined from the time where the decay has decreased from its initial value to $1/e$ or by measuring the slope of a semi-log plot of counts (or intensity) vs. time [171]. Determining the lifetime depends on the type of decay and the model being applied, as shown in Table 13.

**Table 13 – Different exponential fits used for the calculation of lifetime (τ) where, *A* is the pre-exponential and the subscript denotes the lifetime component, *t* is time channel/interval, τ is the lifetime, *y(t)* is the number of counts with respect to the time channel/interval, β is related to the distribution of decay times, *b* depends on the quencher concentration and diffusion coefficient**

| Model | Fitting equation |
|---|---|
| Mono-exponential | $y(t) = A_0 \exp^{(-t/\tau)}$ |
| Bi-exponential | $y(t) = A_1 \exp^{\left(-t/\tau_1\right)} + A_2 \exp^{\left(-t/\tau_2\right)}$ |
| Multi-exponential | $y(t) = \sum_n A_n \exp^{\left(-t/\tau_n\right)}$ |
| Stretched exponential | $y(t) = A_0 \exp^{\left[\left(-t/\tau\right)^{\beta}\right]}$ |
| Non-exponential | $y(t) = A_0 \exp^{\left[\left(-t/\tau\right)-\left(2bt^{1/2}\right)\right]}$ |

Mono-exponential decays refer to population of fluorophores decaying during a measurement at the same rate. Bi-exponential refers to two of the same or different fluorophore populations decaying in the same measurement at different rates. It therefore requires identification of the separate component decays. This model is also used to describe the occurrence of fluorescence resonance energy transfer (FRET) where the excited energy is transferred to another, dependent on distance. Multi-exponential is used for more than two fluorophores in the same decay, but attempting to derive these values can be difficult as with more components there are more unknowns. Stretched exponentials have been used to study dielectric relaxation in polymers where there is an expected distribution of relaxation times [237] [171]. It is also used in tissues with complex multi-exponential decays and autofluorescence, where there is a continuous distribution of lifetimes rather than a few discrete lifetime components [178]. Non-exponential or transient effects can be used in collisonal quenching and resonance energy transfer (RET) for rapid quenching of closely spaced fluorophore-quencher pairs. In this instance the decay is not related to the number of excited molecules as would normally be the case. Instead the fluorescence is restricted by the close proximity of quenchers [171]. The initial decision of which model to use can be derived from prior knowledge of the system and number of fluorescent components or if unknown, based on the goodness of fit. The goodness of fit is used as a comparison between the fitted models and the experimental data. In these

experiments the single exponential model will be used as it is well documented that $[Ru(bipy)_3]^{2+}$ in aqueous solution has a mono-exponential response [91, 171, 257, 279].

#### 3.4.6.1 Mono-exponential decay fitting

Initially when fitting the data, cursors were used to manually select the maximum and minimum boundary time points an hence the data range that should be modelled. This approach was useful for excluding scattering arising from coverslips or other reflective surfaces. The modelling software estimates the values based upon an iterative process to minimise the discrepancy between the fit and data, while maintaining the boundaries of the model. There are different analysis methods that can be used for this purpose including, maximum likelihood estimator (MLE) [108], methods of moments [75], least-square Marquardt-Levenberg [108], global analysis [171], Monte-Carlo [265], maximum entropy method (MEM) [15] and Bayesian [75]. The different analysis options have varying levels of complexity and speed, some are better at precision, but take a long time to process and others are used for specific types of data, low count levels or FRET analysis. The most widely used method is the least-squares Marquardt-Levenberg, which can be found in most statistical software and is also available in the TCSPC analysis software. In order to use this analysis it is necessary to make a set of assumptions about the collection of the data as listed by Lakowicz [171]:

1) All experimental uncertainty is dependent on time (y-axis)
2) Measured values (in y-axis) have a Gaussian distribution centred on the correct value
3) No systematic errors exist in either time or counts (x-y axis)
4) Assumed fitting function is the correct mathematical description of the system and incorrect models will yield incorrect parameters
5) Data points are independent observations
6) Sufficient number of data points exists to over determine parameters

These generally fit well with operation of the TCSPC experiment.

#### 3.4.6.2 Goodness of fit

The goodness of fit is assessed with the Chi-square ($\chi^2$) describing the level of difference between the fitted model and the experimental data. The Chi-square is weighted by the standard deviation of each interval $\sigma_i$, as shown in Eq. 30,

**Eq. 30**
$$\chi^2 = \sum_{i=1}^{n} \omega_i \left[ y(t_i) - f(t_i) \right]^2 ; \qquad \omega_i = \frac{1}{\sigma_i^2}$$

where, $f$ is the fitted data, $y$ is the experimental data, and $\omega_i$ is the applied weighting described by the squared standard deviation $\sigma_i$ for each data point prior to summation [155, 213]. The standard deviation specific to lifetime decay can be assumed as Poissonian distributed. This relates to the photon emission being independent to one another [213], where each photon has an equal mean and variance of arriving at a particular interval [155]. Therefore the Poissonian statistical noise or standard deviation per interval is described as the square root of the number of photon counts in each interval $\sigma_i = y(t_i)^{1/2}$ [155, 171, 213]. Applying this to Eq. 30 provides weighted chi-square value Eq. 31,

**Eq. 31**
$$\chi^2 = \sum_{i=1}^{n} \frac{\left[ y(t_i) - f(t_i) \right]^2}{y(t_i)}$$

This forces the fit to rely more heavily on the time intervals with more counts, at the beginning, rather than treating all the time channels equally [171]. The only issue with using the weighted $\chi^2$, as a determination for goodness of fit, is the dependence on the number of channels or data points. This creates a difficulty when comparing results from experiments with a different number of data points. By accounting for the degrees of freedom ($v$) a reduced Chi-square $\chi_r^2$ can be used to account for the data points ($n_1$ being, $n_2$ end channel number) and number of fitting parameters ($p$), as shown in Eq. 32.

**Eq. 32**
$$\chi_r^2 = \frac{\chi^2}{n_2 - n_1 + 1 - p} = \frac{\chi^2}{\nu}$$

As the $\chi_r^2$ is normalised it provides a minimised value that is optimally 1 for data with Poisson noise or 0 for no Poisson noise [171]. These experiments contain Possionian noise therefore values greater than one suggest a poor fit between the model and data. This can occur from other unknown exponential components in the decay or the presence of systematic error. The manifestation of a poor fit can be visually observed from the residual plot, $R_i$, between the data, $y(t_i)$, and the fit, $f(t_i)$, as shown in Eq. 33.

**Eq. 33**
$$R_i = y(t_i) - f(t_i)$$

In this instance a weighted residual plot ($r_W$) can be applied to account for the relationship between Possionian noise and the number of counts per time interval, as shown in Eq. 34. This residual plot relies more heavily on the earlier time channels.

**Eq. 34**
$$r_W(t_i) = W_i R_i ; \qquad W_i = \frac{1}{\sqrt{y(t_i)}}$$

A visual inspection between the model and data facilitates another aspect of determining a good or poor fit by observing all the fitted data points and identifying any discrepancies. A more sensitive approach is to consider the $\chi_r^2$ value to warrant rejection of the data or model. Standard mathematical tables for $\chi_r^2$ distribution [34] provide a predicted probability that random error is the cause of the value. Typically probabilities greater than 5% are not rejected. Based on the number of data points acquired in these lifetime decays (≥200) fits are accepted if $\chi_r^2 \leq 1.17$. Therefore if ample counts were obtained any $[Ru(bipy)_3]^{2+}$ decay displaying a mono-exponential characteristic decay $\chi_r^2$ >1.17 would indicated possible problems with the sample, contamination, or systematic error in the experiment.

### 3.4.7 Systematic error

An inherent problem referred to as 'pile-up' exists within in every single photon counting system [224]. It is based on the electronics of the system regarding the number of photons that the TAC can process during one excitation cycle, as discussed in section 3.4.2.3. The process of logging a photon takes a finite period of time referred to as the 'TAC start-stop' time, while the ADC processes the photon the TAC enters a 'TAC dead time'. A combination of these two periods is referred to as the system dead time. During this dead-time any second photon arriving at the PMT cannot be processed by the TAC and are therefore excluded from the final decay. The effect is seen mainly during low repetition rate experiments observing long decaying dyes. Therefore the later part of the decay is more susceptible to the loss of photons. This can affect the accuracy of the lifetime decay through false manifestation of other lifetime components termed 'classic pile-up' [27].

In low repetition rate lifetime experiments a constant battle is waged to acquire data with the shortest possible collection time, but long enough to acquire an accurate lifetime decay, whilst maintaining low repetition rates to minimise the effects of pile-up on lifetime. There are varying ways to minimise or correct for pile-up using pile-up rejection circuits, multiplexing, or mathematical correction equations [27, 224].

#### 3.4.7.1 Pile-up rejection circuit

The pile-up rejection circuit is used to detect the arrival of a second photon in the same excitation cycle, if two photons are detected both are rejected. However, this technique has a significant flaw relating to the detection of the two photons within the width of the detector response. If a second photon arrives within the detectors response to the first photon the second photon cannot be registered [27]. There are possible ways of

overcoming this limitation by using multiple detectors to distinguish the arrival of two or more photons during the response of the detector or multiplexing.

#### 3.4.7.2 Multiplexing

There are two types of multiplexing methods, namely pulse-by-pulse multiplexing [27] and multiplexed TCSPC [282]. Pulse-by-pulse multiplexing creates different optical delays, but uses the same detector and TAC range [27]. This method suffers at high repetition rates with overlapping of the detected signals. Alternatively multiplexed TCSPC uses signals that switch several diode lasers and route the detected photon distribution into different memories, all controlled via a switching signal [27]. In addition multiplexed TCSPC can be used to describe multiple detectors that detector channels to distinguish two photons arriving within the detector response. This method is useful as it relies only on one TAC module to process the information [282].

#### 3.4.7.3 Mathematical equations

The final option uses a mathematical equation written by Coates [56] to correct for pile-up. This method is not widely applied because its assumes that all the excitation pulses are of equal energies [306]. Another iterative algorithm written by Walker [306] does take into account the variation in excitation energies.

The first two options require additional component support to assist with the effects of pile-up and despite the mathematical equations aim to remove the effects of pile-up the general consensus is to avoid these equations and rather reduce the collection rate. Prior to the undertaking of additional costs to the system the extent of pile-up interference in data collection should be determined and a future decision base on this assessment. The optimum count rate for collection is disputed among different users quoting collection rates between 10% - 0.1% of the excitation cycle [27, 224]. These are stated as inducing minimal effects from pile-up or determined as an accepted level of error within the decay.

### 3.4.8 Determining the onset of pile-up

Understanding when and why pile-up occurs and establishing a protocol to follow are vital for obtaining accurate reliable lifetimes. Experiments were conducted on the occurrence of classic pile-up. This examined the effects of dye concentrations, laser power, excitation wavelengths, and oxygen levels. Levels of discrimination between an accepted and rejected lifetime were also assessed.

#### 3.4.8.1 Sample preparation and FLIM setup

A stock solution (13.34 mM) of oxygen sensitive dye Tris(2,2′-bipyridyl) ruthenium(II) chloride hexahydrate, $[Ru(bipy)_3]^{2+}$ (224758, Sigma-Aldrich, UK) was prepared with deionised water. Samples at four concentrations of $[Ru(bipy)_3]^{2+}$ (0.334, 0.845, 1.67, and 3.34 mM) were created from the stock solution and deionised water. A coverslip (thickness 1.5, 22x32 mm) (Cat. No. 631-0134, VWR Ltd., UK) was mounted on an x63 oil immersion objective (NA 1.4) lens (506192, HCX PL APO, Leica Microsystems Ltd., GmbH) and 20 µl of each solution was pipetted onto the coverslip; for ambient oxygen measurement. For low oxygen samples, airtight sample chambers were used with $Na_2SO_3$ (100 mM) added to solutions.

The laser excitation was either set to 780 nm or 880 nm, uses a repetition rate of 500 kHz, and emission captured over 500 – 670 nm. The TCSPC module (SP830, Becker&Hickl, GmbH) parameters were set to: ADC 1024, EOM gain was varied from 0-60%, TAC Gain was 1, time range was 2 µs and collection time was 800 sec. This long collection time ensured that the maximum dynamic range was utilised, but if it was reached prior to the collection time completing then the elapsed time was noted down. The mono-exponential model from Table 13 was applied to each decay using OriginPro8. The data points between 100 and 1900 sec were selected for fitting the model using the data cursor. The produced fit also provided the calculated $\chi_r^2$, but the residual plots were determined using Eq. 34 from the experimental and fitted data provided by OriginPro8.

#### 3.4.8.2 Assessment of using visual inspection for determining pile-up

The sample preparation and instrument setup was conducted as outlined above. The lifetime decay of $[Ru(bipy)_3]^{2+}$ dissolved in deionized water at a concentration of 0.845 mM is plotted in all of Figure 71 on a semi-log graph against time. The lowest power has the EOM at 0% (black) increasing to 20% (left, red) and then the maximum at 60% (right, blue). All graphs have reached the maximum dynamic range of 65535 and the fitted mono-exponential models have an adjusted $R^2$ >0.99 for each graph. Fitting of the derived lifetime data shows 0%, 20%, and 60% EOM gain producing a lifetime of 388.78 ns, 366.99 ns, and 240.26 ns, respectively. The EOM gains of 20% and 60% have a decreased lifetime of 5.6% and 38.4%, respectively, in comparison to 0% EOM gain. Visual inspection of the graphs shows no difference between 0% and 20% EOM gain (left), but there is a noticeable difference between 0% and 60% EOM gain (right) where pile-up has been induced.

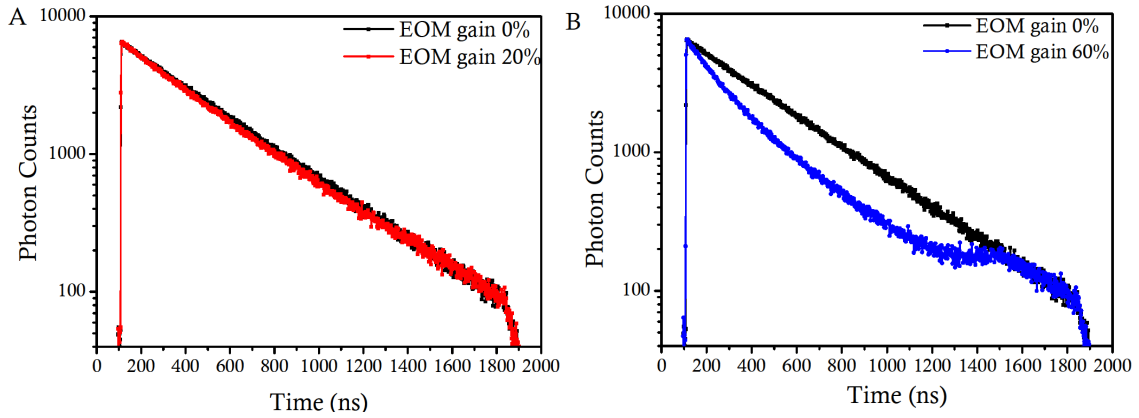


**Figure 71 – Lifetime decay with time of $[Ru(bipy)_3]^{2+}$ in a deionized water solution (0.845 mM) plotted on semi-log graph. A: has EOM gains of 0% (black) and 20% (red) which appears to not induce visible pile-up, by constrast B: replicates the EOM gains of 0% (black), but pile-up was visible apparent for EOM gain 60%(blue).**

Closer examination between the fits and data can be seen in Figure 72, with the weighted residual plots of Figure 71. The plots only show the residuals between the fitting regions selected by the data cursor. Visual inspection of the weighted residuals plots show no obvious difference between 0% and 20% EOM gain, but a large variation can be seen between 0% and 60% EOM gain. At 60% EOM gain the weighted residuals show a greater discrepancy between the data and the fit at the start (<400 ns) and end (>1600 ns) of the lifetime. The discrepancies seen in the residual plots are also confirmed in the goodness of fit, where 0%, 20% and 60% EOM gain have an $\chi_r^2$ of 0.994, 1.33, and 4.67, respectively.

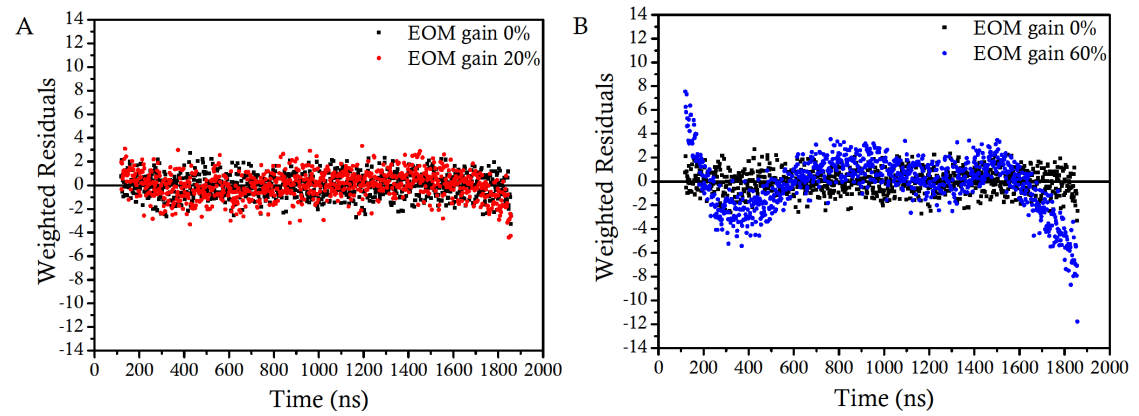


**Figure 72 – Weighted residual plots with time of $[Ru(bipy)_3]^{2+}$ in deionized water solution (0.845 mM) at different EOM gain level compared. A: is the EOM gain at 0% (black) and 20% (red) and B: is the EOM gain at 0% (black) and 60% (blue).**

The graphs in Figure 71 and Figure 72 both show no obvious difference between 0% and 20% EOM gain, but there is a large discrepancy for 0% and 60% EOM gain, where the difference in lifetime is up to 34%. Solely using visual means for determining discrepancies the residual plot easily highlights the problem between 0% and 60%, but the 20% and 0% lack a definitive conclusion. Prior knowledge of the measured background from section 3.4.5 shows that for a collection time of 800 sec the minimum background count/channel should be in the region of 7 to 12 for an ADC with 1024 time channels.

Viewing the offset data for 0%, 20%, and 60% EOM gains, an offset of 11, 37.9, and 136.5 is displayed. This demonstrates that the fitting model is altering the other parameters in an attempt to provide a reasonable fit by biasing the offset. Using the cut-off value by disregarding $\chi_r^2 \geq 1.17$ confirms pile-up occurring for 20% and 60% EOM gain from the determined reduced chi-squares values of 1.33 and 1.46, respectively. This shows that reliance purely on visible inspection is not justified and offset, background, and reduced chi-square also need to be considered to confirm if pile-up is influencing the lifetime.

#### 3.4.8.3 Effect of dye concentration and repetition rate on pile-up

Figure 73 displays the lifetimes at increasing concentrations, between 0.334 – 3.34 mM, of $[Ru(bipy)_3]^{2+}$ in deionised water for an excitation wavelength of 780 nm. The measurements were conducted at ambient temperatures with increasing EOM gain. At the lowest concentration (0.334 mM) there is a discrepancy of 87 ns between the 0% and 60% EOM gain, while at the maximum concentration (3.334 mM) the discrepancy is 265 ns a difference of 38% and 232%, respectively. The mean lifetime and standard deviation at the lowest and highest concentration is 354.5±37 ns and 237.5±114 ns, respectively. A statistically significant negative correlation ($p<0.05$) exists between concentration and lifetime at all EOM gains. An increase in EOM gain (laser power) induces a decrease in lifetime, and this relationship is magnified at increasing dye concentration. The exception is the 51% EOM gain, which appears to have induced a larger effect on the lifetime than the 60% EOM. This is due to the peak point of maximum transmission in the EOM lying between the two gain values. This was tested prior to running experiments to determine maximum transmission of laser light through the EOM, as described in section 3.2.3.

At an excitation wavelength of 880 nm (Figure 74), the relationship is similar except that there is a reduced discrepancy between 0% EOM gain and gains up to and including 60%. The discrepancy between 0% and 60% EOM for the lowest and highest concentrations induced a decrease in lifetime of 8% and 66%, with a mean lifetime and standard deviation of 381±11.5 ns and 327.6±67 ns, respectively. There is little or no correlation ($p>0.05$) between concentration and lifetime at EOM gain <31%, but there is a negative linear ($p<0.05$) correlation at 40% and EOM gains above.

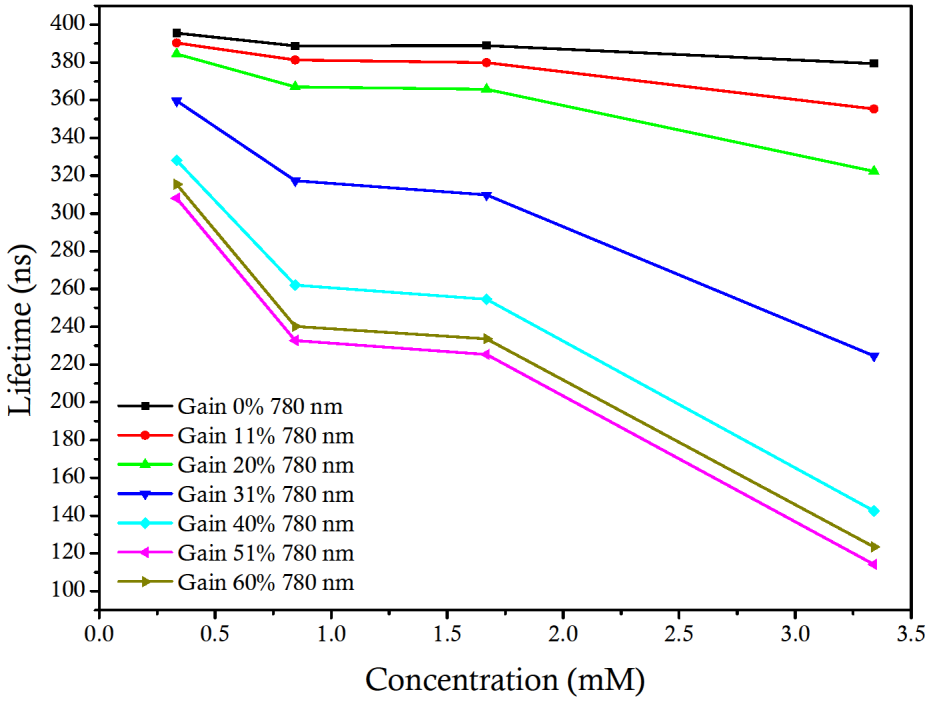


**Figure 73 – Lifetime decay of $[Ru(bipy)_3]^{2+}$ in deionised water at a concentration of 0.334, 0.845, 1.67, 3.34 mM, measured at incrementing EOM gain between 0-60% with laser excitation wavelength at 780 nm and laser repetition rate of 500 kHz.**

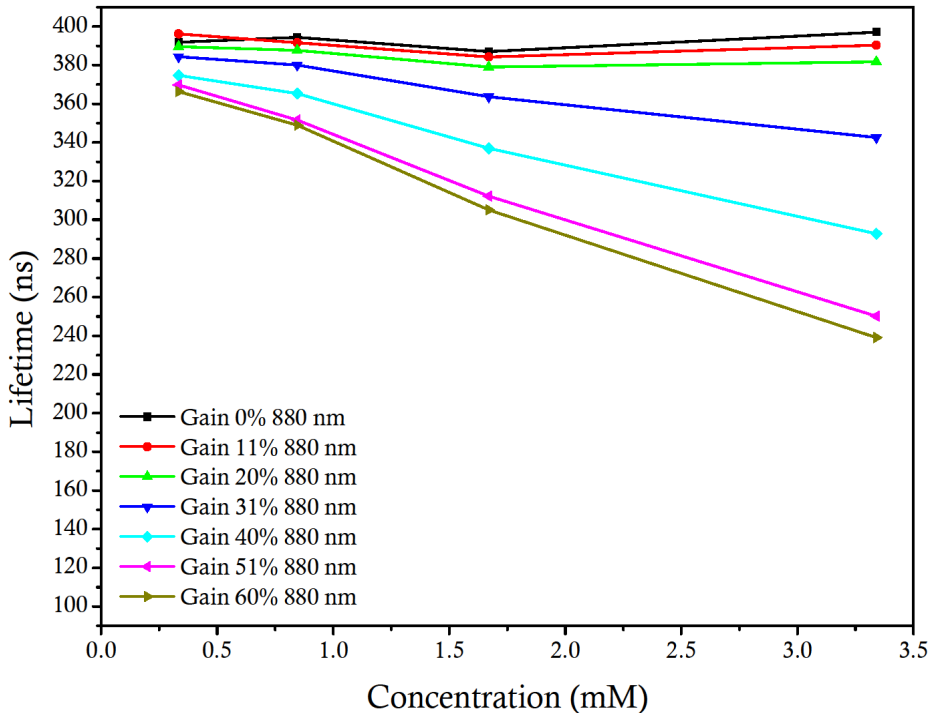


**Figure 74 – Lifetime decay $[Ru(bipy)_3]^{2+}$ in deionised water at a concentration of 0.334, 0.845, 1.67, 3.34 mM, measured at incrementing EOM gain between 0-60% with laser excitation wavelength at 880 nm and laser repetition rate of 500 kHz.**

The measured lifetime in Figure 73 and Figure 74 has been directly compared with the collection rate as a function of repetition rate for 780 nm and 880 nm excitation as shown in Figure 75. It is apparent that a decaying exponential model fits the relationship for 780 nm excitation (adjusted $R^2 > 0.99$), however the 880 nm excitation appears to warrant a linear model (adjusted $R^2 > 0.99$). This difference is also noticeable in Figure 73

and Figure 74. The higher rate of photon detection at the start of the lifetime decay is affecting the detection of photons arriving later within the same excitation cycle creating pile-up exponentially for 780 nm and linearly for 880 nm due to the large difference in laser power and therefore emission. This highlights the need for a separate parameter to distinguish acceptable lifetime values, which can be determined using the $\chi_r^2$.

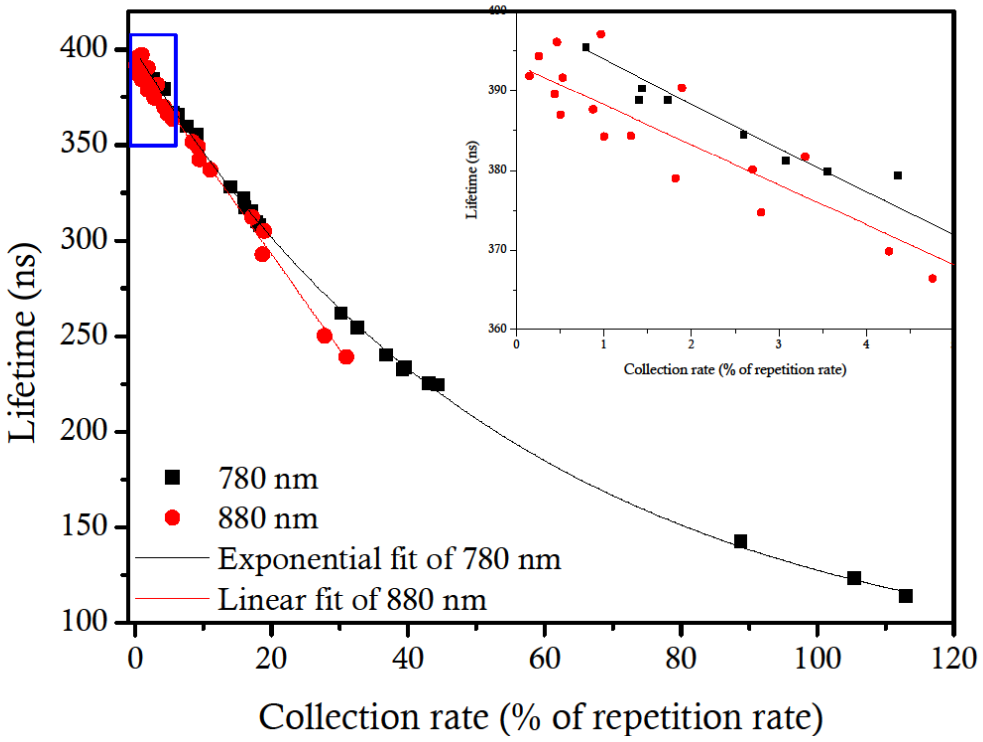


**Figure 75 – Collation of all concentration measurements taken and separated into 780 nm (black squares) and 880 nm (red circles) excitation to display the relationship with the collection rate as a function of repetition rate. Data collected with 780 nm excitation was fitted with exponential model adjusted $R^2$ >0.99 and 880 nm excitation was fitted with linear model adjusted $R^2$ >0.99. Inset graph represents zoomed in section of graph identified by the blue box.**

The calculated reduced chi-square from the fitted data in Figure 73 is displayed in Figure 76 against the derived lifetime for excitation at 780 nm. The standard deviation of the fit is represented by the error bar. The number displayed above the data points described the count rate. This is described by the collection rate divided by the laser repetition rate and is dependent on laser power (EOM gain) and dye concentration. The full-scale is represented by the smaller graph and the larger graph represents a zoomed in observation of the red box. The colours represent the different concentrations used in the experiment. The cut-off value, represented by the dashed line, is determined by $\chi_r^2 \leq 1.17$. This ensures there is at least a 5% probability that the $\chi_r^2$ value is due to random deviations and the fit can be accepted [171], as described in section 3.4.6.2.

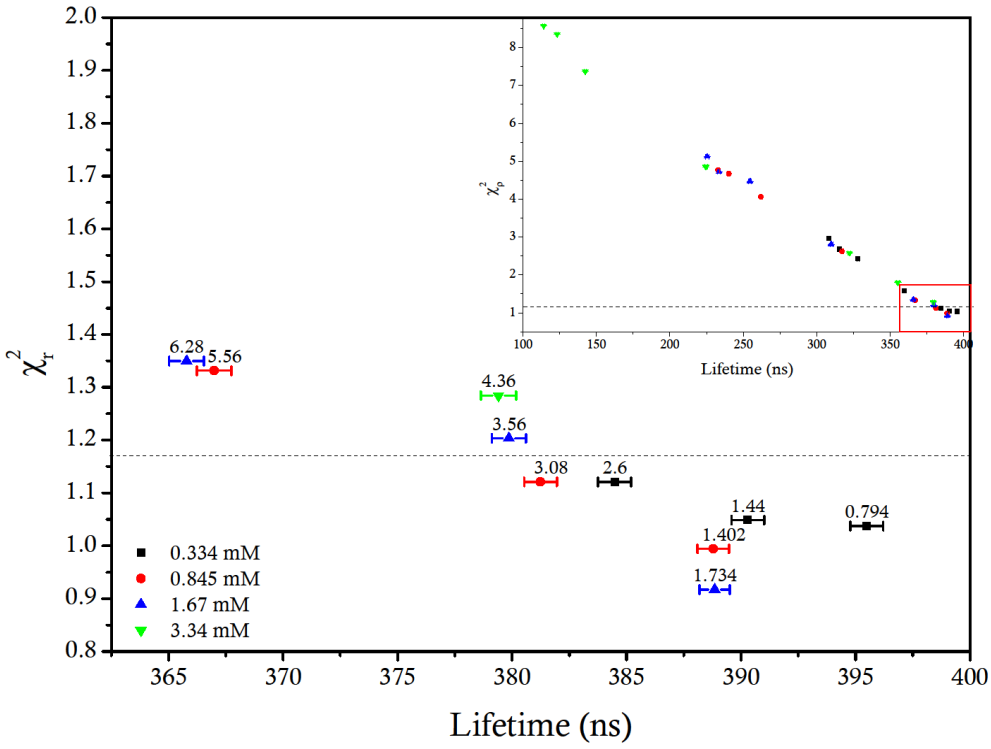


**Figure 76 – The calculated reduced chi-square of mono-exponential lifetime fitting $[Ru(bipy)_3]^{2+}$ at varying concentrations between 0.334 mM – 3.34 mM and increasing EOM gain at an excitation 780 nm. The inset graph represents the full range of lifetimes measured and the red box represents the zoom in of the full size graph. The error bars represent the standard deviation of lifetime fitting. The dashed line dictates $\chi_r^2 \leq 1.17$ and the values above the data points are the count rate percentage.**

The maximum and minimum $\chi_r^2$ at 780 nm (lifetime) was 8.5 (113 ns) and 0.9 (388 ns) at a concentration of 3.34 mM and 1.67 mM, respectively. The count rate at the maximum and minimum $\chi_r^2$ was 113% and 1.73%, respectively. The maximum count rate under the cut-off line was 3.08%. The EOM gain value is not of importance as it is described by the count rate. The maximum concentration (3.34 mM) does not reach below the cut-off limit. The number of collected photons in the decay is not affected at lower concentration, i.e. at 0.334 mM and an EOM gain of 0% and 60% the number of counts are maintained between 1.3 $x10^6$ - 1.07 $x10^6$. But at 3.34 mM between an EOM gain of 0% and 60% the number of counts drop from 1.27 $x10^6$ to 0.474 $x10^6$, respectively.

The calculated reduced chi-square from fitted data in Figure 74 is displayed against the determined lifetime in Figure 77 for the excitation wavelength of 880 nm. The maximum and minimum $\chi_r^2$ is 5.59 (238 ns) and 0.92 (394.3 ns) at a concentration of 3.34 mM and 0.845 mM and count rate of 31% and 0.256 %, respectively. The maximum count rate below the $\chi_r^2$ cut-off is 2.8%.

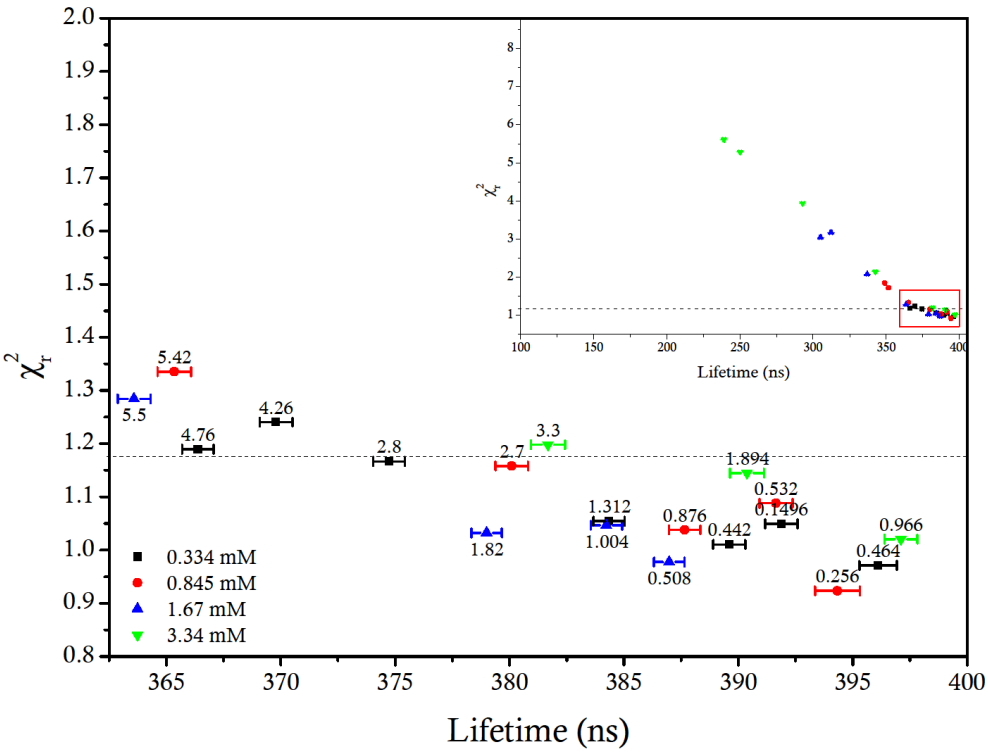


**Figure 77 – The calculated reduced chi-square of mono-exponential lifetime fitting $[Ru(bipy)_3]^{2+}$ at varying concentrations between 0.334 mM – 3.34 mM and increasing EOM gain at 880 nm excitation. The small graph represents the full range of lifetimes measured and the red box represents the zoom in of the full size graph. The error bars represent the standard deviation of lifetime fitting. The dashed line dictates $\chi_r^2 \leq 1.17$ and the values above the data points are the count rate percentage.**

The lifetime measurements below the $\chi_r^2 \leq 1.17$ cut-off for excitation of 780 nm and 880 nm are displayed in Figure 78. The number of lifetimes below the cut-off out of a possible 24 decays (4 concentrations, 6 EOM gains) for 780 nm is 6, which is only a quarter of the decays. For an excitation of 880 nm the number of decays below the cut-off is 14, half of the available decays. As these lifetimes meet the cut-off values they are determined to have minimal influence from systematic error (pile-up). Therefore the accepted mean lifetimes and standard deviations for 780 nm and 880 nm are 388.18 ±4.89 ns and 387.71 ±6.63 ns, respectively. This shows a difference of 0.1%, between the mean lifetimes.

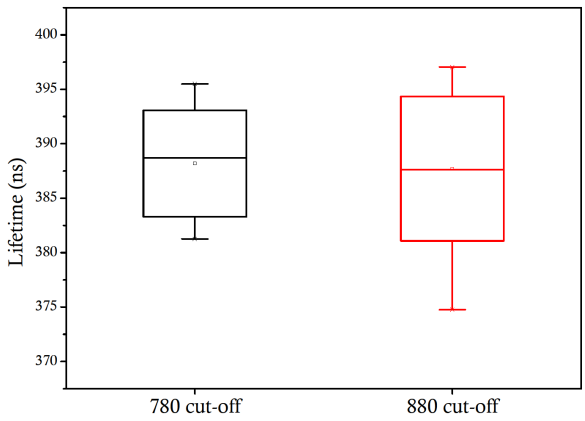


**Figure 78 – Box and whiskers plot of minimal pile-up influence over lifetime variability below the cut-off limit $\chi_r^2 \leq 1.17$ at an excitation of 780 nm (black box) and 880 nm (red box). The whiskers represent the maximum and minimum values the box size is the standard deviation, the open square is the mean.**

The increasing EOM gain has a large influence over lifetime, which can be magnified at higher $[Ru(bipy)_3]^{2+}$ concentrations. There is a negative linear relationship with lifetime at an excitation wavelength of 880 nm, but is more exaggerated at 780 nm. This observation is reinforced when observing the calculated reduced chi-square. At 780 nm excitation, only 25% of decays reach below the cut-off compared with 50% at 880 nm. Similarly, the variability in calculated reduced chi-square at 780 nm excitation is 50% greater than at 880 nm. It also affects the number of photons processed due to pile-up. At 780 nm excitation with a concentration of 3.34 mM the number of counts collected is reduced by 63.3% compared to equivalent conditions using 880 nm excitation. The major difference between 880 nm and 780 nm excitation is the energy in the wavelength. As shown in section 3.2.4, at repetition rate of 500 kHz there is a power difference between 780 and 880 nm excitation of 120 μW of power.

This data shows that higher EOM gain and therefore energy into a fluorophore creates an increased photon emission [171]. This effect is magnified with higher dye concentration as more photon will be absorbed and therefore a higher probability of emitting. This will increase the likelihood of pile-up as more photons will emit during the same excitation cycle, if the EOM gain is not adjusted to compensate.

Even though the number of decays accepted below the cut-off differs the mean lifetime at excitation wavelengths 780 nm and 880 nm is approximately 388 ns with similar standard deviations. The maximum count rate for decays below the count rate cut-off limit for both is approximately 3% for both excitation wavelengths. Compared with a count rate of 1% to acquire the same number of photons this would decrease the imaging time by a third. This decrease in imaging time would make a huge difference when scanning cellular samples reduce the possibility of photon damage.

#### 3.4.8.4 Effect of oxygen concentration of pile-up

Sample preparation, FLIM setup and decay fitting followed procedures outlined in section 3.4.8.1. Lifetime decay measurements of two $[Ru(bipy)_3]^{2+}$ solutions in deionized water at atmosphere and the other in $Na_2SO_3$ using a concentration of 0.167 mM at 37°C, are shown in Figure 79. Lifetime decays were collected for 120 sec at a collection rate of $10x10^3$ photons/sec, 3% of the excitation rate 500 kHz. The number of photons collected in atmosphere (Atm) and $Na_2SO_3$ was 992589 and 995889 photons, respectively, a difference of approximately 3000 photons. For Atm and $Na_2SO_3$ the calculated lifetimes were 298 ns and 455 ns, which is reflected by the decay gradient in Figure 79.

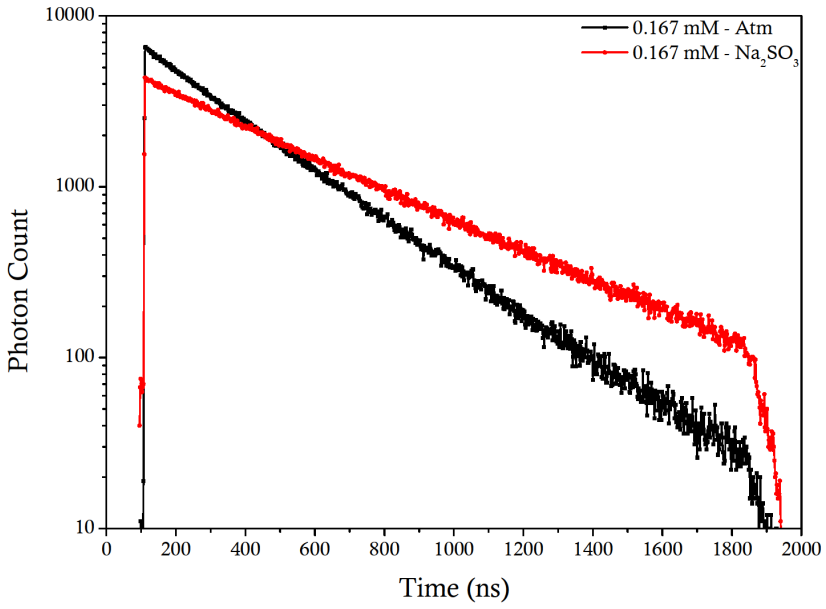


**Figure 79 – Lifetime decay of $[Ru(bipy)_3]^{2+}$ and deionised water solution at a concentration of 0.167 mM in atmosphere (Atm: black square and line) and with sodium sulfite ($Na_2SO_3$: red cicrle and line). Solutions were maintained at 37°C and approximately $1x10^6$ photons were collected in 120 sec.**

The weighted residual plots for both decays are shown in Figure 80 where the $\chi_r^2$ was 1.101 and 2.175 for Atm and $Na_2SO_3$, respectively. The discrepancy between Atm and $Na_2SO_3$ can be visually seen in the plot. The Atm is evenly distributed about the zero line, and the $Na_2SO_3$ begins evenly distributed for the first 700 ns, but then deviates from the zero line. This indicates a poor fit between modelled and experimental data, which was confirmed by the $\chi_r^2$.

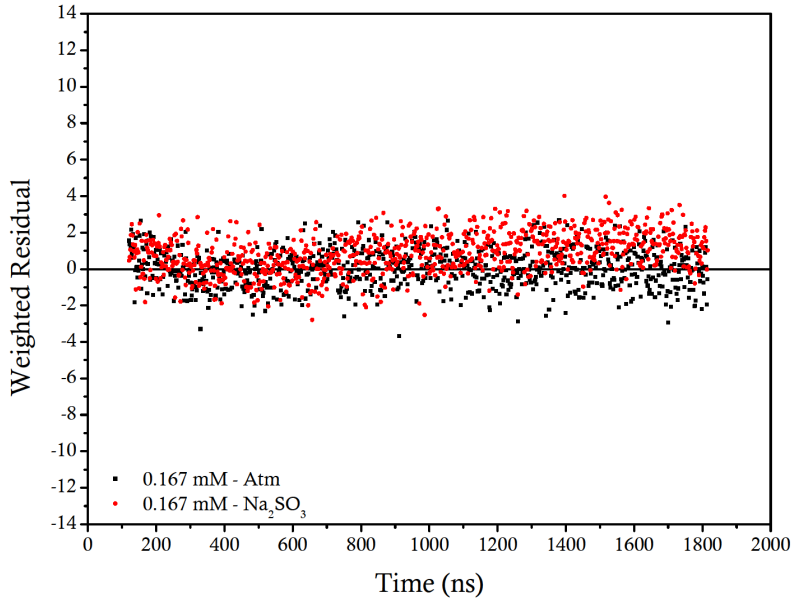


**Figure 80 – Weighted residual plot of mono-exponential fit with lifetime decay data for $[Ru(bipy)_3]^{2+}$ and deionised water solution at a concentration of 0.167 mM in atmosphere (Atm: black square) and with sodium sulfite ($Na_2SO_3$: red circle), $\chi_r^2$ is 1.101 and 2.175, respectively.**

The previous results in section 3.4.8.3 gave the impression that a faster collection of data was possible, but it now appears that this advantage has quickly disappearing. In

Figure 79, the two decays of $[Ru(bipy)_3]^{2+}$ in deionized water, are at atmospheric oxygen and in a reduced oxygen environment, $Na_2SO_3$. Both decays were recorded at 37°C and had a concentration of 0.167 mM with the same parameters ADC 1024, excitation rate 500 kHz, collection rate 3%, total collected photons $0.99x10^6$. Inspection of the calculated lifetimes shows 298 ns and 455 ns, and $\chi_r^2$ as 1.101 and 2.175, for Atm and $Na_2SO_3$, respectively. This discrepancy is also apparent in the weighted residual plots shown in Figure 80 where the Atm is evenly distributed about the zero line, but the $Na_2SO_3$ is evenly distributed above the zero line. The difference in lifetime values for Atm and $Na_2SO_3$ would be expected due to the difference in oxygen levels and therefore quencher. But under current criteria for rejection of induced pile-up the Atm decay would be accepted and the $Na_2SO_3$ would be not.

The reason for this discrepancy is pile-up and the reason behind this can be seen from applying an equation written by Coates [56] to the collected data. As it is known from section 3.4.7 pile-up occurs when more than one count appears within the same excitation cycle. Here the goal is to determine the probability of detecting a photon or count in channel *i* during one excitation cycle. The effective number of cycles for channel *i* is then:

**Eq. 35**
$$E_i = E - \sum_{j=i}^{i-1} N_j$$

where, the number of counts in time channel $i$ is $N_i$ and the total number of excitation cycles is $E$. A photon in channel $i$ cannot be detected if a photon in a previous channel $j$ has been detected $j<i$. Therefore the probability ($P_i$) of detecting a count ($i$) during each excitation cycle is,

**Eq. 36**
$$P_i = \frac{N_i}{E_i}$$

Applying the above equation Eq. 35 and Eq. 36 to the data sets for atmosphere and $Na_2SO_3$ produces identical graphs to Figure 79. However it displays the probability of detecting a second photon in later channels with time. It showed that with the same number of excitation cycles, the number of photons collected in the later part of the $Na_2SO_3$ decay has a higher likelihood of pile-up occurring, confirmed by current results. Even though the probability of pile-up occurring was extremely low (1.6%) it has been shown to be sufficient enough to induce pile-up and warrant rejection.

Coates equation also shows that the relationship between excitation rate, collection rate and the number of emitted photons play a major role in the development of pile-up, which are dependent on laser power (EOM gain) and dye concentration, as shown in these

results. The model has also identified that experimental collection rates should be matched to the longest anticipated lifetime decay. The lifetime decay of $[Ru(bipy)_3]^{2+}$ is longest with no quencher, therefore for future experiments the collection rate must be maintained at ≤ 1% of the excitation rate.

#### 3.4.8.5 Quantifying repeatability

An important assessment of a newly developed technique is the quantification of systematic error inherent within the system rather than the acquisition of data. Minimising other influences arising from pile-up or the number of photons collected per decay an unbiased assessment of the systematic error can be determined. This provides opportunity for comparison with other researchers the accuracies possible for oxygen discrimination.

A similar sample preparation, FLIM setup, and data analysis was conducted as outlined in section 3.4.8.1. EOM gain adjustment maintained a count rate ≤1% and photons were collected for 800 sec to ensure maximum dynamic range was reached; five repeated measurements were collected.

Lifetime decays of $[Ru(bipy)_3]^{2+}$ in deionized water were measured at room temperature in atmosphere. Five repeated measurements of the same sample provided a mean lifetime of 377.14 ns, a standard deviation of ±1.07 (±0.28%) and standard error of ±0.48 (±0.13%). On average the number of photons collected per decay was in the region of $1.2x10^6$ counts.

The systematic variability of the system was assessed by recording five lifetime measurements of $[Ru(bipy)_3]^{2+}$ in deionized water. Comparing results of this technique with other researchers proved difficult as very few quote the accuracy of their measurements or technique. One researcher, Sud *et al.* [279] did discuss the accuracy of their lifetime measurements based on a wide-field microscope and time-gated lifetime detection system. The lifetime variability of this FLIM system was ±2% or ±6 ns of $[Ru(bipy)_3]^{2+}$ lifetime translating to minimum detection of 8 μM oxygen concentration. The variability quoted for lifetime must be ignored as this change will be dependent on oxygen concentration and temperature. Comparing the percentage standard deviation of the FLIM systems shows the current system has an increased accuracy of up to 7 times. This highlights the advantage of using confocal TCSPC rather than wide-field time-gate. It further shows the potential for providing an increased level of discrimination between oxygen concentrations in the surrounding area.

3.4.8.6 The effect of repetition rate on systematic error

In time-gate experiments the total integration time for two gates is suggested to be optimum at 5τ [19] providing minimal error. The difference with TCSPC is that there are 1024 time channels spread over the decay. The standard deviation of the TCSPC decay is based on Poisson statistics, i.e. higher the photons per channel less the error. The optimum time range window allows the decay to complete to background noise level. This avoids incomplete decays, where the photons wrap around appearing prior to the initial decay peak masking the baseline and restricting the fitting model from determining the offset. If the suggested optimum time range were to be applied to a lifetime at 500 ns it would require 2.5 μs to complete, but the SP830 TAC has a time range limit of 2 μs (500 kHz repetition rate). Therefore in these experiments the time range is dictated by the equipment.

Using a shorter time range than optimum for a decaying fluorophore to relax induces the possibility of stroboscopic excitation affecting measurements. Stroboscopic excitation is where fluorophores electrons are re-excited before returning to the ground state, thus reducing the excitation efficiency per pulse [196]. This subtle effect can interfere with the true lifetime, whereby the excited electrons increasingly do not return to the ground state and create an exponential growth of electrons in a high energy state until equilibrium is reached. Only once this equilibrium is attained can the real lifetime be measured without a changing baseline. Even though the manual states that the limit of the TAC range is 2 μs [27] the time base can actually be adjusted to 5 μs (200 kHz repetition rate), which suggests there might be a problem with photon timing for photons at the start of the decay, but initial test revealed no such issue. In order to determine the possibility of stroboscopic excitation the repetition rates must be varied and compared. If no difference in lifetime is observed it can be assumed that the repetition rates were not fast enough to induce anomalies.

The same sample preparation, FLIM setup and data analysis was used as in section 3.4.8.1. The sample concentration used in these experiments was 0.412 mM and the environment temperature and oxygen level were at ambient and atmospheric, respectively. The laser repetition rates were varied between 1 MHz, 500 kHz, and 200 kHz with respective time ranges of 1 μs, 2 μs, and 5 μs. Collection rates and time channels were maintained at 300 sec to ensure identical photon counts and ADC 1024, respectively.

Lifetime decay of $[Ru(bipy)_3]^{2+}$ in deionized water was measured at three excitation rates 1 MHz, 500 kHz, and 200 kHz, as shown in Figure 81. The lifetimes and total decay counts are similar for repetition rates of 1 MHz, 500 kHz, and 200 kHz as 390.6 ±1%, 390.7 ±0.5%, 391.0 ±0.25% ns and 960710, 929559, 969951 counts, respectively. However,

the peak counts for repetition rates of 1 MHz, 500 kHz, and 200 kHz are different at 2845, 4977, and 12314, respectively.

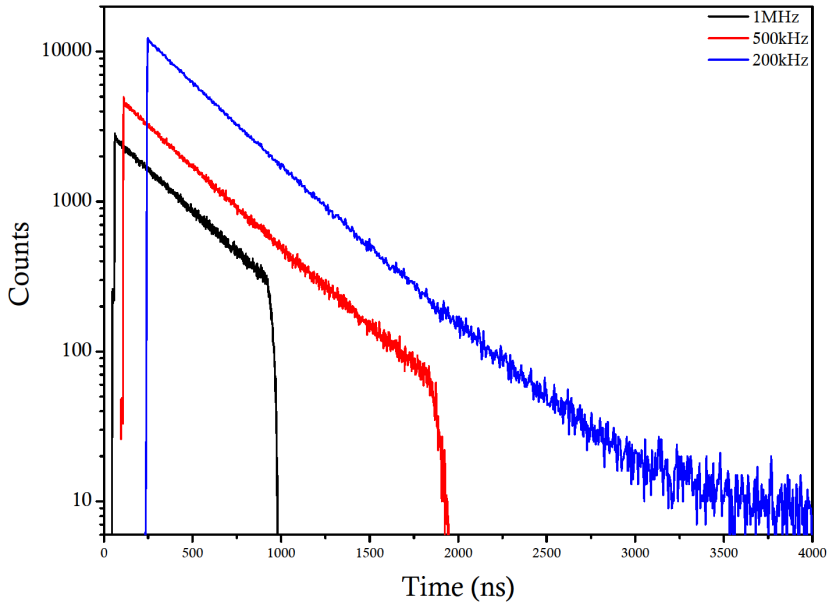


**Figure 81 – Lifetime decay of $[Ru(bipy)_3]^{2+}$ in deionized water at a concentration of 0.412 mM in atmosphere and room temperature, at three laser excitation rates 1 MHz (black), 500 kHz (red), and 200 kHz (blue) using an ADC 1024.**

The variation in excitation rate has had minimal effect on the lifetime values. Although there does appear to be a relationship between repetition rate and standard deviation. Where the repetition rate is halved so is the standard deviation. This might suggest a slight effect from stroboscopic excitation, but not enough to induce an obvious change in lifetime. The number of counts per decay is similar, but the peak counts vary vastly where the largest difference of 77% is seen between 1 MHz and 200 kHz repetition rate. This can be attributed to the number of ADC time channels, as the number of channels are maintained at 1024 for all repetition rates. At 200 kHz the time channels are wider so counts combine incrementing more rapidly. At 1 MHz there is a higher level of segregation between time channels and so counts increment at a slower rate. As the total number of counts collected at each repetition rate is the same it confirms there is just a different distribution. This shows that the different repetition rates do not induce stroboscopic excitation. It needs to be determined what is the minimum number of counts required to maintain an optimum lifetime accuracy.

### 3.4.8.7 The effect of collection time on minimum fitting error

Maintaining a minimum contribution of pile-up does not infer accurate lifetime, it merely accounts for the goodness of fit between the data and the model. It is possible to obtain an excellent chi square, but determined an inaccurate lifetime. Accordingly the greater the number of photons collected the smaller the standard deviation in the data,

reducing the experimental error for lifetime fitting. Therefore another method of quantifying a sufficient number of photons must be employed to provide confirmation that the quality of the data is adequate. This aspect is not an issue if decays are collected to reach maximum dynamic range, but that can cost time. A balance needs to be obtained that meets both a low collection time, but maintains an optimum number of photons for fitting decays with minimum lifetime error.

The same sample preparation, FLIM detection and analysis were conducted as set out in section 3.4.8.1. The effects of collection rates on laser repetition rate used excitation rates of 500 kHz, 400 kHz, and 200 kHz with respective time ranges of 2 µs, 2.5 µs, and 5 µs. Samples were measured a low oxygen level with the addition of $Na_2SO_3$ to air tight sample chambers. At each repetition rate lifetime decays were collected for 0.5, 1, 2, 4, 16, 32, 64,124 sec with triplicate repeats. Data was exported to OriginPro 8 and a one-way ANOVA of the 9 was applied to the lifetimes measured at each collection rate.

$[Ru(bipy)_3]^{2+}$ was dissolved in deionzed water to produce a concentration of 0.414 mM and maintained at 37°C in $Na_2SO_3$. The average lifetime was measured at three excitation rates 200, 400, 500 kHz with incrementing collection times as shown in Figure 82. At the lower collection time of 0.5 sec the average lifetime and standard deviation for all repetition rates was 517.8 ±47.32 ns, respectively. As the collection time increased the lifetime variability decreases i.e. at 128 sec the lifetime and deviation was 492.9 ±0.61 ns. Although a one-way ANOVA showed the mean lifetimes for all collection times were not significantly different ($p>0.8$).

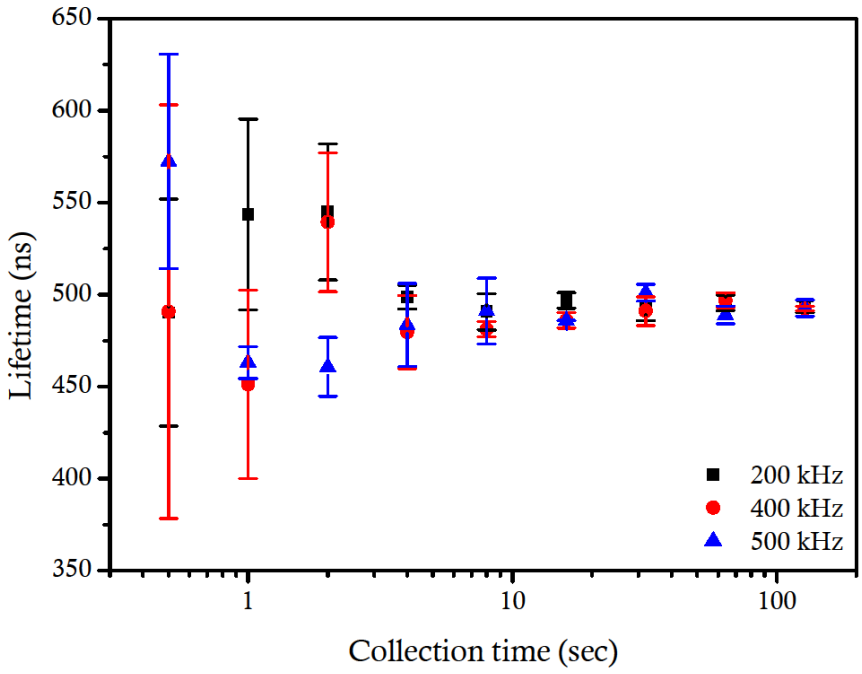


**Figure 82 – Average lifetime and standard error of varied repetition rate 200 kHz (black square), 400 kHz (red circle), 500 kHz (blue triangle) with incrementing collection times (n=3) plotted on a semi-log plot.**

The adjusted $R^2$ for each fit of the lifetime data is plotted against total decay count for each repetition rate, as shown in Figure 83. An inset graph represents a zoomed section of the Figure 83, identified by the red box. This displays the adjusted $R^2$ values greater than 0.90 for maintaining minimum influence in variability. All three repetition rate data follow a double exponential pattern, although at slightly different rates. The adjusted $R^2$ values for each repetition rate exponentially increases rapidly until reaching a plateaux. In order to maintain an adjusted $R^2$>0.9 the minimum required counts for 200, 400 and 500 kHz are 7018, 13,000 and 20,000 counts per decay, respectively.

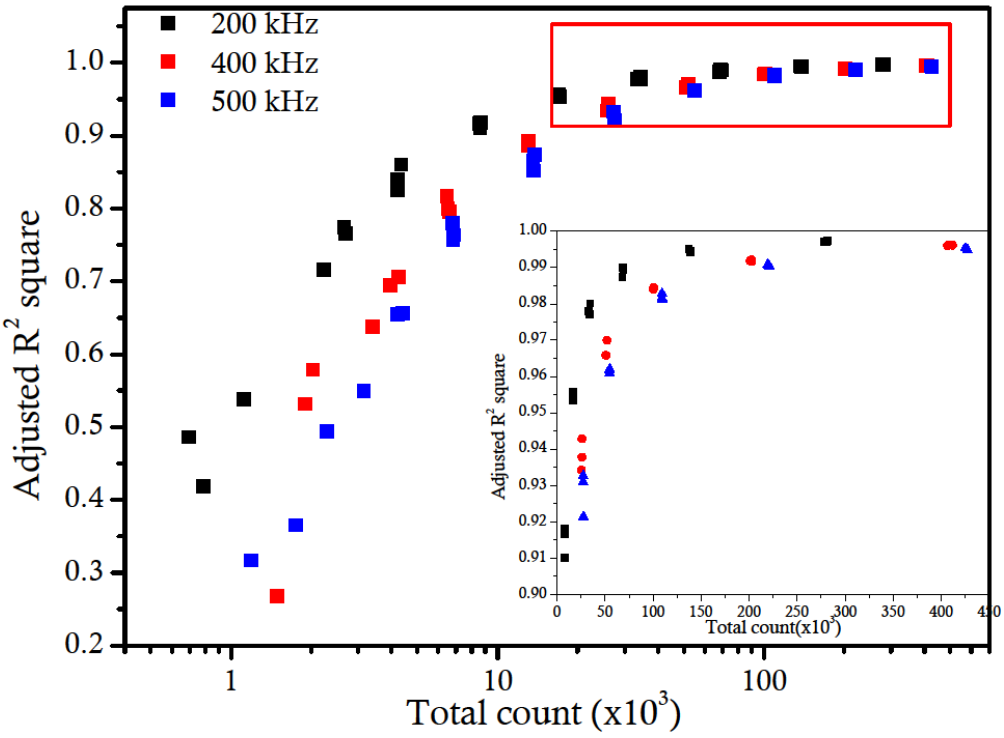


**Figure 83 – Adjusted $R^2$-sqaure of mono-exponential fitted lifetime measurements at repetition rates of 200 (black square), 400 (red circles), and 200 (blue triangle) kHz against total number of photons counted per decay. The inset graph represents a zoomed in section represented by the red box.**

The total and peak counts are displayed against collection time for the three repetition rates in Figure 84. The total and peak number of counts has a positive linear correlation with the collection time for each repetition rate. There are different gradients for each repetition rate with 200 kHz displaying an overall lower total count compared with the other rates, but a high peak count than the other rates. For a total count of 7018, 13,774 and 20,000 the required collection time must be >3.2, 4.2, and 5.7 sec per decay, respectively. Using this collection time the peak count for each repetition rate is determined as 103, 88 and 97 peak counts for repetition rates of 200, 400 and 500 kHz, respectively.

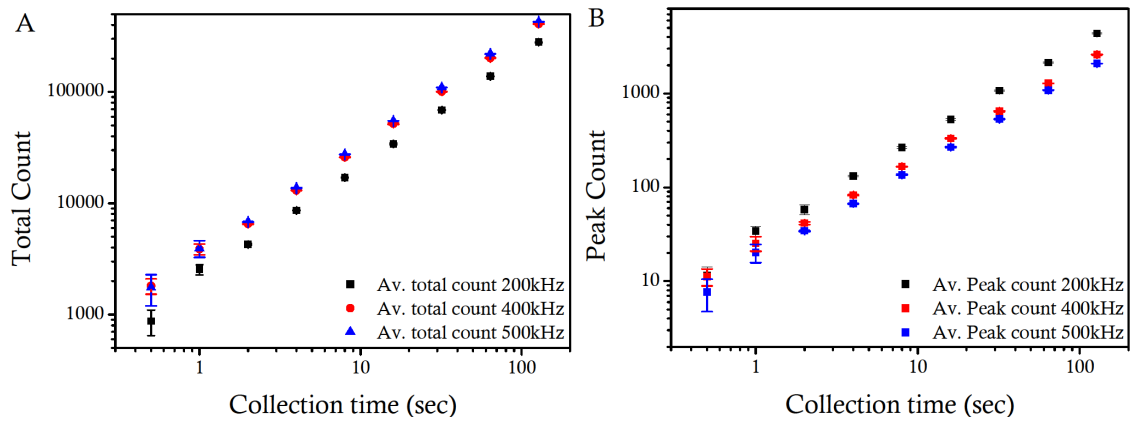


**Figure 84 – The effect on the total and peak count of a lifetime decay through the combined effects of collection time and repetition rate 200 kHz (black squares), 400 kHz (red circles), and 500 kHz (blue triangles) displayed on a log plot. A: represents the total counts and B: represents the measured peak counts.**

The mean lifetimes for all collection times and repetition rates were not statistically different, but the variation in standard deviation was between 25% and 0.02%. The collection rate was maintained at less than 1% during the experiment minimising influences from pile-up ($\chi_r^2 \leq 1.17$). The adjusted $R^2$ had been used to describe the standard deviation in the data rather than just the quality of the fit with the data. To ensure a standard deviation in the lifetime is maintained at <1.5%, the adjusted $R^2$ value must be >0.90. For repetition rates of 200, 400, and 500 kHz the collection time, total count and peak count must be greater than 3.2, 4.2 and 5.7 sec, and 7018, 13,774, and 20,000 total counts and 103, 88 and 97 peak counts, respectively. Even though it has been possible to collect decays at longer repetition rates future experiments will operate at 500 kHz as physically the TAC should not be able to operate efficiently at these longer repetition rates [27].

### 3.4.9 Conclusion

The TCSPC module converts the acquired photon emission into digital counts and assigns them to time channels. Mono-exponential fits of these decaying histograms provide the lifetime of $[Ru(bipy)_3]^{2+}$ in solution. The decays reflect a Poissonian distribution and the standard deviation relies on Poisson statistics to describe the probability of photon emission. The optimised operation of the TCSPC module with $[Ru(bipy)_3]^{2+}$ has verified parameters for future experiments. The IRF does not need to be deconvolved from these lifetime decays as it only contributes to $8x10^{-6}$% of the decay. The relationship between background counts and time is linear and can be used to confirm the correct offset revealing decays affected by pile-up. The systematic variability of measuring the lifetime repeatability is less than 0.3%. Visual inspection of the weighted-residual plot does not always conclude the occurrence of pile-up and so it should be used in conjunction with the $\chi_r^2$. A cut-off value of $\chi_r^2 \leq 1.17$ is to used to accept mono-exponential fits of $[Ru(bipy)_3]^{2+}$ decays,

provided data points exceed 200. Collection rates must be maintained <1% of the excitation rate in the study (<$5x10^3$ photons/sec) so as to minimise the effects of pile-up. Stroboscopic excitation does not affect the accuracy of the lifetime if an ample number of counts are collected. The adjusted $R^2$ is used to confirm a sufficient number of counts have been collected and must be maintained at >0.9 and the minimum collection time per decay must be >5.7 sec for a repetition rate of 500 kHz.

## 3.5 Summary

- Theoretically at 500 kHz fluorophore saturation should not induce photobleaching at maximum power.
- Laser alignment should be checked when traversing through the excitation wavelengths to account for the wavelength dependent laser pointing stability drift.
- To avoid geometric distortions at low laser repetition rates scan speed or image format size should be reduced to increase dwell time/pixel and therefore counts.
- Collected data must produce $\chi_r^2 \leq 1.17$ and adjusted $R^2$ >0.9 otherwise it should be rejected. Also total and peak counts for 500 kHz should be >20,000 and 97 counts, respectively.
- In order to minimse pile-up collection rates should be maintained <1% of the repetition rate (at 500kHz = <5000 photons/sec).
- Using full dynamic range, whilst maintained at maximum collection rate of <1% repetition rate, the systematic lifetime variability measurement was < 0.3%.

# 4 Characterisation of Ruthenium(II)

## 4.1 Introduction

The previous chapter discussed the optimised procedure for detecting accurate lifetime and the parameter settings and limits that should be considered and used. The following chapter will examine the possible environmental fluctuations that $[Ru(bipy)_3]^{2+}$ could be exposed to and determine the implications to the detected lifetime. As discussed previously the dye and detection will be applied to a cell seeded agarose construct submerged in cell culture media for the detection of oxygen concentration surrounding the cell. Therefore to determine the effects on lifetime this chapter will be separated into two sections focusing on:

- Environmental factors – interaction of $[Ru(bipy)_3]^{2+}$ with its surroundings
- Oxygen concentration – establishing a relationship between lifetime and oxygen

## 4.2 Environmental considerations

### 4.2.1 Background

#### 4.2.1.1 Effect of $[Ru(bipy)_3]^{2+}$ concentrations on lifetime

As the dye diffuses through a construct it could be assumed that the spatial localisation in a static system would ultimately become homogenously distributed. But with the addition of cells a more complex diffusional path would be created. Also the effect of using an agarose construct could affect the diffusion coefficient of $[Ru(bipy)_3]^{2+}$. This effect, to the diffusion coefficient, is seen with larger molecules like dextran [242], but the extent of the influence is pore size dependent reliant on the manufacturing process of the agarose gel [242]. In the case of intensity, measurements are concentration dependent and so influenced by any variation of dye presence [171]. The advantage of lifetime

measurement is the independence between concentration and lifetime as it is a measure of the rate processes. However, it is still necessary to confirm that the lifetime measurements are not affected by the concentration of the fluorophore. A set of concentrations shall be tested for two-photon (TP) emission spectra to confirm it produces the same results as for a continuous intensity measurement. This will identify the relationship between concentration and intensity. Finally lifetime measurements will be determined to confirm that concentration does not influence lifetime and investigate any systematic error in the TP confocal FLIM system.

#### 4.2.1.2 Effects of temperature on lifetime

It has been shown that oxygen solubility in solution is temperature dependent [25] and as the oxygen concentration changes it would be expected to affect the decay. However, the $[Ru(bipy)_3]^{2+}$ complex also displays temperature sensitivity to its environment. Van Houten & Watt [300] showed a relationship between temperature and $[Ru(bipy)_3]^{2+}$ in deoxygenated deionised water. These data confirmed that it was the temperature sensitivity of the dye not the response to oxygen that influenced the change in lifetime. Since then many studies have investigated the temperature dependence of the dye, using it as a long lifetime laboratory standard, by varying the oxygen concentration and temperature [212]. It has also been suggested by Harrigan *et al.* [113] that it could be used as a cryogenic temperature sensor, but more recently it has been embedded in a film and used to acquire three-dimensional thermal images using a two-photon microscope [150]. Temperature affects the $\tau_0$ of $[Ru(bipy)_3]^{2+}$, therefore any lifetime relationship established with oxygen should to be conducted at the experimental temperature, as the Stern-Volmer constant will be temperature dependent. A range of temperatures will be tested to confirm that the collated lifetime results are in keeping with those determined at other research facilities and to assess the suitability of the temperature controlled environment.

#### 4.2.1.3 Effects of pH on lifetime

Previous studies have shown changes to oxygen partial pressures induce changes in the pH environment of chondrocytes [210]. It is therefore vital to confirm that pH levels do not induce changes in lifetime measurements in the absence of cells. The physiological range of pH in the body is vast from pH 2 in gastric juice to > pH 8 in the small intestine. However when considering the cellular environment variability it is restrictive [160], i.e. in blood the normal pH range is between 7.35 and 7.45 and in lysosomes it can be between pH 4.5-5.5. The cytoplasm of cells is approximately between pH 7 - 7.3, whereas extra-cellular concentration in cartilage can range from pH 6.6 - 7.1 [93, 296] and in the synovial

fluid up to pH 7.38 [141]. In order to cover a suitable physiological range for cartilage and the prospect of using this technique for other cell types, $[Ru(bipy)_3]^{2+}$ will be dissolved in phosphate buffers varying between pH 5 - 7.5.

#### 4.2.1.4 Effect of cell culture media and serum on lifetime

Chondrocytes, like other cell types, require nutrients and oxygen for survival. Oxygen is delivered via the surrounding environment, but for an *in-vitro* system cell culture media is required that provides key nutrients and growth factors, and tends to be cell-type specific. The nutritional media contains a wide variety of inorganic salts, vitamins, amino-acids, sugars, proteins and pH buffers (see Appendix D), to provide optimal growth conditions. Figure 85 shows the excitation and emission spectra of some of these components of the culture media.

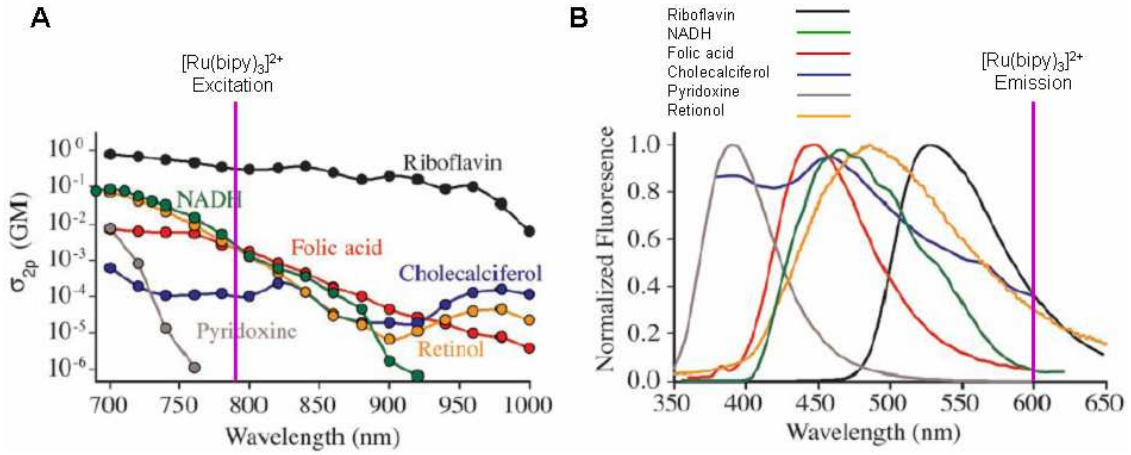


**Figure 85 – Two photon cross-section ($\sigma_{2P}$) of a set of biological molecules and the excitation and emission peaks of $[Ru(bipy)_3]^{2+}$. A: TP absorption cross-section ($\sigma_{2P}$) of intrinsic intracellular fluorophores (1 GM=1x10$^{-50}$) all measured in saline solutions. B: Emission spectra of the intrinsic fluorophores shown on the left. Adapted from Zipfel *et al.* [329].**

The spectra in Figure 85 demonstrate that the possible excitation wavelength for media components are not straight forward Gaussian peaks as generally seen for SP excitation. Instead TP excitation spectra are relatively broad, which means that the likelihood of exciting an endogenous fluorophore associated with these media components are relatively high. However, the emission spectra are focused more towards the UV range (350 - 450 nm) whilst $[Ru(bipy)_3]^{2+}$ peaks at approximately 600 nm. Thus appropriate filters can be used to exclude returning emission from media component, but this is not possible with lifetime, unless there are multiple detectors. It is known that the lifetimes of endogenous fluorophores tend to be very short, in the order 5 ns [236]. This makes it possible to remove their effect by analysing the decays after completion. For example riboflavin has a $\tau_0$ of 4.2 ns in solution [172]. Nevertheless it is necessary to determine the

influences these autofluorescent components could have on the detection of $[Ru(bipy)_3]^{2+}$ lifetime.

### 4.2.2 Materials & Methods

#### 4.2.2.1 Chemical materials

A stock solution of the oxygen sensitive dye Tris(2,2′-bipyridyl)ruthenium(II) chloride hexahydrate, $[Ru(bipy)_3]^{+2}$ (224758, Sigma-Aldrich, UK) was prepared with de-ionized water (13.34 mM). Prior to experimentation the stock solution was pre-filtered through a 0.2 μm Supatop syringe filter cap (ALG422A, Anachem Instruments Ltd., UK). Standard DMEM (D6429) was supplemented with 3.8 g/l HEPES (H0887), 80.6 U/ml penicillin and 80.6 mg/l streptomycin (P4333), 0.12 g/l L-ascorbic acid (A0278), 1% L-glutamine (G7513), and 16% (v/v) fetal bovine serum (FBS) (F7524) (Sigma-Aldrich, UK). Phosphate buffer solutions at varying pH values were made from a mixture of liquid potassium phosphate dibasic solution ($K_2HPO4$, 1 M) (P8584, Sigma-Aldrich, UK), and liquid potassium phosphate monobasic solution ($KH_2PO_4$, 1 M) (P8709, Sigma-Aldrich, UK).

#### 4.2.2.2 TP Confocal TCSPC optimised parameter

All TP confocal FLIM measurements were run at an excitation of 780 nm and repetition rate of 500 kHz. The EOM gain was adjusted to ensure collecting rates were maintained at <1% of the repetition rate (5000 photons/sec) and emission mirrors were set to 600±50 nm. Samples were transferred to coverslips (no. 1.5, 22x32 mm) (Cat. No. 631-0134, VWR Ltd., UK) and mounted on to x63 (NA 1.4) oil immersion objective lens (506192, HCX PL APO, Leica Microsystems Ltd., GmbH). Equipment parameters were set to ADC 1024, time range 2 μs, fully open pinhole (600 μm), and image format 256x256. Single lifetime decays were converted from '.std' to '.asc' files using SPCM software and transferred to OriginPro8 (SR0, OriginLab Corportation, USA). Any mono-exponential lifetime decay fits with a $\chi_r^2$ >1.17 or an adjusted $R^2$<0.90 were rejected. All experiments followed the same procedure unless otherwise stated.

#### 4.2.2.3 Emission spectra and intensity measurements

Four concentrations of $[Ru(bipy)_3]^{+2}$ ranging from 0.208 - 3.34 mM in de-ionized water were prepared from stock solutions and maintain in atmosphere. The solutions were transferred to air tight sample chambers and mounted into a heating plate on the microscope stage, set to 37°C; the stage was enclosed with an environmental chamber set

to 35°C. For recording the emission spectra, the PMT was set to 11 nm and a series of 19 images were recorded incrementing between 507 nm to 722 nm; recorded with 2 line averages and 3 frame averages. A stack profile with a ROI of the series was taken and exported to Origin. The intensity measurements involved drawing a ROI over the image and recording the mean intensity for the full PMT range 507-722 nm for each concentration at a TPE of 780 nm; measurements were repeated three times and averaged.

#### 4.2.2.4 Lifetime concentration dependence

Doubling dye concentrations, between 0.104-3.34 mM, were prepared with $[Ru(bipy)_3]^{+2}$ in de-ionized water. A glass bottomed 12 well dish (P12G-1.5-10-F, MatTek Corportation, MA, USA) was filled with six 1 ml aliquots of each concentration. The dish was mounted on the microscope stage and maintained in atmosphere at room temperature (25°C) to remove the possibility of inducing temperature gradients across well dish. Lifetime decays were collected for 150 sec, in replicates of three, averaged and plotted on a semi-log graph.

#### 4.2.2.5 Temperature variation

Pre-calibration of the heating plate was completed prior to experiments, using digital hand-held T-type thermocouple temperature sensor (accuracy ± 0.2°C) (311-1658, Digitron, RS components, UK). A single chamber, normally used for airtight measurements, was filled with a 0.412 mM solution of $[Ru(bipy)_3]^{+2}$ in deionized water. Direct temperature measurements of the solution were performed using the handheld digital thermocouple. A T-type thermocouple was positioned at the centre of the coverslip inside the chamber. The thermocouple was sealed into position using 12 sections of parafilm, restricting sample solution evaporation. Base heating was maintained via an environmental chamber to provide a controlled ambient temperature of 35ºC, and the stage mounted heating plate (14-002-08, Intracel Ltd., UK) was adjusted to provide a finer temperature control of 32 to 39ºC with temperature increments of 1-2ºC. Temperatures were set and left to stabilise for 40 mins between increments and lifetime decays were collected for 400 sec. The temperatures were noted at the start and completion of each lifetime measurements, to account for possible drift during the experiment.

#### 4.2.2.6 Susceptibility of pH concentration on lifetime

Pre-prepared solutions of phosphate buffer (50 mM) at pH 9 ($K_2HPO_4$) and pH 4 ($KH_2PO_4$) were combined to create six 1 ml aliquots with pH ranging between pH 5 - 7.5 with pH 0.5 increments. The final pH concentrations were confirmed using a 3 mm

specialist pH meter (Orion 3-Star Plus Benchtop, ThermoScientific, MA, USA), with an accuracy of ±0.002 pH. The stock solution of $[Ru(bipy)_3]^{+2}$ was combined with the desired pH range to produce a final working concentrations of 0.412 mM. Each concentration was transferred into the wells of a glass bottomed 12 multi-well dish (P12G-1.5-10-F, MatTek Corportation, MA, USA) and mounted on the microscope stage. Measurements were performed at room temp (25°C) and the decay was collected for 150 sec; five replicates were measured for each pH concentration.

#### 4.2.2.7 Media autofluorescence

Five samples were prepared: FBS, water+16% FBS (v/v), standard DMEM, standard DMEM+HEPES+l-ascorbic acid, and DMEM+16%FBS; DMEM with all chemical components required for cell culture media as stated in section 4.2.2.1. To enable a comparison, stock solutions of $[Ru(bipy)_3]^{2+}$ was mixed with DMEM+16%FBS (media) to provide a concentration of 0.412 mM. Autofluorescent measurements used a laser repetition rate of 8 MHz, time range was 125 ns, each decay was collected for 120 sec. For the comparison between autofluorescence (DMEM+16%FBS) and $[Ru(bipy)_3]^{2+}$+ media the laser repetition rate was dropped to 500 kHz, time range 2μs, and collection for 800 sec or until dynamic range was reached.

#### 4.2.2.8 Fetal bovine serum (FBS) concentrations

Stock solution of $[Ru(bipy)_3]^{2+}$ was diluted in deionized water and FBS to produce nine FBS concentrations, between 0-40% and final $[Ru(bipy)_3]^{2+}$ concentration of 0.412 mM; solutions were mixed by inversion before pipetting. For intensity measurements 200 μl aliquots of each concentration were transferred to a 96 well plate (CLS3790, Costar, Corning), in replicates of 5, and excited using a fluorescence fluorimeter (Galaxy, BMG LABTECH GmbH, Germany). The excitation and emission filters were set to, 485 nm and 610±10 nm, respectively. The fluorimeter uses a xenon flash lamp with 50 excitation cycles and a gain adjustment of 48.

Time-resolved measurements and emission wavelength spectrum were completed on the TP confocal FLIM system. The multiple replicates used for the intensity measurements were recombined and transferred to single wells of a glass-bottomed 12 well dish (P12G-1.5-10-F, MatTek Corportation, MA, USA) and mounted on the microscope stage. Five replicate time-resolved single lifetime decays were collected for 100 secs at 500 kHz and converted to ASCII files before importing to Origin; single exponential decays were fitted between 200 and 1500 ns for each file. The emission spectrum of each dilution was measured between 500–750 nm in 5 nm increments. Images at each wavelength were

captured with 2 line and frame scans and analysed using the Leica stack profiling tool to produce the emission spectrum, which was then exported to Origin. All measurements were performed at room temperature.

### 4.2.3 Results

#### 4.2.3.1 The TPE emission peak for $[Ru(bipy)_3]^{+2}$ replicates that of SPE

The emission intensity from two-photon excitation of $[Ru(bipy)_3]^{2+}$, dissolved in water at 37°C, at varying concentrations is shown Figure 86. At a concentration of 0.208 mM the measured intensity at each point was too low to produce an emission spectrum and has not been included. As the concentration of the dye increases the magnitude of the emission intensity peaks also increases. The emission peak profiles were slightly asymmetric and so an asymmetric double sigmodal model was used to derive the central peak and FWHM of each concentration. The mean centre peak and standard deviation for all four concentrations was 608.8 ±0.11 nm (±0.02%). The FWHM and standard deviation for all four concentrations was 72.1 ±0.78nm (±1.1%); (adjusted $R^2$ >0.99). Compared against the SP emission spectra in chapter 2 at an excitation wavelength of 468 nm the $[Ru(bipy)_3]^{2+}$ emission peak has red-shifted by 4 nm (0.6%) and the FWHM has increased by 28.62 nm (40%). This spectral broadening could arise from higher energy level absorption combined with thermal changes affecting radiative pathways as in seen in laser material [204].

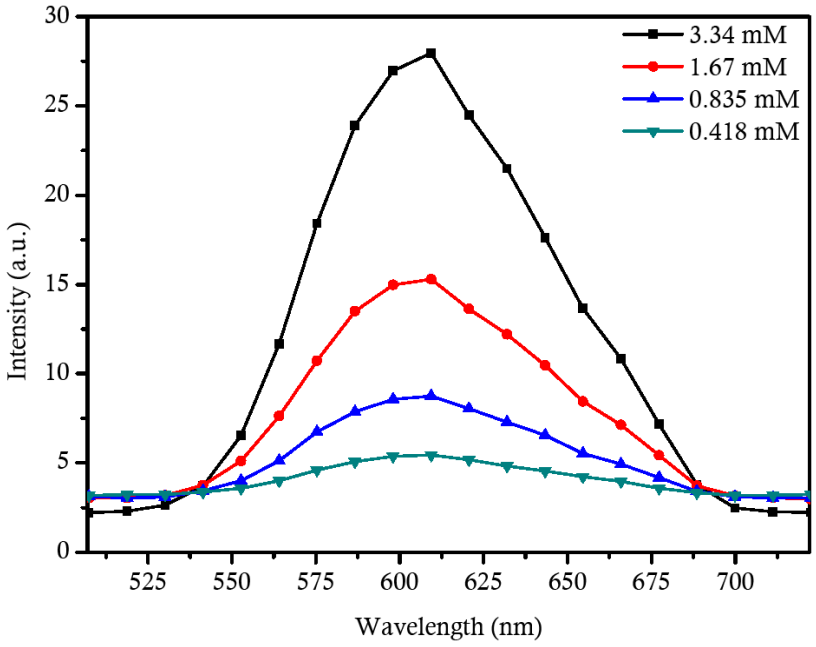


**Figure 86 – Emission spectra with TP excitation at varying concentrations of $[Ru(bipy)_3]^{2+}$. Four concentrations of $[Ru(bipy)_3]^{2+}$ dissolved in water at 3.34 mM (black squares), 1.67 mM (red circle), 0.845 (blue up pointing triangle), and 0.418 mM (green down pointing triangle) were excited at 780 nm TPE and intensity emission spectra captured between 507 nm and 722 nm.**

### 4.2.3.2 Intensity has a linear relationship with $[Ru(bipy)_3]^{+2}$ concentration

TP intensity measurements of incrementing concentrations of $[Ru(bipy)_3]^{2+}$ dissolved in water at 37°C and maintained in atmosphere, are shown in Figure 87. A linear fit was performed on the data points and a positive linear correlation (adjusted $R^2$ >0.99) was established between intensity and $[Ru(bipy)_3]^{+2}$ concentration.

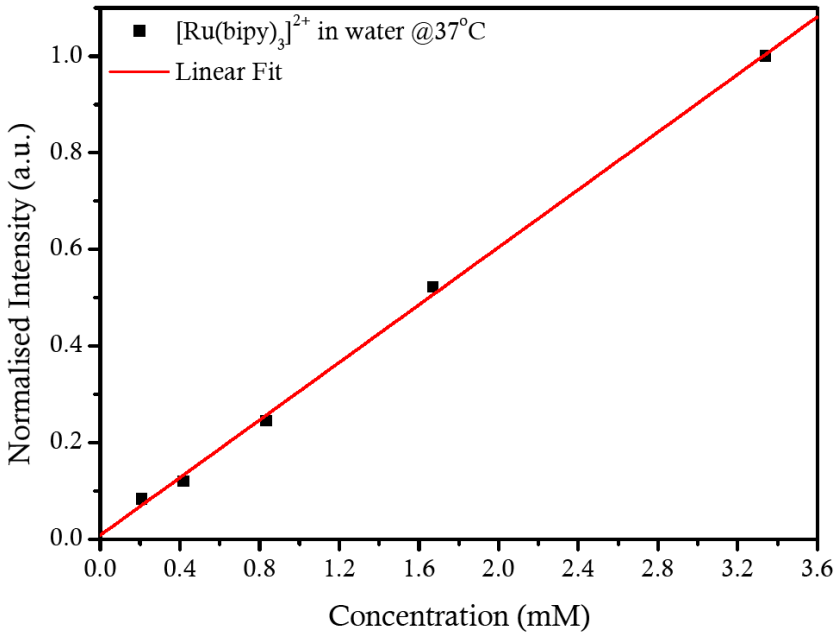


**Figure 87 – The effect of incrementing dye concentration on emission intensity. Increasing concentrations of $[Ru(bipy)_3]^{+2}$ dissolved in water at 37°C shows a positive linear relationship with increasing fluorescence intensity, adjusted $R^2$>0.99.**

### 4.2.3.3 Lifetime is unaffected by $[Ru(bipy)_3]^{+2}$ concentration

Lifetime measurements of increasing concentrations 0.104 mM - 3.34 mM, at 25°C in atmosphere of $[Ru(bipy)_3]^{+2}$ in deionized water, showed no correlation with lifetime, as shown in Figure 88. Sud *et al.* [279] measured lifetimes of $[Ru(bipy)_3]^{+2}$ at 25°C in phosphate buffered saline (PBS) over a varying dye concentration between 0.67 mM - 6.67 mM using a wide-field time-gate microscope. A comparison of the average measured lifetime for the current system, TP confocal TCSPC, against a wide-field time-gate [279] shows a mean lifetime and standard deviation of 375.45 ±1.36 ns (0.36%) and 363 ±8.9 ns (2.45%), respectively.

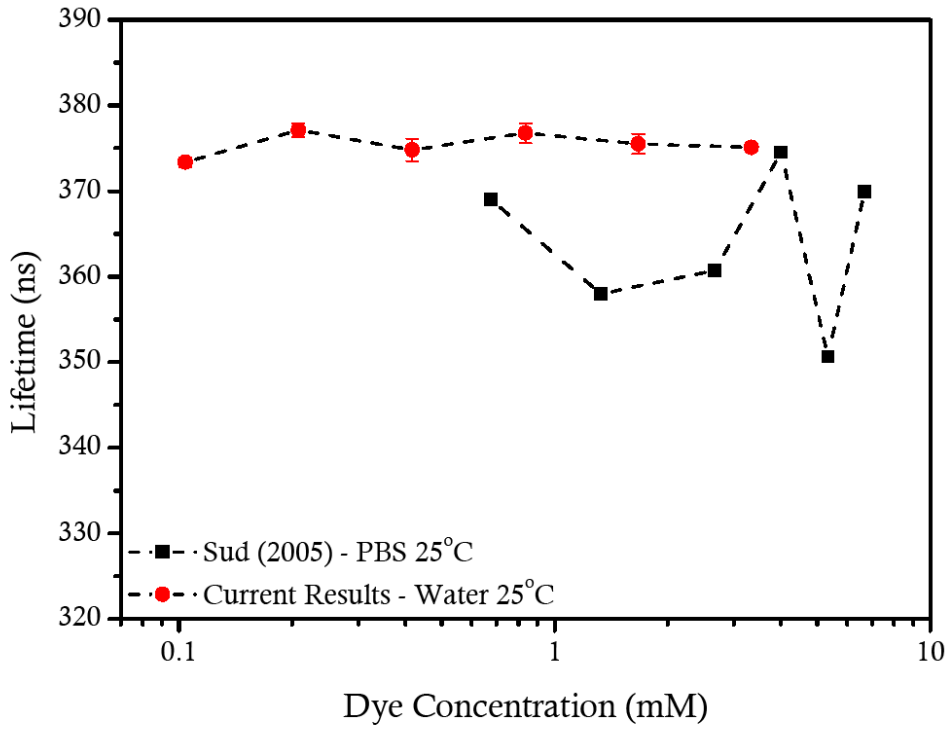


**Figure 88 –The lifetime of $[Ru(bipy)_3]^{2+}$ in water has been measured at varying dye concentration and plotted on a semi-log graph. Incrementing dye concentration measured using the current system TP confocal TCSPC (red circles) compared with a wide-field time-gated system (black squares), used by Sud[279], at a temperature of 25°C. Each point represents the mean and standard deviation of 3 replicates.**

#### 4.2.3.4 $[Ru(bipy)_3]^{+2}$ shows temperature dependence

Figure 89 provides an example of the response of $[Ru(bipy)_3]^{+2}$ to change in temperature. A shift in lifetime gradient is clearly seen in the inset of Figure 89. The measured lifetimes for the temperatures of 32, 33, 34, 35, 37, and 39°C are 343, 336, 332, 328, 319, and 311 ns, respectively. The standard deviation for the fitting of each lifetime is <0.2%. There is also a statistically significant negative correlation ($p<0.05$) between the temperature and the total number of counts collected; an increase in temperature reduces the number of counts collected.

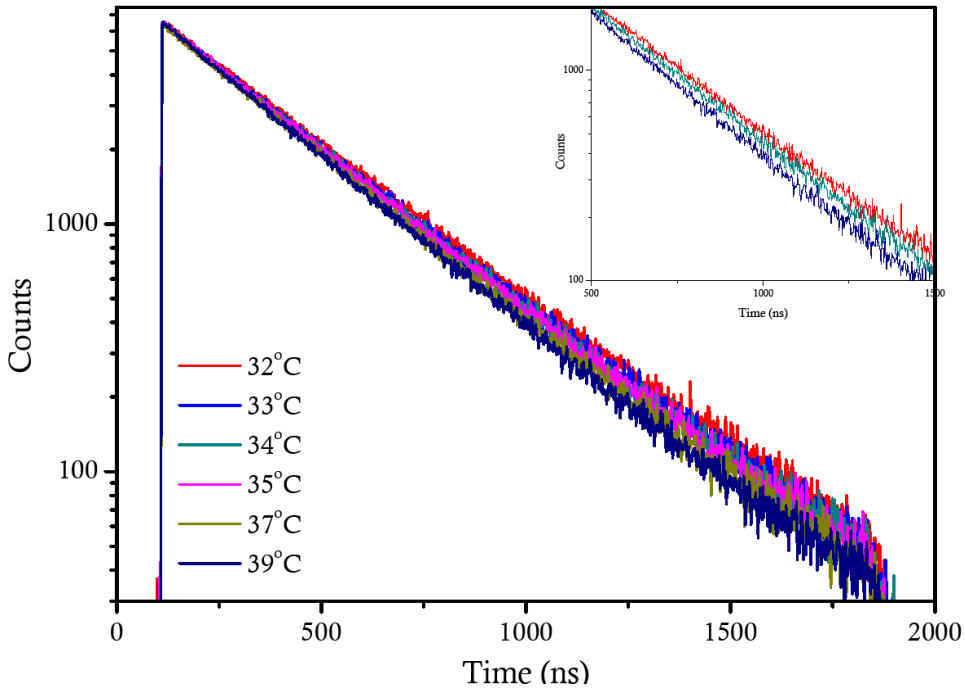


**Figure 89 – Semi-log plot showing decay of photon counts with time and the effect induced by temperature. Inset: represents the central section of the decay between 500-1500 sec displaying the shift in gradient when $[Ru(bipy)_3]^{+2}$ is exposed to 32°C (red line), 34°C (green line), and 39°C (dark blue line).**

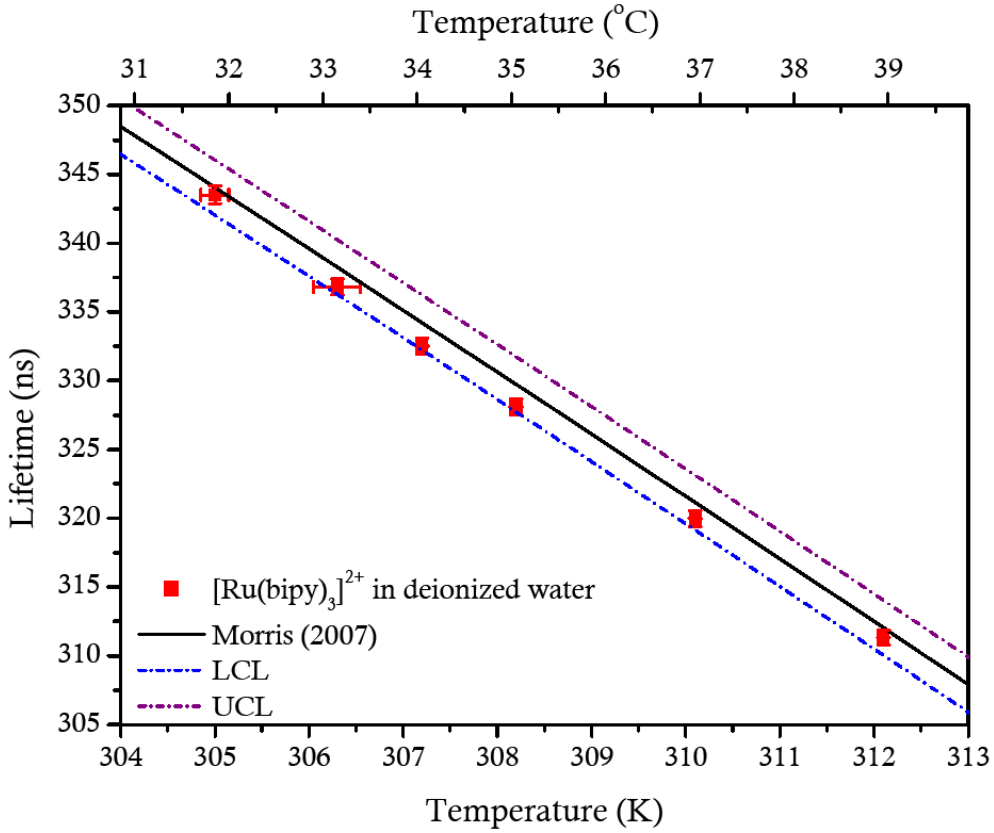


**Figure 90 – Response of $[Ru(bipy)_3]^{2+}$ in deionized water to incremental changes in temperature. Lifetime measurements (red squares) are shown with error bars in x-axis representing temperature drift and error bars y-axis representing standard deviation of fit. Measured data compared with Morris [212] (black line) shown with upper (UCL – purple dot dash line) and lower confidence limits (LCL – blue dot dash line).**

The lifetime decays shown in Figure 89 have been plotted against the measured temperature, as shown in Figure 90. The standard deviation in lifetime and temperature

come from the five repeated measurements and variation during collection time, respectively. The upper and lower confidence limits of the Morris [212] data agree with the measured results. Initially a linear relationship appears to exist between $[Ru(bipy)_3]^2$ and temperature, but over a larger temperature range the data from Morris [212] shows that a binomial models fits Morris's data over large temperature ranges.

#### 4.2.3.5 No correlation between $[Ru(bipy)_3]^{+2}$ lifetime and pH

The stock solution of $[Ru(bipy)_3]^{2+}$ was dissolved in phosphate buffer between pH 5 - 7.5 to produce a final $[Ru(bipy)_3]^{2+}$ concentration of 0.412 mM. Replicate lifetime measurements (n=5) at room temperature were taken of each pH concentration as shown in Figure 91. There was no correlation (p=0.8) between lifetime and pH concentration between 5 and 7.5 pH. The mean and standard deviation of the measured lifetimes were calculated as 388.4 ±0.76 ns (0.19%), respectively.

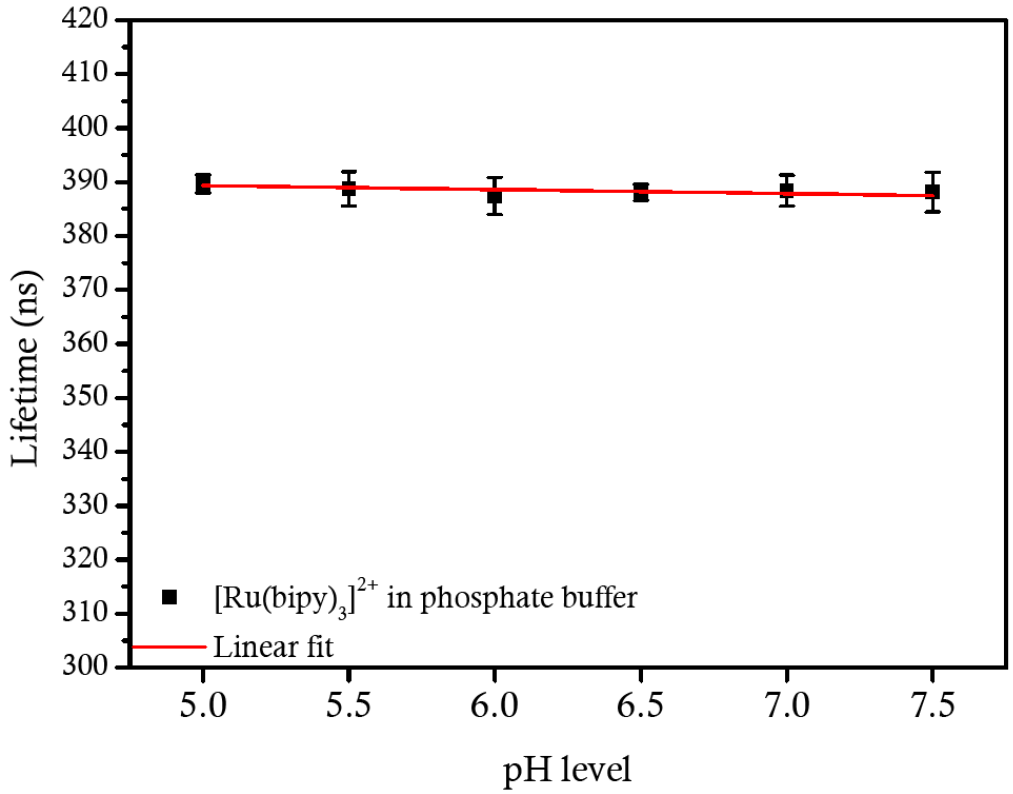


**Figure 91 – Measured lifetime of $[Ru(bipy)_3]^{+2}$ in phosphate buffer with incrementing concentration of pH. $[Ru(bipy)_3]^{+2}$ dissolved in varying concentrations of phosphate buffer between 5-7.5 pH at room temperature with a linear fit.**

#### 4.2.3.6 Cell culture media exhibits autofluorescent components

Autofluorescence decays arising from cell culture media are shown in Figure 92. All five samples exhibit complex multi-exponential decay profiles and were fitted with tri-exponential decays. For comparison purposes the mean lifetimes ($\tau_m$) for water+16%FBS,

FBS only, DMEM all, DMEM H&A, DMEM only, were 2.7 ns, 2.5 ns, 3.18 ns, 2.9 ns, and 3.19 ns, respectively. The full exponential details are listed in Table 14. There is no difference in the mean lifetime of sample 5 and 3, which is also confirmed by looking at the individual components. But for sample 4 the amplitude percentage of all the components differs from samples 3 and 5 with a more equal distribution for component $a_1$ and $a_2$. The lifetime of component 3 is longer, but component 2 is slightly shorter. The mean lifetimes of the FBS samples are shorter than the DMEM samples, but when observing the breakdown of components the percentage of the first and second have risen and decreased, respectively.

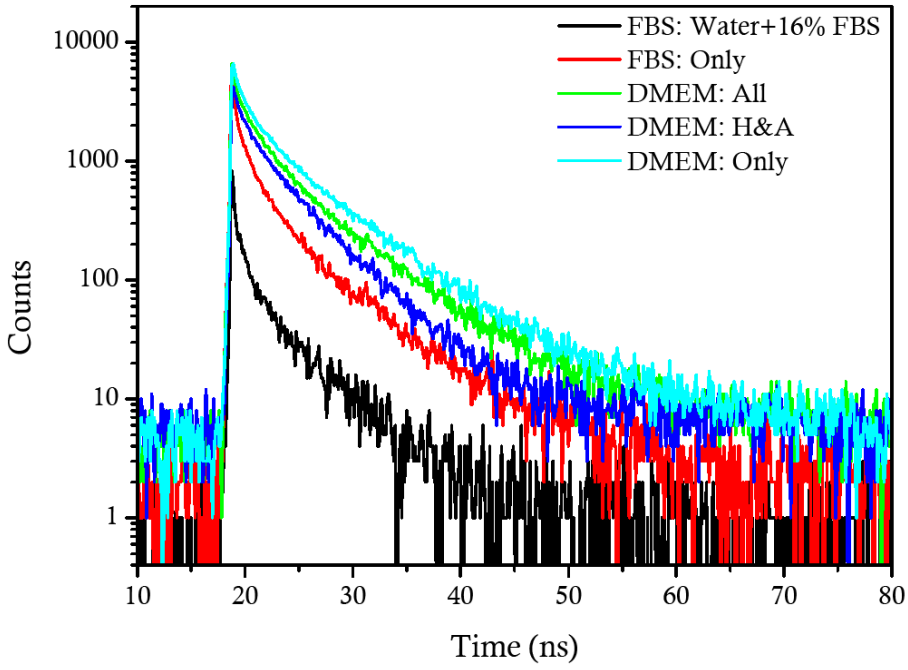


**Figure 92 – Autofluorescent lifetime decays of DMEM and the components that make up cell culture media excited with a 8MHz repetition rate at 780 nm. Abbreviation: FBS – Fetal Bovine Serum, DMEM – Dulbecco's Modified Eagle Medium, H&A – HEPES and L-Ascorbic acid.**

**Table 14 – Fitted tri-exponential decay components of above sample.**

| Samples | Components | | | | | |
|---|---|---|---|---|---|---|
| | $\tau_1$ (ps) | $a_1$ (%) | $\tau_2$ (ps) | $a_2$ (%) | $\tau_3$ (ps) | $a_3$ (%) |
| **1) water+16%FBS** | **1013** | **71** | **4662** | **28** | **17764** | **0.8** |
| **2) FBS only** | **1230** | **69** | **4713** | **29** | **12881** | **2** |
| **3) DMEM all** | **1457** | **59** | **5332** | **38** | **13317** | **2.2** |
| **4) DMEM H&A** | **1175** | **49** | **4515** | **50** | **21286** | **0.3** |
| **5) DMEM only** | **1197** | **58** | **5613** | **39** | **14129** | **1.9** |

In Figure 93, the autofluorescent 'Media' is compared with 'Ru' sample using a 500 kHz excitation rate. The autofluorescence has a rapid decay in comparison to $[Ru(bipy)_3]^{2+}$. An initial peak is displayed in the $[Ru(bipy)_3]^{2+}$ sample matching that of the autofluorescence confirming that it is not a scattering effect. Using a bi-exponential decay to fit the $[Ru(bipy)_3]^{2+}$+media sample shows that the percentage of the autofluorescent

amplitude contribution to the $[Ru(bipy)_3]^{2+}$ sample is 75%, which means that the dynamic range can be reached prematurely due to the media. Using data from the table the largest expected autofluorescent lifetime is 21 ns where as the lifetime of this $[Ru(bipy)_3]^{2+}$ is 370 ns, 20 times longer that any autofluorescence sample.

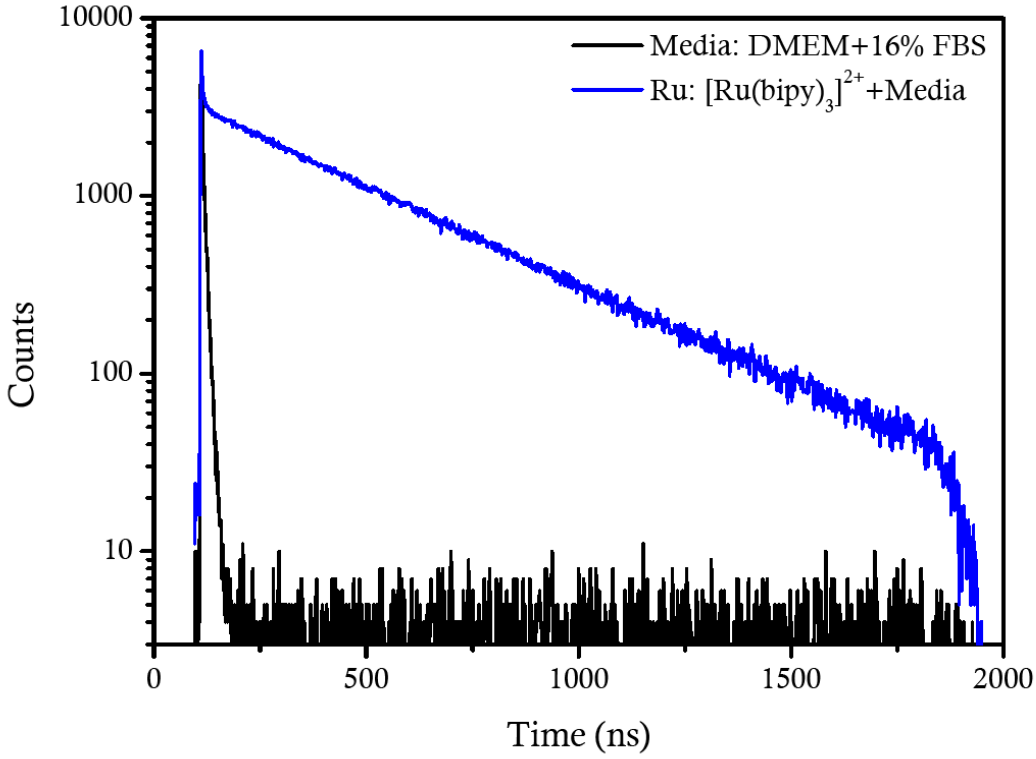


**Figure 93 – Lifetime decay of cell culture media and $[Ru(bipy)_3]^{2+}$+media plotted on a semi-log graph with a 500 kHz repetition rate. Autofluorescence can be seen in the media decay and the $[Ru(bipy)_3]^{2+}$ + media decay.**

### 4.2.3.7 Fetal bovine serum (FBS) shields $[Ru(bipy)_3]^{2+}$ from quenching

The emission wavelength of increasing concentration of FBS diluted in deionised water with $[Ru(bipy)_3]^{2+}$ (0.412mM) are presented in Figure 93. All emission spectra are identical regardless of percentage FBS concentration, with similar asymmetric responses. An asymmetric double sigmodal peak function was used to determine the peak emission and FWHM as 608.14 ±0.27 ns and 60.13 ±0.64 ns, respectively.

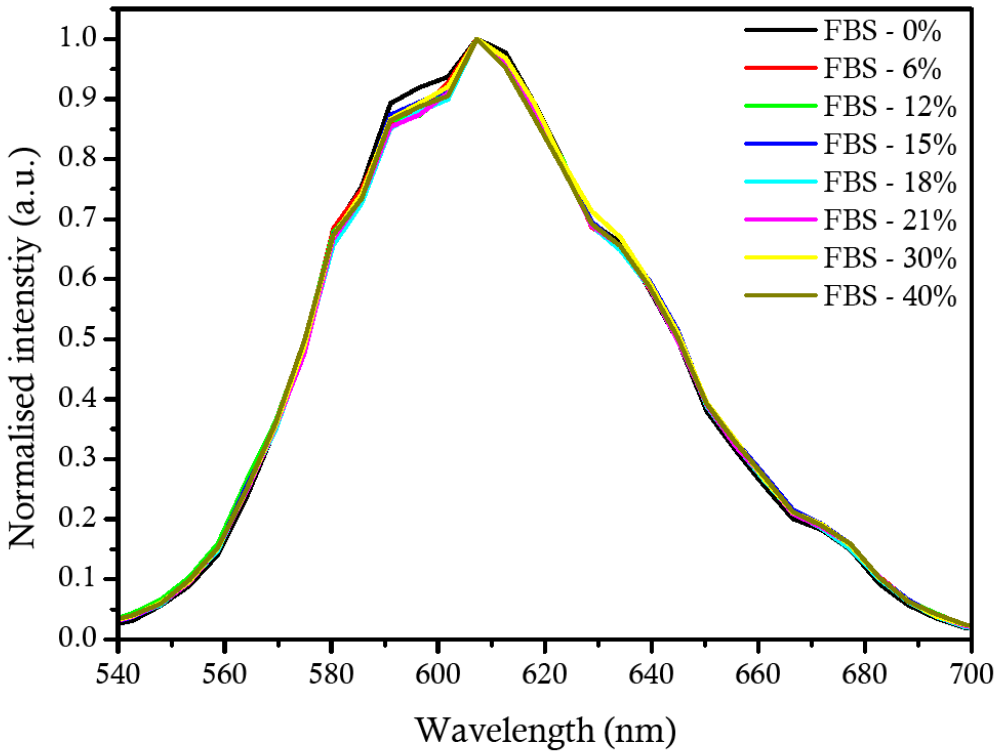


**Figure 94 – Emission wavelength of $[Ru(bipy)_3]^{2+}$ with incrementing concentrations of FBS. Normalised intensity measurements at an excitation of 780 nm and repetition rate of 500 kHz across an emission range of 540-700 nm.**

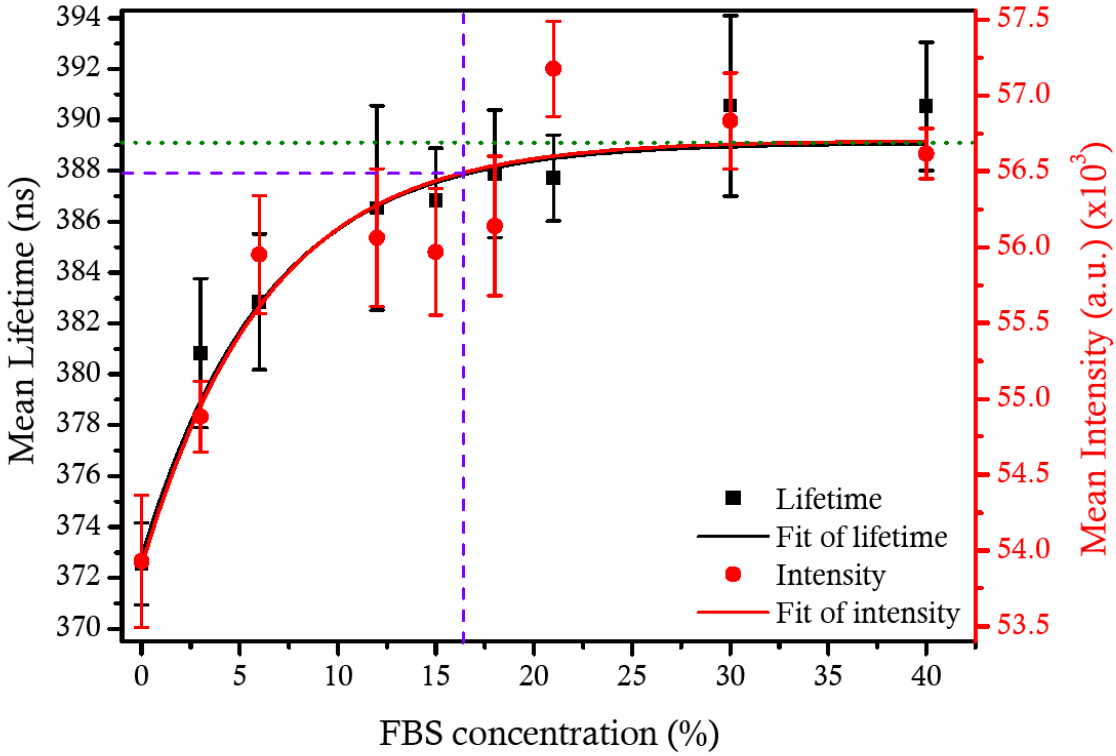


**Figure 95 – Mean intensity (n=4) and lifetime decays (n=5) of $[Ru(bipy)_3]^{2+}$ with increment concentrations of FBS . Left y-axis displays the mean lifetime (black squares) and right y-axis refers to mean intensity (red circles). Data points are fitted with a dose response curve described by the solid red and black line (adjusted $R^2$>0.96). The percentage of FBS in the cell culture media is represented by the purple dashed line, which corresponds to a lifetime of 388 ns. The maximum response is represented by the dotted green line with a lifetime of 389 ns.**

The mean lifetime and intensity of $[Ru(bipy)_3]^{2+}$ have been plotted for increasing percentage of FBS in solution at ambient temperatures, as shown in Figure 95. The standard deviations for the data of both lifetime and intensity were between 1%-0.29% of the measurement. Measurements for lifetime and intensity were acquired using the same sample. Both display an identical response to the increase in FBS concentration with an initial change in lifetime with increasing concentration that subsequently plateaus at the higher concentrations. Both sets of data have been fitted with a dose response curve (adjusted $R^2$>0.96) reaching a maximum for the lifetime and intensity at 389.09 ns and 56702, respectively, represented by the green dotted line. The percentage of FBS used in the cell culture media is 16%, represented by the purple dashed line; it reaches a point on the curve that corresponds to a lifetime of 387.9 ns. The difference between the lifetime at the cell culture concentration and the maximum response of the fitted lifetime is 0.28%.

### 4.2.4 Discussion

#### 4.2.4.1 Emission spectra

Comparing the results from the continuous and TP emission spectra revealed a slight red-shift and broadening of the peak almost double the size for TPE. This shows that rather than there being a narrow selection of emission pathways for $[Ru(bipy)_3]^{2+}$ there appears to be an increase in the available deactivation pathways, which would not normally be seen when exciting with SPE at 468 nm. Using TPE has induced a wider range of energy levels involved in the process of emission and is therefore not identical to SPE [236].

#### 4.2.4.2 Concentration dependence

Over the concentration range 0.208-3.34 mM the emission intensity, shown in Figure 87, a linear response to increasing concentrations. This slightly contradicts the results in chapter 2 where a partial non linear plot of $[Ru(bipy)_3]^{2+}$ concentration intensity determined the limit of self-quenching. This discrepancy between a linear and non-linear response arises due to the measurement techniques. Sud *et al.* [279] also noted that their intensity measurements of $[Ru(bipy)_3]^{2+}$ in water saturated at 2.5 mM. They determined that the effect was due to the geometric setup and retested it on a fluorimeter noting a decrease at higher concentration consistent with other reports [170] and the findings in Chapter 2. The influence of the setup and dye concentration on intensity measurements confirms the unreliability of quantifiable and repeatable measurements when using only intensity.

The lifetime measurements made with the same $[Ru(bipy)_3]^{2+}$ concentrations confirmed that no correlation exists between lifetime and concentration. The measured standard deviation of the mean (±0.36%) compares well with the repeatability measurement conducted in Chapter 3. This also revealed a variability for the same measurement as <0.3%. The TCPSC has demonstrated a 7-fold improvement in the accuracy of lifetime measurements when compared with that of the time-gate (standard deviation ±2.45%) used by Sud *et al.* [279]. The variability of the mean lifetime between TCPSC (375.45 ns) and time-gate (363 ns) can be attributed to variations in the recorded absolute temperatures and errors in the time-gate measurement.

#### 4.2.4.3 Temperature effect

There is a negative correlation between temperature and lifetime measurements, in accordance other researchers [144, 212, 300]. In Figure 90 the relationship between lifetime and temperature appears and can be assumed to be linear, but over a larger temperature scale a polynomial relationship exist [212]. An increase in the temperature of water reduces dissolved oxygen and therefore should reduce the quenching and increase the lifetime. At the same time there is an increase in the rate of diffusion and therefore collisional quenching. However studies of the temperature effect on $[Ru(bipy)_3]^{2+}$ without oxygen present have shown that this relationship is due to the activation of a non-radative pathway that operates via the non-luminescent d-d energy state [212, 300], as shown in Figure 96.

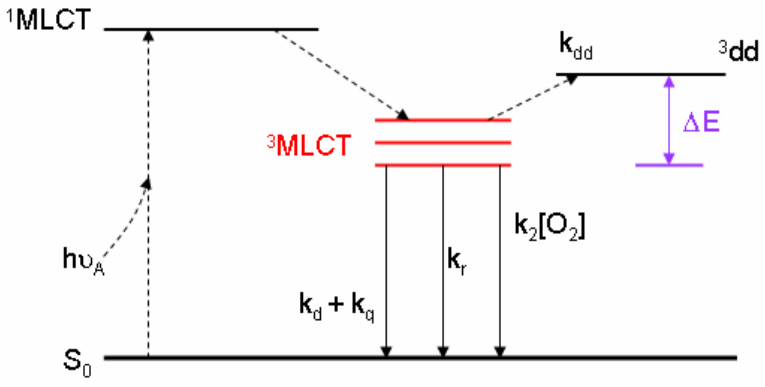


**Figure 96 – A Jablonski schematic diagram representing the electronic energy states of $[Ru(bipy)_3]^{2+}$ and the thermally activated non-luminescent energy state $k_{dd}$. The electron is excited from ground state ($S_0$) by light energy ($h\upsilon_A$) to the singlet metal-to-ligand charge transfer ($^1$MLCT) where the electron dissipates to the triplet metal-to-ligand charge transfer ($^3$MLCT). At this point it can take optional pathways: non-radiative ($k_d+k_q+k_2[O_2]$), radiative ($k_r$) or thermal activation ($k_{dd}$). Abbreviation: energy change ΔE[212].**

The change in temperature induces a change in the energy levels of $k_{dd}$, which is the thermally activated quenching rate constant [144, 212]. For example a change of 1°C in $[Ru(bipy)_3]^{2+}$+water can induce a 1% change in the lifetime. This highlights the vital

importance of maintaining stable and reliable temperature control system to obtain accurate results.

#### 4.2.4.4 pH concentration

Altering pH to mimic the physiological range, did not affect the measured $[Ru(bipy)_3]^{2+}$ lifetime. The variability between the measurements across all pH levels shows a standard deviation of 0.19% below the variability of dye concentration or systematic error. These data are consistent with previous studies [72].

#### 4.2.4.5 Media concentration

The autofluorescence produced in the cell culture media was measured with lifetime. The mean lifetime only differed by 700 ps between all samples tested and was not longer than 3.2 ns. The longest lifetime component was 21 ns in the DMEM H&A sample. Using the estimated completion of lifetime of 5τ [19] it can be determined that any autofluorescence arising from the cell culture media would have completed by 105 ns. Comparing this to the lifetime of a $[Ru(bipy)_3]^{2+}$ decay (2500 ns) the autofluorescence only occupies 4% of the total decay. This means that when fitting the lifetime decay of $[Ru(bipy)_3]^{2+}$+media, in order to avoid the autofluroescent signal creating another fitting component the decay can be modelled after 150 ns to the end of the decay. It also highlights an important reason for using the 1024 ADC instead of 256 ADC. A mono-exponential decay requires ≥200 data points for utilising a $\chi_r^2$ value 1.17. However if data points are excluded due to autofluoresence, noise and TAC lower limit the number of data points removed would be greater than 50 jeopardising the $\chi_r^2$ fitting. It is therefore more appropriate to use an ADC 1024 time channels.

#### 4.2.4.6 FBS effect

The emission spectra showed identical profiles and no spectral shift for increasing concentrations of FBS in water+$[Ru(bipy)_3]^{2+}$. Comparing the emission spectra between the dependence of concentration on $[Ru(bipy)_3]^{2+}$ (section 4.2.3.1) against the incrementing concentration of FBS revealled near identical peak emission; with a peak-to peak difference of 0.7 nm this was within the measured emission standard deviation. No spectral shift suggests that there is no physical binding to ruthenium(II) [171] and that only one population of fluorophores are emitting, i.e. rather than bound to FBS and free in solution [170].

Examining the lifetime and intensity measurements of $[Ru(bipy)_3]^{2+}$ with increasing concentrations of FBS reveals similar responses with a positive correlation that gradually

decreases to disassociation (Figure 95). At low concentrations of FBS, oxygen produces a change in lifetime and intensity, but as the concentration increases there is a weaker correlation until there is no correlation with oxygen. Since both the lifetime and intensity increase this indicates that there is less oxygen quenching the fluorophore. However as the overall oxygen concentration has not been changed it suggests that the FBS must be abating the oxygen surrounding the $[Ru(bipy)_3]^{2+}$.

This is supported by previous studies by Vaughan and Weber [301] who looked at pyrenebutyric acid (PBA) as a dynamic probe for microenvironments. They showed that if PBA was conjugated to by bovine serum albumin (BSA) there was no response to changes in oxygen, but when free in solution, there was a positive linear relationship. Lakowicz and Weber [172] stated that this effect is caused by the protein structure that prevents the diffusion of oxygen reaching the fluorophore. However the fluorophores used in these previous studies were conjugated to BSA and showed a slightly different response between the intensity and lifetime measurements, which was a combination of static and dynamic quenching. The intensity measurements were unaffected by BSA concentration and produced a linear response, but the lifetime measurements only produced a partial response and then became static, as found in the current study [172]. This suggest that $[Ru(bipy)_3]^{2+}$ is not conjugated to FBS or its constituents. This was further supported by the fact that there was no shift in the emission spectra.

Similar effects are also seen when $[Ru(bipy)_3]^{2+}$ comes into contact with DNA, although in this case it can become electrostatically bound or can exhibit partial intercalation depending on the ratio of dye and DNA [99]. It has been shown by Jain *et al.* [139] that $[Ru(bipy)_3]^{2+}$ has the weakest binding of all ruthenium(II) complexes to DNA, proteins and serum, which has been suggested is due to the hydrophobic organic ligands. This suggests that FBS is partially shielding $[Ru(bipy)_3]^{2+}$ from oxygen until the FBS increase in concentration has shielded all $[Ru(bipy)_3]^{2+}$ at which point no further response is seen with increasing FBS concentrations.

### 4.2.5 Conclusion

There is no correlation between lifetime and pH or $[Ru(bipy)_3]^{2+}$ concentration level. Results confirmed that an oxygen calibration should be completed at the operational temperature of the experiments. The cell culture media contains autofluorescent components, but by applying the mono-exponential fit after 150 ns minimises any influence from autofluorescent interference. It is suspected that there will be a difference between the Stern-Volmer relationship of oxygen and lifetime in a solution of water and media due to

other dissolved solutes as has been seen in FBS. It is therefore required that a Stern-Volmer relationship be conducted for $[Ru(bipy)_3]^{2+}$ in both water and media.

## 4.3 Oxygen concentration

To enable lifetime measurements to be used for quantitative analysis of oxygen concentrations in a cellular system a relationship between oxygen and the lifetime of $[Ru(bipy)_3]^{2+}$ must be established. The relationship is established from the bimolecular rate of the dye in that particular environment and derived from the response of lifetime to changes in oxygen, referenced against the lifetime without quencher.

Measurement of oxygen in atmosphere or gas phase is usually described in terms of pressure, Torr, Atm, bar, or Pascal (Pa) or more specifically partial pressure. Using Raults law the total pressure is equal to the sum of the combined pressures of all the gases. But when describing oxygen in water or dissolved oxygen, the terms are only capable of quantifying pressure and so units must be converted in order to describe concentration, which requires theoretical derivation. In biological and limnological literature concentration is generally the preferred measure of solubility [95], and IUPAC standards suggest the use of molality to remove the effect of temperature.

### 4.3.1 Theoretical calculation of oxygen in water

In order to calculate the oxygen concentration in water it is necessary to derive a relationship between oxygen in gas phase and oxygen dissolved in water. A gas at equilibrium with a liquid is referred to as a 'vapour' (saturated vapour) and considered to have the same properties as a 'gas' [261]. The environmental conditions dictate the relationship and therefore the thermodynamic analysis of this solute-solvent system. The considered system is at constant pressure, volume, and temperature and is assumed to be in equilibrium at the point of measurement. The phase equilibrium fundamental relies on the chemical potential of each component being equal [311]. For the condition of thermodynamic equilibrium at constant temperature and pressure a vapour-liquid system can be described using fugacity, a chemical quantity describing a realistic gas rather than an 'ideal gas' with the units of pressure, as shown in Eq. 37 [248].

**Eq. 37**
$$f_i^V = f_i^L$$

where, $f_i^V$ and $f_i^L$ are the fugacities of component $i$ (oxygen) and the superscripts denote the vapour phase (V) and the liquid phase (L), respectively. At equilibrium the fugacities of one component (oxygen) in two phases (vapour, liquid) must be equal [140]. As fugacity cannot be directly measured [140], it is necessary to relate them to determinable

components. This is achieved by rewriting Eq. 37 in terms of the fugacity coefficients, as shown in Eq. 38.

**Eq. 38** $$\phi_i y_i P = \gamma_i x_i f_i^o$$

where $f_i^V$ is the product of total pressure *P*, mole fraction $y_i$, and $\phi_i$ is the fugacity coefficient [248]. The $f_i^L$ is expressed in terms of the liquid-phase activity coefficient and is equal to the liquid activity coefficient $\gamma_i$, the mole fraction $x_i$, and $f_i^o$ is an appropriate standard-state fugacity [311].

The $\phi_i$ is the ratio of fugacity to the partial pressure of a gaseous constituent [200], and is dependent on temperature, pressure and all mole fractions in the vapour phase [248]. The fugacity coefficient can be calculated from the virial equation of state, truncated after the second virial coefficient [169], but for gases below the normal boiling point of water and at pressures of a few atmosphere, it is considered negligible [312]. This allows Lewis's rule to be used, which states that at low pressures where the gas phase is nearly ideal the fugacity coefficient can be considered $\phi_i = 1$ [248], providing Eq. 39:

**Eq. 39** $$f_i^V = y_i P$$

In the ideal vapour phase *P* = 1 atm therefore the solute (oxygen) is a component of this pressure and can be referred to as the partial pressure ( $p_i$ ), further simplifying Eq. 39 by replacing the mole fraction and total pressure [105, 116].

**Eq. 40** $$f_i^V = y_i P = p_i$$

For an ideal solution the activity coefficient is considered equal to unity [248] therefore in an ideal solution for each component of $i$, $\gamma_i \to 1, x_i \to 1$ reducing the equation to Raoult's law [248] $f_i^L = x_i f_i^\circ$. But for an ideal-dilute solution, i.e. air dissolved in water is weakly soluble [50], the 'symmetric convention' does not hold true for both dissolved solute and solvent. Instead the activity coefficient adopts an [312] 'unsymmetric convention' [223].

**Eq. 41** $\gamma_1 \to 1, x_1 \to 1$ **(Solvent)** $\gamma_2 \to 1, x_2 \to 0$ **(Solute)**

This convention leads to the use of Henry's law [32, 186] where the real and hypothetical states of the solvent are equal, but the solute is related by Henry's constant $k_{H,2\to1}$. This involves a pure solute in a hypothetical liquid state corresponding to extrapolation from infinite dilution [311].

**Eq. 42**
$$f_i^L = x_i \cdot k_{H,2\to1}$$

Substituting Eq. 40 and Eq. 42 back into Eq. 37 provides,

**Eq. 43**
$$p_i = x_i \cdot k_{H,2\to1}$$

Rearranging for dissolved oxygen concentration,

**Eq. 44**
$$x_{O_2} = \frac{p_{O_2}}{k_{H,O_2\to H_2O}}$$

where $x_{O_2}$ is the mole fraction of oxygen dissolved in water, $p_{O_2}$ is the partial pressure of oxygen, and $k_{H,O_2\to H_2O}$ is Henry's constant for the interaction between dissolved oxygen and water. Therefore to calculate the mole fraction of oxygen dissolved in water Henry's constant and the partial pressure of oxygen must be known or identified.

#### 4.3.1.1 Henry's constant

Henry's constant is not a directly measured value, but instead is derived empirically from experiments [273]. Investigations of oxygen dissolved in water date back to 1889 by Winkler and Fox, whose values were standard for over 50 years, until doubts were raised about their accuracy [32]. It wasn't until 1979 when Benson and Krause [33] produced the most reliable and precise results to-date. Even now calculations and models are based on their empirical approach to extracting Henry's law constants from solubility measurements [250]. Using a simple three-term power series ($1/T$) allowed the relationship between the molecular properties of the pure gases and the thermodynamic properties of their solutions [33] to be established:

**Eq. 45**
$$\ln k_{H,O_2\to H_2O} = a_0 + \left(\frac{a_1}{T}\right) + \left(\frac{a_2}{T^2}\right)$$

where, $T$ is the temperature (Kelvin), $a$ is a constant, and $k_{H,O_2\to H_2O}$ is the derived Henry's constant ($Pa^{-1}$). Rettich *et al.* [250] used Benson-Krause's equation to provide an improved set of constants due to the very accurate fit of Henry's constants over large temperature ranges and it is relative simplicity to apply [250]. The derived constants are listed below in Table 15.

**Table 15 - Parameter for Correlation of Henry's constant for interaction between $O_2$ and $H_2O$ in Eq.(13)[250]**

| Model | T (K) | $a_0$ | $a_1$ (K) | $a_2$ ($K^2$) |
|---|---|---|---|---|
| Rettich (2000) | 283.17-328.14 | 14.835722 | $5.837177\times10^3$ | $-1.085201\times10^6$ |

4.3.1.2 Partial pressure of oxygen

As identified with Eq. 44 the partial pressure of oxygen is equal to the mole fraction multiplied by the total pressure. Assuming that all components are in equilibrium the gas immediately adjacent to the water has 100% relative humidity [116]. It is therefore considered as a separate pressure, exerted by water vapour, as the saturated vapour pressure, $p_w^{sat}$. This reduces the total pressure immediately above the water interface and means that the partial pressure of oxygen can be described as:

**Eq. 46**
$$p_{O_2} = y_{O_2}(P_T - p_w^{sat})$$

where, $P_T$ is the total pressure of the environment, $y_{O_2}$ is the mole fraction of oxygen in a dry gas mixture. The atmospheric pressure is defined as 101.325 kPa (1 atm) as recommended by the Committee on Data for Science and Technology CODATA [209]. The mole fraction of oxygen in standard dry air is 0.20939 [92]. The saturated vapour pressure of water, $p_w^{sat}$, is temperature dependent and can be calculated using an equation derived by Saul and Wagner [259]:

**Eq. 47**
$$\ln\left(\frac{p_w^{sat}}{P_C}\right) = \left(\frac{T_C}{T}\left(a_1\dot{\tau} + a_2\dot{\tau}^{1.5} + a_3\dot{\tau}^3 + a_4\dot{\tau}^{3.5} + a_5\dot{\tau}^4 + a_6\dot{\tau}^{7.5}\right)\right)$$

Rearranged to make vapour pressure the subject gives:

**Eq. 48**
$$p_w^{sat} = \left(\exp\left(\frac{T_C}{T}\left(a_1\dot{\tau} + a_2\dot{\tau}^{1.5} + a_3\dot{\tau}^3 + a_4\dot{\tau}^{3.5} + a_5\dot{\tau}^4 + a_6\dot{\tau}^{7.5}\right)\right)\right) \cdot P_C$$

where, $T_C$ is the temperature at the critical point and is equal to 647.14 K, $P_C$ is the pressure at the critical point and is equal to $2.21 \times 10^7$ $Pa^{-1}$, $\dot{\tau}$ refers to the relationship between the temperature and the critical temperature $1-(T/T_C)$, and $a_{1-6}$ are constants displayed in Table 16 [259].

**Table 16 - Vapour Pressure constants for Eq. 48**

| $a_1$ | $a_2$ | $a_3$ | $a_4$ | $a_5$ | $a_6$ |
|---|---|---|---|---|---|
| **-7.85823** | **1.83991** | **-11.7811** | **22.6705** | **-15.93** | **1.77516** |

Substituting Eq. 48 into Eq. 46 provides the real atmospheric pressure and allows the partial pressure of oxygen in the vapour phase to be determined. Combining Eq. 46 and Eq. 45 and substituting into Eq. 44 the temperature dependent mole fraction of oxygen dissolved in water can be determined. This equation is sufficient for calculating the

concentration of oxygen in water, but for cellular experiments culture media will be used and this contains other solutes with ion charges that can effect the solubility of oxygen [94].

### 4.3.2 Calculating the molality of dissolved oxygen

In order to convert the mole fraction of dissolved oxygen into molality it is necessary to calculate the number of moles of oxygen per kg of water. The reason behind using molality (mol/kg) instead of molarity (mol/l) is to remove the dependence of water density on temperature in accordance with the IUPAC suggested standard for dissolved gases in liquid [209]. The molality of oxygen solute in water solution is given by:

**Eq. 49**
$$c_{O_2} = \frac{n_{O_2}}{m_{H_2O}}$$

where, $c_{O_2}$ is the molality of oxygen (mol/kg), $m_{H_2O}$ is the mass of water (kg), and $n_{O_2}$ is the number of moles of oxygen (mol). To calculate the number of moles of oxygen the mole fraction $x_{O_2}$ can be used [209].

**Eq. 50**
$$x_B = \frac{n_B}{\sum n_A} = \frac{n_{O_2}}{n_{O_2} + n_{H_2O}} = x_{O_2}$$

where, $x_B$ is the mole fraction of the solute, $n_B$ is the number of moles of the solute, $\sum n_A$ is the sum of solute and solution moles, $n_{H_2O}$ is the number of moles in water. One mole of water has a mass of 18.016 g [310] therefore in 1 kg there are $n_{H_2O}$ = 55.5084 moles [209]. Rearranging Eq. 50 and substituting into Eq. 49 provides Eq. 51 [291].

**Eq. 51**
$$n_{O_2} = \frac{55.5084 \cdot x_{O_2}}{1 - x_{O_2}}$$

The temperature dependence on the concentration of dissolved oxygen in water can be viewed by applying Eq. 51 to Eq. 44.

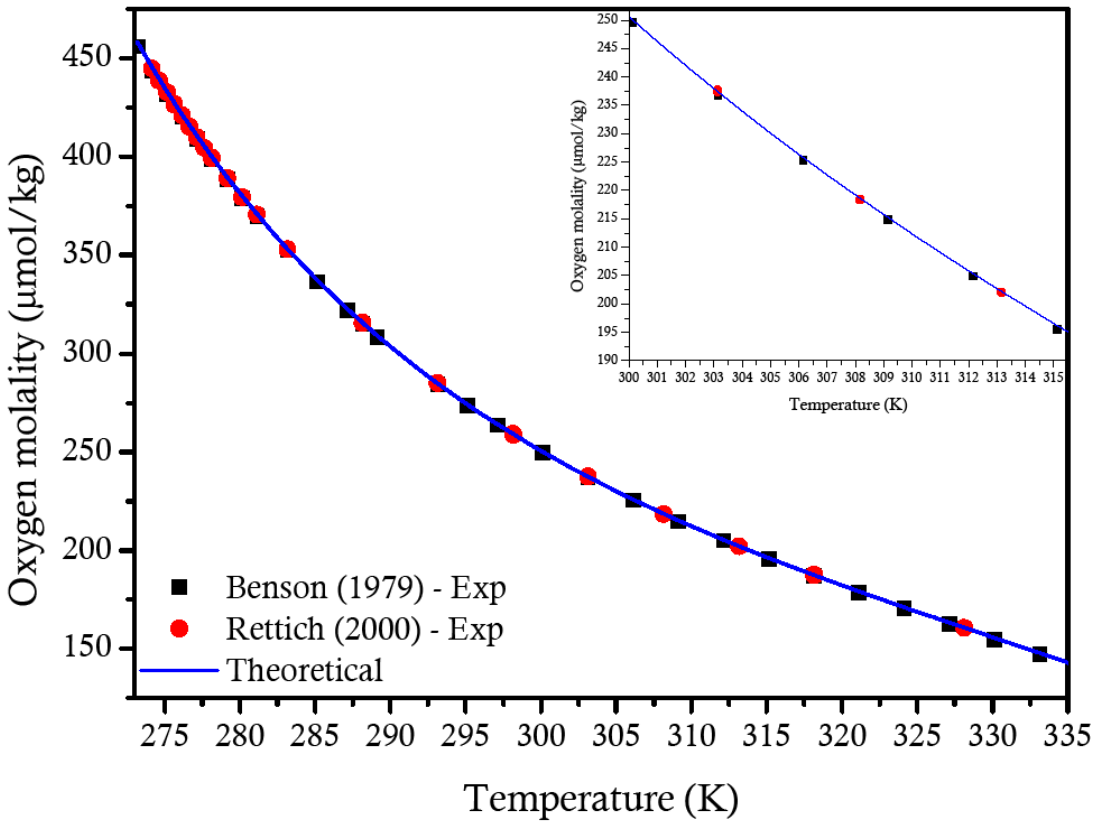


**Figure 97 – Effect of temperature on concentration of dissolved oxygen. Experimental data of Benson (black squares) [33] and Rettich (red circles) [250] plotted against a theoretical model (blue line - Eq. 51) for determining the oxygen molality based on atmospheric mole fraction of oxygen (0.20939). Inset figure shows an expanded section of the response between temperature of 300 and 315K.**

The relationship between oxygen molality and temperature is shown in Figure 97 for an oxygen mole fraction of 0.20939. Increasing temperature has a decreasing polynomial effect on the oxygen molality. For a variation of 1°C between 25 - 42°C the oxygen molality is expected to change between 5 – 3 µmol/kg. The equations derived so far are temperature dependent and complex and a further simplification can be applied. Combining Eq. 44, Eq. 46, and Eq. 48 for a working cell culture temperature of 37°C provides Eq. 52:

$$x_{O_2} = \frac{y_{O_2}\left[101325 - \left(\left(\exp\left(\frac{T_C}{T}\left(a_1\tau + a_2\tau^{1.5} + a_3\tau^3 + a_4\tau^{3.5} + a_5\tau^4 + a_6\tau^{7.5}\right)\right)\right)\cdot P_C\right)\right]}{\left[\exp\left(14.989460 + \left(\frac{5.742622\times10^3}{T}\right) + \left(\frac{-1.070683\times10^6}{T^2}\right)\right)\right]}$$

**Eq. 52**

$$x_{O_2} = y_{O_2}\,1.82307\times10^{-5}$$

substituting Eq. 52 into Eq. 51 to provide Eq. 53,

$$c_{O_2} = \frac{55.5084\cdot x_{O_2}}{(1-x_{O_2})} = \frac{55.5084\cdot y_{O_2}\,1.82307\times10^{-5}}{(1-y_{O_2}\,1.82307\times10^{-5})}$$

**Eq. 53**

$$c_{O_2} = \frac{a \cdot y_{O_2}}{c - y_{O_2}}$$

where, a = 55.5084, and c = 54852.53. This provides a simplified equation for the oxygen molality in water at 37°C dependent on the mole fraction of oxygen in the dry gas above the water. It is only valid and suitable at a temperature of 37°C and the interaction between oxygen and water, but in these experiments the interaction between oxygen and biological solvents is also of interest.

### 4.3.3 Theoretical determination of oxygen molality in cell culture media

Oxygen solubility is affected by temperature, partial pressure of oxygen in the gas phase and inorganic electrolyte solutes [292]. The salting out effect has been investigated with regard to the salinity of salt water and its effect on the solubility of oxygen in water [88, 95]. The reason behind this is that the interactions of ions influence the overall average spacing between water molecules so that the partial molar volume of the water component changes from that of pure water to an apparent value [292]. The water component has therefore less "volume" in which to accommodate the dissolved oxygen species and is "forced" from the solution [292], i.e. it is expected that there would be less dissolved oxygen in media based solutions than compared with pure water. Tromans [292] has developed an empirical equation based on thermodynamics to describe the solubility of oxygen gas in liquid as shown in Eq. 54.

**Eq. 54**

$$\frac{c_{O_2}}{p_{O_2}} = S_{O_2}$$

$$S_{O_2} = \exp\left\{\frac{\left[0.046T^2 + 203.35T\ln\left(\frac{T}{298}\right) - (299.378 + 0.092T)(T - 298) - 20591\right]}{8.3144 \cdot T}\right\}$$

**Eq. 55**

where $c_{O_2}$ is the molality of oxygen in water (kg/mol), $p_{O_2}$ is the partial pressure of oxygen (Pa), and $S_{O_2}$ is the solubility of oxygen in water (kg/mol/Pa). Complex interactions between polar water molecules and the ionic components in inorganic electrolytes (I) create disturbances that influence the overall spacing between $H_2O$ molecules [292]. This suggests that only a fraction ($\phi$) of the water component is available for dissolving oxygen whereas the remaineder involved in the ion-water interaction, providing the relationship in Eq. 56.

**Eq. 56**
$$\left(c_{O_2}\right)_I = \phi \cdot c_{O_2} = \phi \cdot p_{O_2} \cdot S_{O_2}$$

The fraction is treated as an empirically function of the solute concentration $c_I$ and is derived from experimental solubility data to fit the function in Eq. 57.

**Eq. 57**
$$\phi = \left\{1 + \kappa\left(c_I\right)^y\right\}^{-h}$$

**Eq. 58**
$$\left(c_{O_2}\right)_I = p_{O_2} \cdot S_{O_2} \cdot \left\{1 + \kappa\left(c_I\right)^y\right\}^{-h}$$

where, $c_I$ is the solute concentration (mol/kg), κ is a coefficient, and y, h are exponents that are tabulated in Tromas's paper [292]. Eq. 58 is only relevant for analysing one solute component, but using Eq. 59 multiple solute components can be considered together in one aqueous solution.

**Eq. 59**
$$\phi_{eff} = \phi_1 \cdot \left(\prod_2^z \phi_i\right)^q$$

where, $\prod_2^z \phi_i$ represents $\phi_2 \times \phi_3 \times ... \phi_z$ and $q$ is an empirical exponent 1> $q$ >0. It has been shown to have a value of 0.8 [291], the individually calculated solute values are arranged so that $\phi_1 < \phi_2 < ... < \phi_z$ ; $\phi_{eff}$ replaces $\phi$ in Eq. 56 to provide Eq. 60.

**Eq. 60**
$$\frac{\left(c_{O_2}\right)_I}{p_{O_2}} = S_{O_2} \cdot \phi_{eff} = S_{O_2} \cdot \phi_1 \cdot \left(\prod_2^z \phi_i\right)^q$$

The inorganic salt concentrations present in the DMEM cell culture media that have also been investigated by Tromas [292] are presented below in Table 17 with the correlating coefficients and exponent values. Three inorganic salts are not included, ferric nitrate (0.0001 g/l), sodium phosphate monobasic (0.109 g/l), and sodium bicarbonate (3.7 g/l) being the largest of the three. Inputting the coefficients and exponent values into Eq. 57 provides the ion fraction of each component. The full DMEM media composition and the conversion from g/l to mol/kg is listed in Appendix D, but at 37°C the change in water density is 0.993443 kg/l.

**Table 17 – List of ions in DMEM cell culture media also included in Tromas's paper [292]**

| Type of Ion | Conc. (g/l) | Molar mass (g) | Conc. (mmol/kg) | Fractions | $y$ | $h$ | $\kappa$ | Ion fractions |
|---|---|---|---|---|---|---|---|---|
| **NaCl** | **6.4** | **58.44** | 110.23682 | $\phi_{NaCl}$ | **1.01** | **4.224** | **0.076** | **0.9661** |
| **KCL** | **0.4** | **74.56** | 5.40021 | $\phi_{KCL}$ | **1.116** | **0.842** | **0.407** | **0.998991** |
| **$MgSO_4$** | **0.09767** | **120.37** | 0.81677 | $\phi_{MgSO_4}$ | **1.108** | **5.456** | **0.12** | **0.999752** |
| **$CaCl_2$** | **0.2** | **111** | 1.81369 | $\phi_{CaCl_2}$ | **0.985** | **2.711** | **0.18** | **0.999028** |

Substituting the ion fractions into Eq. 59 provides a fraction effect $\phi_{eff}$ equal to 0.96439. Using Eq. 55 for a temperature of 37°C the solubility of oxygen is 10.6 nmol/kg/Pa. Substituting Eq. 46, Eq. 55 and Eq. 59, into Eq. 60 produces the molality of oxygen in an ion aqueous solution at 37°C. Varying the mole fraction of oxygen allows a relationship between partial pressure and molality to be established as shown in Figure 98. A comparison of the theoretical and experimentally calculated solubilities and molalities of dissolved oxygen are shown in Table 18.

**Table 18 – List of experimental and theoretical ($x_{O2}$ = 0.20939) oxygen solubilities and concentrations in water at 37°C.**

| Researcher | Solvent | Solubility (nmol/kg/Pa) | Concentration (µmol/kg) |
|---|---|---|---|
| Gnaiger (2007) [95] Theo | Water @37°C | 10.63 | 208.67 |
| Benson (1980) [32] Exp | Water @37°C | - | 211.64 |
| Current theory | Water @37°C | 10.6 | 211.48 |
| Gertz (1954) [96] Exp | Pure serum @37°C | 9.462 | 188.31 |
| Current theory | Est. Media @37°C | 10.22 | 203.37 |

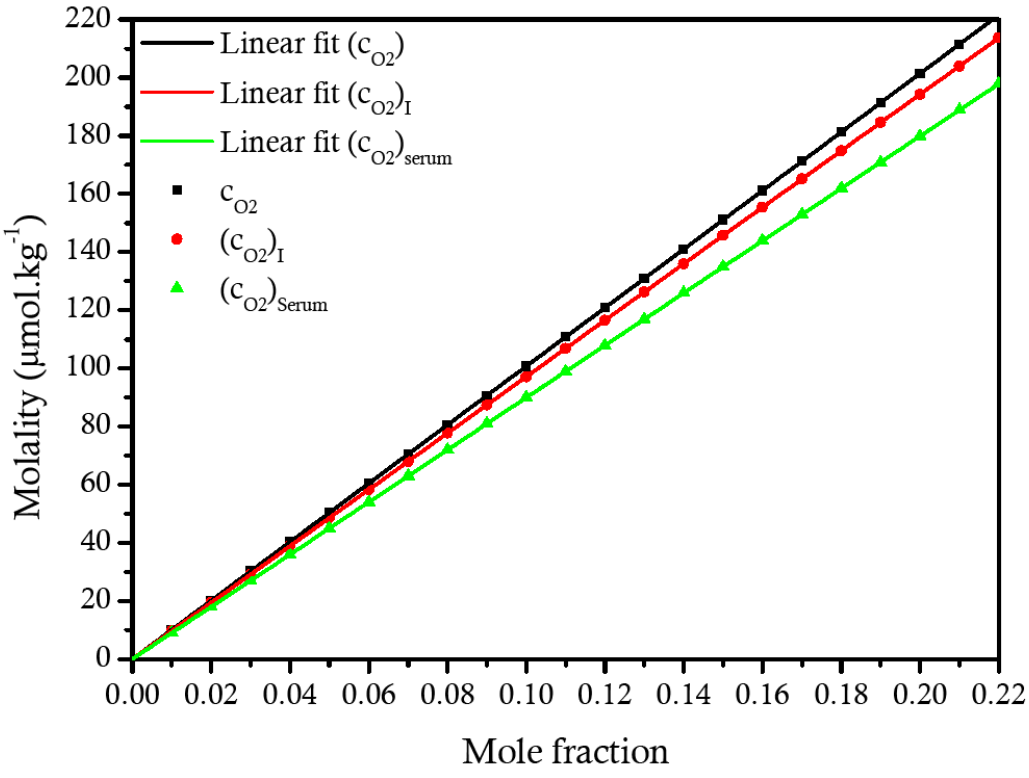


**Figure 98 – Estimate oxygen molality in solutions at 37°C with incrementing oxygen mole fractions Theoretically calculated oxygen concentration in pure water ($c_{O2}$ black squares), media solution ($(c_{O2})_I$ red square). Experimentally measured results from Gertz *et al.* [96] of pure serum ($(c_{O2})_{Serum}$ green triangles) are plotted with linear fits.**

The theoretical determination of oxygen molality dependence on mole fraction is shown in Figure 98. The dependence of oxygen molality on serum established by Gertz *et al.* [96] has also been included. Each concentration type shows a linear relationship with

the mole fraction and all intercept at zero. The gradients of each molality are $c_{O_2} = 10.1 \times 10^{-4} x$, $\left(c_{O_2}\right)_I = 9.71252 \times 10^{-4} x$, and $\left(c_{O_2}\right)_{serum} = 8.99327 \times 10^{-4} x$ (mol/kg) (adjusted $R^2$= 1). The added ion content reduces the concentration of oxygen when compared with pure water, but serum has an increased effect e.g. at a mole fraction of 0.15 the molality would be $c_{O_2} = 151.5$, $\left(c_{O_2}\right)_I = 145.69$, and $\left(c_{O_2}\right)_{serum} = 134.9$ (μmol/kg). These equations can be used to convert partial pressures into oxygen molalities and determine the quenching relationship.

### 4.3.4 Relationship between oxygen and lifetime

Determining a relationship between oxygen and lifetime provides a conversion factor for reverting measured fluorescence lifetime into a quantifiable oxygen concentration. This can be achieved by calibrating the measured fluorescence lifetime with known partial pressures of oxygen. As the oxygen environment is controlled via partial pressure the theoretical analysis must be used to convert them into quantifiable oxygen concentrations or molalities.

#### 4.3.4.1 Methodology

The chemicals used in these experiments are the same as outlined in section 4.2.2.1. The desired oxygen partial pressures where created using a sealed incubation system (Xvivo, Biospherix Ltd., USA) consisting of a gloved chamber and hydrated incubators. This utilised automated and independently controlled temperature and gas partial pressure ($N_2$, $O_2$, $CO_2$) between chamber and incubator; maintained at a barometric pressure of 1 atm (101.325 kPa). For these experiments the temperature and gas partial pressures were maintained at 37°C and 5% $CO_2$, $N_2$ balance. The only variability was the oxygen partial pressure between 0-19%; accuracy and precision was 0.1%. Calibration of the Xvivo and independent oxygen probe (OxyValidator Model F series, Biospherix Ltd.) used research grade $N_2$ gas and air cylinders to replicate zero and atmospheric oxygen (20.9%), respectively. The oxygen probe used an embedded temperature sensitive dye that required an independent temperature probe to be present to correct for a change in environment temperature and had a barometer to account for the atmospheric pressure. The XVivo system was calibrated against the gas partial pressure where the oxygen and temperature probe were submerged into deionised water; equilibrating for 40 min consecutively with each gas. Oxygen sensor accuracy was ± 2 Torr (0-160 Torr), repeatability <0.2% (relative standard deviation over 10 repeated measurements); Temperature sensor, ± 0.2°C, resolution 0.001°C; Pressure transducer ± 2%, resolution 0.001 Torr [314].

Stock solutions of $[Ru(bipy)_3]^{2+}$ were diluted with deionised water or media for a final concentration of 0.412 mM. 500 µl of solution were dispensed into six specially designed air-tight sample chambers and left to equilibrate at the desired oxygen partial pressure overnight, in the hydrated incubator at 37°C. The oxygen probe was used to confirm dissolved partial pressures of oxygen in sample chambers. Each day chambers were sealed, transferred to the temperature-equilibrated FLIM system, and loaded into the heating plate located on the microscope stage. FLIM measurements were conducted as described in section 4.2.2.2 and single lifetime decays collected for 800 sec in replicates of 10. This was repeated for each chamber and at each oxygen partial pressure.

#### 4.3.4.2 Data analysis

Lifetime decays were converted to ASCII files and extracted to Origin where mono-exponential models were applied to extract τ. Decays were only accepted if $\chi_r^2 < 1.17$ and $R^2 > 0.90$. The Stern-Volmer equation provides a direct relationship between oxygen and lifetime, as shown in Eq. 61 [46, 67, 257].

**Eq. 61**
$$\frac{\tau_0}{\tau} = 1 + K_{sv}[O_2]$$

where, $\tau_0$ is the lifetime with no quencher, τ is the lifetime measured at varying oxygen partial pressures, $[O_2]$ is the concentration of quencher (mol/kg), and $K_{SV}$ is the Stern-Volmer constant. The Stern-Volmer constant is described by the bimolecular quenching constant $k_2$ and the lifetime with no quencher $\tau_0$, as shown in Eq. 62 [67].

**Eq. 62**
$$K_{sv} = k_2 \tau_0$$

Plotting a graph of $\tau_0/\tau$ against $[O_2]$ produces the required relationship where the intercept should be equivalent to 1 and the gradient provides $K_{SV}$. It is assumed that only dynamic collisional quenching will be involved, as the fluorophore is in solution, and therefore the graph is expected to be linear. Diversion from this would indicate other forms of quenching described in section 4.2.4.6.

#### 4.3.4.3 Results

#### 4.3.4.4 Oxygen has linear relationship with $[Ru(bipy)_3]^{2+}$ lifetime

Lifetime measurements of $[Ru(bipy)_3]^{2+}$ dissolved in water and media at a temperature of 37°C have been acquired at incrementing concentrations of dissolved oxygen, as shown in Figure 99. A linear correlation can be seen between lifetime and oxygen molality this is confirmed with a negative linear fit producing (adjusted $R^2 > 0.98$):

**Eq. 63** $$\tau_{water} = 464.869 \times 10^{-9} (\pm 1.1\%) - 689.11 \times 10^{-6} (\pm 5.5\%) \cdot [O_2]$$

**Eq. 64** $$\tau_{media} = 460.421 \times 10^{-9} (\pm 0.49\%) - 616.598 \times 10^{-6} (\pm 2.8\%) \cdot [O_2]$$

The measured $\tau_0$ for deionized water and media was 470.94 nm and 463.5 ns respectively. Comparing the standard deviation of the linear fits, represented by the bracket in the equations, for water and media solution shows that media has less variation between the measurements. The gradient for $\tau_{water}$ is steeper than for media with a slightly different intercept (4 ns difference). By rearranging Eq. 63 and Eq. 64 the oxygen molality can be calculated from the measured lifetime by applying Eq. 61 which produces Figure 100.

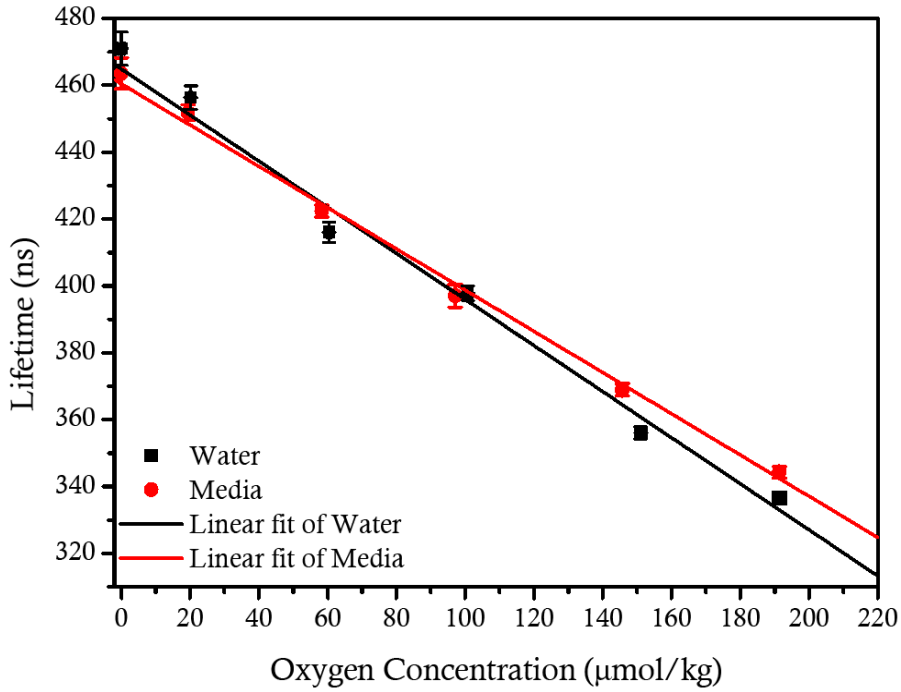


**Figure 99 – The effect of oxygen quenching on $[Ru(bipy)_3]^{2+}$ in solutions of deionized water (black squares) and media (red circles) at 37°C. The average water and media data points (n=10-20) are fitted with linear fits and have error bars in the x-axis relating to 0.1% for the accuracy of the Xvivo system and error bars in the y-axis representing the standard deviation between the results.**

Figure 100 depicts the ratio of $\tau_0/\tau$ plotted against oxygen molality for $[Ru(bipy)_3]^{2+}$ in water and in media. Linear fits of both sets of data show a positive linear relationship between the ratio $\tau_0/\tau$ and oxygen molality. The linear fits provide Eq. 65 and Eq. 66 for water and media, respectively, from which $K_{SV}$ can be determined (adjusted $R^2$>0.99).

**Eq. 65** $$\frac{\tau_0}{\tau}_{water} = 0.99425 + 2108.79 \cdot [O_2] \text{ (mol/kg)}$$

**Eq. 66** $$\frac{\tau_0}{\tau}_{media} = 0.9936 + 1819.84 \cdot [O_2] \text{ (mol/kg)}$$

The gradient for water is steeper than for media, but both intercept at approximately 1. The determined Stern-Volmer constant can now be used to calculate the bimolecular rate with Eq. 62: $k_{sv_{water}} = 2108.79$ mol/kg, $k_{sv_{media}} = 1819.79$ mol/kg, $k_{2\_water} = 4.478 \times 10^9$ mol/kg/s, $k_{2\_media} = 3.926 \times 10^9$ mol/kg/s.

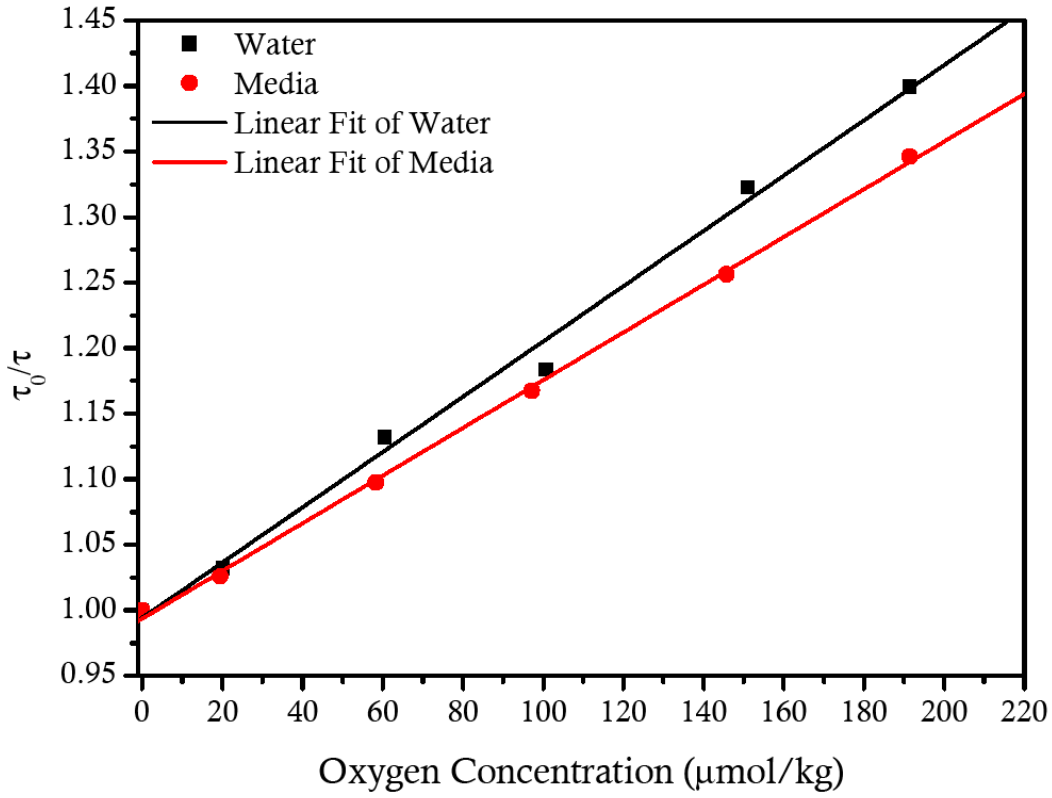


**Figure 100 – Determining $K_{SV}$ with linear fits of water (black squares) and media (red circles) measurements of $\tau_0/\tau$ against [$O_2$] concentration.**

Using the derived values of $K_{SV}$ and $\tau_0$ the efficiency of quenching or accessibility of the fluorophore to the quencher can be solved by rearranging the equation for $k_2$. By combining this with the diffusion-controlled bimolecular rate constant $k_0$ the efficiency of quenching $f_Q$ can be determined by using Eq. 67 [171].

**Eq. 67**

$$k_2 = f_Q \cdot k_0$$

The efficiency of quenching $f_Q$ requires the diffusion-controlled bimolecular rate constant $k_0$ to be determined. This uses Smoluchowki's equation, which relates the collisional radius and the diffusion coefficient of the fluorophore and quencher in the solvent of interest as shown in Eq. 68 [171].

$$k_0 = 4\pi N \cdot RD/1000$$

**Eq. 68**

$$R = \left(R_f + R_q\right) \quad D = \left(D_f + D_q\right)$$

where, R is the collisional radius, D is the sum of the diffusion coefficients and N is Avogardro's number ($6.0221367 \times 10^{23}$ $mol^{-1}$)[209]. The subscripts refer to the fluorophore (*f*), $[Ru(bipy)_3]^{2+}$ and the quencher (*q*), oxygen. The collisional radius is assumed to be equivalent to the sum of each molecular radii [171]. The terms in the calculations must be identified for 37°C and using the SI units cm. In order to calculate the diffusion coefficient of $[Ru(bipy)_3]^{2+}$ the standard Stokes-Einstein equation can be used, as shown in Eq. 69 [171].

**Eq. 69**

$$D = \frac{kT}{6\pi\eta R_q}$$

where, T is the temperature (310 K), D is the diffusion coefficient ($m^2/s$), *k* is the Boltzmann constant ($1.380658 \times 10^{-23}$ $m^2.kg/s/K$) [209], $\eta$ is the viscosity of the solvent (water) at 37°C (kg/m/s), and $R_q$ is the molecular radii of $[Ru(bipy)_3]^{2+}$ (239.7 pm Ru-N length that is affected by quenching [77]). The viscosity of water at 37°C can be determined from Eq. 70 derived by Korson *et al.* [161], but is only valid at temperatures between 10-70°C.

**Eq. 70**

$$\log\frac{\eta_t}{\eta_{20}} = \frac{A(20-t) - B(t-20)^2}{t+C}$$

where, $\eta_t$ is the viscosity at the temperature of interest (cP), *t* is the temperature (°C), $\eta_{20}$ is the viscosity at 20°C (1.002 cP), A = 1.1709, B = 0.001827, and C = 89.93; conversion for 1 cP = 0.001 kg/m/s. This calculates a viscosity of water at 37°C as $6.9 \times 10^{-4}$ kg/m/s and a diffusion coefficient for $[Ru(bipy)_3]^{2+}$ in water at 37°C as $1.373 \times 10^{-5}$ $cm^2/s$. The Stokes-Einstein equation tends not to be used for small molecules as it underestimates the diffusion coefficient [171]. However, it can be adapted to consider diffusion of molecules and solvent the same size by changing the factor 6 to 4, but if molecules are smaller than the solvent the factor is further reduced [131].

As dioxygen has a molecular radii of 140 pm [147] and the solvent water is 135 pm [222] they display similar radii. This changes the factor in Eq. 69 to 4 and produces a diffusion coefficient for oxygen at 37°C to $3.52 \times 10^{-5}$ $cm^2$/sec. Lakowicz *et al.* suggests using the nomogram graph method [171] established by Othmer *et al.* [230] to derive the oxygen diffusion coefficient. This only requires knowledge of the temperature and the molar volume of oxygen (26 $cm^3$/g.mol) [230]. A line is drawn between two reference points on the nomogram graph to reveal that the oxygen diffusion coefficient as $3 \times 10^{-5}$ $cm^2$/sec at

37°C. In this case the Stokes-Einstein equation has overestimated the oxygen diffusion coefficient, but if a factor of 6 was used it would be 2.35x10$^{-5}$ cm$^2$/sec underestimating the correct value.

Inputting these values into Eq. 68 calculates the diffusion-controlled bimolecular rate constant $k_0$ as 1.248x10$^{10}$ mol/kg/s. A summary of these values are shown in Table 19.

**Table 19 – Summary of values for diffusion coefficient and radius of molecules in water at 37°C**

| | R Radius (pm) | D Diffusion Coefficient [a] (x10$^{-5}$) (cm$^2$/s) |
|---|---|---|
| Oxygen (*q*) | 140 | 3 |
| $[Ru(bipy)_3]^{2+}$ (*f*) | 239.7 | 1.37 |
| Total | 379.7 | 4.37 |

[a] @37°C in water

A comparison is shown in Table 20 of the currently determined values in water and media to other values obtained by other researchers. As the other researchers have not disclosed the temperatures to allow for an exact comparison all calculated values have been converted to mol/l from mol/kg by multiplying by 0.993443 kg/l.

**Table 20 – A bimolecular compilation of the interaction of oxygen and $[Ru(bipy)_3]^{2+}$ for $K_{SV}$, $k_2$, $k_0$, and $f_Q$.**

| Researcher | Temp. (°C) | $\tau_0$ (ns) | $K_{SV}$ ($M^{-1}$)[a] | $k_2$ x10$^9$ ($M^{-1}s^{-1}$) [a] | $k_o$ x10$^9$ ($M^{-1}s^{-1}$) [a] | $f_Q$ |
|---|---|---|---|---|---|---|
| Rusak [257] | 25 | 562 | 1863 | 3.31 | 7.4 | 0.447 |
| Demas [65] | Unknown | 660 | 2130 | 3.2 | 6 | 0.533 |
| Saez [258] | Unknown | 600 | - | 3 | - | - |
| Maheswari [188] | 25 | 406 | 3300 [a] | - | 7 | - |
| Gorner [99] | Unknown | 590 | - | 3.9 | - | - |
| Mulazzani [217] | 23 | 610 | - | 3.4 | - | - |
| Current study water | 37 | 470 | 2094.96 | 4.45 | 12.39 | 0.36 |
| Current study media | 37 | 463 | 1807.92 | 3.901 | 12.39 | 0.31 |

[a] in the presence of DNA

Observing the $\tau_0$ it is possible to determine that the majority of the other researchers have conducted the measurements at room temperature. The bimolecular quenching constant only describes the interaction of the two molecules therefore should not be influenced by $\tau_0$ or $K_{SV}$. The $k_2$ is influenced by the diffusion coefficient which is temperature dependent. It would be expected that with higher temperature there would be faster diffusion and so a faster collision rate [257], which is reflected in the results.

### 4.3.5 Discussion

#### 4.3.5.1 Theoretically determined oxygen molality in water and media

The current theoretically calculated solubilities of oxygen dissolved in pure water are similar to the experimental results of Benson *et al.* [33], but differs from the theoretical results of Gnaiger *et al.* [95]. However this is accounted for by the fact that Gnaiger *et al.* used a value for $p_{O2}$ as 19.63 kPa derived by assuming a barometric pressure of 100 kPa instead of using the total atmospheric pressure of 101.325 kPa to calculate a $p_{O2}$ of 19.9 kPa as used in the current study. Translating the barometric pressure of 100 kPa at 37°C to height above sea level it suggests that their experiments were conducted 390 m above sea level. In comparison our laboratory is only 11 m above sea level which would have minimal effect on the barometric pressure.

The list of solutes provided by Tromas [292] did not include three inorganic salts present in media, with the largest missing concentration being sodium bicarbonate. This suggests that the theoretically derived molality of oxygen in media does not fully account for the missing solutes or serum, which are seen to have an effect on the solubility data shown by Gertz *et al.* [96]. One thing that is clear, the molality and solubility of oxygen in media is at least 4% less than in water at the same environmental partial pressures and 12% less between pure serum and pure water. The reason for the effect of serum could be attributed to a change in the chemical potential by increasing the solute concentration [172].

#### 4.3.5.2 Determining oxygen molality and relationship with lifetime

Experiments have confirmed that there is a negative linear relationship between lifetime and oxygen molality. As the oxygen partial pressure increases so does the molality leading to fluorescence quenching and a decrease in lifetime. The $\tau_0$ for water and culture media containing FBS are different, which indicates that some form of electrostatic binding could be affecting the radiative rates as was observed for the interaction between water and FBS in section 4.2.4.6.

The linear fits that establish the relationship between $[Ru(bipy)_3]^{2+}$ in water and media (Figure 99) display smaller standard deviations for media than for water. This indicates that the dye is less sensitive to the environmental changes when in media i.e. oxygen concentration or temperature fluctuations. The Stern-Volmer plots indicate dynamic quenching is involved due to the linear lifetime measurement [171]. This relationship has also been confirmed by other researchers [257, 279]. The difference in the Stern-Volmer gradients between water and media reflects different bimolecular quenching

interactions. It shows that $[Ru(bipy)_3]^{2+}$ in water is 12% more accessible to oxygen than in media the same percentage difference between water and serum oxygen molality.

The increased $k_2$, non-radiative bimolecular rate, in the current study compared with the other researcher in Table 20 suggests there is an increase in energy deactivation. This is most likely due to the increasing temperature effect on $k_{dd}$, the non-radiative pathway as discussed in section 4.2.4.3. However, the $k_2$ media value is 14% less than for water suggesting less non-radiative deactivation, where the $k_{dd}$ has been restricted by the effect of serum. The $K_{SV}$ values are reflective of the fluorophores environment i.e. the influence of temperature, viscosity and binding. The largest effect to $K_{SV}$ was reported by Maheswari *et al.* [188] where $[Ru(bipy)_3]^{2+}$ was measured in the presence of DNA due to electrostatic intercalation with DNA base pairs. The effect of binding is apparent in Maheswari *et al.* [188] data with an 83% greater $K_{SV}$ value in comparison to the current study for $[Ru(bipy)_3]^{2+}$ in media. This confirms that $[Ru(bipy)_3]^{2+}$ in media is not bound, but rather has a restrictive quenching relationship.

The large differences seen for the calculated diffusion-controlled bimolecular constants in Table 20 can be explained by the presumptions undertaken by Demas *et al.* [64] and Rusak *et al.* [257]. They assumed that the size and the specific molecules were unimportant, and rather only the temperature and viscosity of the solvent need to be considered, Eq. 71 shows their applied equation [257],

**Eq. 71**
$$k_o = \frac{8RT}{3\eta}$$

where, T is the temperature (K), R is the gas constant ($8.314472 \times 10^3$ L.Pa/mol.K) and $\eta$ is the viscosity (kg/m/l). Using this same equation and applying it to the current studies values it provides a corrected value for $k_o$ $9.968 \times 10^9$ M/s.

It would be expected that an increase in temperature would increase the diffusion rate and therefore the number of collisions. This is reflected by the reduced lifetime, as shown in section 4.2.3.4, however it would also be counteracted by a reduction in the oxygen concentration. The frequency of collisions was lower for the current study than those calculated for Demas *et al.* [64] and Rusak *et al.* [257], however when applying the adjust $k_0$ the frequency of collisions change to 0.449 and 0.394 for water and media, respectively. The adjusted frequency of collision for water is identical with the value derived by Rusak *et al.* [257], however the media value remains 14% less than water. Identical values of $k_0$ were used for water and media not taking into account the difference in viscosity due to serum this would increase the $k_0$ value. Whether this adjustment would match the frequency of collisions for water requires further investigation.

### 4.3.6 Conclusion

Serum and ion solutes in water have adverse effects on the solubility of oxygen, reducing the molality in comparison to pure water by at least 4%, and could be as much as 12%. A negative linear relationship between oxygen and lifetime was established for water and media. However, the media solution appeared to be less sensitive to environmental changes, such as temperature. It also showed oxygen was 12% less accessible to $[Ru(bipy)_3]^{2+}$ in media than in water. The results from this study have confirmed that the reduced $K_{sv}$, $k_2$ or $f_Q$ media values are due to the restricted access of oxygen quenching on $[Ru(bipy)_3]^{2+}$ by the serum in media rather than any physical binding and the effect of viscosity. Using the corrected equation of Demas *et al.* [64] and Rusak *et al.* [257] to calculate the adjusted $k_o$ provided identical values between Rusak *et al.* and water for the current study. This identifies that a 48% increase in temperature also increases the bimolecular rate constant by 34% and the lifetime by 9% for water samples. It has been identified that the difference between lifetimes with no quencher for water and media samples is 1.5% highlighting the influence of media solutes on the non-radiative component.

## 4.4 Summary

- Using the TP confocal TCSPC system it was established that TPE maximum was 780 nm and emission peak was maintained at 608 nm± 35 nm.
- No correlation was found between lifetime and varying $[Ru(bipy)_3]^{2+}$ concentrations or pH levels.
- Temerature was shown to effect $[Ru(bipy)_3]^{2+}$ lifetime and highlighted the importance that temperature stability is vital for accurate lifetime measurements.
- Cell culture media contain autofluorescent components like riboflavin or FBS.
- $[Ru(bipy)_3]^{2+}$ lifetime data should be fitted after 150 ns with a monoexponential model to avoid fitting other lifetime components associated with autofluroscence.
- FBS has been shown to acts as a collisional protector of $[Ru(bipy)_3]^{2+}$ from oxygen quenching dependant on concentration.
- The Stern-Volmer constant has identified that $[Ru(bipy)_3]^{2+}$ in water is 12% more accessible to oxygen that in media
- The non-radiative rate ($k_2$) for $[Ru(bipy)_3]^{2+}$ in media is 14% slower than in water and could be attributed to the additional media components

- The adjusted formula for $k_0$ provides an identical frequency of collision for $[Ru(bipy)_3]^{2+}$ in water as Rusak *et al.* [257].

# Data Acquisition 5

## 5.1 Introduction

The previous chapter discussed the effects of environmental conditions on the measured $[Ru(bipy)_3]^{2+}$ lifetime. It established that $[Ru(bipy)_3]^{2+}$ was a temperature sensitive dye not influenced by dye concentration or pH level in solution, but lifetime measurements were susceptible to serum at low concentrations of FBS or high concentrations of $[Ru(bipy)_3]^{2+}$. The relationship between oxygen and $[Ru(bipy)_3]^{2+}$ was also verified for experimental conditions providing a means of converting lifetime into oxygen concentrations.

However previous equipment parameters have only referred to acquisition of lifetime from a single point or area, without spatial resolution. The requirement for spatial resolution necessitates an increase in the acquisition time if the same level of lifetime accuracy is applied to each pixel. Thus the technique requires a balance between lifetime accuracy, appropriate spatial resolution and practical acquisition times. The method of image data analysis and collection will be critical to the quality and quantity of information that can be extracted within these restrictive working criteria. Further investigation of equipment parameters is required to enable two or three dimensional information to be collected. Once these issues have been overcome, application of the optimised FLIM technique can finally be used for spatial oxygen mapping in living three-dimensional cellular systems. Initially, confirmation of the proposed imaging protocol was applied to three-dimensional cell seeded agarose constructs in order to determine possible impact from phototoxicity caused by laser exposure to tissue or dye.

Therefore this chapter will be sectioned into two areas examining the level of phototoxicity and the methods for data analysis in two-dimensions. All experiments were conducted in accordance to parameters outlined in chapter 3.

## 5.2 Laser induced phototoxicity

In order to examine the effects of phototoxicity an understanding of the underlying mechanism from fluorophore excitation is required. During the excitation of $[Ru(bipy)_3]^{2+}$ cations, the electrons initially delocalise from the metal and localise on to one of the three bipyridyl ligands. It then relaxes through internal conversion to the lowest excited triplet state [99]. During this process, $[Ru(bipy)_3]^{2+}$ can be quenched by oxygen using two mechanisms; charger transfer (Eq. 72) or energy transfer (Eq. 73) [217],

**Eq. 72** $$^{*}\left[Ru(bipy)_3\right]^{2+} + O_2 \rightarrow \left[Ru(bipy)_3\right]^{3+} + O_2^{\bullet -}$$

**Eq. 73** $$^{*}\left[Ru(bipy)_3\right]^{2+} + O_2 \rightarrow \left[Ru(bipy)_3\right]^{2+} + O_2\left(^1\Delta_g\right)$$

where the superscript * refers to $[Ru(bipy)_3]^{2+}$ in an excited state. In Eq. 72 $^*[Ru(bipy)_3]^{2+}$ is quenched by oxygen via charge transfer creating a superoxide ($O_2^{\bullet -}$). In Eq. 73, the quenching by oxygen produces singlet oxygen ($O_2$ $^1\Delta_g$). There has been much investigation into the different mechanism of ruthenium(II) complexes. It was thought that $[Ru(bipy)_3]^{2+}$ quenching with oxygen was dominated by energy transfer due to electron charge transfer being less energetically favourable [68]. It was also thought that charge transfer actually returned the electron and reverted $[Ru(bipy)_3]^{2+}$ back to its original state [87, 217]. Mulazzani *et al.* [217] showed that 50% of collisions between $[Ru(bipy)_3]^{2+}$ and $O_2$ ($^3\Sigma_g^-$) lead to the excited singlet states $O_2$ ($^1\Delta_g$ or $^3\Sigma_g^+$) [1], energy transfer. Recently researchers have noted that the large discrepancy between diffusion-controlled estimations, $k_O$, and measured bimolecular quenching, $k_2$, values as seen in chapter 4 could arise from a charge transfer process [1, 2], but it is still unclear which method is the dominate process. However it is known that the excitation process creates ROS, which as discussed in Chapter 1 can lead to cellular toxcitiy and damge.

This has been shown by Dobrucki [72] who investigated the impact of laser excitation on $[Ru(bipy)_3]^{2+}$ and $[Ru(phen)_3]^{2+}$ incubated with macrophage cells. He suggested that the creation of reactive oxygen species from the illumination of $[Ru(bipy)_3]^{2+}$ and $[Ru(phen)_3]^{2+}$ lead to cellular membrane permeability, collapse and eventually cell death. The concentration level at which phototoxicity occurs is disputed among researchers and can be between 0.2 mM to 1.34 mM [72, 91, 279], therefore it is essential that an assessment of phototoxicity is completed. This variation can arise from the excitation source, method of excitation (widefield, confocal), number of illuminations, and length of illumination period can all influence the optimum concentration.

ROS can also induce damage to the dye causing increased photobleaching. This has been shown in silicon based encapsulation systems where $[Ru(bipy)_3]^{2+}$ is embedded in

silica [84]. In this case the restriction to diffusion prevents radical oxygen dissipating away from the dye and has a higher likelihood of reacting with the immediate environment causing photobleaching. The dependence of phototoxicity on excitation variables highlights the importance of conducting independent assessments of the current system.

### 5.2.1 Methodology

#### 5.2.1.1 Cell preparation

Chondrocyte-agarose constructs were prepared as outlined in section 5 of Chapter 2. Briefly, cartilage was dissected from adult bovine metacarpal-phangel joints (n=3) and sequentially digested in an oven at 37ºC with pronase and collagenase enzymes, for one and 14 hours respectively. The digest solutions were sieved, washed three times with DMEM+16%FBS, pooled together, and resuspended in 30 ml fresh DMEM+16%FBS. Cells were counted and seeded at $20x10^6$ cell/ml in 3% (w/v) agarose, type VII (A4018). The cell-agarose mixture was gelled at 4°C for 20 mins in specially designed air-tight chambers (see Appendix B). Each chamber was filled with 1 ml of media, caps loosely fitted, incubated in a 5%$CO_2$ at 37ºC and left overnight to stabilise. Prior to a chamber being imaged, the media was replaced with $[Ru(bpy)_3]^{+2}$+DMEM+16%FBS (0.412 mM) and incubation continued at 37˚C for a further 1.5 h.

#### 5.2.1.2 Cellular photo-exposure

Chambers were numbered and coverslips marked with perpendicular lines using permanent marker pen to aid re-location of the specific cells exposed to laser excitation. Chambers were individually mounted into the heating plate at 37˚C, positioned on the inverted microscope stage, within an environmental chamber set to 35°C. The perpendicular lines were located using the eye piece and orientated so that the intersection was positioned in the top left corner of the field of view (FOV), as shown in Figure 101A.

A single brightfield image was taken using the transmitted PMT and x20 (N.A.=0.5) objective lens (506503, HC PL FLUOTAR, Leica-Microsystems, GbmH) with a 2048 x 2048 format, two line averages, and two frame average (Figure 101A). Excitation was provided at 633 nm via a helium/neon laser, to avoid direct excitation of $[Ru(bipy)_3]^{2+}$. This image was used to relocate the specific cells and FOV 24 hours after excitation of $[Ru(bipy)_3]^{2+}$. A x63 objective lens (NA = 1.4) was used with an image format, speed and laser repetition rate of 1024x1024, 400 Hz and MP 4 MHz, respectively, to select two cells for illumination, as shown in Figure 101B. The image format was adjusted to 256x256 and

a zoom in of the selected cell produced an image voxel sizes of 130x130 nm, half the Rayleigh criteria for maximum resolution, therefore maximising possible photodamage. The selected cell was located centrally for maximum exposure, as shown in Figure 102A, and the detector switched to TCSPC PMT. The laser repetition rate was dropped to 500 kHz and EOM gain adjusted to provide a count rate $<5x10^3$ counts/sec. The TCSPC parameters were also set to 256x256 image format and 256 time channels with a collection/exposure time of 1800 sec, producing an image as shown in Figure 102B.

After the laser exposure, agarose constructs were washed three times in media and continued incubation with 1 ml DMEM+16%FBS for a further 24 hours at 37°C (5%$CO_2$). Two cells were imaged per chamber and the procedure was repeated for a total of 11 cells. The control cells were treated in an identical manner, and mounted on the microscope for the same length of time with the $[Ru(bipy)_3]^{2+}$, but without excitation.

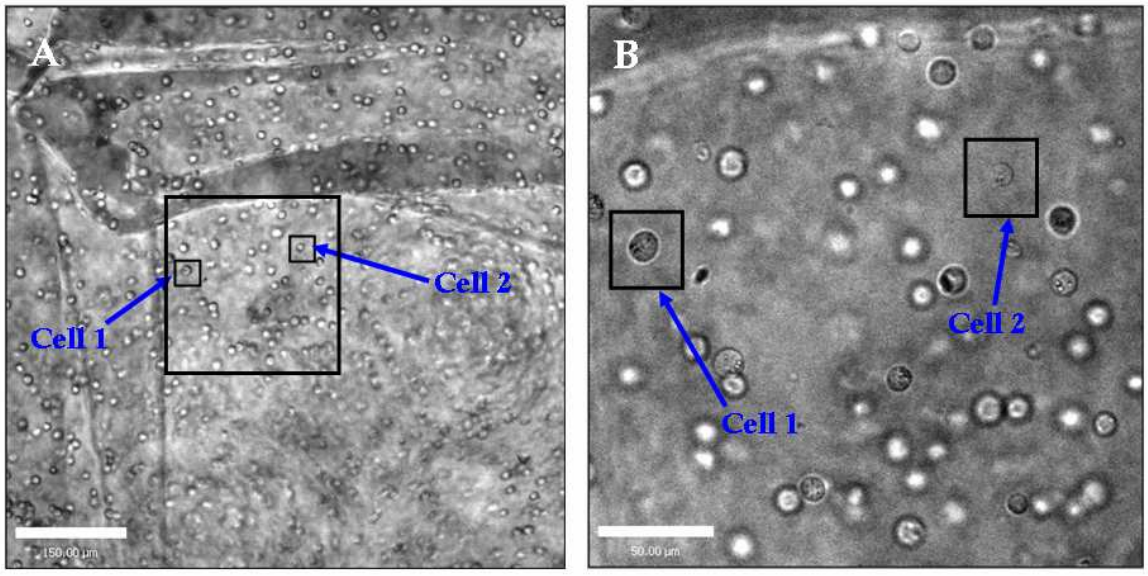


**Figure 101 - Brightfield images were used to identify the two exposed cells seeded in agarose within a single chamber to aid relocation during viability tests. A: Two perpendicular lines appearing as dark colouration on the left and top of the image were drawn on the underlying coverslip and used for positioning markers; the image was taken using x20 objective lens and 2048x2048 image format (scale bar = 150 µm). B: The large box shown in A is represented by the zoomed in image of B, where the same two cells have been identified as cell 1 and cell 2 using a x63 objective lens with an image format of 1024x1024 (scale bar = 50 µm).**

### 5.2.1.3 Cellular viability

Cellular viability was determined 24 hours after excitation of $[Ru(bipy)_3]^{2+}$ including the corresponding control studies. The chambers were removed from the incubator and 5 µl/ml of Calcein AM (C3099, Invitrogen™ Ltd., UK) and Ethdium homodimer-2 (EthD-2) (E3599, Invitrogen™ Ltd., UK) were added. The chambers then

continued incubation for a further 1 hour. Brightfield images from the previous day were used to locate each exposed cell by realigning the perpendicular lines in the FOV. For the live/dead stain a FITC and TRITC program stored on the Leica confocal was reloaded. The FITC and TRITC programs were run using an Argon (ex 488 nm, em 500-535 nm, gain 17%) and He/Neon laser (ex 543 nm, em 555-700 nm, gain 69%), respectively. The pre-adjusted programs were placed into a sequence file and the selected cells imaged using two line and frame averages per image. This process was repeated for each chamber (see Figure 101) including controls producing a total of 11 cells in each group.

### 5.2.2 Results

Using the above relocation it was possible to identify the same cell 24 hours after excitation of $[Ru(bipy)_3]^{2+}$ and to assess viability (Figure 102C). The percentage viability 24 hours after exposure was 90% with an identical 90% viability for control cells.

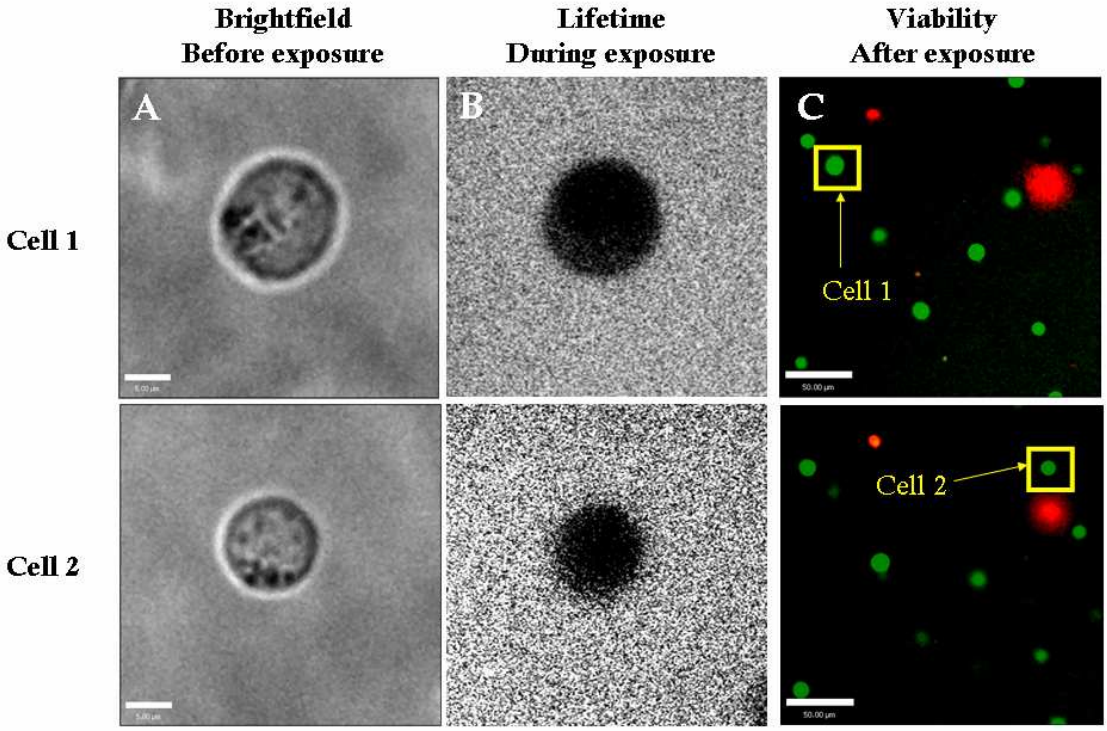


**Figure 102 – Process of selecting and identification of cells 1&2 prior and after exposure to asses viability. A: Brightfield image of identified cells before exposure, scale bar = 5 µm. B: Lifetime image cells exposed to the imaging protocol and then chamber returned to the culture incubator for 24 h. C: Same cells relocated using brightfield (Figure 101A,B) and imaged using 488 nm and 564 nm excitation to reveal cells labelled with calcien AM (live-green) and EthD-2 (dead-red), respectively, scale bar = 50 µm.**

### 5.2.3 Discussion

Cells maintained >90% viability after 1800 sec of laser exposure to the surrounding $[Ru(bipy)_3]^{+2}$ at a concentration of 0.412 mM. This is in contradiction to Dobrucki who exposed macrophages up to 112 illuminations using a confocal before cellular membrane break down (phototoxicity) occured at concentrations of 0.2 mM [72]. However other researchers have used concentrations up to 1.34 mM with no reported loss of viability [279]. However the difference stems from the power of the excitation which governs the generation of reactive oxygen species created by oxygen quenching $[Ru(bipy)_3]^{2+}$ and confirms the variability between imaging protocols and excitation methods influence the possibility of phototoxicity. Dobrucki states that the high pressure mercury arc lamp used in the experiments delivered a light beam with 0.1 mW of light that focused onto a diffraction limited spot delivering 0.16 J/cm$^2$ for one scan/pixel. The current systems excitation wavelength was 780 nm at 500 kHz repetition rate and, according to the power measurements taken in Chapter 3, had a 160 μW of average power at the sample. The energy per pulse $E$, is calculated as $3.2 \times 10^{-10}$ J using Eq. 74,

**Eq. 74**
$$E = \frac{P}{R_r}$$

where, $P$ is the power and $R_r$ is the repetition rate. The fluency can then be calculated by dividing the energy by the area of the beam exposure. The pixel size was 130x130 nm, so assuming a circular beam diameter of 130 nm the fluency can be calculated by dividing the energy by the area to provide 2.46 J/cm$^2$. This fluency is 15 times higher than the value calculated by Dobrucki and suggests that the slow repetition rate provides the damaging radicals time to diffuse away. This means that the cell has minimal ROS exposure and cellular viability is maintained. These experiments confirm that the image protocol and $[Ru(bipy)_3]^{2+}$ concentration are suitable for the assessment of lifetime without effecting chondrocyte viability in agarose.

## 5.3 Data collection methodology

Previously only single decay collection and analysis has been discussed forming the basis for image acquisition of 500 kHz lifetime decays. Expanding this knowledge and applying it to an imaged based setting requires further investigation. It is important to strike a balance between providing information of local oxygen distribution and maintaining quantitative oxygen concentration. This balance is determined though lifetime spatial resolution and accuracy. These issues are primarily restricted by imaging time and number

of photons collected. The following section will examine the optimum image format judged on collection time and required photon counts.

### 5.3.1 Image format adjustment

Adjustment of the laser repetition rate requires a TCSPC imaging protocol to be setup for each rate and image size. The setup for imaging acquisition of TCSPC can be viewed in two phases. Phase one requires a single decay to be recorded at the chosen repetition rate, with CFD, SYNC, and TAC parameters characterising the laser operation. The settings obtained from this initial phase are the basis for deriving single lifetime decays at that repetition rate. Phase two ensures that prior knowledge of minimum number of photon and collection time defines the acquisition of each pixel. Correlating the Leica setup, consisting of image format and raster scanning speed, with the TCSPC finally completes the image production of a lifetime map.

The single decay files that had previously been setup for 500 kHz are the basis of phase 1 and the statistical analysis of photon collection is the basis of phase 2, both defined in Chapter 3. The final stage is to replicate the image obtained on the Leica with the TCSPC system. In some systems the scanning speed of the Leica communicates directly with the TCSPC though the pixel clock [27] automatically adjusting the pixel dwell time, but is currently not available in this system. To enable user adjustment a sample containing structure must be used to provide visual markers for correlating image registration.

#### 5.3.1.1 Methods

A cell-agarose sample was prepared as in section 5.2.1.1. The sample consisted of isolated chondrocyte cells, at 40 x $10^6$ cells/ml, in 3% (w/v) agarose deposited at the base of a sealed sample chamber in a solution of 1 ml 0.412 mM $[Ru(bipy)_3]^{+2}$ with DMEM+16%FBS. A cluster of cells were selected and intensity image on the Leica were obtained using the 4 MHz MP laser to provide reference images at varying image formats. Using a scanning speed of 400 Hz, two line and frame averages, images were recorded for each format size 256 x 256, 128 x 128, and 64 x 64. The laser repetition rate was then dropped to 500 kHz and emission diverted to the FLIM detector. In the TCSPC system the original ‘single’ operation acquisition decay file for 500 kHz was loaded; it contained the pre-set parameters for optimum photon collection. The collection time used was 20 sec with a count increment of 100.

The operation mode was then changed to ‘Scan Sync In’ providing communication between the Leica microscope and TCSPC module. The spatial registration of the image in

the SPCM was manipulated via the pixel dwell time to replicate the original intensity image produced on the Leica at 4 MHz. There is no established method for translating this and is regarded as a trial and error process [27]. Adjustment of the pixel dwell time is located in 'more parameters'. The upper and left boarders can be adjusted to effectively crop the image to avoid dynamic effects. These are induced from the galvanometer mirrors in the first pixels of a frame or during flyback that prevent an adequate signal being recorded [27].

#### 5.3.1.2 Results

The trial and error registration process between a Leica intensity image and FLIM TCSPC image, for a 64x64 image format at a repetition rate of 500 kHz, is shown in Figure 103. A comparison between the Leica intensity image A and the SPCM images B and C are either too compressed or too stretched, respectively. The SPCM image in D does show a good correlation to the Leica image A, which is highlighted by the yellow circle showing the matching positions of the cells. To ensure the cells are in the correct positions the pixels are counted from the edge and compared with the array numbers of the SPCM image.

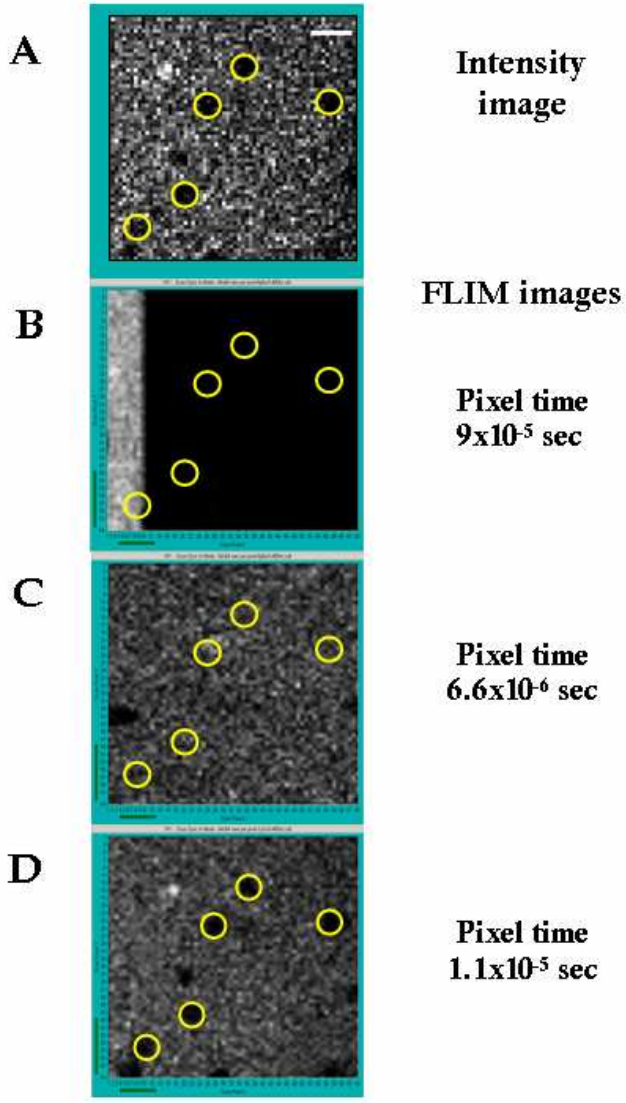


**Figure 103 – Image adjustment of 64x64 image format of a cell-agarose construct $40x10^6$ cells/ml. A: Leica intensity image, B: Lifetime image pixel time 90 µsec C: Lifetime time pixel time 6.6 µsec, D: Lifetime image pixel time 11 µsec. Yellow circles represent matching cells. Scale bar =20 µm.**

#### 5.3.1.3 Discussion

An estimate of the pixel dwell time can be achieved from knowledge of Leica scan rate, which in this case is 400 Hz. Converted into scan time per line 400 Hz is equivalent to 2.5 ms/line and for a 64x64 pixel image format it provides an estimated pixel dwell time of 39.1 µs/pixel. However image registration was only achieved once the pixel dwell time was reduced to 11 µs/pixel (Figure 103D). The reason behind this discrepancy is described by Becker *et al.* who states that as the scanning speed of the microscope (39 µs), i.e. pixel rate, is higher than the photon count rate (< 2µs) it leads to a recording process that is random [27]. Also small discrepancies may arise due to differences in the internal pixel clock on the SPC board and in the PC. The only way to avoid this is to use an external pixel clock

linked to the Leica system. However this is currently unavailable. This entire process was successfully completed for each image format and scan speed, with all settings saved for future experiments.

### 5.3.2 Image analysis

There are a variety of methods available that can translate the collected photons/ time channel/pixel and process them into an intensity image. Through application of an appropriate fitting model, a lifetime image based on the generation of lifetime for each pixel is determined. The restriction arises from the programs available for data logging, i.e. processing the thousands of counts into the correct time channels, pixel arrays and spatially registering the location in combination with an intensity image. The TCSPC module uses a specific file type '.sdt' that can only be opened with a few designated programs, namely the single photon correlation module (SPCM); Edinburgh instruments; Time Resolved Imaging (TRI2)(Version 2.4.1.1, Gray Institute for Radiation Oncology and Biology) [22]; and Matlab (only using a user written program). The two programs available that provide specifically designed graphical user interfaces (GUI) for lifetime analysis are the single photon correlation image (SPCImage), provided with the TCSPC, and the TRI2, that can be acquired free from Paul Barber at Oxford University.

The two programs have different advantages. The SPCImage is directly linked to the SPCM where all images or single lifetime files can be transferred and is purpose built for lifetime analysis. The TRI2 on the other hand requires the files to be imported and can not analyse single lifetime decays yet. However it does provide greater flexibility for processing the data. The following investigation shall identify the imaging parameters and how they affect image acquisition. Finally a comparison between the analysis programs and methods for data extraction will identify the final parameters required to obtain oxygen gradient information.

#### 5.3.2.1 Image Format

Determining a suitable image format requires a compromise between the required spatial resolution (image format), the accuracy of the lifetime (number of counts required), the collection rate and the total collection time. Thus an estimation of the required collection time can be derived from Eq. 75,

**Eq. 75**

$$C_T = \frac{F_I \cdot N_C}{C_R}$$

where, $F_I$ is the total number of pixels in the image format, $N_C$ is the number of required photon counts per pixel, $C_R$ is the collection rate, and $C_T$ is the collection time. The minimum number of photons required, as established in chapter 3, is $N_C$ = 20,000 counts/pixel, and the maximum collection rate whilst avoiding systematic pile-up, is $C_R$ = 5000 counts/sec. By using these optimised parameters the relationship between image format and collection time can be represented graphical, as shown in Figure 104. Based on the known parameters in Eq. 75 and the minimum image format available from the Leica microscope $F_I$ (64x32) the minimum collection of time for imaging is $C_T$ = 8,192 sec or approximately 2 h 27 min per image (Figure 104). Based on these settings it would take over 14 days of imaging for 8 hours per day to obtain the information from 50 cells. Also, this is beyond the accepted phototoxicity time for laser exposure as established in section 5.2.1.2. Therefore other means of reducing the imaging time require consideration without jeopardising the integrity of the experiment.

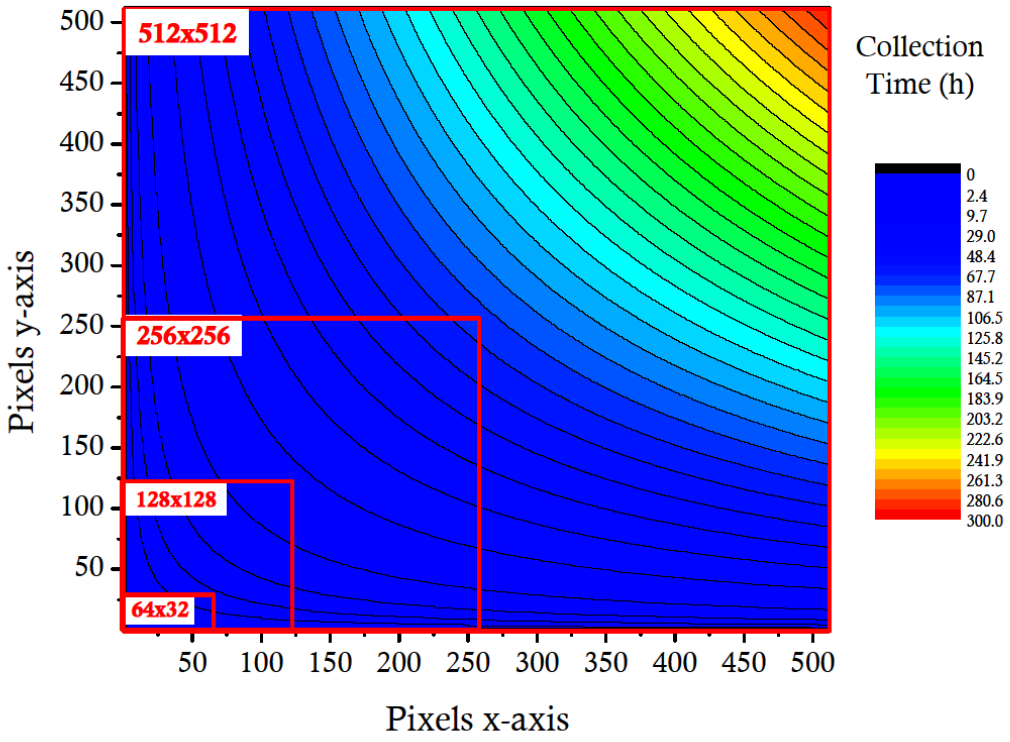


**Figure 104 – Estimated collection times for various image formats with a minimum of 20,000 counts per pixel necessary to give a adjusted $R^2$>0.9. Colour contour represents the number of hours for the total collection time and the red boxes are the standard image formats available on the Leica system including the minimum image format.**

### 5.3.2.2 Binning

One method for reducing the exposure time would be the use of binning, by adds the surrounding counts into the pixel of interest. This effectively increases the total count per pixel and can act as a form of decay averaging, which reduced noise and variability between pixels. However excess binning can smooth the image to such an extent that the

differences in lifetime are reduced affecting the spatial lifetime resolution. Generally in microscopy, images tend to be over sampled to extract more structural information and so in these cases use of binning does not induce a loss of spatial lifetime resolution [27], see Chapter 3 section 3.2 on image resolution. Therefore a balance is necessary between the number of required photons, total imaging time and the spatial lifetime resolution. An example of a form of binning that uses square expansion is shown in Figure 105.

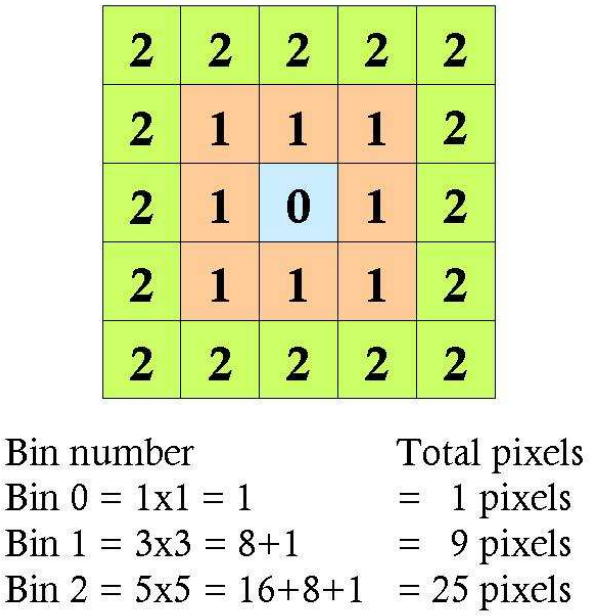


**Figure 105 – Example of square binning selection for a single central pixel. The number inside the boxes represents the bin number and the total pixel shows how many pixels the bin number is equivalent to, adapted from Becker [27].**

The lifetime of interest is the central pixel referred to as 'Bin 0'. The adjacent pixels that surround the central pixel form a larger square. Using a 'Bin 1' or 3x3 binning refers to the pixels adjacent to the central pixel being included. The user determines if enough counts are available to apply a mono-exponential fit, otherwise the next set of pixels are incorporated, referred to as 'Bin 2' or 5x5 binning. This continues until a sufficient number of counts are available for lifetime fitting.

Once the correct bin setting for that pixel has been determined the software will apply the same settings to each pixel and then perform a lifetime fitting. The effect of binning on the collection time can be modelled for different image formats based on the minimum number of counts required per pixel (20,000) and the maximum collection rate (5000 counts/sec), as shown in Figure 106.

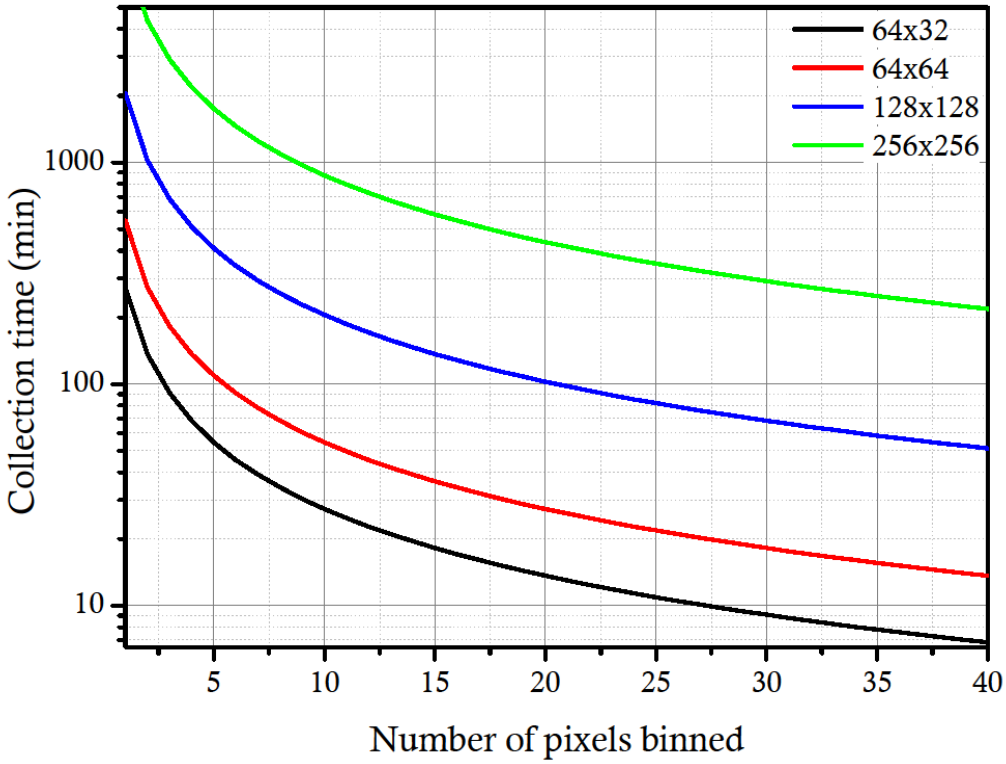


**Figure 106 – Semi-log plot of the variation of pixel binning and the effect on collection time for varying image format sizes based on 20,000 counts per pixel and a collection rate of 5000 counts/sec.**

A bi-exponential relationship exists between the collection time and the number of pixels binned for each image format size. Imaging times beyond 10 mins are not only impractical and reduce the possibility of observing the dynamics of oxygen utilisation. According to Figure 106 the minimum number of bins for a collection time of <10 min is >27 pixels based on the smallest image format of 64x32. In comparison for the same number of binned pixels it would take an estimated collection time of 20 mins for a format of 64x64, 75 mins for 128x128 and 325 min for 256x256.

#### 5.3.2.3 Discussion

The spatial resolution is determined by the size of the pixel rather than the number of pixels, therefore image format is not necessarily the determining factor in this process but rather it is the imaging time that is of importance. Minimum exposure will help to reduce phototoxicity and maintain viability, but also allow a faster analysis of the oxygen environment. As cells are dynamic in their behaviour it is assumed that oxygen gradients will adjust over time depending on the surrounding oxygen concentration. Therefore systems need to produce oxygen maps with both good spatial and temporal resolution. The average size of an isolated chondrocyte is 10 μm [156], thus the pixel size should be at most approximately 350 nm based on a 64x33 image format and an intended image layout as shown in Figure 110. Future experiments should be run at most, half the exposure time

used in phototoxicity experiments (15 min) to maintain good viability. This will ensure at least double the minimum number of photons will be collected based on a 64x32 image with binning of at least 27 pixels to account for possible photon loss in the system during the acquisition process. The initial image format parameters have been theoretically suggested and now quantification of experimental system losses will confirm the actual binning and software processing that should be applied.

### 5.3.3 Parameter control image test run

During lifetime acquisition it is assumed that photons will be lost through detection and data processing. Therefore an experimental test run was completed to confirm the actual acquired photon count based on the theoretically determined collection rate. The test run mimicked the intended experimental protocol using agarose and $[Ru(bipy)_3]^{2+}$+media without cells to provide baseline data and avoid lifetime influences from cellular oxygen consumption effects.

#### 5.3.3.1 Method

The air-tight sample chamber and coverslips were autoclaved along with a separate glass bijou of agarose powder mixed at 3% (w/v) with Hanks buffer. The autoclaved gel was transferred to a 60ºC oven to cool for 1.5 hour and was then transferred to a second oven to cool to 37ºC for a further 30 mins. During this process the sample chamber was constructed and coverslips added using autoclaved tweezers in a sterile environment. A sterile Pasteur pipette was used to transfer the agarose gel to the chambers creating an agarose layer, 10 mm in thickness. The chambers were covered and transferred to the fridge for 20 min to gel the molten agaose. A sterile scalpel was then used to extract quarter sections of agarose. Quarter sections of the agarose gel were removed to provide fast delivery of $[Ru(bpy)_3]^{+2}$, aid diffusion and produced a clear boundary between media and agaose in the x-y plane. 1 ml of DMEM+16%FBS was added to each chamber, the lids where loosely sealed and the chambers transferred to a hydrated incubator at 37ºC (5%$CO_2$, air balance) and left overnight.

Prior to imaging (1.5 hours), a preheated (to 37°C) solution of $[Ru(bipy)_3]^{2+}$+ DMEM+16%FBS (0.412 mM) was exchanged with DMEM+16%FBS. The sealed chamber was then transferred to a preheated stage heating plate (37ºC) and environmental chamber (35ºC). The chamber was mounted on the microscope stage and a x63 oil objective lens was used to locate the coverslip. The position of the lens was adjusted to a depth of 100 nm and 8 separately located images at 64x33 image format were recorded

from the non-cellular agarose sample. The laser excitation was 780 nm at a repetition rate of 500 kHz and photons were collected for 900 sec.

Each captured image was sent to SPCImage from SPCM, which displayed the non-cellular agarose image. The cross-hair automatically located the peak intensity pixel in the acquired image providing maximum number of acquired counts, which was recorded for later analysis. To determine the total number of counts recorded per image datasets were transferred to TRI2 software where all pixels can be binned deriving the counts per image. The count rates for the photon processing elements of the system were obtained from constant fractional discriminator (CFD), time-to-analogue converter (TAC) and analogue to digital converter (ADC). This requires the original '.sdt' image file to be reloaded into the SPCM. It produces a simulation of the maximum and minimum counts rates for the CFD, TAC and ADC during that experiment. It is important to identify the location of losses in the system to propose possible solutions.

#### 5.3.3.2 Results

The maximum and minimum collection rates for the CFD and TAC during measurements of non-cellular agarose constructs bathed in $[Ru(bipy)_3]^{2+}$+media at 37°C are shown in Figure 107. The mean (± standard deviation) values for the maximum and minimum collection rate for the CFD was 2285 (±154) and 1218 (±85) counts/sec, respectively. Similarly for the TAC the maximum value was 1828 (±103) and the minimum values was 1083 (±72) counts/sec. The difference between the mean maximum and minimum values for both the CFD and TAC are similar at 47.8% and 42.5%, respectively. The difference between the maximum CFD and TAC was on average 25%, where as between the minimum CFD and TAC it was 12%.

The mean collection rate for the CFD and TAC were 1751±563 and 1456±394 count/sec, respectively, shown in Figure 107. This shows as an average loss of 20% between the registered photons and the converted photons to count. The collection rates for the TAC and ADC were identical showing no loss between the two processes (not shown here), which means the TAC logged photons are not lost during conversion to digital count.

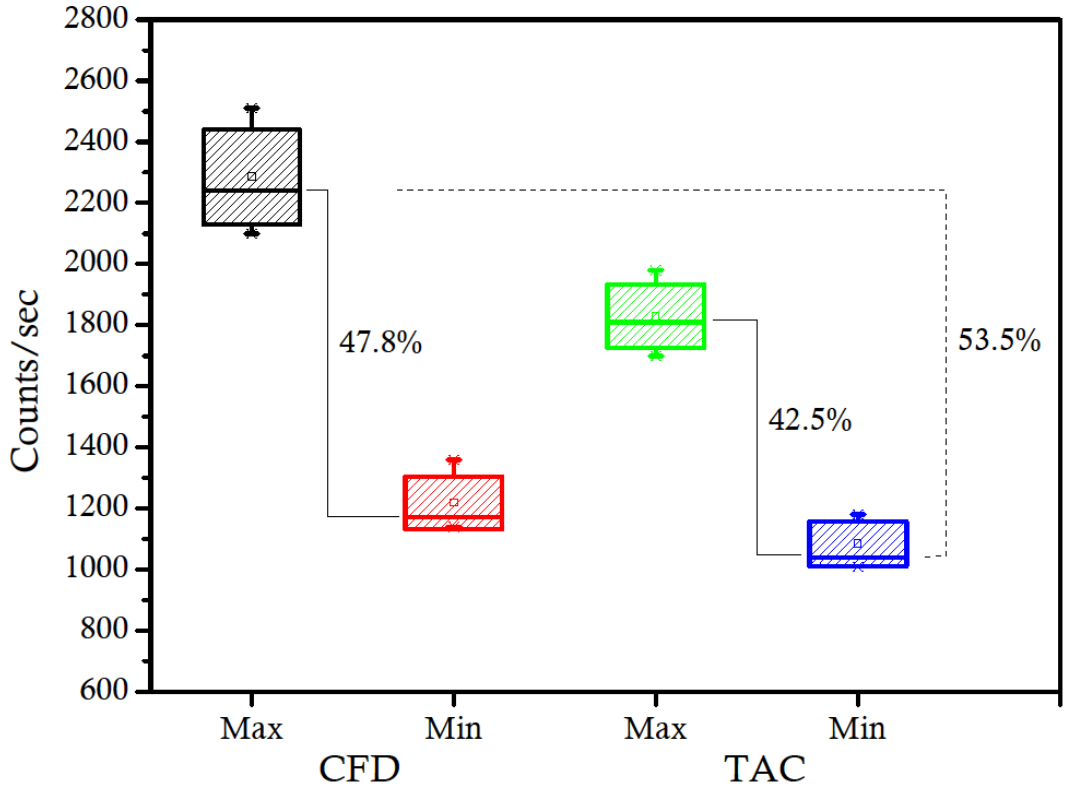


**Figure 107 – Box and whiskers plot of the counts recorded per sec in the CFD and TAC of a non-cellular agarose sample. A comparison between max and min CFD (black and red) and TAC (green and blue), respectively, described as a percentage difference. Box and whiskers represent maximum and minimum values (n=8) and standard deviation, respectively.**

As the TAC and ADC are producing identical results it is important to determine if the counts are translated to the acquired image. The peak and mean collected count per pixel from the imaged samples are compared against the maximum and minimum ADC, respectively, as shown in Figure 108. The mean (±standard deviation) peak pixel counts in the acquired images and the maximum converted counts by the ADC were 509.5 (±25.5) and 779.3 (±44.1) counts/pixel, respectively. The minimum number of photons converted to digital counts is 461.8±30.9 counts/pixel, but there are on average only 351.6±20.4 counts/pixel arriving in the image this is a loss of at least 23% in the processing of data.

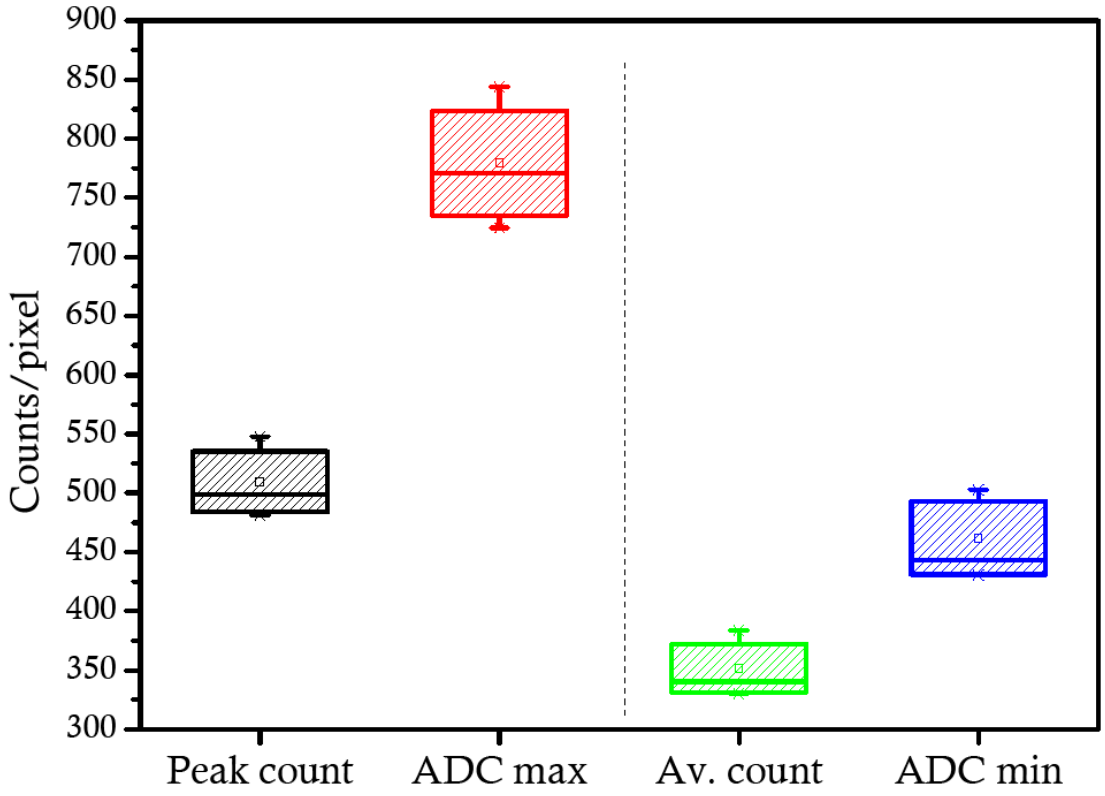


**Figure 108 – Box and whiskers plot of the peak and average counts/pixel in the non-agarose cellular sample. Compared with the estimated peak and minimum count of the max ADC and min ADC, based on the collection rate. Box and whiskers represent standard deviation and maximum and minimum values.**

#### 5.3.3.3 Discussion

Non-cellular agarose samples were tested in experimental conditions to determine effects to photon collection induced during image collection. Low variation between samples was seen for the total number of counts acquired with a difference of approximately 5-7%. The average loss of photons between CFD detection and TAC logging is 20%, but the average loss between mean converted count in the ADC to mean pixel count/image counts could be up to 43%. Therefore, from the mean CFD to the mean pixel count/image there could be as much as a 63% loss of counts. An example showing the maximum collection rate at the CFD would translate to the number of counts/pixel in a 64x33 image format based on the identified variation has been shown in Figure 109.

Even though collection rates have been set within the collection rate limits of minimising pile-up effects a loss is still experienced between the CFD and TAC most likely this arises from classic pile-up [27]. Where the photons are detected at the PMT, but arrive during the dead-time of the TAC during one cycle and are therefore not recorded. This is confirmed by the identical count rates for the TAC and ADC showing no loss between these processes.

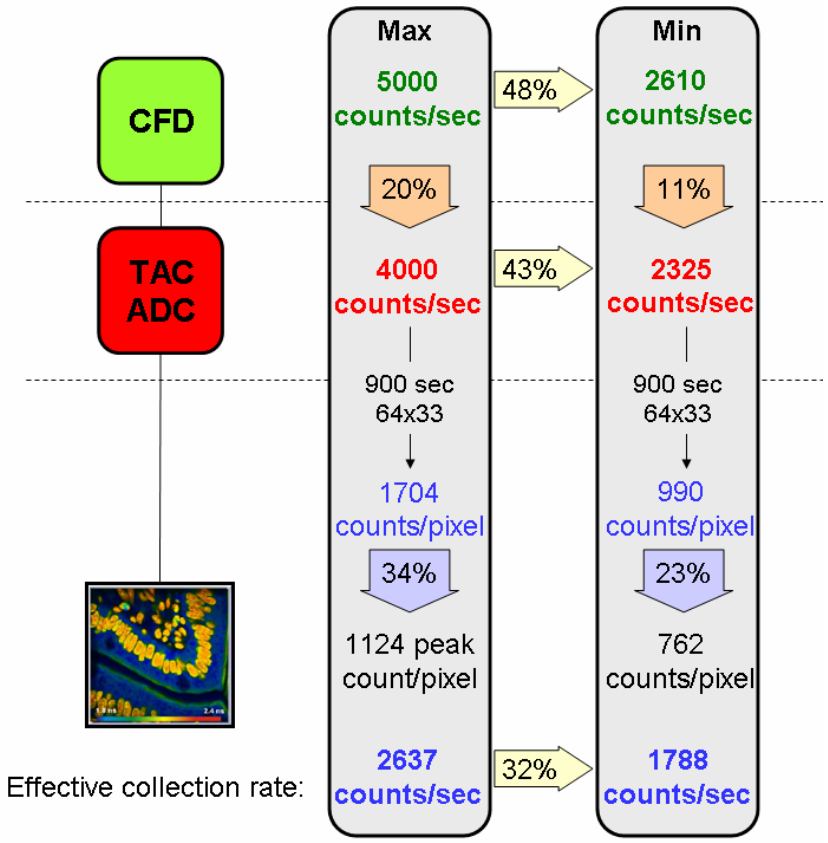


**Figure 109 – Diagrammatic example of the photon counting loss from CFD to acquired image. The components are shown on the left with the CFD, ADC, and example image. Based on the maximum collection rate and outcome from non-cellular agarose images an example estimates the effective collection rate of the setup.**

There is little reason as to why a count loss would occur between the ADC and the image, but there are known issues with regards to electrostatic noise interfering with the time resolution of the ADC by broadening the signals [27]. However this should not affect the conversion of the signal from the ADC to the image unless there is a problem with during the fly back of the laser creating a loss of counts in the pixel. The likelihood is that a combination of this and translation of the counts to the correct pixels in the image. Confirmation of this was seen by comparing other image format sizes, where a 256x256, (data not shown) displayed identical loses of 20% between the CFD and TAC in terms of maximum and minimum values, but only a 9% loss between the estimated total counts and the min ADC. Whereas the 64x33 image had a difference of 23% this shows a large discrepancy.

This has shown that the image acquisition process is also limited by pile-up affecting the TAC. It is important to consider the minimum ADC when estimating the intended collection of counts. However, the max CFD must be used for adjusting the EOM gain and maintaining the collection rate <1% to avoid pile-up. It is assumed that the ADC to image effects seen would be minimised if the pixel clock of the Leica was communicated

directly to the TCSPC. Without this an extra test should be completed comparing the total number of counts in an image to the minimum ADC conversion rate and collection time. This will identify the minimum collection time required for optimum counts/pixel.

### 5.3.4 Image acquisition

A test cell has been used to determine the most appropriate method for displaying the lifetime information and suitable quantitative analysis. Two different software systems were investigated namely SPCImage and TRI2. The test cells was imaged using the proposed experimental method and the analysis method investigated the effect of binning on the image quality and whether an alternative method can or should be used. Cellular preparation and FLIM setup were conducted as described in section 5.2.1.1 and the data analysis methods SPCImage and TRI2 are described below.

#### 5.3.4.1 Single Photon Counting Imaging (SPCImage)

The acquired image of the test cell was transferred from the SPCM to the SPCImage. In 'options' the model preferences are changed to allow for long lifetimes to be analysed. Initially an intensity image is displayed in the top left corner of the SPCImage window (Figure 110A). The cross hairs on the image indicate the peak intensity in the intensity image with the corresponding decay shown in the plot below (Figure 110B). Selecting the appropriate settings for analysis, i.e. shifting the cursors and fixing the 'scatter' to zero, allows the software to apply the exponential fit to each pixel and calculate the lifetime, amplitude, offset and $\chi_r^2$ for each pixel in the image applying a lifetime map superimposed over the intensity image. A histogram of all the calculated lifetimes are displayed in the top right hand corner (Figure 110C) with a rainbow 'look up table'. The size of the 'look up table' can be adjusted by shifting the hue cursors, which assign colours to a particular lifetime range. The overlaid lifetime map is represented by the selected colours.

The pixels that appear inside the cell were thresholded out by placing the cross-hair on a pixel inside the cell and then increasing the threshold 'thld' until the red fitted decay line disappears. The image then requires recalculation. Each time the 'Bin' is adjusted the threshold also requires adjustments and recalculation. The reason for binning is described in section 5.3.2.2, essentially it is a means of reducing the collection time. However the effect to the image quality can only be seen through experimentation.

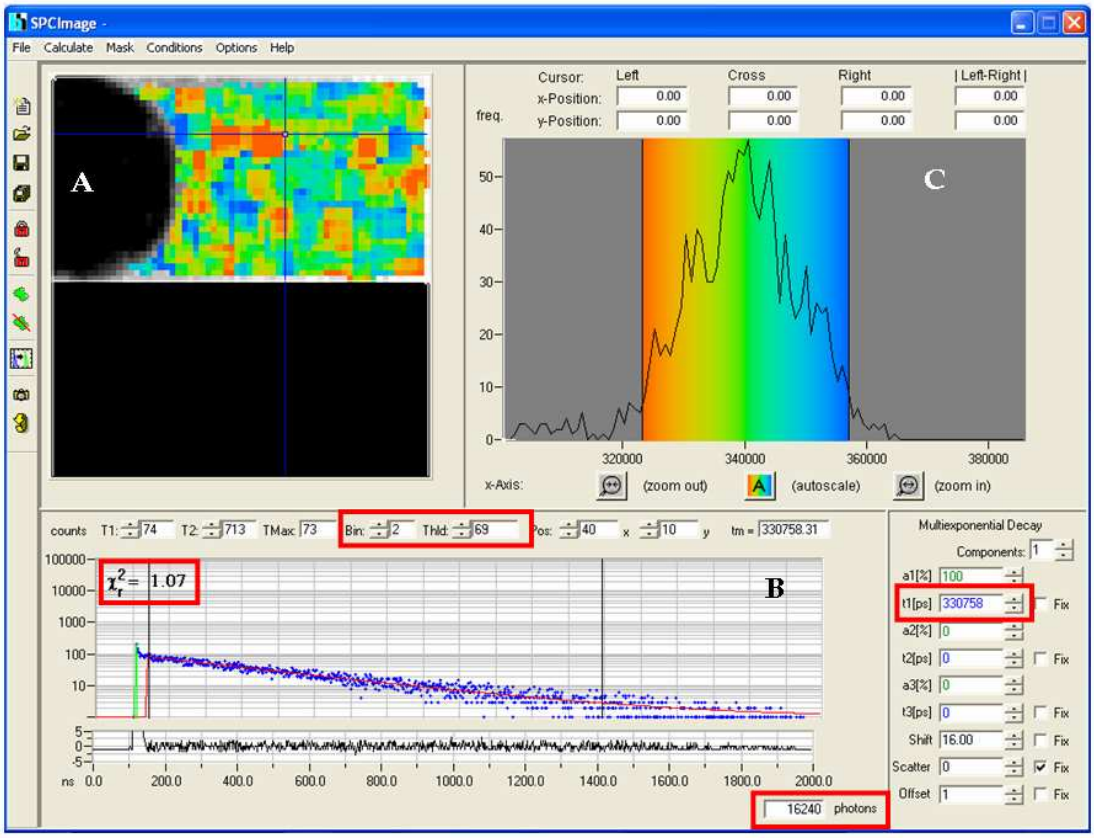


**Figure 110 – Example of test cell in SPCI data analysis program used for determining the lifetime components in the measured data set. A – Original intensity image, latter overlaid by lifetime data, B – lifetime plot for pixel selected by cross hairs. This is automatically selected as the pixel maximum intensity but this can be adjusted by moving the cross hair on the intensity/lifetime image. Highlighted red boxes identify where the binning, tau, threshold 'thld', total number of counts and reduced chi-square are displayed corresponding to this lifetime. C – Histogram of number of pixels at each lifetime values and the rainbow lookup table which can be adjusted by moving the max and min markers. The lifetime of each pixel are then displayed on the intensity image (A) based on this rainbow lookup table.**

Different binning sizes were applied to the test cell as shown in Figure 111. The cross-hair identifies the same pixel in all images. The left side uses the same histogram bandwidth whereas the right-side varies the bandwidths in line the peak base width. It is apparent that with the increasing bin size in Figure 111 the FWHM and peak height of the histogram decreases and increases, respectively. The peak becomes smoother due to the improved fitting from higher counts/pixel. However the lifetime becomes more averaged with decreased FWHM. Without adjustment of the histogram cursors with increase bin size the lifetime contrast disappears (Figure 111 left). To maintain the same level of contrast the cursor requires adjustment to the same percentage of the histogram as shown in Figure 111 right.

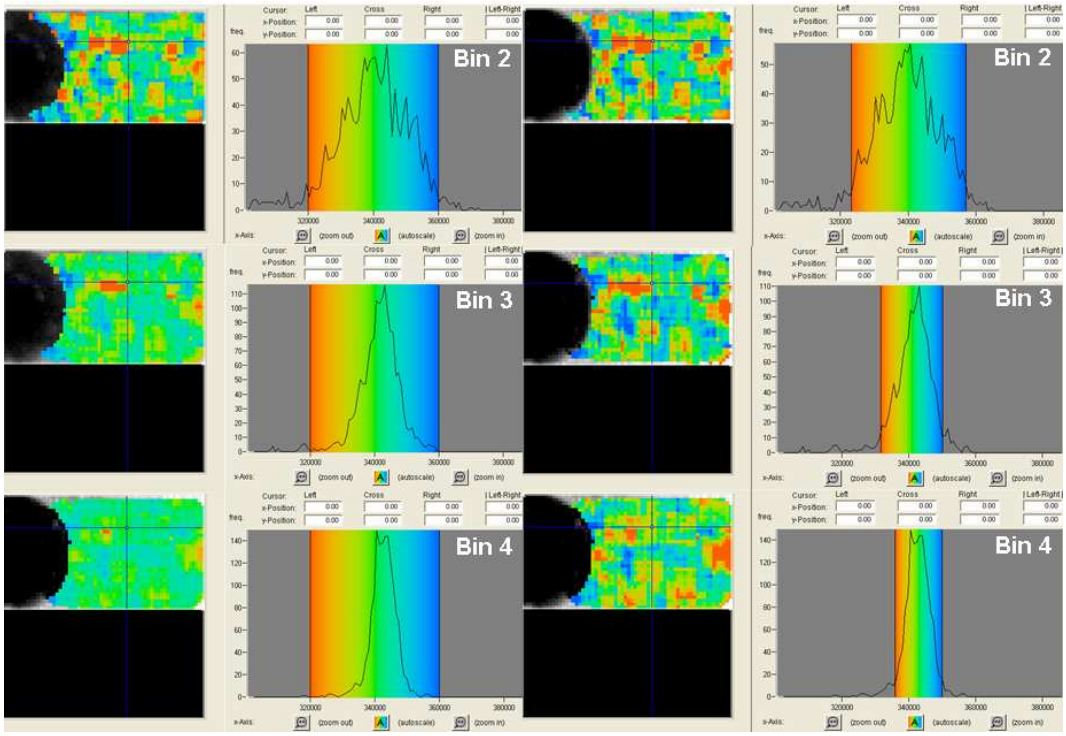


**Figure 111 – Lifetime maps of test cell in agarose with varying binning regimes and colour map selections. Left: Same colour map cursor selection, but varying bin setting from 2, 3, and 4. Right: Adjusted colour map cursor selection cutting off wings of histogram, but using the same bin settings as in left side images.**

### 5.3.4.2 TRI2

The saved files recorded in SPCM are reopened in the TRI2 software. The time resolved analysis is selected from the tool bar opening a separate window, as shown in Figure 112. The intensity image (Figure 112A) has a square box identifying the location of the lifetime decay display (Figure 112B). Adjustment of the cursor in the decay window selects the section of the decay required for fitting with the residual fit below (Figure 112C). Adjustment of the fitting parameters are displayed bottom left, with a selection of fitting models, a targeted Chi-square, and type of noise model. Parameters were set in accordance to these defined in Chapter 3 where the type of fit was set to mono-exponential (Marquardt) and the target Chi-square was set to <1.1 prior to fitting the decay, and the noise model used was based on a Poisson estimate. The fitting function used in these experiments was the Levenberg-Marquardt fitting model.

**Eq. 76**

$$f(t) = Z + A\exp^{\left(-t/\tau\right)}$$

where, $Z$ is the offset, $A$ is the amplitude, $t$ is the time and $\tau$ is the lifetime. Once the selected parameters are set, a variety of options are available for extracting lifetime information.

Pre-processing was selected from 'experimental functions' which applied a threshold excluding low and high values the intensity image. The effect of adjusting these cursors can be seen immediately in the intensity image and the same settings are maintained for future experiments. Adjacent to the threshold is a binning option where a variety of pixel bin types and sizes can be applied to each pixel. Instead of using the standard binning types, square or circle, another option available is a mask. This allows any shape to be designed and applied to the image and binning all the pixels in the mask. The transient decay fitting can be set to automatically update when any adjustments has been made, providing the ability to instantly observe any changes.

The fitted values can be saved separately for individual or multiple images. Experimental and fitted data points can be saved for individual pixels. A global fitting option can be applied to a data set and a lifetime image produced of the fitted values. With the chosen option four images are produced in a separate window consisting of intensity, lifetime, amplitude and $\chi_r^2$. This allows a comparison between the different parameters and can determine possible error or influences from the appearance of similar patterns.

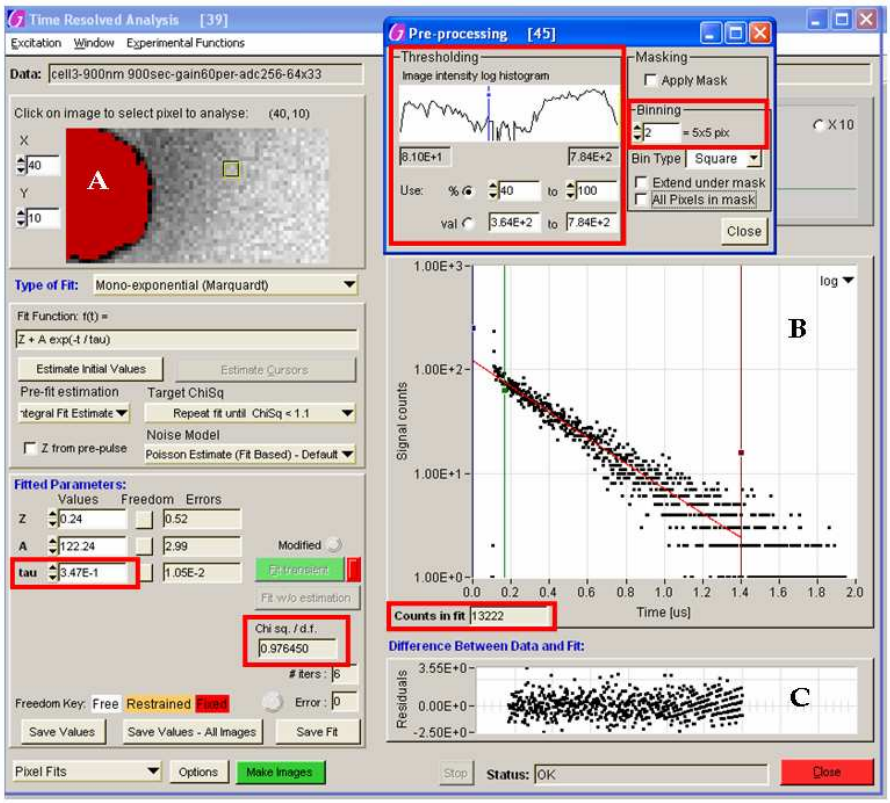


**Figure 112 – Example of test cell in TRI2 time resolved data analysis software for extraction of lifetime information. A – Intensity image, B- Lifetime plot for pixel selected in intensity image, C- Residual corresponding to the lifetime plots above. Highlighted red boxes identify where the binning, tau, total number of counts and reduced chi-square are located.**

The test cell image was applied to the TRI2 software with incrementing bin sizes, as shown in Figure 113. As the bin is increased from Bin 2 (left) to Bin 4 (right) the bin box size increases as well as the amplitude of the decay. The increase in bin provides an increase in the total count such that the decay is less noisy and has an improved weighted residual plot. The histogram variations in lifetime image from bin size adjustment is seen in SPCImage, but does not occur in TRI2 as the cursors position is based on histogram percentage.

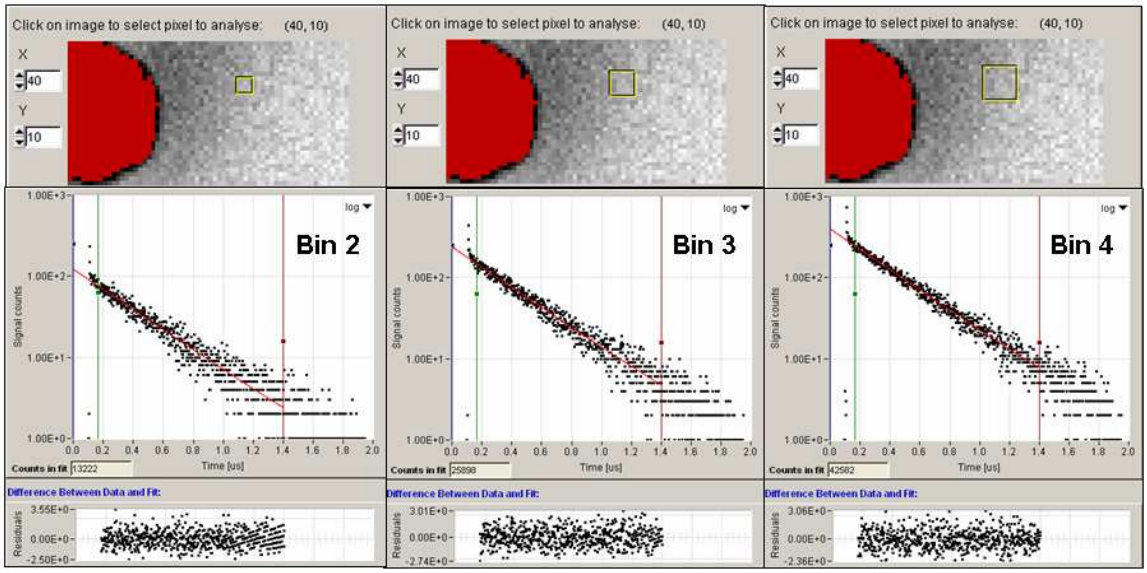


**Figure 113 – Lifetime decay of selected pixel in the intensity image of the test cell at different square binning sizes 2, 3, and 4. The increasing area of the bin is also shown by the yellow box in intensity images, with corresponding lifetime decay and residual plot below.**

### 5.3.4.3 Comparison between SPCImage and TRI2

The test cell has been applied to both software packages with incrementing bins and a direct comparison of the lifetime images produced are shown in Figure 114. The colour maps have been produced with identical mono-exponential decay models that use a least squares Leverburg-Marquadt fitting method. The length of time taken to process the SPCImage and TRI2 image with a bin of 2 was 39 sec and 2.3 sec, respectively. As the bins increase, the contrast between the pixels start to blur and a smoothed less distinct image is produced with reduced spatial resolution. In Figure 114, highlighted regions, depicted by the purple circles in the TRI2 software are maintained in the binned images, but this was not observed in the SPCImage software. As a direct comparison between the software packages the fluorescence decay in one pixel, identified by the cross-hair, was analysed for each bin setting and results displayed in Table 21.

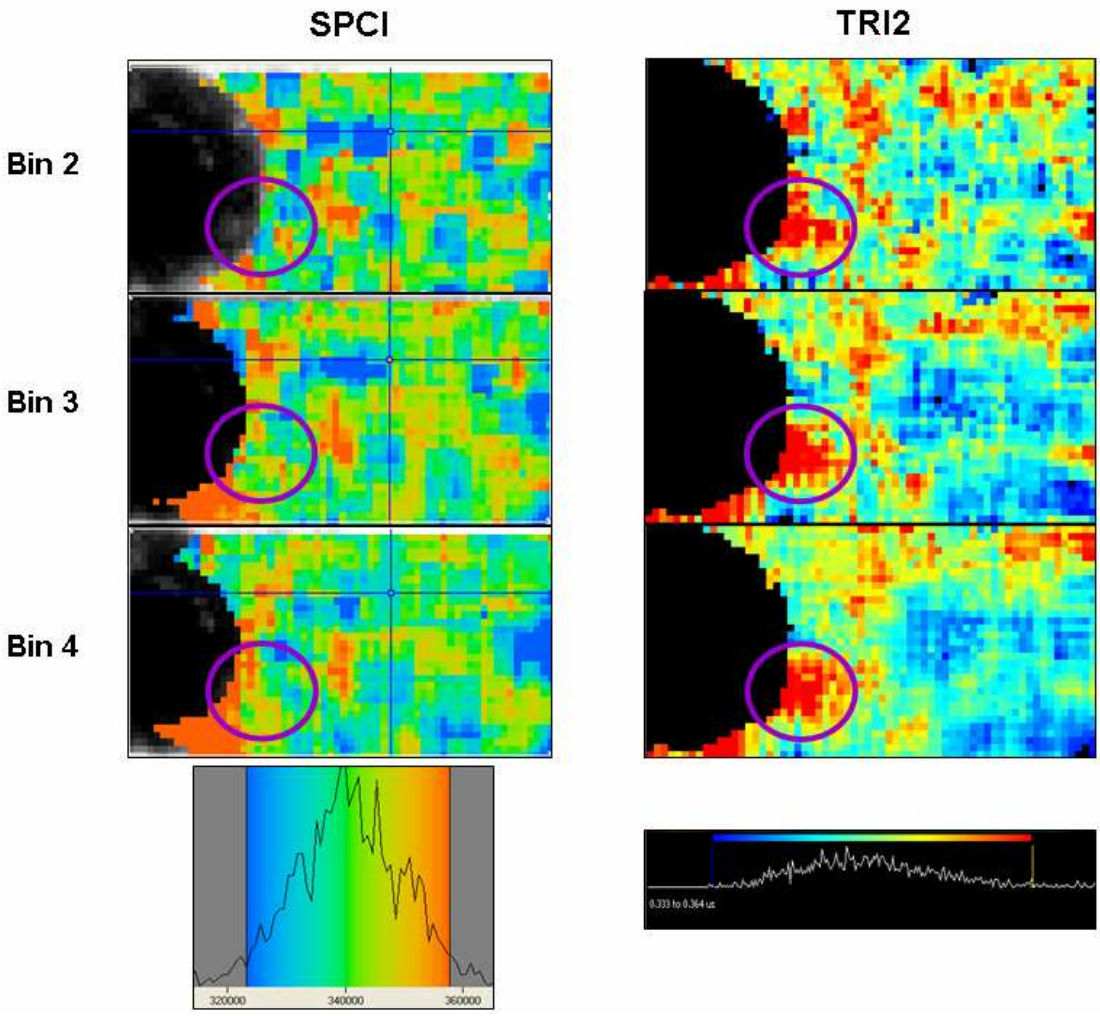


**Figure 114 – Comparison of lifetime maps from the test cell using TRI2 and SPCImage software with binning of 2,3, and 4. The TRI2 software lifetime colours blue to red as 322 to 368 ns and the SPCI the reversed colour red to blue, but the lifetime range changes as shown in figure 13 right.**

**Table 21 – Comparison of data analysis methods using same test cell image with variation in bin number**

| Bin | Data analysis software | | | | | | |
|---|---|---|---|---|---|---|---|
| | SPCI | | | TRI2 | | | |
| | τ (ns) | Total photons | $\chi_r^2$ | τ (ns) | ±sd (ns) | Total photons | $\chi_r^2$ |
| 2 | 330.75 | 16240 | 1.07 | 347 | 10.5 | 13222 | 0.97 |
| 3 | 335.99 | 31693 | 0.95 | 347 | 6.7 | 25898 | 1.02 |
| 4 | 342.0 | 52266 | 1.01 | 345 | 4.8 | 42582 | 0.99 |

Table 21 for both software types shows an increase in the number of counts with increasing bin number. The TRI2 does not have as many counts as the SPCImage due to the TRI2 considering only the number of counts in the fit rather than the total decay as with SPCImage. The TRI2 shows a decrease in the standard deviation with increasing

counts confirming that less variability is seen with higher counts in excellent agreement with Figure 82. Althought for the TRI2 software in Table 21 the lifetime has no decimal places as is displayed in the GUI when the data is exported it provides upto three decimal places matching that of the SPCI software. The $\chi_r^2$ is unaffected by the binning, except maybe a slight improvement from SPCImage. The $\tau$ values calculated with the SPCImage increase with increasing bin size, but for TRI2 there is very little variation. This suggests that the fitting algorithm used for TRI2 is superior to that in the SPCImage and that at lower counts the calculated lifetime will be more reliable. TRI2 has faster data analysis that also produce a visual representation of the fitting parameters as a map and most importantly multiple data files can be analysed simultaneously. A summary of the advantages and disadvantages are discussed in Table 22.

**Table 22 – Summary of advantages and disadvantages of the SPCI and TRI2 lifetime software analysis packages**

| Software | Advantages | Disadvantages |
|---|---|---|
| **SPCI** | - Directly link to acquisition software<br>- Simple to use | - Only one image can be analysed at a time<br>- Only two methods of fitting available<br>- No information on the equations used to fit the decays<br>- Slow data analysis (39 sec) |
| **TRI2** | - Multiple image analysis<br>- Data analysis is faster (2.3 sec)<br>- Threshold is in % therefore automatically adjusts for each bin<br>- All statistical information on screen<br>- Large variety of statistical analysis<br>- Greater flexibility with regards to creating masks and binning | - More complex due to the variety of applications |

The numerous advantages of the TRI2 software outweigh the disadvantaged of increased complexity and suggest that the more proficient software package to use would be TRI2 and thus this software has been selected for all subsequent data analysis.

#### 5.3.4.4 Masking and binning using TRI2

Analysis of preliminary lifetime maps (Figure 114) showed considerable high frequency spatial heterogeneity. A masking binning procedure was used to attempt to reduce the variability and determine the existence of any spatial oxygen gradients that occur with distance from the cell, as might be produced by cellular oxygen consumption. Binning or masking the data in TRI2 can be completed using any shape or number of pixels. If it is assumed that chondrocytes consume oxygen uniformly around the cell periphery, then it is acceptable to image one side of the cell. Binning pixels around the

circumference and shifting the mask radially away from the cell in incrementing steps will provide the ability of a gradient to be determined.

Using TRI2 software, a mask is drawn and loaded on to the FLIM image. The pixels in the mask are binned and time resolved analysis applied only to the masked pixels to create appropriate lifetime decay. This represents one point at a specific distance from the cell (Figure 115) providing single point lifetime measurements at discrete distances from the cell, as shown in Figure 116.

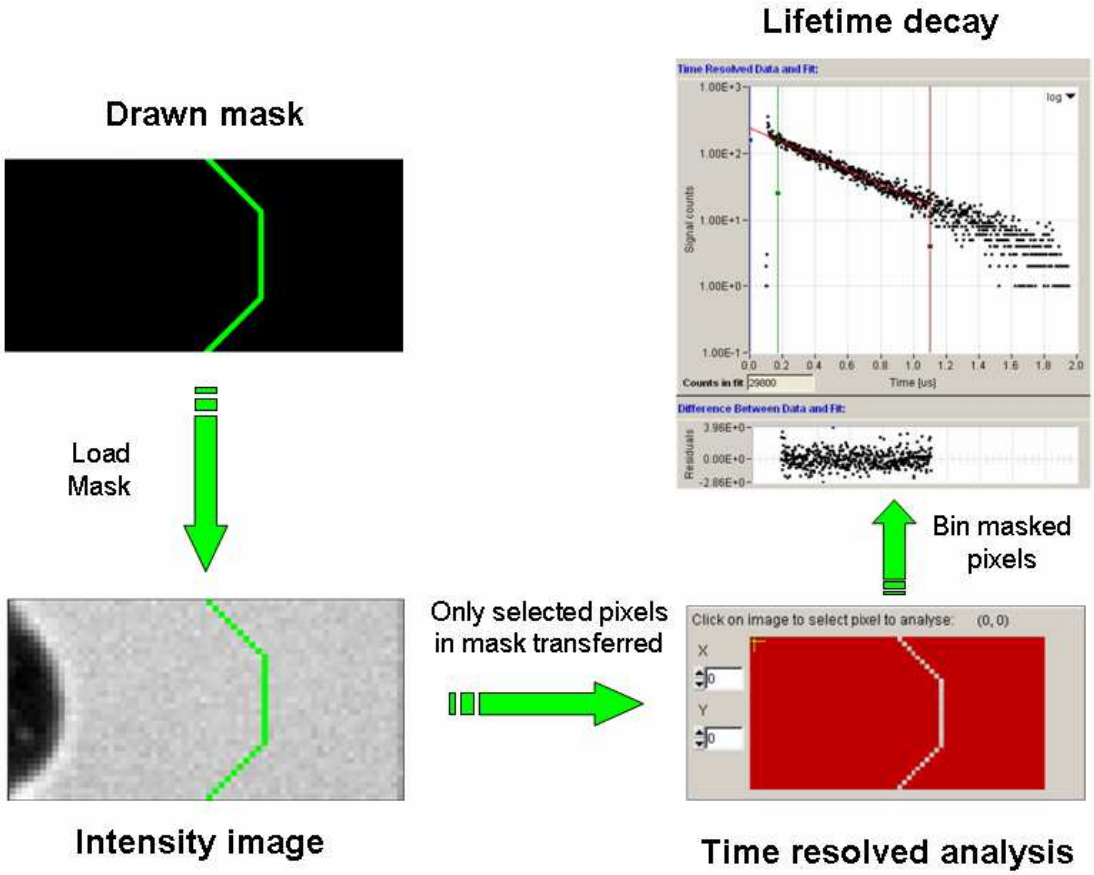


**Figure 115 – Diagrammatic representation of a user defined mask applied to extract lifetime decay information. The mask is used on an intensity image of an unresolved test cell where only the selected pixels in the mask are transferred to the time resolved analysis section and binned to produce a lifetime decay. Separate masks are created along the entire image to produce a single data set of lifetime values versus distance from the cell periphery.**

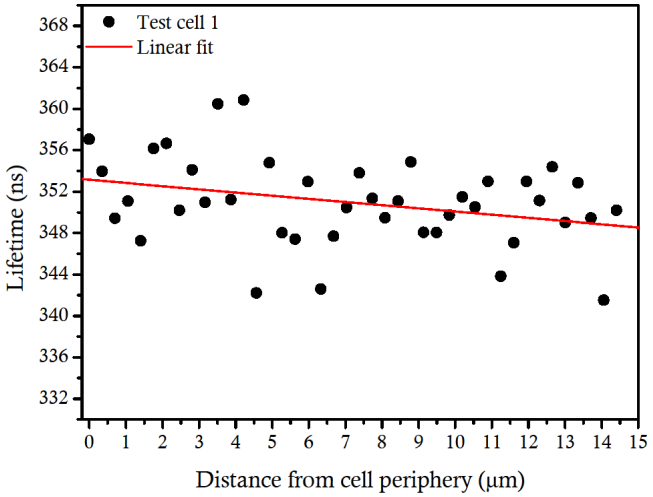


**Figure 116 – Extracted lifetime measurements from chondrocyte with incrementing distance from cell periphery with assumed linear fit (red line) in close proximity to the cell. Test cell 1 shows a significant ($p<0.05$) negative gradient with increasing distance from the cell periphery.**

### 5.3.5 Discussion

The comparison between which analysis software is appropriate for investigating lifetime decays has shown that the TRI2 produces reliable lifetime measurements that can quickly analyse multiple images at the same time. It provides the user with flexibility and allows user defined masks to be generated. Examination of the data extraction process has shown that cellular periphery masks are an appropriate method for completing large scale comparison analysis of lifetime data. By converting lifetime values into oxygen concentration and fitting assumed linear models at close proximity to the cell, gradients can be extracted that will provide a means of quantifying oxygen gradients.

### 5.3.6 Conclusion

The pixel dwell time must be pre-adjusted and saved for each image format and scan speed. A trial and error approach has been used to determine an appropriate pixel dwell time. It is a required step before image acquisition can be correctly processed. This lack of correlation between pixel dwell time could be the source of the discrepancy between the ADC and image counts. A more efficient method would be to install a communication cable between the Leica and TCSPC to avoid this unnecessary step and provide greater flexibility in the adjustment of parameters. The image analysis has shown that the maximum image format size that should be used is 64x33 and that binning pixels within the image is paramount to maintaining low image collection times with high counts per pixel for fitting.

The TRI2 has proven to be the most appropriate software to use for analysing the lifetime decay providing fast, reliable and flexible interfacing software that can implement masking features to extract comparable information. The most appropriate method for mass comparison uses assumed linear fits for deriving the gradients.

## 5.4 Summary

- Chondrocyte cells maintained viability of >90% after laser exposure of 1800 sec at a concentration of 0.412 mM $[Ru(bipy)_3]^{2+}$, showing limited phototoxic effects.
- Pixel dwell time is important for minimsing loss of counts between ADC and image count collection.
- There is a 20% loss of counts between CFD and TAC due to pile-up eventhough the collection rate has been maintained <1% of the repetition rate.
- TRI2 has been chosen as the superior software package to allow flexible masking and application.
- Linear fits applied to the extracted data can be used to derived spatial oxygen gradients assuming that the gradient is linear over the short distance.
- The estabilished protocol uses image settings for future experiments as 900 sec collection time full binning of mask containing 33 pixels.

# Pericellular $O_2$ Investigation

# 6

## 6.1 Introduction

The previous chapter identified that no phototoxic effects were induced by the imaging protocol. A data analysis procedure has been established and can now be applied to live cell quantification of spatial oxygen gradients in conjunction with the developed imaging protocol. Application of the optimised FLIM technique can finally be used to quantify spatial oxygen gradients in living three-dimensional cellular systems. Confirmation that the information acquired is derived from cellular consumption and not an artificial artefact arising from the surrounding cell will complete the validation of this technique. All experiments were conducted in accordance to parameters outlined in chapters 3 and 5.

### 6.1.1 Pericellular oxygen quantification

Researchers have shown that the same cell types exhibit different rates of oxygen consumption depending on cell location within the native tissue and associated access to nutrients and oxygen. Specifically in articular cartilage, chondrocytes isolated from the deep zone display larger morphology and higher rates of oxygen consumption compared to the superficial zone cells [127]. The optimised FLIM system was applied to 50 individual bovine articular chondrocytes seeded in agarose constructs from within air tight chambers. Established analysis procedures were applied for investigating pericellular oxygen concentrations at the periphery of the chondrocytes. The chondrocyte diameters were measured in an attempt to determine a relationship between gradient and chondrocyte size.

### 6.1.2 Extrinsic manipulation of oxygen consumption

In order to confirm that the spatial oxygen gradients observed occur from cellular oxygen consumption, further studies were conducted in which cellular oxygen consumption was manipulated artificially. Cellular oxygen consumption was elevated by

addition of oligomycin, which decreases oxygen consumption or CCCP which increase consumption. In addition oxygen consumption was also increased by reducing the glucose concentration within the cell culture media. All cellular preparation, FLIM setup, data acquisition and data analysis was conducted as outline in section 6.2.

## 6.2 Materials and Methods

### 6.2.1 Normal cell culture media preparation for imaging spatial oxygen gradients

#### 6.2.1.1 Cell preparation

Chondrocyte-agarose constructs were prepared as outlined in section 3 of chapter 2. Briefly, cartilage was dissected from adult bovine metacarpal-phangel joints (n=3) and sequentially digested in an oven at 37ºC with pronase and collagenase enzymes, for one and 14 hours respectively. The digest solutions were sieved, washed three times with DMEM+16%FBS, pooled together, and resuspended in 30 ml fresh DMEM+16%FBS. Cells were counted and seeded at $4x10^6$ cell/ml in 3% (w/v) agarose, type VII (A4018). The cell-agarose mixture was gelled at 4°C for 20 mins in specially designed air-tight chambers (see Appendix B). Quarter sections of the cell-agarose gelled mixture were removed to provide fast delivery of $[Ru(bpy)_3]^{2+}$ to cells and to enable studies to investigate the relationship between depth within the agarose and oxygen consumption. Each chamber was filled with 1 ml of media, caps loosely fitted, in a 5%$CO_2$ incubator at 37ºC and left overnight to stabilise. Prior to a chamber being imaged, the media was replaced with $[Ru(bpy)_3]^{2+}$+DMEM+16%FBS (0.412 mM) and returned for further incubation at 37°C for 1.5 h. Once chambers had completed the incubation period with $[Ru(bipy)_3]^{2+}$+media chambers were transferred sequentially to the heating plate on the microscope stage.

#### 6.2.1.2 Imaging protocol

Chambers were rotated to allow the removed quarter section to be imaged in the top right corner. Cell location in relation to the agarose edge was identified with the aid of a transmitted PMT using He/Neon laser (ex 633nm, image format 512x512) and a x63 oil immersion objective lens (N.A. 1.4).

The chosen cell was centred in the x-y axis then the image format and voxel size was adjusted to 64x33 pixels and to 350x350 nm, respectively. The right side of the cell was positioned on the left of the image, as shown in Figure 117. The detector was switched to the TCSPC PMT and repetition rate was dropped to 500 kHz with a collection rate $<5x10^3$ counts/sec. The TCSPC parameters were set as described in Chapter 3 with a collection

time of 900 sec and image format set to 64x33 to match the Leica file setup. This method was repeated for each cell and as a control applied to chambers with cell free agarose.

#### 6.2.1.3 Data acquisition

A set of 59 masks were created that mapped the curvature of the cell periphery at incrementing points along the x-axis. FLIM experimental data sets for each cell (n=52) and control (n=8) were loaded in TRI2 for analysis. The furthest mask from the cell periphery was loaded first and applied to each data set. Each mask was binned and a mono-exponential fit was applied and decays were accepted based on established parameters namely $\chi_r^2 \leq 1.17$ and adjusted $R^2 > 0.9$. This was maintained for each mask fitting and the fitted parameters for each data set were saved into an Excel file. A Matlab file was created (Appendix E) that extracted the fitted parameters, $\tau$ and amplitude. This correlated each mask to the corresponding location in x-axis of the image and compiled it for each data set. It finally produced two separate spreadsheet files containing $\tau$ values and the corresponding amplitude values of that decay for each data set. These were imported into OriginPro8.

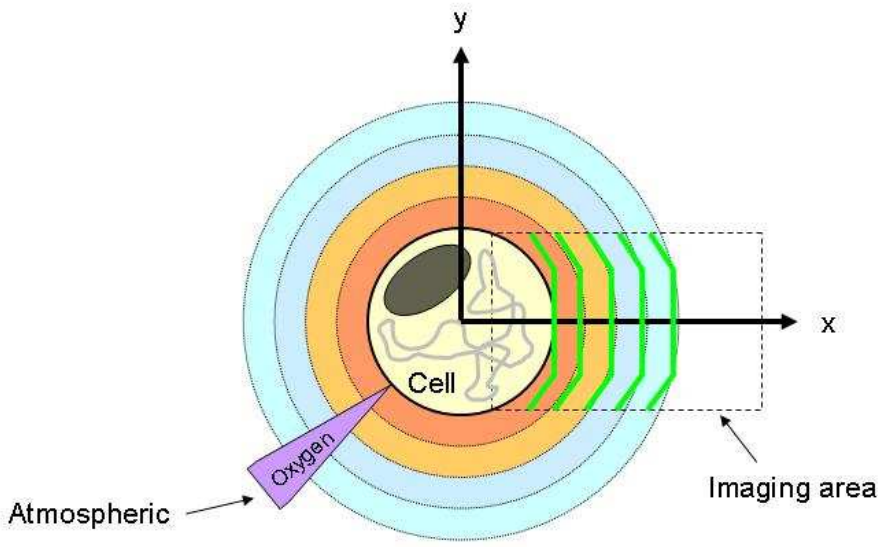


**Figure 117 – A schematic representation of the theoretical pericellular oxygen gradient and the imaging approach used for quantification. The green lines indicate the binning masks (n=59) used during the data processing.**

The edge of the cell, identified from the brightfield image correlated with the drop in amplitude in the two photon image presumably where the $[Ru(bipy)_3]^{2+}$ was excluded from the viable cell (Figure 118A). Thus it was possible to use the amplitude data with a high pass cut-off threshold value to identify the location of the cell periphery. All amplitude values below this cut off value were removed along with the corresponding $\tau$ values. The adjusted $\tau$ data sets were plotted against distances using the imaged voxel size as a measure of distance from the cell periphery.

### 6.2.1.4 Data analysis

Post-processing was performed to determine the cell diameter (Figure 118A) and distance of the cell from agarose edge, as shown in Figure 118B & C. This was achieved by importing the Leica 4 MHz intensity and brightfield images into Volocity (Version 5.1). The τ values were converted to oxygen concentrations using the rearranged equation defined in Chapter 4 section 4.3, as shown in Figure 122:

**Eq. 77**

$$[O_2] = \frac{\tau - 460.421 \times 10^{-9}}{-616.598 \times 10^{-6}}$$

The resulting oxygen concentrations were plotted against distance from the cell periphery for each cell. It was assumed that over such a short distance linear fits were an appropriate approximation to determine the gradient at close proximity to the cell. This would identify which cells presented a significant level of change in the oxygen concentration in relation to the distance from the cell periphery.

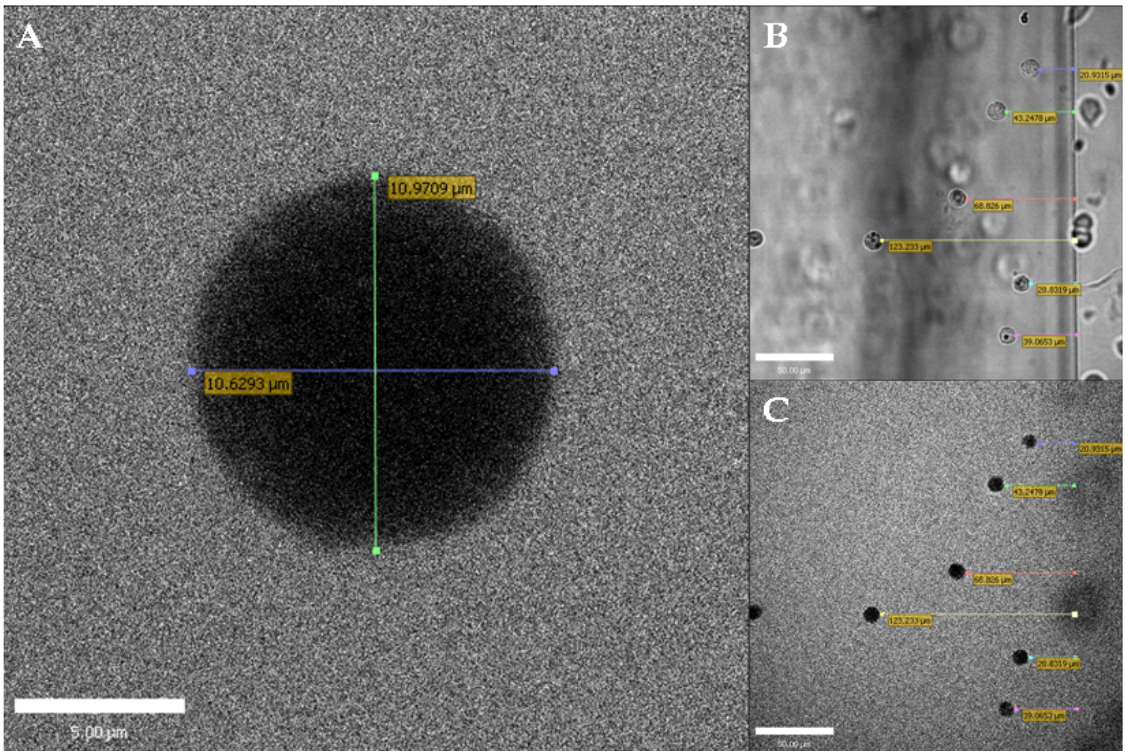


**Figure 118 – Two-photon and brightfield image of chondrocytes embedded in agarose and bathed in $[Ru(bipy)_3]^{2+}$+DMEM+16%FBS. A: 4 MHz TP zoomed in image of a chondrocyte appearing as the black void and the grey intensity as $[Ru(bipy)_3]^{2+}$ in solution in agarose. The green and blue lines are drawn on measurements using Volocity™ displaying the x and y diameters of the cell. Scale bar for A = 5 µm. B: Brightfield and C: 4 MHz TP image of a cluster of cells next to agarose edge, the coloured lines are measurements from the edge of the cell to the agarose edge. Scale bar for B&C = 50 µm.**

### 6.2.2 Regulation of respiration through addition of CCCP and oligomycin

The rate of oxidative phosphorylation is based on the level of proton gradient across the mitochondrial membrane and regulated by the synthesis of ATP, as shown in Figure 119A. It is possible to bypass this regulation by uncoupling the mitochondrias reliance on the ATPase pump for maintaining proton levels. Uncouplers of oxidative phosphorylation are weak organic acids with delocalised negative charge allowing the uncoupler molecule to penetrate the membrane [145]. In an attempt to compensate, the negatively charged compound is translocated out of the mitochondria, while the protonated uncoupler diffuses back into the matrix, thus degrading the proton gradient.

Two types of uncoupling exist intrinsic and extrinsic. Intrinsic arises from degradation of the proton gradient within the cell, whilst extrinsic is caused by an externally applied compound that restricts proton pump transportation [145]. The most commonly used uncouplers are carbonyl cyanide 3-chlorophenylhydrazone (CCCP) and carbonylcyanide-4-trifluoromethoxyphenylhydrazone (FCCP). Both have been used in numerous studies on various cell types including chondrocyte cells [125, 126]. The uncoupler compound bypasses the normal ATPase pump (coupled) and permeates the membrane, as shown in Figure 119B. However, specific dosing must be used otherwise the oxidative pathway becomes inhibited affecting oxygen utilisation. However when used at an adequate dose it inhibits ATP synthesis, while upregulating oxygen utilisation [287].

Inhibition of oxygen utilisation can be achieved through the addition of oligomycin. This inhibits $H^+$ entry through $H^+$-ATP synthase [287] by binding to the transmembrane $H^+$ carrier, the $F_0$ subunit, of the ATPase pump [5] , as shown in Figure 119C. This blocks the movement of protons through $F_0$ and therefore inhibits transportation of $H^+$ effecting the ability of the mitochondria to regulate the proton gradient and reduces the consumption of oxygen [266].

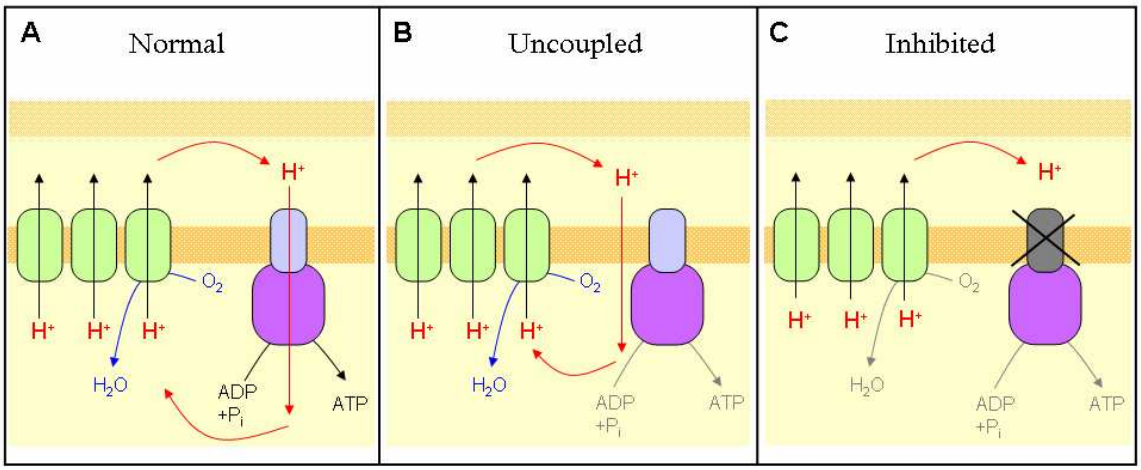


**Figure 119 – Schematic diagram describes the proton pumps involved in the electron transport chain (green) and ATP synthesis ($F_0$ - light purple, $F_1$ - dark purple) used for oxygen consumption and ATP production, respectively. A: Normal production, B: CCCP uncouples flow of $H^+$ through ATP synthase and permeates membrane with $H^+$ inhibiting ATP production, C: Oliomycin inhibits $F_0$ of ATP synthase restricting proton flow and production of ATP.**

#### 6.2.2.1 Cell culture preparation for incubation with inhibitor and uncoupler

Normal DMEM+16%FBS culture media was used as the control solution and prepared as previously described in Chapter 2. Stock solutions of CCCP (C2759, Sigma-Aldrich, UK) and oligomycin (O4876, Sigma-Aldrich, UK) where created with dimethyl sulfoxide (DMSO) (D2560, Sigma-Aldrich, UK) at a concentration of 4 g/l and 1.23 g/l. Stock solutions were separately diluted with 10 µl of dissolved in 90 µl of normal DMEM+16%FBS media. Filtered 1 ml $[Ru(bipy)_3]^{2+}$+media (0.412 mM) was incubated with cells for 1.5 h prior to imaging. Half an hour prior to the start of imaging 5 µl of the oligomycin or CCCP was added to $[Ru(bipy)_3]^{2+}$+media in chambers and then return for continued incubated. This created a final concentration of 2 µg/ml and 3 mM for oligomycin (Olig) and CCCP, respectively [125, 129]. These concentrations had been previously tested on chondrocytes by Heywood *et al.* [125] to determine the optimum level and incubation period to induce inhibition and upregulation of oxygen consumption.

### 6.2.3 Regulation of oxygen consumption through changes to glucose concentration

In articular cartilage, oxygen consumption is inhibited by glucose [127], which is defined as the Crabtree effect and sometimes referred to as 'negative Pasteur effect'. Heywood *et al.* [127] and Zhou *et al.* [326] investigated the oxygen consumption response of isolated bovine articular chondrocytes to different concentrations of glucose cell culture media. Zhou *et al.* measured the response of chondrocytes in alginate to changes in cell culture glucose over a wide range of concentrations 0-10 mM. Whereas Heywood *et al.* measured the effect of glucose concentration over 0-22 mM on the oxygen consumption

rates of subpopulations of superficial and deep zone chondrocytes seeded in agarose constructs. Figure 120 shows the results of the two experimental studies which indicate that an increase in oxygen consumption occurs when glucose concentration is reduced to less than approximately 5 mM.

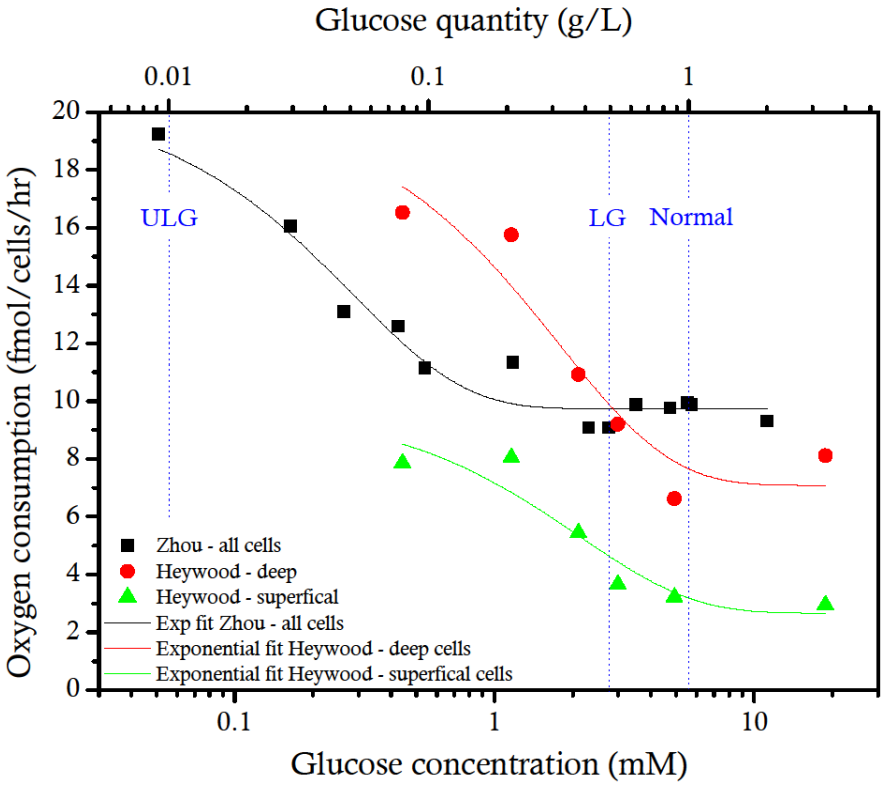


**Figure 120 – Response of chondrocyte oxygen consumption rates to glucose concentrations in cell culture media. Plot shows a comparison between two investigating researchers using different matrix substrate for chondrocyte cell culture. Chondrocytes cultured in alginate beads (black squares) represented by averaged extracted data from Zhou *et al.* [326]. Chondrocytes separated into superficial (red circle) and deep (green triangle) populations seeded in agarose constructs represented by extracted and unnormalised data from Heywood *et al.* [127]. Dashed lines represent the suggested quantities of glucoses that should be added to solution**

### 6.2.3.1 Cell culture media preparation

For these studies, ultra low glucose (ULG) and low glucose (LG) media were created from powdered DMEM (D5030, Sigma-Aldrich, UK) following company instructions [269]. Briefly, 8.3 g/l powered DMEM was dissolved in deionised water with 3.7 g/l sodium bicarbonate (S8875, Sigma-Aldrich, UK). For ULG and LG DMEM solutions 0.01 g/l and 0.5 g/l of glucose (G6152, Sigma-Aldrich, UK) were added respectively. Osmolarity and pH levels were adjusted between 320-340 mOsm and pH 6.8-7.1, respectively. Prior to filtering, 3.8 g/l HEPES (H0887), 80.6 U/ml penicillin and 80.6 mg/l streptomycin (P4333), 0.12 g/l L-ascorbic acid (A0278), 1% L-glutamine (G7513), and 16% (v/v) fetal bovine serum (FBS) (F7524) (Sigma-Aldrich, UK) were added to 500 ml of DMEM ULG and LG. Normal media solution was prepared as previously described in Chapter 2 and contains 1 g/l of glucose.

## 6.3 Results

### 6.3.1 Pericellular spatial oxygen gradient quantification under normal conditions

#### 6.3.1.1 Statistically significant pericellular oxygen gradient occurs around a subpopulation of cells

A subpopulation of 54% (28/52) of cells in agarose gel had no statistically significant correlation between oxygen concentration and distance from the cell periphery (Figure 122A). For the other 46% of cells, there was a statistically significant positive correlation ($p<0.05$) (Figure 122B). Only 4% of cells (2/52) showed a negative gradient, however, neither of these were statistically significant (Figure 123).

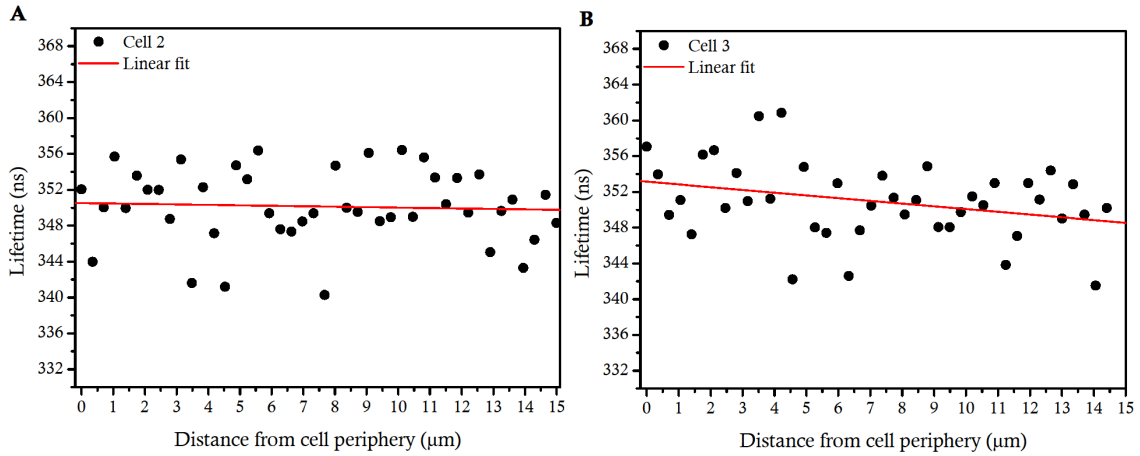


**Figure 121 – Representative raw data displaying the change in lifetime with spatial variation from the cell periphery with assumed linear models applied at close proximity to the cell. (A) Cell 2 displays no statistical significant correlation with distance, however (B) Cell 3 does display a significant negative correlation ($p<0.05$) with a gradient.**

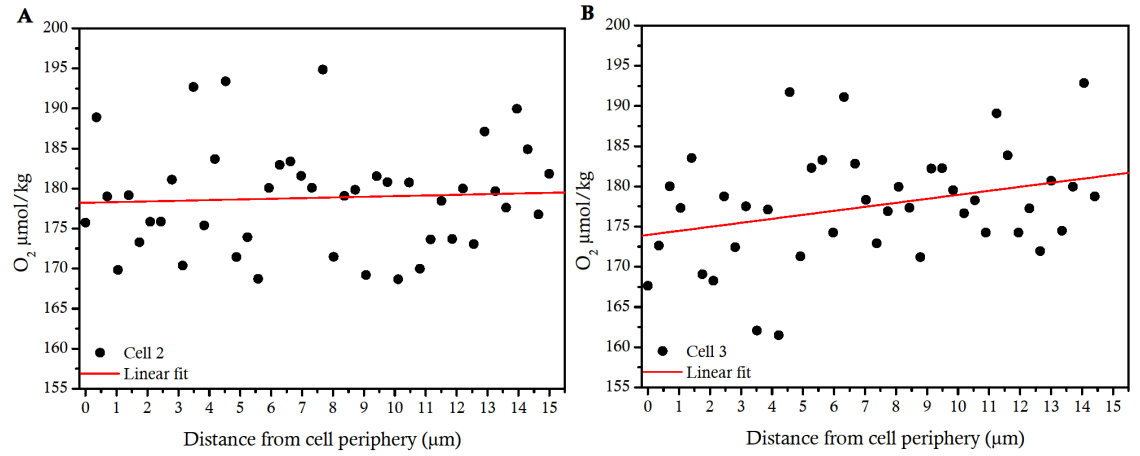


**Figure 122 – Converted lifetime data of representative cells in graph above showing spatial variation in oxygen concentration with distance from the periphery of two cells with linear models assumed at close proximity to the cell were fitted to the data. For cell 2 (A), the linear model shows no statistically significant correlation. For cell 3 (B), there is a significant positive correlation ($p<0.05$) with a gradient of 0.5 µmol/kg/µm and pericellular oxygen concentration of 174 µmol/kg.**

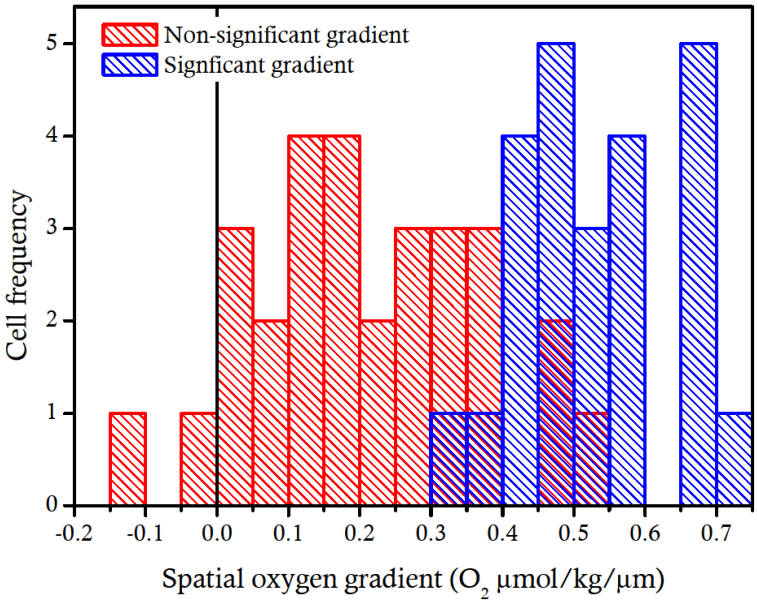


**Figure 123 – Cellular frequency distribution of spatial oxygen gradients derived from linear models fitted to data sets of change in oxygen concentration versus distance from the cell periphery.**

### 6.3.1.2 Cells with significant pericellular gradient are larger than those without

The significance of the linear fit for each cell has been plotted against cell diameter in Figure 124. The dashed line identifies the cut-off between significant ($p<0.05$) and non-significant ($p>0.05$) gradients.

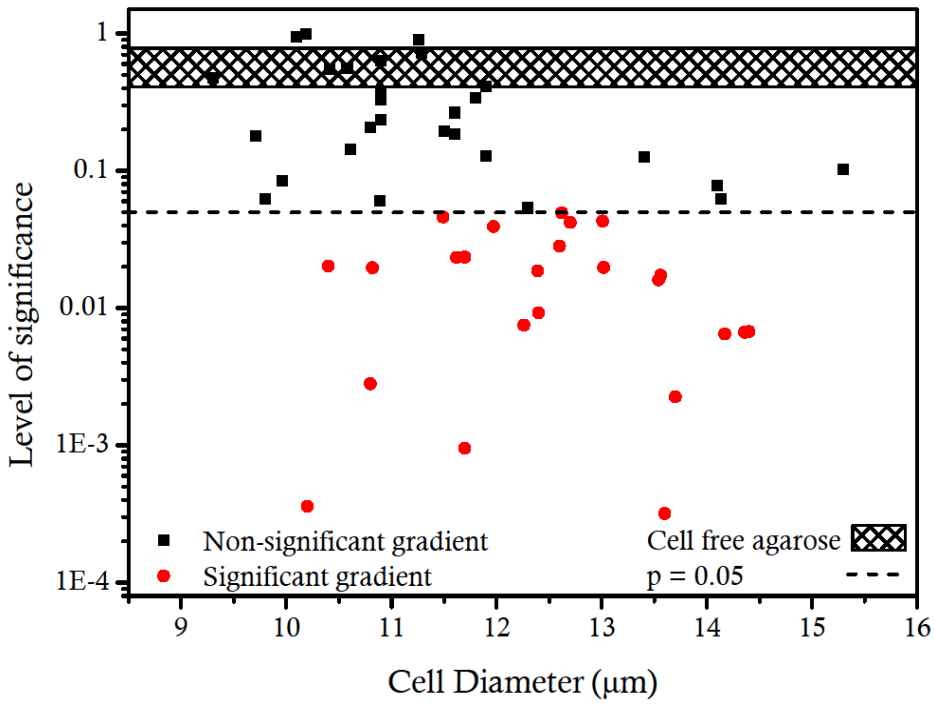


**Figure 124 – Significance of gradient verse cell diameter (n=52). The level of statistical significance (p) of the correlation between oxygen and distance from cell periphery is plotted against cell diameter. A statistically significant gradient was indicated by a p-value<0.05 (red circles). The hashed area represents the range of measurements taken from agarose with no cells.**

The cells associated with statistically significant oxygen gradients were larger than those with no statistical significant gradient (Figure 125). The significant set of cells had a median diameter of 12.5 μm whereas the non-significant cells had a median diameter of 10.9 μm. This difference in cell size was itself statistically significant based upon a Mann-Whitney U-test ($p<0.05$).

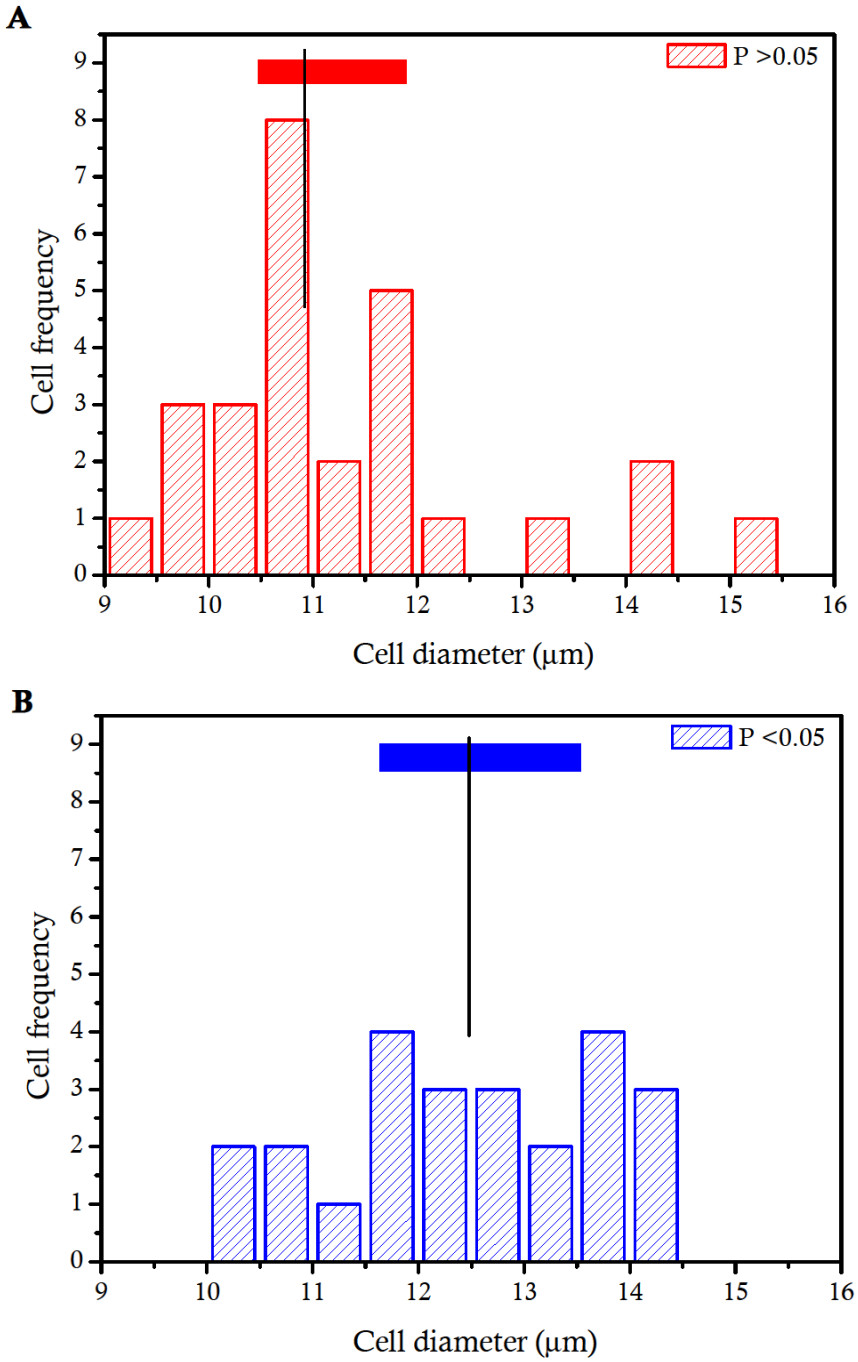


**Figure 125 – Histograms depicting the frequency of significant and non-significant cells in relation to cell diameter. A: Non-significant ($p>0.05$) population (red hash), B: Significant ($p<0.05$) cell population (blue hash). The bars and black lines above the histograms display the lower/upper quartiles and the median values, respectively.**

6.3.1.3 No correlation was found between cells with significant pericellular gradient and cell diameter

The relationship between cell diameter and oxygen gradient is shown in Figure 126. The linear model was applied to those gradients that were statistically significant (circles). However there was no significant correlation between oxygen gradient and cell size ($p>0.05$). However if all the data points are included there was a statistically significant positive correlation between oxygen gradient and cell diameter ($p<0.0005$).

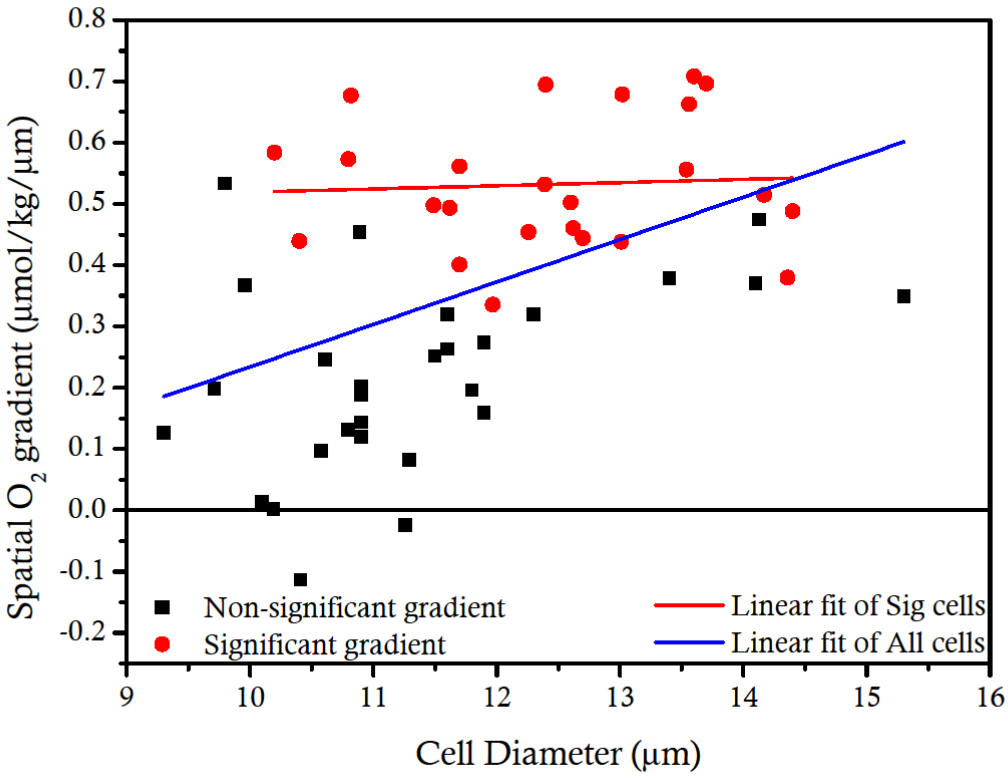


**Figure 126 – Relating the change in oxygen concentration per micrometer to cell diameter for all cells. Non-significant (black squares) and significant (red circles) cells are plotted and correlated to cell diameter. A linear fit is completed for the significant cells (red line) and all cells (blue line).**

6.3.1.4 No correlation was found between depth of measurement into agarose and spatial oxygen gradient or pericellular oxygen concentration

The correlation of cellular oxygen spatial gradient with cell depth in relation to the pericellular oxygen concentration and agarose edge is shown in Figure 127 and Figure 128, respectively. Linear fits were applied to the populations of significant spatial oxygen gradient cells and whole cell population. Both populations showed no significant correlation of spatial oxygen gradient with pericellular concentration or cell depth ($p>0.05$).

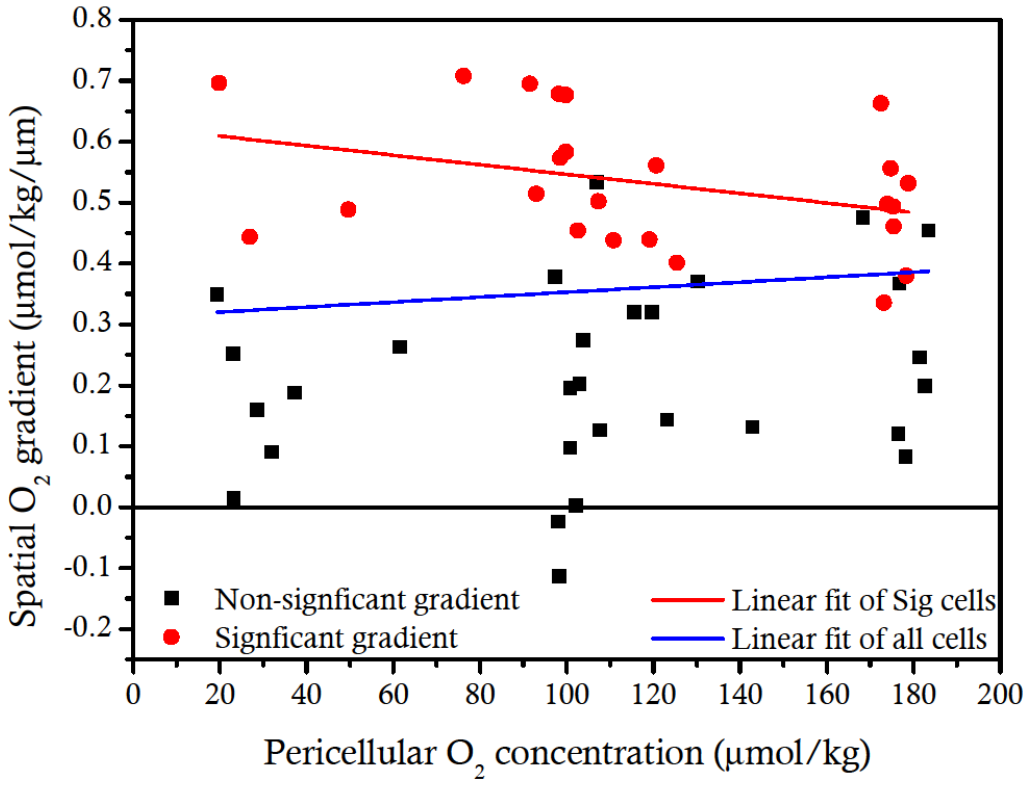


**Figure 127 – Linear fits between the pericellular oxygen concentration and the spatial oxygen gradient showed no statistically significant correlation (p>0.05).**

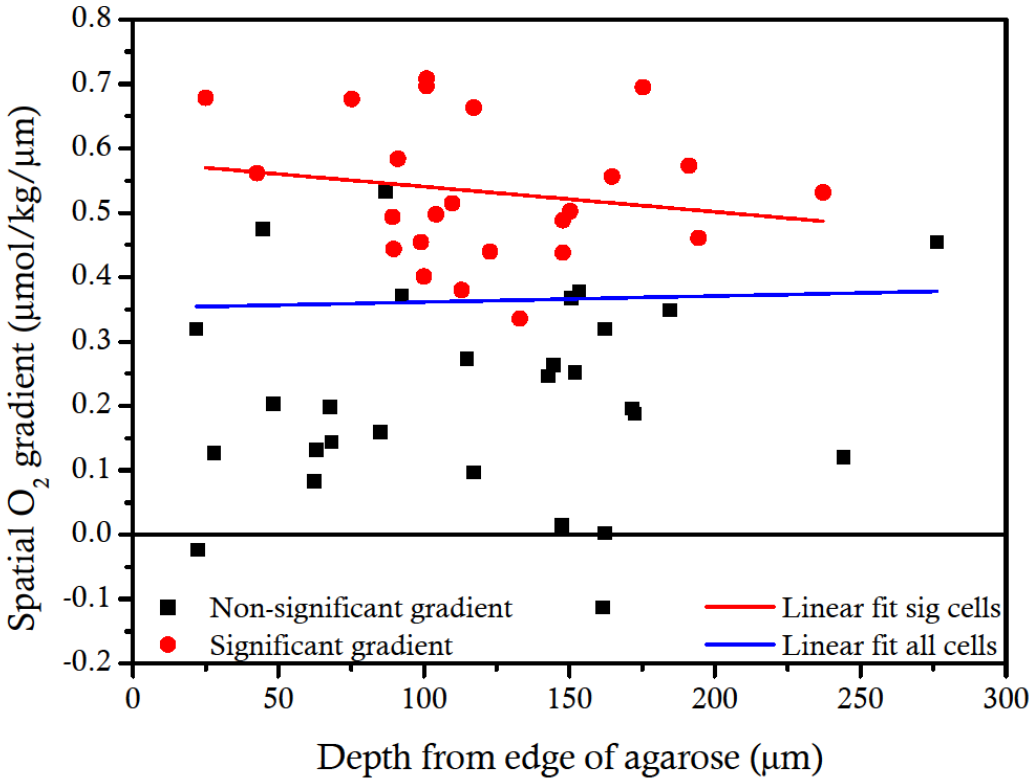


**Figure 128 – Cellular oxygen gradient related to depth of cell in agarose from nutritional access. Linear fit in statistically significant cells and all cells showed no significant correlation between spatial oxygen gradient and depth of cell (p>0.05).**

### 6.3.2 Extrinsic manipulation of oxygen consumption rate can effect spatial oxygen gradient

The percentage of cells displaying statistically significant spatial oxygen gradients was 46% for normal DMEM, 39% for media supplemented with oligomycin, 45% for media supplemented with CCCP, 53% for cells incubated in ultra low glucose and 48% for cell incubated in low glucose media (Figure 129). Using $\chi^2$ analyses of proportions no statistically significant difference was see between any of the conditions for the effect to cell populations exhibiting statistically significant spatial gradients.

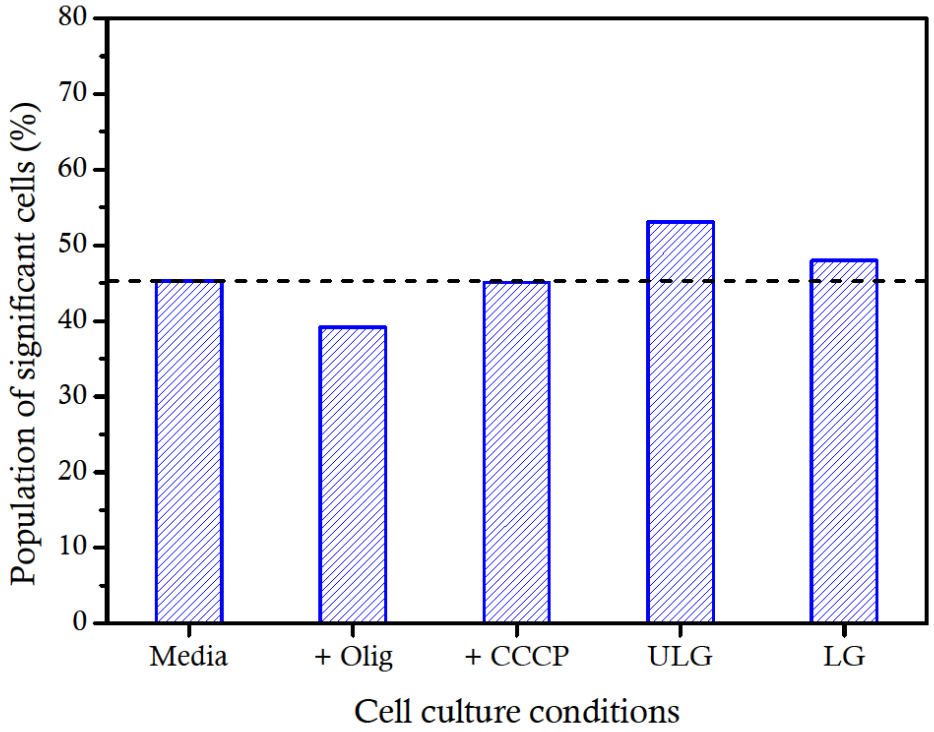


**Figure 129 – Bar graph displays the population of significant cells in different cell culture conditions. Normal cellular media (DMEM+16%FBS) and then supplemented with Olig (oligomycin) or CCCP and cells cultured in ultra-low glucose (ULG) and low-glucose (LG) media.**

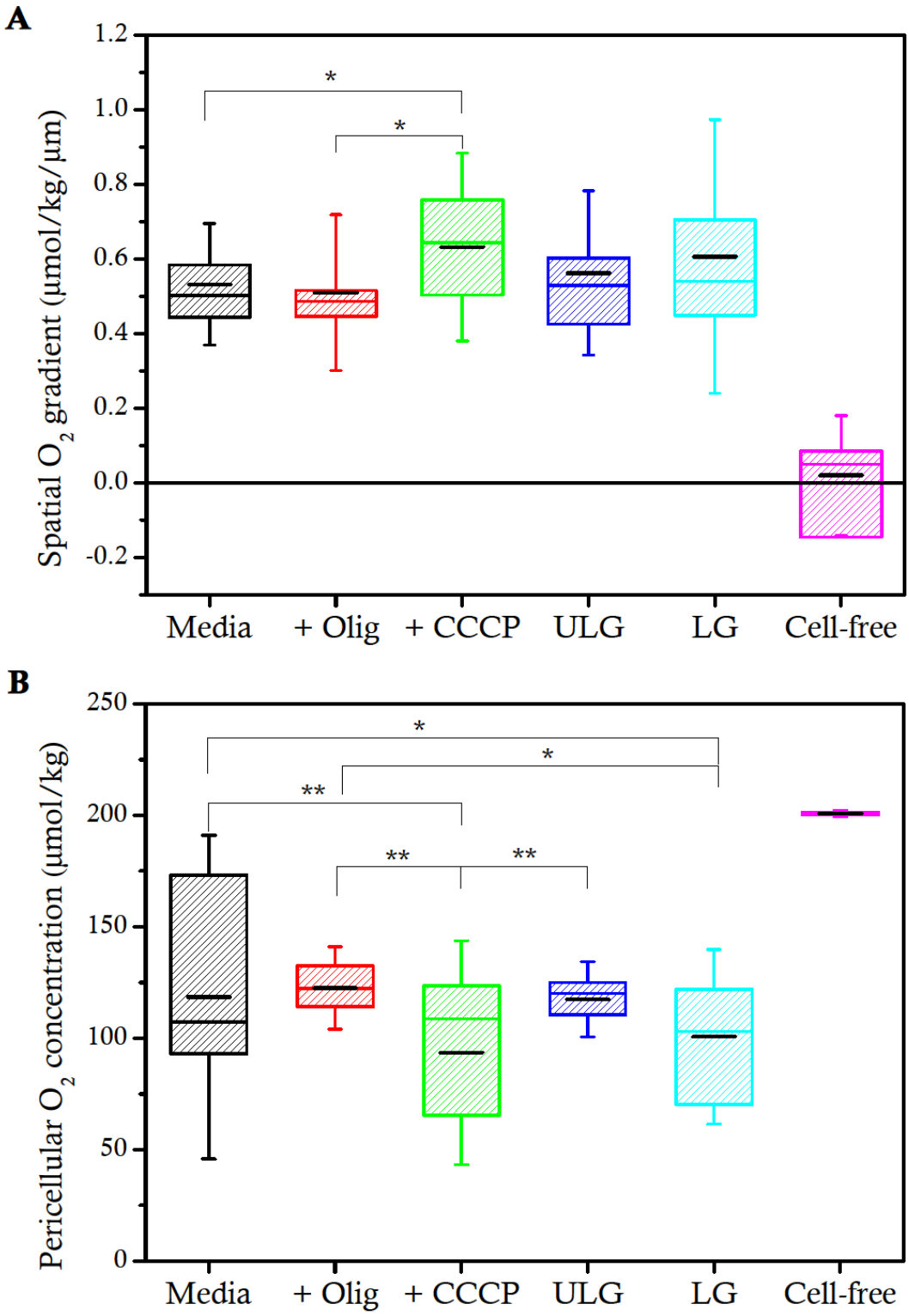


**Figure 130 – Box plot of significant oxygen measurements taken from cellular experiments and cell-free control for A: Spatial oxygen gradient and B: Pericellular oxygen concentration. Experiments consisted of cells exposed to $[Ru(bipy)_3]^{2+}$ and normal media (DMEM+16%FBS) supplemented with either, oligomycin (Olig) or CCCP. In addition data is shown for the response of cells cultured in low glucose media (LG) and ultra-low glucose (ULG). The boxes represent 1st and 3rd quartile with error bars as standard deviation and thick black line as mean. Values in parentheses represent the percentage of cell showing a statistically significant spatial oxygen gradient statistically significant differences are indicated at $p<0.05$ (*) or $p<0.01$ (**).**

For the cells in Figure 130A, the mean (±standard deviation) oxygen gradients were 0.53 (±0.11), 0.51 (±0.14), 0.63 (±0.17) 0.56 (±0.15) and 0.61 (±0.24) μmol/kg/μm for normal media, plus oligomycin, plus CCCP, ultra low glucose media (ULG) and low glucose media (LG), respectively. Figure 130A also shows the magnitude of spatial oxygen gradient measured in cell free agarose although it should be noted that none of these were statistically significant. Based upon an one way ANOVA Fisher Test CCCP was significantly different from both normal cell culture media and oligomycin $p<0.05$ and $p<0.01$, respectively, whereas no significant difference was seen with the cells cultured in ultra-low and low glucose media.

Figure 130B shows the box plots of the identical cells in Figure 130A, but describes the effect of culture conditions on the pericellular oxygen concentrations. The mean (±standard deviation) pericellular oxygen concentrations were 118.4 (±48.4), 122.4 (±12.3), 93.5 (±33.6), 117.5 (±11.3), 100.7 (±26.1) and 200.6 (±9.6) μmol/kg for normal media, plus oligomycin, plus CCCP, ultra low glucose media (ULG), low glucose media (LG) and cell-free agarose, respectively. A one way ANOVA Fisher t-Test was used to compare the culture conditions where statistically significant differences between the means were seen for CCCP against normal media, oligomycin and ultra low glucose all with $p<0.01$. Also a statistically significant difference was seen for low glucose media against normal media and oligomycin ($p<0.05$). All conditions were significantly different to cell-free agarose.

## 6.4 Discussion

### 6.4.1 Pericellular quantification of spatial oxygen gradient in normal media

Analysing the correlation of oxygen concentration at close proximity and with distance from the cell periphery has identified a sub-population of 46% of the measured cells exhibiting a statistically significant positive spatial oxygen gradient ($p<0.05$). Furthermore those with a statistically significant oxygen gradient had a steeper gradient than those without (Figure 123). This suggests an overall trend such that all cells generate a pericellular oxygen gradient, but only the larger gradients reach statistical significance. This is consistent with the fact that all cells are likely to be consuming oxygen whilst some do so at a faster rate. None of the gradients measured from the population displayed any statistically significant negative spatial oxygen gradients ($p>0.05$). This relationship between significant changes in oxygen concentration with distance from the cell periphery reflects oxygen consumption by the cells at a rate greater that the diffusional rate of oxygen in agarose at 37°C, which will be concentration dependent. The diffusion coefficient of

oxygen in water at 37°C is $3x10^{-5}$ $cm^2/s$, as established in chapter 4 section 3. The effective diffusion rate for oxygen through agarose is conflicting between published theoretical and experimental results [242]. However, it can be estimated based on the agarose volume fraction of fibres calculated from Eq. 78,

**Eq. 78**
$$\phi = c_{agarose} / \rho_{agarose} \cdot \omega_{agarose}$$

where, $c_{agarose}$ % (w/v) is the agarose concentration, $\rho_{agarose}$ is the dry agarose density (1.64 g/l) and $\omega_{agarose}$ is the mass fraction of agarose in a fibre (0.625) [242]. Therefore a 3% of agarose construct would have an estimated 0.02927 volume fraction of fibres. By considering the diffusion of oxygen through agarose as a network of randomly orientated cylindrical fibres the agarose fraction of fibres can be applied to Eq. 79,

**Eq. 79**
$$\frac{D_a}{D_w} = \exp\left[ -\sqrt{\phi} \cdot \frac{R_H}{r_f} \right]$$

where, $R_H$ is the hydrodynamic radius of the diffusing molecule oxygen, $r_f$ is the radius of the fibres, $D_w$ and $D_a$ is the diffusion of oxygen in water and agarose, respectively [201, 242]. As the diffusing molecule of oxygen is so small Meeren *et al.* [201] used a corrected version of Eq. 79 as,

**Eq. 80**
$$D_a = 3 \times 10^{-5} \exp\left[ -0.2 * \sqrt{\phi} \right]$$

This equation calculates the effective diffusion rate of oxygen in agarose at 37°C as $2.899x10^{-5}$ $cm^2/s$. Meeren *et al.* [201] calculated an oxygen diffusion coefficient at 30°C in 2% (w/v) agarose as 97.7% lower than pure water, whereas the increase in temperature to 37°C and agarose concentration to 3% (w/v) only reduces to 96.6% of the diffusion coefficient of pure water. As the temperature increases the diffusion coefficient should also increase whereas the restriction to diffusion has a fractional effect dependent on diffusion.

Comparing the cell diameters of the subpopulations has shown that cells displaying significant spatial oxygen gradient are also significantly larger in diameter than cells associated with no significant spatial oxygen gradient. The size of cells with significant oxygen gradients are 15% larger in diameter than those associated with non-significant oxygen gradients. This difference is also statistically significant (Figure 125).

The sub-population of cells with significant gradients did not show any correlation between cell diameter and the magnitude of spatial oxygen gradient, which has a mean (±standard deviation) value of 0.53 (±0.13) μmol/kg/μm. However, incorporation of all cells did produce a significant correlation between cell diameter and oxygen gradient ($p<0.0005$). This suggests that as cells increase in size the consumption rate of oxygen also increases until a plateau level is reached whereby no further increase in oxygen

consumption takes place (Figure 126). This increase in consumption rate by larger deep zone cells is consistent with published results by Heywood *et al.* [127].

Previous studies have shown that chondrocytes isolated from the deep zone of bovine metacarpal joint articular cartilage are larger than cells from the superficial zone [177]. The deep zone cells are also more metabolically adjusted than superficial zone cells as shown by greater synthesis of extracellular matrix in agarose [177]. Furthermore it is perhaps unsurprising that deep zone cells also consume oxygen faster that superficial zone cells [127]. It is therefore tempting to speculate that the sub-population of cells with a significant spatial oxygen gradient are isolated from the deep zone of the articular cartilage.

To exclude any possibility that these spatial oxygen gradients were induced due to oxygen levels in the environment or distance of the measurement in the agarose linear fits were applied to spatial oxygen gradient data. Although it did appear that there was an increase of significant spatial oxygen gradients towards lower pericellular concentration no statistically significant correlation ($p>0.05$) was found for either population (Figure 127). Also no statistically significant correlation ($p>0.05$) between spatial gradient and depth of measurement in agarose was seen for both populations (Figure 128). This confirms that the environmental oxygen concentration and agarose depth was not influencing cellular spatial oxygen gradient measurements for this study.

### 6.4.2 Extrinsic manipulation of cellular oxygen consumption rate and its effects on the spatial oxygen gradient

Oxygen consumption rates in bovine chondrocytes have previously been shown to be down- or up-regulated by oligomycin, CCCP and low glucose in cell culture media [126, 127, 129]. The same concentrations were applied to Day 1 isolated bovine chondrocytes seeded agarose constructs as for Heywood *et al.* study, however their method of culture was a monolayer [129]. The application of oligomycin to the media would be expected to inhibit oxygen consumption rates of cells by knocking out oxidative phosorphorylation. In these results there is a reduction of 7% for the number of cells exhibiting a significant spatial gradient and a 4% reduction in the mean spatial oxygen gradient. At the same time the pericellular oxygen concentration increases by 3% showing that a reduction in number of cells and significant spatial oxygen gradient minimises the consuming potential of the cell. Although none of the oligomycin results were statistically significant against normal media there was a significant difference with CCCP for the spatial oxygen gradient and pericellular oxygen concentration, also for low glucose media for pericellular oxygen concentration. This may explain the limited effect seen with chondrocytes exposed to oligomycin. There is a ratio of 0.1 between the percentage change in the mean spatial

oxygen gradient of the current study and the percentage change in consumption rate upon addition of oligomycin to media from Heywood *et al.* [129] study. However, it should also be noted that chondrocytes are mainly glycolytic cells and so will be less sensitive to oligomycin affecting the oxidative pathway [127].

In comparison the upregulation of oxygen consumption with CCCP uncoupler has maintained the same percentage of cells with statistically significant oxygen gradients as in normal media. However, there is a significant increase of 18% in the measured mean spatial oxygen gradients, while the pericellular oxygen concentration has significantly decreased by 21%. This confirms the dependence between oxygen consumption, significant spatial oxygen gradient and pericellular oxygen concentration. These results are in agreement with the findings of Heywood *et al.* [129] for CCCP applied to monolayer cells. This showed an increase of 63% in oxygen consumption rates with the addition of CCCP. The ratio of percentage change between the consumption rate and spatial oxygen gradient 0.3 and between the pericellular oxygen concentration is -0.3.

As chondrocytes are glycolytic cells and observe a crabtree effect, studies have shown that a reduction of glucose in cell culture media stimulates the cells requirement for energy through upregulation of oxidative phosphorylation and therefore oxygen consumption. For cells incubated in ultra-low glucose (0.06 mM) an increase of 7% is seen for the number of cells displaying a significant oxygen gradients and a 6% increase in the mean spatial oxygen gradient. However only a 0.8% decrease of oxygen concentration was seen pericellularly compared with normal media. Although no significant difference was seen between media and ultra-low glucose media the shift is in the correct direction, in agreement with Zhou *et al.* [326] who showed an 87% increase in chondrocyte consumption rates for the same glucose cell culture media concentration. However there were construct composition differences, in Zhou *et al.* study alginate beads were used, whereas in the current study agarose was used. As discussed previously, there are differences in the effectively oxygen diffusion rates for agarose and alginate at 37°C at a 3% concentration, estimated as $2.89 \times 10^{-5}$ $cm^2/s$ and reported as $2.58 \times 10^{-5}$ $cm^2/s$ [326], respectively. Whether this could impact the large variations between these two results remains to be determined. More likely the differences are due to the incubation period of cells with the very low glucose levels and reduced oxygen levels down regulating cellular consumption levels. When oxygen environmental levels reduce, cells adapted by reducing their oxygen consumptions rates, which has been shown in superficial and deep cells [127]. However the pericellular oxygen concentrations had not reduced significantly in the ultra-low glucose in comparison with normal media.

In order to compare the low glucose concentration of Heywood *et al.* [127] with the current study the average of the superficial and deep consumption rates at 2.8 mM and 5.5 mM for low and normal glucose concentrations were taken, respectively, as shown in Table 23. The low glucose level only increased the number of cells exhibiting significant spatial oxygen gradients by 2%, however the mean spatial oxygen gradient increased by 14%. A statistically significant drop of 15% for the pericellular oxygen concentration compared with normal media was also found. A ratio of 0.4 and -0.4 for the percentage change in spatial oxygen gradient and pericellular oxygen concentration, respectively, compared against the percentage change in oxygen consumption rate for Heywood *et al.* [127] with the same change increased glucose concentration.

**Table 23 – Consumption rate changes due to cell culture conditions from other studies compared with cell number, mean significant spatial oxygen gradients and pericellular oxygen changes of current study. Study data observed from isolated bovine chondrocyte from day zero.**

| **Cellular consumption rates** | | | **Current study – change to normal media and consumption rate** | | | | |
|---|---|---|---|---|---|---|---|
| Conditions | % change to media | Study | Cell number | Spatial | $\frac{\%\Delta Spatial}{\%\Delta Cons}$ | Pericellular | $\frac{\%\Delta Peri}{\%\Delta Cons}$ |
| Olig | -42% | [129] | -7% | -4% | 0.1 | +3% | -0.07 |
| CCCP | +61% | [129] | -1% | +18%* | 0.3 | -21%* | -0.3 |
| ULG | +87% | [326] | +7% | +6% | 0.07 | -0.8% | -0.01 |
| LG | +34% | [127] | +2% | +14% | 0.4 | -15%* | -0.4 |

* refers to statistically significant difference to media results

## 6.5 Conclusion

The calibrated and optimised pulse-picked two-photon confocal TCSPC technique has been applied to isolated individual chondrocyte cells for determining spatial oxygen gradients. Lifetime analysis was performed on user defined binned masks to provide high spatial resolution with distance from the cell.

In relation to chondrocytes this technique has established that a sub-population of cells demonstrate statistically significant spatial oxygen gradients, suggesting that they are more metabolically active and therefore have a higher oxygen consumption rates. This sub-populations is significantly larger than cells without a significant oxygen gradient. It indicates that these cells are more likely to be isolated from the deep zone, which are known to be larger [294] and more metabolically active [127].

Through extrinsic manipulation of oxygen consumption rates it was possible to influence the spatial oxygen gradients of chondrocytes. These results have established a

direct link between cellular consumption rates, spatial oxygen gradient and pericellular oxygen concentration. It also suggests that for chondrocytes exhibiting statistically significant oxygen gradients a percentage change in the oxygen consumption rate would reflect in a ratio increase and decrease of 0.3-0.4 for the spatial oxygen gradient and pericellular oxygen concentration, respectively. The results collated in this study are consistent with those observed by Heywood *et al.* and Zhou *et al.* [127, 129, 326].

Thus the developed and optimised TCSPC TP FLIM technique in this study has successfully been used to quantify spatial oxygen gradients around individual cells in three-dimensional scaffolds. Furthermore it has been validated that the spatial oxygen gradient and pericellular oxygen concentration is dependent on the cellular oxygen consumption rate. This information has the potential for use in modelling and could aid the creation of further robust models in assessing tissue gradients in native or tissue engineered constructs.

## 6.6 Summary

- A sub-population of chondrocytes exhibit statistically significant spatial oxygen gradients that appears linear at close proximity to the cell.
- This subpopulation is significantly larger in diameter and is assumed to be deep zone chondrocytes.
- No statistically significant negative gradients were seen for normal media culture conditions.
- Spatial oxygen gradient increases with cell size until gradient become significant at which point the relationship ceases to exist.
- Cellular oxygen consumption can be adjusted through chemical compounds and regulated through glucose concentration.
- A percentage change in the cellular oxygen consumption rate is reflected by a positive and negative ratio of approximately 0.35 for the percentage change in the spatial oxygen gradient and pericellular oxygen concentration, respectively.

# Conclusion 7

The aim of this thesis was to detect or quantify the presence of cellular induced spatial oxygen concentration gradients within a 3D tissue engineered agarose construct. The method for the intended investigation was a time-resolved time-domain lifetime detection technique applied to an oxygen sensitive ruthenium(II) complex. The objectives were to:

1) Examine the available time-resolved time-domain techniques using a selection of ruthenium(II) complexes.

2) Select and optimise a time-resolved time-domain technique.

3) Characterise the chosen ruthenium(II) complex with envisaged environmental components and establish dissolved oxygen relationship.

4) Combine the optimised technique and dye to assess the method of data acquisition, cellular phototoxicity and image processing.

5) Apply the developed FLIM system to measure oxygen concentrations in a three-dimensional agarose construct seeded with chondrocytes and to determine cellular induced spatial oxygen gradients.

6) Regulate cellular respiration to confirm that the measured spatial oxygen gradients are attributed to cellular oxygen consumption and to establish a relationship.

## 7.1 Development of FLIM system

### 7.1.1 Ruthenium(II) complex and time-domain

A selection of ruthenium(II) complexes were investigated and based on literature searches (Chapter 1 section 6) of which the most established for oxygen detection were $[Ru(bipy)_3]^{2+}$, $[Ru(phen)_3]^{2+}$ and $[Ru(dpp)_3]^{2+}$. Subsequently it was determined that $[Ru(bipy)_3]^{2+}$ and $[Ru(phen)_3]^{2+}$ were the most suitable fluorophores for investigating

oxygen concentrations in an aqueous system (Chapter 2 section 4). Interestingly at a concentration and cellular incubation period of less than 2.5 mM and 24 h, respectively, $[Ru(bipy)_3]^{2+}$ produced minimal cytotoxic effect and maintained chondrocyte viability at greater than 90% for 24 h (Chapter 2 section 5). A comparison between three time-domain techniques proved that with adaptation of a two-photon laser scanning confocal with TCSPC lifetime detection would provide superior spatial resolution, maintain low noise photon collection and was applicable to 3D cellular constructs.

### 7.1.2 Multi-photon laser

A Mai-Tai: Sapphire multi-photon tunable laser was applied for fluorophore excitation. The tested system provided two-photon excitation at 780 nm, which avoided direct excitation of the chosen oxygen sensitive dye $[Ru(bipy)_3]^{2+}$ (ex 468 nm and em 608 nm). The incorporation of a pulse picker to the optical path reduced the laser repetition rate from 80 MHz to 500 kHz. This affected the average power delivered to the sample reducing it from 2.5 mW at 8 MHz down to 160 μW at 500 kHz for an excitation of 780 nm. The low laser power at the 500 kHz repetition rate ensured that the $[Ru(bipy)_3]^{2+}$ sample would not be saturated during excitation at maximum power (Chapter 3 section 2).

### 7.1.3 Confocal Microscope

A Leica laser scanning confocal microscope was used for optical imaging. Point spread function testing confirmed that the spatial resolution was able to facilitate restricted excitation through optical sectioning by combining the MP laser and confocal microscope. In the z-axis a spatial resolution of >830 nm was achieved and a confocal high spatial resolution was maintained in the x-y axis >260 nm in accordance with theoretical calculations [70]. Data collection at this resolution is greater than any currently available oxygen detection technique (Table 3).

The low repetition rate of the laser was tested with the raster scanning module of the confocal and found that geometric distortions were introduced. Compensation for the low repetition rate requires a reduction in either the image scan speed or format size (Chapter 3 section 3).

### 7.1.4 TCSPC

The time-resolved time-domain lifetime detection was enabled with the uses of TCSPC. Testing of the instrument response function identified that during the analysis processing deconvolution was unnecessary due to the width only contributing to $8x10^{-6}$% of the final decay. It is well established that low repetition rate experiments suffer from ‘classic

pile-up' [27]. Tests showed that laser power, dye concentration and oxygen concentration were all contributing factors that could influence the occurrence of pile-up in these experiments (Chapter 3 section 4). It was determined that these influences could be controlled by maintaining the collection rate at less than 1% of the laser repetition rate, which for these experiments was $5x10^3$ photons/sec.

Confirmation of pile-up occurrence could be monitored by examining the goodness-of-fit. Decays were accepted on the basis that the reduced chi-square was less than or equal to 1.17. This produced low noise photon collection with minimal systematic variability of less than 0.3%. Acquisition of lifetime data with less than ±1.5% lifetime error requires at least a 97 peak count or 20,000 total decay counts for a repetition rate of 500 kHz, which can be confirmed by maintaining an $R^2$ greater than 0.9. A ±1.5% lifetime error is reflected as a maximum lifetime error of ±5 ns equivalent to a maximum error of oxygen concentration ±7 μmol/kg for a media solution at a temperature of 37˚C. This system has achieved greater oxygen detection resolution than the currently used wide-field time-gate system [279].

### 7.1.5 Characterisation of $[Ru(bipy)_3]^{2+}$

No correlation was found between lifetime measurements and changes in pH levels or dye concentrations, in accordance with other studies [72, 279]. However $[Ru(bipy)_3]^{2+}$ was found to have a negative linear relationship with temperature between 31-39˚C consistent with physiological temperatures and other researchers [144, 212]. It was identified that an inherent non-radiative decay component $k_{dd}$ within the dye was susceptible to temperature changes [212, 300] i.e. a 1˚C change in temperature would manifest as a 1% change in lifetime. This highlighted the importance of temperature control and stability within the system facilitated by a confocal environmental chamber and sample chamber heating plate. The autofluorescent components identified within the cell culture media had very short lifetimes. These were avoided from the data analysis process by a fitting mono-exponential model 150 ns after the start of the decay. Concentration effects of fetal bovine serum (FBS) to lifetime identified a restrictive barrier to oxygen quenching of $[Ru(bipy)_3]^{2+}$, consistent with other researchers [172]. However at the FBS concentrations used in the cell culture media for the current experiment produces a difference of 0.3% between the maximum response and that derived from the measured lifetime with 16% FBS (Chapter 4 section 2).

The oxygen molality in pure serum at 37˚C is 12% less than in pure water. The lifetime of $[Ru(bipy)_3]^{2+}$ without quencher is 1.5% less in media than in water highlighting the slight influence of media components over the physical dye. The Stern-Volmer constant

shows that $[Ru(bipy)_3]^{2+}$ in water is 12% more accessible to oxygen than in media. The non-radiative rate is 14% less in media than water and must be attributed to the additional media components interacting with $[Ru(bipy)_3]^{2+}$. The adjusted formula derived by Demas *et al.* [64] and Rusak *et al.* [257] and applied to calculate the diffusion controlled bimolecular constant provides an identical frequency of collision for $[Ru(bipy)_3]^{2+}$ in water as Rusak *et al.* identified (Chapter 4 section 3).

### 7.1.6 Establishing method of data acquisition

Phototoxicity tests exposed chondrocytes, seeded in 3D agarose constructs and incubated with $[Ru(bipy)_3]^{2+}$+media, to 30 mins of direct MP laser exposure. Cells maintain 90% viability 24 h after imaging in contradiction to a study done by Dobrucki [72] who stated that 120 illuminations saw breakdown of the cellular membrane. Interestingly this number of illuminations is only relevant for the individual setup of each system explaining the discrepancy (Chapter 5 section 2).

The communication between the TCSPC and Leica system is important for relaying information regarding pixel dwell time. To adhere to the minimum number of photons collected per pixel the image format size was determined as 64x33 and a collection time of 15 mins was assigned for practicality. Investigations showed that 20% of the collected photons were lost between the CFD and TAC identifying that at least 33 pixels require binning to maintain accurate lifetime decay. A comparison of SPC analysis software identified the TRI2 as the superior option for speed of calculation, manipulation of binning regions, analysing multiply data sets in tandem and accuracy of lifetime fits and spread. A new method for data analysis was developed specifically for extraction of high spatial resolution information to avoid the averaging effects induced from generalised binning as found in most SPC software. This method followed the curvature of the cell periphery to emphasize the suspected morphology of cellular oxygen consumption. The application of linear fits to pericellular spatial distribution of oxygen concentrations identified differences between significant and non-significant lifetime gradients and therefore oxygen gradients (Chapter 5 section 3).

### 7.1.7 Application to chondrocytes

The ability of measuring individual cellular gradients has revealed a subpopulation of chondrocytes that exhibit significantly steeper spatial oxygen gradients (0.5 μmol/kg/μm) without the requirement for prior identification or separation of cells during isolation. This identified a subpopulation that displayed a significantly larger mean cell

diameters (12.5 μm) and upregulated metabolic systems consistent with deeper zone cells (Chapter 6 section 2).

Confirmation that the oxygen gradient arose from cellular consumption was confirmed with the use of extrinsic chemical compound that directly affect ATP production. This used established applications in cellular oxygen consumption inhibition and upregulation [127] to display changes in oxygen consumption rates and therefore to asses the relationship to spatial oxygen gradients. Expected cellular response to application of CCCP upregulation of oxygen consumption were mimicked as a percentage change ratio. This ratio was seen as a 0.3 increased and decreased spatial oxygen gradient and pericellular oxygen concentration, respectively, against oxygen consumption rate. The same effect was also seen with low glucose concentration cell culture media highlighting the glycolytic dependence and crabtree relationship with glucose and oxygen consumption, as identified by other researchers [126, 324]. The cellular response to extrinsic manipulation of consumption identified by other studies [127, 129] are replicated in these results and identified in the spatial oxygen gradient. This establishes a relationship between consumption, gradient and pericellular oxygen concentrations. However, whether this utilisation is consumption from the cell membrane or from the mitochondria has not been confirmed.

Although for a negative or positive linear concentration gradient the change must be associated in one direction and governed by diffusion. This identifies that the significant cells are consuming oxygen at a higher rate than the diffusion rate of oxygen in agarose at 37°C, $2.899 \times 10^{-5}$ $cm^2/s$ (Chapter 6 section 4). It has been established that a subpopulation of chondrocytes create significant oxygen gradients that can be detected using the developed system. The development of these gradients arises due to cellular utilisation of oxygen and demand out-weighing the availability of intracellular oxygen.

## 7.2 Comparison with other available techniques

Invasive probes have been used to determine spatial oxygen in tissue engineered constructs, but they do not facilitate spatial registration of the measurement with sample, damages the tissue in the process [51], or in the case of oxygen electrodes consume oxygen in the measurement process [295].

The majority of previous non-invasive systems have focused on global oxygen consumption rates [128], single point measurements over large distances [104] or intracellular oxygen concentrations [279] (Chapter 1 section 3). The global systems tend to facilitate rapid detection on monolayer cell cultures using multi-plate fluorimeter readers.

This method does not provide spatial resolution, but has the ability of measuring multiple samples with a rapid temporal measurement. Single point measurement systems can be combined with microscopes to provide spatial resolution (limited >1 μm), but tends to be used on very long lifetime fluorescent dyes. This means only single point measurements are collected in order to maintain a higher temporal resolution [79, 82, 104, 208].

The wide-field time-gate systems have limited detection capabilities that would have masked the obtain measurements [279, 324]. Also the use of the $[Ru(bipy)_3]^{2+}$ intracellularly has caused interaction issues leading to a recent incorporation of applying EPR separately to quantify the correct oxygen concentrations in specific solute solution [278]. A comparison of these techniques against the developed system is described in Table 24 listing the advantages and disadvantages of the current system based on limitations and advantages of the other systems. To address the disadvantages of the current system further discussion is provided in section 7.3.

**Table 24 – List of advantages and disadvantages of the current developed system TP confocal TCSPC**

| Advantages | Disadvantages |
|---|---|
| - High spatial resolution: <400 nm | - Limited temporal resolution: >15 min |
| - High lifetime discrimination: <±5 ns | - Pile-up currently restricting optimum photon collection |
| - Non-invasive measurement | - Restricted FOV due to collection time |
| - Investigation in 3D cellular structure | - Depth of imaging restricted by working distance of objective lens |
| - Captures lifetime and intensity map | - Currently not possible to apply to human *in vivo* |
| - Could be applied to animal models *in vivo* | - Only one cell per time can be imaged at that resolution |
| - Spatial registration of measurement | |

## 7.3 Future improvements to the system

Improvement of the fitting methods for lifetime data analysis would have the potential to convert collected data into images without the need for binning. It would also mean that larger spatial areas could be acquired maintaining high spatial resolution and lifetime accuracy or imaging time could be reduced to provide rapid measurements for determining oxygen consumption rates. These advantages achieved with the development of Bayesian analysis currently being proposed by Gray's Laboratory (Oxford). At the time of writing their analysis technique was unable to cope with the type of decay recorded

using this system, but it is hoped that in the future this could be come a real possibility of determining decays with as little as 100 photons or less. Also automating the analysis process would reduce the currently labour intensive data analysis procedure.

Upgrading certain equipment of the system would also reduce the effects pile-up causes to the collection of photons with the potential for more rapid collection rates. This could involve the addition of extra detectors to reject the arrival of more than one photon within the same time period and installing a cable to commicate between microscope and TCSPC regarding pixel dewel time.

The recent development of a wide-field photon counting imaging system [283] has the potential of capturing complete lifetime images 1000 times faster than previously possible and minimises the problems associated with pile-up. This novel development could hold the potential for applying the background knowledge derived here for FLIM detection of individual oxygen consumption rates and creation of gradients in real-time. However it would restrict the axial spatial resolution due to limited optical sectioning and it remains to be seen whether the use of this wide-field technique would also create lifetime variability due to wide field collection as seen in prior wide-field systems.

## 7.4 Potential applications of the technique

In consideration to the work that has currently been conducted on chondrocytes confirmation that the larger subpopulation displaying significant spatial oxygen gradients derives from deeper zone cells would confirm the suggested correlation. This would be achieved by repeating the experiment on separated superficial and deep populations during the isolation process and comparing results. Also applying the same oxygen detection method to chondrocytes seeded in different 3D tissue engineered constructs will identify differences induced by diffusional restrictions to the developed spatial oxygen gradients and pericellular oxygen concentration, i.e. for instance alginate and agarose. Further testing of cartilage components with dye would provide the potential for investigation of native cartilage tissue spatial oxygen gradient and facilitate comparison between native and engineered constructs. This could be achieved simply by extracting articular cartilage plugs from the bovine metacarpal-phangel joint and incubating with $[Ru(bipy)_3]^{2+}$+media in sample chambers. Expanding the FOV to measure macrogradients across constructs or cartilage tissue with an adjusted set of binning masks would provide the opportunity of measuring at high spatial resolution the development of long distance gradients, which could be compared against local pericellular gradients. This would aid the understanding for more complex computational models for gradient development.

Incorporating the spatial oxygen gradient as an oxygen flux would allow 2D oxygen maps to be developed based on the fitted gradients. The addition of a visual perspective would provide comparison of cellular spacing to asses the influence of adjacent cell distance on the oxygen flux patterns. This has the potential to then be applied to large scale simulations observing the effects of chondron size on the oxygen delivery or model the effect of a full depth cartilage tissue based on cellular distance. Determining the location of the oxygen consumption utilisation where it occurs from the cell membrane or from the mitochondria would provide an understanding of cellular function and energy requirements.

Applying this technique in combination with other metabolites of interest such as glucose or NADH would allow a complete view of the metabolic makeup and energy production and requirements of chondrocytes, aiding development of future bioreactors for tissue engineering. To determine the difference ratio between oxygen consumption arising from the mitochondria or the cellular membrane a technique based on excitation of endogenous protoporphyrin IX within the mitochondria could been used to quantify oxygen concentrations [207]. Incorporating both applications on the same system would require the setup a delayed fluorescence lifetime technique. If this was feasible it would be able to quantify the different compartment of cellular consumption providing invaluable information regarding cell metabolism.

Further adjustment of environmental effects on chondrocytes to replicate those found in the progress of cartilage disease or trauma can be applied to observe the impact to consumption, gradient development or degradation. It has been shown that oxygen concentrations change when disease is present [290]. If successful this could potentially be used as an early identification tool for the onset of cartilage degradation by adapting the system for endoscope surgery.

All these applications could be applied to investigate other tissue engineering cells types. This technique has the potential to show more distinctive results as chondrocyte cellular oxygen consumption is extremely low. In comparison to other cells such as hypertrophic located in avian growth plate cartilage their consumption rate is 14 times greater than deep zone chondrocytes [117].

## 7.5 Summary of key achievements

The TP confocal TCSPC system has provided a minimally invasive method of detecting oxygen concentrations around single living cells within a 3D environment. The high level of spatial resolution and oxygen discrimination has identified for the first time

the existence of pericellular spatial oxygen gradients on a micron scale around individual cells. The method provides a potentially non-invasive technique for investigating cellular oxygen consumption within three-dimensional tissues on an individual basis.

- An oxygen detection technique has been developed with the highest x-axis spatial resolution currently available (>350 nm) and with high z-axis spatial resolution (>830 nm).
- The FLIM system has achieved high oxygen concentration discrimination >±7 μmol/kg.
- It has for the first time verified that individual cells exhibit a spatial oxygen gradient.
- Determination of significant spatial oxygen gradients has identified a subpopulation of chondrocytes displaying larger cell diameters similar to deep zone cells.
- This subpopulation of cells exhibits a spatial oxygen gradient of 0.5 μmol/kg/μm.
- It has established that changes to cellular oxygen consumption have a direct influence over individual cellular spatial oxygen gradients and pericellular oxygen concentrations.

# Appendix – AlamarBlue™ A

Using 96 well-plate with chondrocytes in monolayer at different seeding densities and fluorescence recorded at different time points. The results show the optimum cell density for chondrocytes cells are 25000 cells/cm$^2$ and an incubation time of 48 hours.

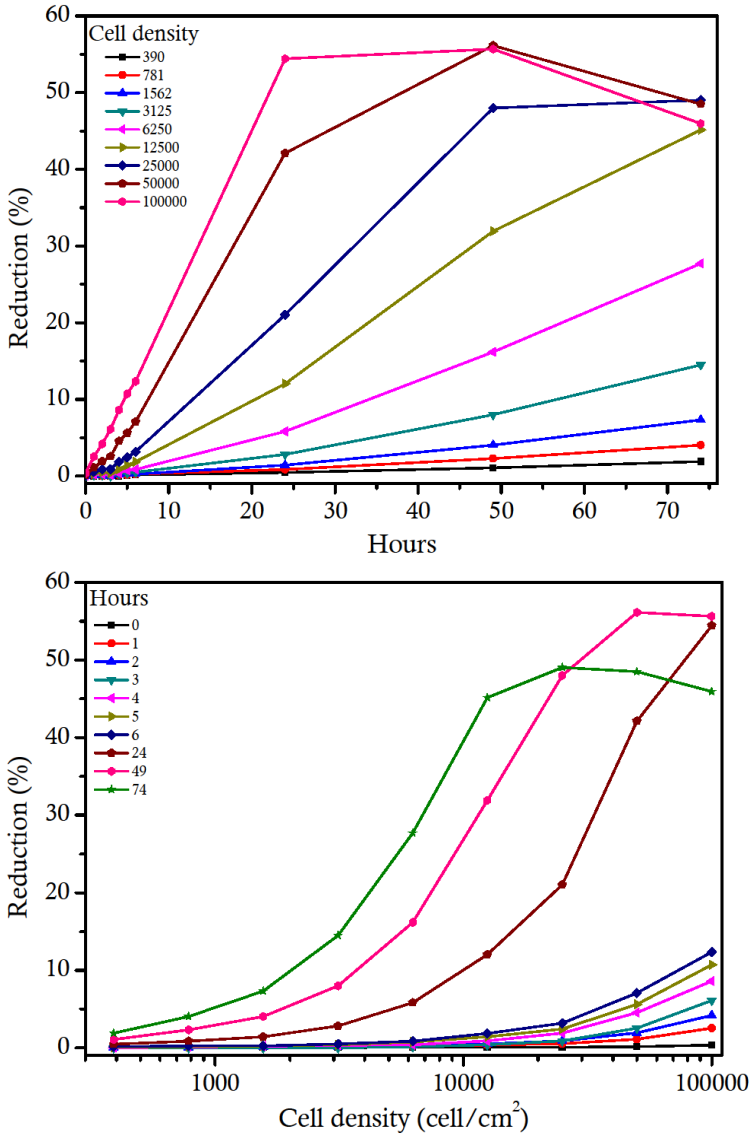


**Figure 131 – Effect of incrementing cellular density and incubation time on AlamarBlue™ reduction. Top: Determined cellular density, Bottom: Determined incubation time.**

# Appendix – Sample Chambers B

### Air-tight chamber schematics

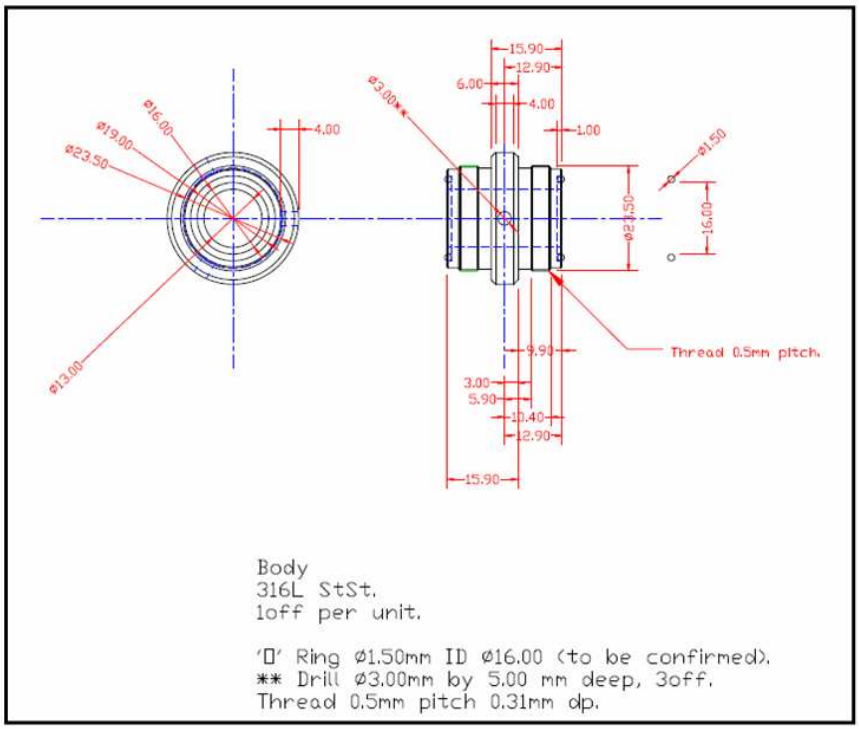

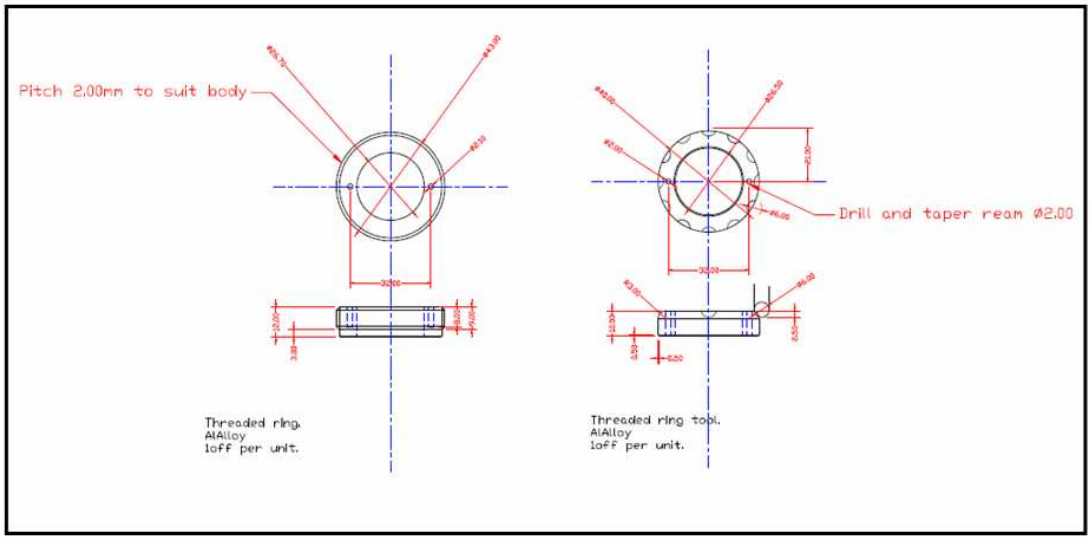
Pitch 2.00mm to suit body
Drill and taper ream Ø2.00
Threaded ring.
AlAlloy
1off per unit.
Threaded ring tool.
AlAlloy
1off per unit.

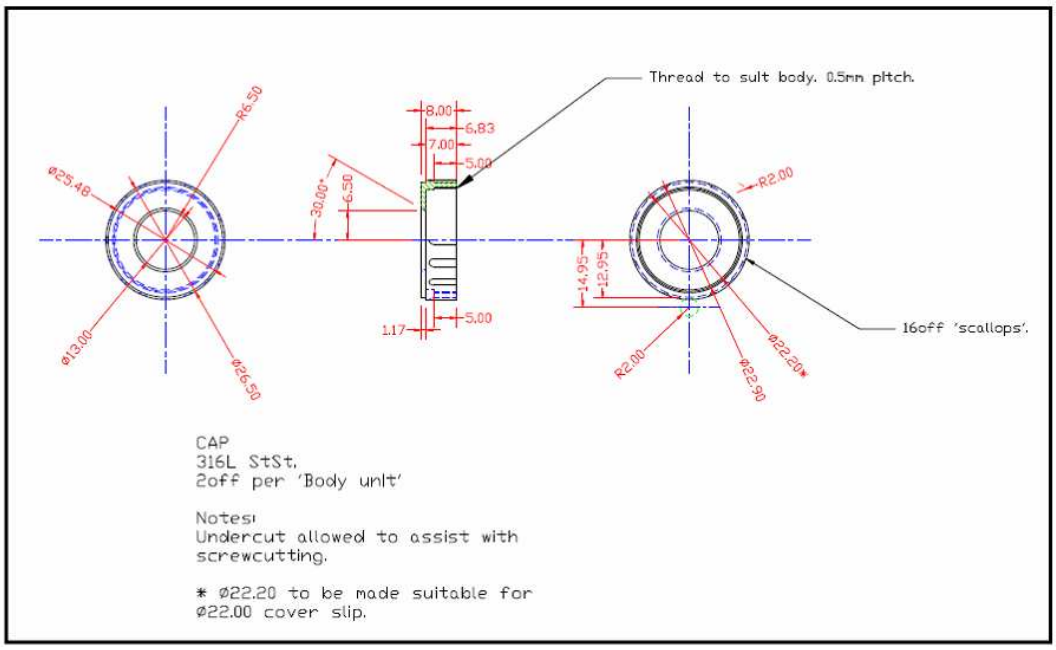
Thread to suit body. 0.5mm pitch.
R6.50
Ø25.48
Ø13.00
Ø26.50
8.00
6.83
7.00
5.00
30.00°
6.50
1.17
5.00
R2.00
14.95
12.95
R2.00
Ø22.20*
Ø22.90
16off 'scallops'.
CAP
316L StSt.
2off per 'Body unit'
Notes:
Undercut allowed to assist with screwcutting.
* Ø22.20 to be made suitable for Ø22.00 cover slip.

# Appendix – Laser Alignment C

## SOP Alignment of Multi-Photon (MP) Laser

For general use during an experiment the beam is totally encased within a sealed enclosure and therefore has no risk to the user. This protocol details the necessary procedure required to implement a re-alignment of the multi-photon laser located in confocal lab of the tissue engineering laboratory. The re-alignment of the laser allows a trained user to direct the beam through or around a pulse picker located within a laser enclosure. This protocol is only to be used by trained personnel named: Neveen Hosny and Chris Mole, at no time may other confocal users attempt this protocol. Information about how the laser should be operated can be found in the confocal lab, this document will not refer to it. Normal laboratory rules apply during this procedure.

## 7.6 Security

1) Access to the laboratory is controlled via security cards.
2) Signs out side the confocal lab notify staff/students/contractors of the dangers before entering
3) An extra sign is placed outside the confocal lab to notify when the microscope is in operation
4) Door is locked from the inside to stop staff/students/contractors from walking in. This can be unlocked from the other side of the door for emergency access.

## 7.7 Precautions

1) Before ever using the laser ensure the water chillier is on, this should never be turned off.
2) Remove all watches and rings to avoid reflections

3) Wear safety coat and gloves
4) Ensure warning sign is outside the confocal door
5) Ensure door has been locked from the inside
6) NEVER adjust the beam in far IR; adjust wavelength to below 780nm so that the beam is visible (red)
7) Beam must be operated at low power during re-alignment
8) Do not sit down when re-aligning laser, if someone needs to sit then they must wear the laser safety goggles; located in the cupboard.

These issues must be adhered to before opening the top of the safety enclosure.

## 7.8 Laser Safety Features

1) There are two shutters located on the system these are on the laser and the scanner shutters. Operating these shutters can be achieved via "laser control config" and "active" on the beam panel.
2) Four security screws lock down the safety panel on the laser enclosure, it is not possible to unscrew these without an appropriate security key.
3) Computers are password protected and the laser cannot be initialised without accessing the relevant computer program.
4) Laser safety enclosure creates a beam stop that surrounds exposed beam.

## 7.9 Alignment

Use a fluorescein sample or a fluorescent green plastic with a 20x dry lens objective. This is then used to provide a constant fluorescent field of view that will allow the operator to adjust the fluorescent settings.

## 7.10 Changing from Pulse Picker to MP 80MHz

### 7.10.1 Flipping the Mirrors

In the "IR/MP" tab click the "crtl" button and adjust the laser wavelength to below 780nm, this brings the beam into the visible spectrum. Close laser shutter by holding down the button for 3 sec. To ensure that the beam is off, open the safety lids on the enclosure and check, using a piece of white card, that there is no red beam exiting from the laser

aperture. If the wavelength has not been adjusted to below 780nm the beam will be invisible to the naked eye, and therefore not appear on the card.

Switch the two flip mirrors (circled with the dotted lines) very carefully, trying to avoid any twisting movement. Replace safety lid and check to see if there is an image produced, most probably not, if not then close down the MP Leica software and open "No MP Leica" software.

### 7.10.2 Re-aligning the Mirrors

Reopen the Spectra-Physics Mai Tai software, choosing com port 2, and turning on the laser emission with a wavelength below 780nm. Wait for the laser to power up to 4.5 Watts at which point it will start pulsing. It is too dangerous to align in pulsing mode and so the laser must be put in to a continuous wave (CW) mode.

### 7.10.3 Continuous Wave

From the task bar select "View" and then "Setup", a new window will appear. In the window check the "Green Power" box and adjust the number to the side of it down to 4.5Watts. In the original window the red bar will start to decrease, the aim being to reduce the red bar so that the laser is only delivering a power around 2 to 1.2 without reducing the red bar too much that it disappears. The numbers won't be exactly the same each time as the power varies with wavelength. If the red power bar does disappear then that number next to the green power box must be increased again to get the laser lasing again at which point the process must be repeated.

### 7.10.4 Pinhole Alignment

Once the laser power has been reduced open the safety lid and check with the piece of card that the beam is exiting from the laser. Using the card follow the path of the beam to ensure it is following the correct path and that it is going into the EOM and coming out into the block just before the second shutter. Close pinhole (3), if it is not aligned it will not go to the center of the pinhole, switch flip mirror (1) between its two set points to see it if alignment improves, this can then be further improved by the fine adjustment of the mirror knobs located behind the mirror. The center point of the pinhole can be easily determined by slightly opening the orifice of the aperture, once the flares of the beam are only visible then it is certain that beam is passing through the center.

Once pinhole (3) is ok open the pinhole fully and check pinhole (2) repeating the same process, but only improving the alignment via flip mirror (1). If pinhole (2) is ok, re-

check pinhole (3), misaligned readjust the knobs on flip mirror (1) and re-check pinhole (2). Once pinhole (3) & (2) are aligned remove the safety guide and box it goes into between the safety enclosure and the environmental chamber, attach the target guide to the 3 pin mirror.

Open the shutter behind the EOM by click "Continuous" on the Leica software this will and allow pinhole (1) to be checked for alignment. If this is misaligned adjust flip mirror (2) in the same manor as for flip mirror (1). Check that the entire beam is entering the EOM if there is some reflection adjust flip mirror (2). If all the pinholes are aligned check the beam entering the target tube and last the pinhole before the mirrors. Now the alignment is complete, if there are still problems with the alignment do not adjust any other mirror only the flip mirror marked with black pen should be adjusted.

### 7.10.5 Near & Far Adjustment

In the Leica Software perform the EOM adjustment for the gain and offset and then close the shutter in the laser control. Go to Spectra Physics and adjust wavelength by 1nm this will power up the laser again and start the system pulsing. In the Leica software check that the "SP700" filter is off, "pinh" is at 600μm, open the shutter and start the system scanning.

Adjust the two knobs, one at a time, located on top of the telescopic mirror to obtain the maximum power by viewing the scanning image. Reduce PMT1 (to stop saturation) and pinhole to 50μm and, using an allen key, adjust each of the 3 pins in the mirror to obtain maximum power. Increase the pinhole back to 600μm and adjust the telescopic mirror as before, keep repeating this process until no more improvement is seen in the image. To confirm the efficiency of alignment the pinhole should be able to be reduced from 600μm down to below half the pinhole size before a power drop off is seen.

It is now ready to be used closed down the Leica and Spectra Physics software and restart "MP Leica" software.

## 7.11 Changing from MP 80MHz to Pulse Picker

In the "MP Leica" software make sure that the wavelength is below 780nm, close the shutter in the laser control, using a piece of paper to check that the beam is not exiting the laser aperture. The IR power must be on maximum to produce image for pulse picked signal. Carefully flip both mirrors out of the path of the beam, open the shutter and turn on the scanning, check pinhole (1) is aligned adjust the telescopic mirror. Check "pinh" is at

600μm, PMT1 is collecting all the wavelengths and is turned up, SPC700 is in place, adjust EOM as before, and then repeat the “Near & Far Adjustment”.

## 7.12 Schematic diagram of system overview

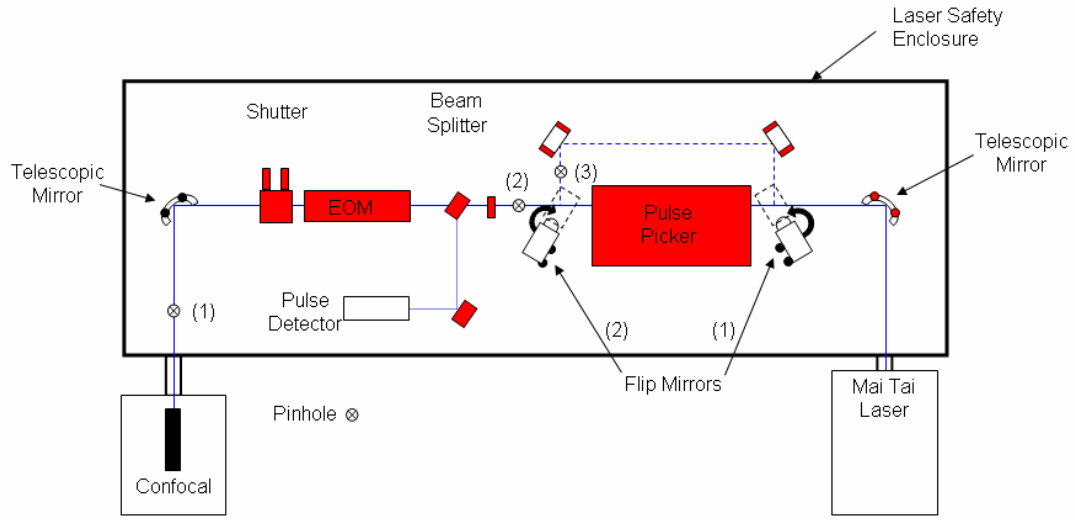

# Appendix – Media Composition D

Standard DMEM media components (D6429, Sigma-Aldrich, UK)

## Conversion of g/l to mol/kg

$$m = M \cdot V \cdot MW$$

Where
m = mass (kg) = 6.4 g
M = mol
V = volume (ltr.) = 1 ltr.
MW = molecular weight (g/mol)

$$M = \frac{m}{V \cdot MW} \qquad \text{(mol/l)}$$

## Conversion of water density with temperature

$$p_1 = \frac{p_0}{(1 + \beta(t_1 - t_0))}$$

Where
$p_1$ = final density (kg/m³)
$p_0$ = initial density (kg/m³) = 1000 kg/m³
$\beta$ = Volumetric temperature expansion coefficient (m³/m³°C) = 0.0002
$t_1$ = final temperature (°C)
$t_0$ = inital temperature (°C) = 4°C
1 m³ = 1000 dm³ = 1000 ltr.

# Appendix – Matlab E

**Data extraction file for 'Masks'**

```
clear all
clc

! Fixed zero
fid_zero{1}  = fopen('Mask 016- fixed zero.csv');
fid_zero{2}  = fopen('Mask 015- fixed zero.csv');
fid_zero{3}  = fopen('Mask 014- fixed zero.csv');
fid_zero{4}  = fopen('Mask 013- fixed zero.csv');
fid_zero{5}  = fopen('Mask 012- fixed zero.csv');
fid_zero{6}  = fopen('Mask 011- fixed zero.csv');
fid_zero{7}  = fopen('Mask 010- fixed zero.csv');
fid_zero{8}  =  fopen('Mask 09- fixed zero.csv');
fid_zero{9}  =  fopen('Mask 08- fixed zero.csv');
fid_zero{10} =  fopen('Mask 07- fixed zero.csv');
fid_zero{11} =  fopen('Mask 06- fixed zero.csv');
fid_zero{12} =  fopen('Mask 05- fixed zero.csv');
fid_zero{13} =  fopen('Mask 04- fixed zero.csv');
fid_zero{14} =  fopen('Mask 03- fixed zero.csv');
fid_zero{15} =  fopen('Mask 02- fixed zero.csv');
fid_zero{16} =  fopen('Mask 01- fixed zero.csv');
fid_zero{17} =   fopen('Mask 1- fixed zero.csv');
fid_zero{18} =   fopen('Mask 2- fixed zero.csv');
fid_zero{19} =   fopen('Mask 3- fixed zero.csv');
fid_zero{20} =   fopen('Mask 4- fixed zero.csv');
fid_zero{21} =   fopen('Mask 5- fixed zero.csv');
fid_zero{22} =   fopen('Mask 6- fixed zero.csv');
fid_zero{23} =   fopen('Mask 7- fixed zero.csv');
fid_zero{24} =   fopen('Mask 8- fixed zero.csv');
fid_zero{25} =   fopen('Mask 9- fixed zero.csv');
fid_zero{26} =  fopen('Mask 10- fixed zero.csv');
fid_zero{27} =  fopen('Mask 11- fixed zero.csv');
fid_zero{28} =  fopen('Mask 12- fixed zero.csv');
fid_zero{29} =  fopen('Mask 13- fixed zero.csv');
fid_zero{30} =  fopen('Mask 14- fixed zero.csv');
fid_zero{31} =  fopen('Mask 15- fixed zero.csv');
fid_zero{32} =  fopen('Mask 16- fixed zero.csv');
fid_zero{33} =  fopen('Mask 17- fixed zero.csv');
fid_zero{34} =  fopen('Mask 18- fixed zero.csv');
fid_zero{35} =  fopen('Mask 19- fixed zero.csv');
fid_zero{36} =  fopen('Mask 20- fixed zero.csv');
fid_zero{37} =  fopen('Mask 21- fixed zero.csv');
fid_zero{38} =  fopen('Mask 22- fixed zero.csv');
fid_zero{39} =  fopen('Mask 23- fixed zero.csv');
fid_zero{40} =  fopen('Mask 24- fixed zero.csv');
fid_zero{41} =  fopen('Mask 25- fixed zero.csv');
```

```
fid_zero{42} =  fopen('Mask 26- fixed zero.csv');
fid_zero{43} =  fopen('Mask 27- fixed zero.csv');
fid_zero{44} =  fopen('Mask 28- fixed zero.csv');
fid_zero{45} =  fopen('Mask 29- fixed zero.csv');
fid_zero{46} =  fopen('Mask 30- fixed zero.csv');
fid_zero{47} =  fopen('Mask 31- fixed zero.csv');
fid_zero{48} =  fopen('Mask 32- fixed zero.csv');
fid_zero{49} =  fopen('Mask 33- fixed zero.csv');
fid_zero{50} =  fopen('Mask 34- fixed zero.csv');
fid_zero{51} =  fopen('Mask 35- fixed zero.csv');
fid_zero{52} =  fopen('Mask 36- fixed zero.csv');
fid_zero{53} =  fopen('Mask 37- fixed zero.csv');
fid_zero{54} =  fopen('Mask 38- fixed zero.csv');
fid_zero{55} =  fopen('Mask 39- fixed zero.csv');
fid_zero{56} =  fopen('Mask 40- fixed zero.csv');

fid_zero{57} =  fopen('Mask 41- fixed zero.csv');
fid_zero{58} =  fopen('Mask 42- fixed zero.csv');
fid_zero{59} =  fopen('Mask 017- fixed zero.csv');


for i=1:59

    mask_zero{i} = textscan(fid_zero{i},'%s %f %f %f %f',...


            'headerlines', 3,'delimiter', ',');

end

for i=2:60

    fixed_zero_Tau(:,i) = mask_zero{1,i-1}{:,4};

end

for i=2:60

    fixed_zero_Amp(:,i) = mask_zero{1,i-1}{:,3};

end
```

# References


[1] Abdel-Shafi, A. A., Ward, M. D. and Schmidt, R., "Mechanism of Quenching by Oxygen of the Excited States of Ruthenium(Ii) Complexes in Aqueous Media. Solvent Isotope Effect and Photosensitized Generation of Singlet Oxygen, O2(1g), by [Ru(Diimine)(Cn)4]2- Complex Ions," Dalton Trans. 24), 2517 - 2527 (2007)

[2] Abdel-Shafi, A. A., Worrall, D. R. and Ershov, A. Y., "Photosensitized Generation of Singlet Oxygen from Ruthenium(Ii) and Osmium(Ii) Bipyridyl Complexes," Dalton Transactions 1), 30-36 (2004)

[3] Acosta, M. A., Ymele-Leki, P., Kostov, Y. V. and Leach, J. B., "Fluorescent Microparticles for Sensing Cell Microenvironment Oxygen Levels within 3d Scaffolds," Biomaterials 30(17), 3068-3074 (2009)

[4] Adam, C., Eckstein, F., Milz, S., Schulte, E., Becker, C. and Putz, R., "The Distribution of Cartilage Thickness in the Knee-Joints of Old-Aged Individuals -- Measurement by a-Mode Ultrasound," Clinical Biomechanics 13(1), 1-10 (1998)

[5] Alberts, B., Molecular Biology of the Cell, Garland, New York; London (1994).

[6] Alberts, B., Essential Cell Biology : An Introduction to the Molecular Biology of the Cell, Garland Pub., New York (1998).

[7] Albota, M. A., Xu, C. and Webb, W. W., "Two-Photon Fluorescence Excitation Cross Sections of Biomolecular Probes from 690 to 960 Nm," Appl. Opt. 37(31), 7352-7356 (1998)

[8] Alessandro, E., Federico, F., Cesare, U., Fabio, C., Giuseppe, C., Maddalena, C. and Alberto, D., "Notes on Theory and Experimental Conditions Behind Two-Photon Excitation Microscopy," Microscopy Research and Technique 63(1), 12-17 (2004)

[9] Almarza, A. J. and Athanasiou, K. A., "Design Characteristics for the Tissue Engineering of Cartilaginous Tissues," Ann Biomed Eng 32(1), 2-17 (2004)

[10] Altınoğlu, E. İ. and Adair, J. H., "Near Infrared Imaging with Nanoparticles," Wiley Interdisciplinary Reviews: Nanomedicine and Nanobiotechnology 2(5), 461-477

[11] Amao, Y., "Fundamental Review: Probes and Polymers for Optical Sensing of Oxygen," Microchimica Acta 143(1), 1-12 (2003)

[12] Amos, W. B., "Achromatic Scanning System," W. I. P. Organistation, Ed. (1990).

[13] Amos, W. B. and White, J. G., "How the Confocal Laser Scanning Microscope Entered Biological Research," Biol. Cell 95(6), 335-342 (2003)

[14] Angelescu, D. and Vasilescu, M., "Quenching of Pyrene Derivatives' Fluorescence by Nitroxide Radicals in Sodium Dodecyl Sulfate Micellar Solutions," Journal of Colloid and Interface Science 244(1), 139-144 (2001)

[15] Apreleva, S. V., Wilson, D. F. and Vinogradov, S. A., "Tomographic Imaging of Oxygen by Phosphorescence Lifetime," Appl Opt 45(33), 8547-8559 (2006)

[16] Ashkenazi, S., "Photoacoustic Lifetime Imaging of Dissolved Oxygen Using Methylene Blue," Journal of Biomedical Optics 15(4), 040501-040503 (2010)

[17] Ashkenazi, S., Huang, S.-W., Horvath, T., Koo, L. Y.-E. and Kopelman, R., "Photoacoustic Probing of Fluorophore Excited State Lifetime with Application to Oxygen Sensing," Journal of Biomedical Optics 13(3), 034023 (2008)

[18] Baker, G. A., Wenner, B. R., Watkins, A. N. and Bright, F. V., "Effects of Processing Temperature on the Oxygen Quenching Behavior of Tris(4,7′-Diphenyl-1,10′-Phenanthroline) Ruthenium (Ii) Sequestered within Sol-Gel-Derived Xerogel Films," Journal of Sol-Gel Science and Technology 17(1), 71-82 (2000)

[19] Ballew, R. M. and Demas, J. N., "An Error Analysis of the Rapid Lifetime Determination Method for the Evaluation of Single Exponential Decays," Analytical Chemistry 61(1), 30-33 (1989)

[20] Bambot, S. B., Lakowicz, J. R. and Rao, G., "Potential Applications of Lifetime-Based, Phase-Modulation Fluorimetry in Bioprocess and Clinical Monitoring," Trends in Biotechnology 13(3), 106-115 (1995)

[21] Barber, B. P., Hiller, R. A., Löfstedt, R., Putterman, S. J. and Weninger, K. R., "Defining the Unknowns of Sonoluminescence," Physics Reports 281(2), 65-143 (1997)

[22] Barber, P. R., Ameer-Beg, S. M., Gilbey, J., Carlin, L. M., Keppler, M., Ng, T. C. and Vojnovic, B., "Multiphoton Time-Domain Fluorescence Lifetime Imaging Microscopy: Practical Application to Protein-Protein Interactions Using Global Analysis," J. R. Soc. Interface 6(Suppl 1), S93-S105 (2009)

[23] Barca, A., Pani, B., Tamaro, M. and Russo, E., "Molecular Interactions of Ruthenium Complexes in Isolated Mammalian Nuclei and Cytotoxicity on V79 Cells in Culture," Mutation Research/Fundamental and Molecular Mechanisms of Mutagenesis 423(1-2), 171-181 (1999)

[24] Bashir, A., Gray, M. L., Boutin, R. D. and Burstein, D., "Glycosaminoglycan in Articular Cartilage: In Vivo Assessment with Delayed Gd(Dtpa)(2-)-Enhanced Mr Imaging," Radiology 205(2), 551-558 (1997)

[25] Battino, R. and Clever, H. L., "The Solubility of Gases in Liquids," Chemical Reviews 66(4), 395-463 (1966)

[26] Beaurepaire, E., Oheim, M. and Mertz, J., "Ultra-Deep Two-Photon Fluorescence Excitation in Turbid Media," Optics Communications 188(1-4), 25-29 (2001)

[27] Becker, W., Advanced Time-Correlated Single Photon Counting Techniques, Springer, Berlin, New York (2005).

[28] Becker, W., Bergmann, A., Biscotti, G. and Ruck, A., "Advanced Time-Correlated Single Photon Counting Technique for Spectroscopy and Imaging in Biomedical Systems," Proc. SPIE 5340(1-9 (2004)

[29] Becker, W., Bergmann, A., Haustein, E., Petrasek, Z., Schwille, P., Biskup, C., Kelbauskas, L., Benndorf, K., Klöcker, N., Anhut, T., Riemann, I. and König, K., "Fluorescence Lifetime Images and Correlation Spectra Obtained by Multidimensional Time-Correlated Single Photon Counting," Microscopy Research and Technique 69(3), 186-195 (2006)

[30] Becker&Hickl, "High Speed Pmt Detector Head for Photon Counting: Pmh-100 " Http://Www.Becker-Hickl.Com/Pdf/Dbpmhl.Pdf, Ed., Berlin.

[31] Becker&Hickl, Leica Mp-Flim and D-Flim - Fluorescence Lifetime Microscopy Systems, Leica Microsystems, Germany (2006).

[32] Benson, B. B. and Krause, D., Jr., "The Concentration and Isotopic Fractionation of Gases Dissolved in Freshwater in Equilibrium with the Atmosphere. 1. Oxygen," Limnology and Oceanography 25(4), 662-671 (1980)

[33] Benson, B. B., Krause, D., Jr. and Peterson, M. A., "The Solubility and Isotopic Fractionation of Gases in Dilute Aqueous Solution. 1. Oxygen," Journal of Solution Chemisty 8(9), 655-690 (1979)

[34] Bevington, P. R. and Robinson, D. K., Data Reduction and Error Analysis for the Physical Sciences, McGraw-Hill, New York (1992).

[35] Born, M., Wolf, E. and Bhatia, A. B. D., Principles of Optics : Electromagnetic Theory of Propagation, Interference and Diffraction of Light, Cambridge University Press, Cambridge (1999).

[36] Botchway, S. W., Charnley, M., Haycock, J. W., Parker, A. W., Rochester, D. L., Weinstein, J. A. and Williams, J. A. G., "Time-Resolved and Two-Photon Emission Imaging Microscopy of Live Cells with Inert Platinum Complexes," Proceedings of the National Academy of Sciences 105(42), 16071-16076 (2008)

[37] Brakenhoff, G. J., Voort, H. T. M. V. D., Spronsen, E. A. V. and Nanninga, N., "Three-Dimensional Imaging by Confocal Scanning Fluorescence Microscopy," Annals of the New York Academy of Sciences 483(1), 405-415 (1986)

[38] Bristow, R. G. and Hill, R. P., "Hypoxia and Metabolism: Hypoxia, DNA Repair and Genetic Instability," Nat Rev Cancer 8(3), 180-192 (2008)

[39] Brizel, D. M., Dodge, R. K., Clough, R. W. and Dewhirst, M. W., "Oxygenation of Head and Neck Cancer: Changes During Radiotherapy and Impact on Treatment Outcome," Radiotherapy and oncology : journal of the European Society for Therapeutic Radiology and Oncology 53(2), 113-117 (1999)

[40] Brodkin, K. R., García, A. J. and Levenston, M. E., "Chondrocyte Phenotypes on Different Extracellular Matrix Monolayers," Biomaterials 25(28), 5929-5938 (2004)

[41] Brown, J. Q., Srivastava, R. and Mcshane, M. J., "Encapsulation of Glucose Oxidase and an Oxygen-Quenched Fluorophore in Polyelectrolyte-Coated Calcium Alginate Microspheres as Optical Glucose Sensor Systems," Biosensors and Bioelectronics 21(1), 212-216 (2005)

[42] Brun, P., Abatangelo, G., Radice, M., Zacchi, V., Guidolin, D., Gordini, D. D. and Cortivo, R., "Chondrocyte Aggregation and Reorganization into Three-Dimensional Scaffolds," Journal of Biomedical Materials Research 46(3), 337-346 (1999)

[43] Buckwalter, J. A., Mow, V. C. and Ratcliffe, A., "Restoration of Injured or Degenerated Articular Cartilage," J Am Acad Orthop Surg 2(4), 192-201 (1994)

[44] Buschmann, M. D., Gluzband, Y. A., Grodzinsky, A. J., Kimura, J. H. and Hunziker, E. B., "Chondrocytes in Agarose Culture Synthesize a Mechanically Functional Extracellular Matrix," J Orthop Res. 10(6), 745-758 (1992)

[45] Campbell, A. and Uttamchandani, D., "Optical Dissolved Oxygen Lifetime Sensor Based on Sol-Gel Immobilisation," Science, Measurement and Technology, IEE Proceedings- 151(4), 291-297 (2004)

[46] Carraway, E. R., Demas, J. N., Degraff, B. A. and Bacon, J. R., "Photophysics and Photochemistry of Oxygen Sensors Based on Luminescent Transition-Metal Complexes," Analytical Chemistry 63(4), 337-342 (1991)

[47] Caspar, J. V. and Meyer, T. J., "Photochemistry of Tris(2,2'-Bipyridine)Ruthenium(2+) Ion (Ru(Bpy)32+). Solvent Effects," J. Am. Chem. Soc. 105(17), 5583-5590 (1983)

[48] Castellano, F. N. and Lakowicz, J. R., "A Water-Soluble Luminescence Oxygen Sensor," Photochemistry and Photobiology 67(2), 179-183 (1998)

[49] Castellano, F. N., Malak, H., Gryczynski, I. and Lakowicz, J. R., "Creation of Metal-to-Ligand Charge Transfer Excited States with Two-Photon Excitation," Inorg. Chem. 36(24), 5548-5551 (1997)

[50] Cengel, Y. A., Heat Transfer: A Practical Approach, McGraw-Hill, New York (2003).

[51] Cheema, U., Brown, R., Alp, B. and Macrobert, A., "Spatially Defined Oxygen Gradients and Vascular Endothelial Growth Factor Expression in an Engineered 3d Cell Model," Cellular and Molecular Life Sciences 65(1), 177-186 (2008)

[52] Chen, F. H., Rousche, K. T. and Tuan, R. S., "Technology Insight: Adult Stem Cells in Cartilage Regeneration and Tissue Engineering," Nat Clin Pract Rheum 2(7), 373-382 (2006)

[53] Chow, D. C., Wenning, L. A., Miller, W. M. and Papoutsakis, E. T., "Modeling Po2 Distributions in the Bone Marrow Hematopoietic Compartment. I. Krogh's Model," Biophysical Journal 81(2), 675-684 (2001)

[54] Chowdhury, T. T., Bader, D. L. and Lee, D. A., "Dynamic Compression Counteracts Il-1[Beta]-Induced Release of Nitric Oxide and Pge2by Superficial Zone Chondrocytes Cultured in Agarose Constructs," Osteoarthritis and Cartilage 11(9), 688-696 (2003)

[55] Clark, J. M., "The Structure of Vascular Channels in the Subchondral Plate," Journal of Anatomy 171(105-115 (1990)

[56] Coates, P. B., "The Correction for Photon `Pile-up' in the Measurement of Radiative Lifetimes," J. Phys. E: Sci. Instrum. 8), 878 (1968)

[57] Comper, W. D., Ed., Tissue Function, Overseas Publishers Association, Amsterdam (1966).

[58] Croll, T. I., Gentz, S., Mueller, K., Davidson, M., O'connor, A. J., Stevens, G. W. and Cooper-White, J. J., "Modelling Oxygen Diffusion and Cell Growth in a Porous, Vascularising Scaffold for Soft Tissue Engineering Applications," Chemical Engineering Science 60(17), 4924-4934 (2005)

[59] Da Fonseca, R., Johnson, W., O'brien, S., Ramos, M. and Antunes, A., "The Adaptive Evolution of the Mammalian Mitochondrial Genome," BMC Genomics 9(1), 119 (2008)

[60] Damrauer, N. H., Cerullo, G., Yeh, A., Boussie, T. R., Shank, C. V. and Mccusker, J. K., "Femtosecond Dynamics of Excited-State Evolution in [Ru(Bpy)3]2+," Science 275(5296), 54-57 (1997)

[61] Darling, E. M. and Athanasiou, K. A., "Articular Cartilage Bioreactors and Bioprocesses," Tissue Engineering 9(1), 9-26 (2003)

[62] Datasheet, S. P., "Alamarblue."

[63] Davia, K., King, D., Hong, Y. and Swavey, S., "A Porphyrin-Ruthenium Photosensitizer as a Potential Photodynamic Therapy Agent," Inorganic Chemistry Communications 11(5), 584-586 (2008)

[64] Demas, J. N., Excited State Lifetime Measurements, Academic Press, New York (1983).

[65] Demas, J. N. and Adamson, A. W., "Tris (2,2'-Bipyridine)Ruthenium(Ii) Sensitized Reactions of Some Oxalato Complexes," Journal of the American Chemical Society 95(16), 5159-5168 (1973)

[66] Demas, J. N. and Degraff, B. A., "Applications of Luminescent Transition Metal Complexes to Sensor Technology and Molecular Probes," Journal of Chemcial Education 74(6), 690-695 (1997)

[67] Demas, J. N., Degraff, B. A. and Coleman, P. B., "Oxygen Sensors Based on Luminescence Quenching," Analytical Chemistry 71(23), 793A-800A (1999)

[68] Demas, J. N., Harris, E. W. and Mcbride, R. P., "Energy Transfer from Luminescent Transition Metal Complexes to Oxygen," Journal of the American Chemical Society 99(11), 3547-3551 (1977)

[69] Denk, W., Strickler, J. H. and Webb, W. W., "Two-Photon Laser Scanning Fluorescence Microscopy," Science 248(4951), 73-76 (1990)

[70] Diaspro, A., Confocal and Two-Photon Microscopy : Foundations, Applications, and Advances, Wiley-Liss, New York (2002).

[71] Dickens, F., Neil, E., International Union of, B. and International Union of Physiological, S., Oxygen in the Animal Organism, Pergamon, Oxford (1964).

[72] Dobrucki, J. W., "Interaction of Oxygen-Sensitive Luminescent Probes Ru(Phen)32+ and Ru(Bipy)32+ with Animal and Plant Cells in Vitro: Mechanism of Phototoxicity and Conditions for Non-Invasive Oxygen Measurements," Journal of Photochemistry and Photobiology B: Biology 65(2-3), 136-144 (2001)

[73] Dong, C.-Y., Koenig, K. and So, P., "Characterizing Point Spread Functions of Two-Photon Fluorescence Microscopy in Turbid Medium," Journal of Biomedical Optics 8(3), 450-459 (2003)

[74] Dunphy, I., Vinogradov, S. A. and Wilson, D. F., "Oxyphor R2 and G2: Phosphors for Measuring Oxygen by Oxygen-Dependent Quenching of Phosphorescence," Analytical Biochemistry 310(2), 191-198 (2002)

[75] Eaton, D. F., "Recommeded Methods for Fluorescence Decay Analysis," Pure and Applied Chemistry 62(8), 1631-1648 (1990)

[76] Eberhardt, C., "Photomultiplier Tube," in http://en.wikipedia.org/wiki/File:Photomultipliertube.svg Photomultipliertube.Png, Ed., Arpad Horvath (2006).

[77] Eggleston, D. S., Goldsby, K. A., Hodgson, D. J. and Meyer, T. J., "Structural Variations Induced by Changes in Oxidation State and Their Role in Electron Transfer. Crystal and Molecular Structures of Cis-[Ru(Bpy)2cl2].3.5h2o and Cis-[Ru(Bpy)2cl2]Cl.2h2o," Inorganic Chemistry 24(26), 4573-4580 (1985)

[78] Elas, M., Ahn, K.-H., Parasca, A., Barth, E. D., Lee, D., Haney, C. and Halpern, H. J., "Electron Paramagnetic Resonance Oxygen Images Correlate Spatially and Quantitatively with Oxylite Oxygen Measurements," Clinical Cancer Research 12(14), 4209-4217 (2006)

[79] Estrada, A. D., Ponticorvo, A., Ford, T. N. and Dunn, A. K., "Microvascular Oxygen Quantification Using Two-Photon Microscopy," Opt. Lett. 33(10), 1038-1040 (2008)

[80] Fermor, B., Christensen, S., Youn, I., Cernanec, J. M., Davies, C. M. and Weinberg, J. B., "Oxygen, Nitric Oxide and Articular Cartilage," Eur. Cell. Mater. 13(56-55 (2007)

[81] Finan, J. D. and Guilak, F., "The Effects of Osmotic Stress on the Structure and Function of the Cell Nucleus," Journal of Cellular Biochemistry 109(3), 460-467 (2010)

[82] Finikova, O. S., Lebedev, A. Y., Aprelev, A., Troxler, T., Gao, F., Garnacho, C., Muro, S., Hochstrasser, R. M. and Vinogradov, S. A., "Oxygen Microscopy by Two-Photon-Excited Phosphorescence," ChemPhysChem 9(12), 1673-1679 (2008)

[83] Finkel, T., "Signal Transduction by Reactive Oxygen Species in Non-Phagocytic Cells," J Leukoc Biol 65(3), 337-340 (1999)

[84] Fuller, Z. J., Bare, W. D., Kneas, K. A., Xu, W. Y., Demas, J. N. and Degraff, B. A., "Photostability of Luminescent Ruthenium(Ii) Complexes in Polymers and in Solution," Analytical Chemistry 75(11), 2670-2677 (2003)

[85] Gao, F. G. and Bard, A. J., "Solid-State Organic Light-Emitting Diodes Based on Tris(2, 2'-Bipyridine)Ruthenium(Ii) Complexes," Journal of the American Chemical Society 122(30), 7426-7427 (2000)

[86] Gao, F. G., Jeevarajan, A. S. and Anderson, M. M., "Long-Term Continuous Monitoring of Dissolved Oxygen in Cell Culture Medium for Perfused Bioreactors Using Optical Oxygen Sensors," Biotechnology and Bioengineering 86(4), 425-433 (2004)

[87] Garcìa-Fresnadillo, D., Georgiadou, Y., Orellana, G., Braun, A. M. and Oliveros, E., "Singlet-Oxygen (1δg) Production by Ruthenium(Ii) Complexes Containing Polyazaheterocyclic Ligands in Methanol and in Water," Helvetica Chimica Acta 79(4), 1222-1238 (1996)

[88] Garcia, H. E. and Gordon, L. I., "Oxygen Solubility in Seawater: Better Fitting Equations," Limnology and Oceanography 37(6), 1307-1312 (1992)

[89] Gauderon, R., Lukins, P. B. and Sheppard, C. J. R., "Effect of a Confocal Pinhole in Two-Photon Microscopy," Microscopy Research and Technique 47(3), 210-214 (1999)

[90] Gerritsen, H. C., Asselbergs, M. A. H., Agronskaia, A. V. and Van Sark, W. G. J. H. M., "Fluorescence Lifetime Imaging in Scanning Microscopes: Acquisition Speed, Photon Economy and Lifetime Resolution," Journal of Microscopy 206(3), 218-224 (2002)

[91] Gerritsen, H. C., Sanders, R., Draaijer, A. and Levine, Y. K., "Fluorescence Lifetime Imaging of Oxygen in Living Cells," Journal of Fluorescence 7(1), 11-15 (1997)

[92] Giacomo, P., "Equation for the Determination of the Density of Moist Air (1981)," Metrologia 18(1), 33-40 (1982)

[93] Gibson, J., Milner, P., White, R., Fairfax, T. and Wilkins, R., "Oxygen and Reactive Oxygen Species in Articular Cartilage: Modulators of Ionic Homeostasis," Pflügers Archiv European Journal of Physiology 455(4), 563-573 (2008)

[94] Gnaiger, E., "Bioenergetics at Low Oxygen: Dependence of Respiration and Phosphorylation on Oxygen and Adenosine Diphosphate Supply," Respiration Physiology 128(3), 277-297 (2001)

[95] Gnaiger, E., "Oxygen Solubility in Experimental Media," in Mitochondrial Physiology Network, pp. 1-6 (2001-2007).

[96] Gnaiger, E., Gnaiger, E. and Forstner, H., Polarographic Oxygen Sensors : Aquatic and Physiological Applications, Springer-Verlag, Berlin; New York (1983).

[97] Goldman, R. D. and Spector, D. L., Live Cell Imaging : A Laboratory Manual, Cold Spring Harbor Laboratory Press, Cold Spring Harbor, N.Y. (2005).

[98] Gomes, A., Fernandes, E. and Lima, J. L. F. C., "Fluorescence Probes Used for Detection of Reactive Oxygen Species," Journal of Biochemical and Biophysical Methods 65(2-3), 45-80 (2005)

[99] Görner, H., Stradowski, C. and Schulte-Frohlinde, D., "Photoreactions of Tris(2,2′-Bipyridyl)-Ruthenium(Ii) with Peroxydisulfate in Deoxygenated Aqueous Solution in the Presence of Nucleic Acid Components, Polynucleotides, and DNA.," Photochemistry and Photobiology 47(1), 15-29 (1988)

[100] Gratton, E., Breusegem, S., Sutin, J., Ruan, Q. and Barry, N., "Fluorescence Lifetime Imaging for the Two-Photon Microscope: Time-Domain and Frequency-Domain Methods," Journal of Biomedical Optics 8(3), 381-390 (2003)

[101] Grimshaw, M. J. and Mason, R. M., "Bovine Articular Chondrocyte Function in Vitro Depends Upon Oxygen Tension," Osteoarthritis and Cartilage 8(5), 386-392 (2000)

[102] Grimshaw, M. J. and Mason, R. M., "Modulation of Bovine Articular Chondrocyte Gene Expression in Vitro by Oxygen Tension," Osteoarthritis and Cartilage 9(4), 357-364 (2001)

[103] Gu, W. Y., Yao, H., Vega, A. L. and Flagler, D., "Diffusivity of Ions in Agarose Gels and Intervertebral Disc: Effect of Porosity," Annals of Biomedical Engineering 32(12), 1710-1717 (2004)

[104] Guaccio, A., Borselli, C., Oliviero, O. and Netti, P. A., "Oxygen Consumption of Chondrocytes in Agarose and Collagen Gels: A Comparative Analysis," Biomaterials 29(10), 1484-1493 (2008)

[105] Guggenheim, E. A., Thermodynamics - an Advanced Treatment for Chemists and Physicists, Elseveir Science Publishers (1967).

[106] Gundersen, J. K., Ramsing, N. B. and Glud, R. N., "Predicting the Signal of O2 Microsensors from Physical Dimensions, Temperature, Salinity, and O2 Concentration," Limnology and Oceanography 43(8), 1932-1937 (1998)

[107] Hall, B. K. and Newman, S., Cartilage: Molecular Aspects, CRC Press, Boca Raton, FL; London (1991).

[108] Hall, P. and Selinger, B., "Better Estimates of Exponential Decay Parameters," J. Phys. Chem. 85(20), 2941-2946 (1981)

[109] Hamamatsu-Photonics, "Guide to Streak Cameras," in http://sales.hamamatsu.com/en/support/technical-notes.php (2008).

[110] Hamann, S., Kiilgaard, J. F., Litman, T., Alvarez-Leefmans, F. J., Winther, B. R. and Zeuthen, T., "Measurement of Cell Volume Changes by Fluorescence Self-Quenching," Journal of Fluorescence 12(2), 139-145 (2002)

[111] Hamid, R., Rotshteyn, Y., Rabadi, L., Parikh, R. and Bullock, P., "Comparison of Alamar Blue and Mtt Assays for High through-Put Screening," Toxicology in Vitro 18(5), 703-710 (2004)

[112] Hardingham, T., Tew, S. and Murdoch, A., "Tissue Engineering: Chondrocytes and Cartilage," Arthritis Research 4(Suppl 3), S63 - S68 (2002)

[113] Harrigan, R. W., Hager, G. D. and Crosby, G. A., "Evidence for Multiple-State Emission from Ruthenium(Ii) Complexes," Chemical Physics Letters 21(3), 487-490 (1973)

[114] Harrison, K., "$[Ru(Bipy)_3]^{2+}$ - Chemistry, Structures & 3d Molecules @3dchem.Com," (2005-2010).

[115] Harvey, A. and Huang, P., "First-Principles Calculation of the Air–Water Second Virial Coefficient," International Journal of Thermophysics 28(2), 556-565 (2007)

[116] Harvey, A., Kaplan, S. and Burnett, J., "Effect of Dissolved Air on the Density and Refractive Index of Water," International Journal of Thermophysics 26(5), 1495-1514 (2005)

[117] Haselgrove, J. C., Shapiro, I. M. and Silverton, S. F., "Computer Modeling of the Oxygen Supply and Demand of Cells of the Avian Growth Cartilage," American Journal of Physiology 265(2), C497-506 (1993)

[118] Hell, S., Reiner, G., Cremer, C. and Stelzer, E. H. K., "Aberrations in Confocal Fluorescence Microscopy Induced by Mismatches in Refractive Index," Journal of Microscopy 169(3), 341-405 (1993)

[119] Henrotin, Y., Kurz, B. and Aigner, T., "Oxygen and Reactive Oxygen Species in Cartilage Degradation: Friends or Foes?," Osteoarthritis and Cartilage 13(8), 643-654 (2005)

[120] Henrotin, Y. E., Bruckner, P. and Pujol, J. P., "The Role of Reactive Oxygen Species in Homeostasis and Degradation of Cartilage," Osteoarthritis and Cartilage 11(10), 747-755 (2003)

[121] Herman, B., Fluorescence Microscopy, BIOS Scientific Publishers Ltd., Oxford (1998).

[122] Hernández, I., "Personal Communication," Physics Department, Queen Mary (2008).

[123] Herst, P. M. and Berridge, M. V., "Cell Surface Oxygen Consumption: A Major Contributor to Cellular Oxygen Consumption in Glycolytic Cancer Cell Lines," Biochimica et Biophysica Acta (BBA) - Bioenergetics 1767(2), 170-177 (2007)

[124] Heully, J.-L., Alary, F. and Boggio-Pasqua, M., "Spin-Orbit Effects on the Photophysical Properties of $[Ru(Bpy)_3]^{2+}$," The Journal of Chemical Physics 131(18), 184308-184309 (2009)

[125] Heywood, H. K., "Sample Preparation Oligomycin and Cccp," N. Hosny, Ed., Email (2009).

[126] Heywood, H. K., Bader, D. L. and Lee, D. A., "Rate of Oxygen Consumption by Isolated Articular Chondrocytes Is Sensitive to Medium Glucose Concentration," Journal of Cellular Physiology 206(2), 402-410 (2006)

[127] Heywood, H. K., Knight, M. M. and Lee, D. A., "Both Superficial and Deep Zone Articular Chondrocyte Subpopulations Exhibit the Crabtree Effect but Have Different Basal Oxygen Consumption Rates," Journal of Cellular Physiology 223(3), 630-639 (2010)

[128] Heywood, H. K. and Lee, D. A., "Superficial & Deep Chondrocyte Subpopulations Both Express the Crabtree Effect but Exhibit Differences in Oxygen Consumption Rate," Transactions of the Orthopaedic Research Society. (Poster) 31(0392 (2006)

[129] Heywood, H. K. and Lee, D. A., "Monolayer Expansion Induces an Oxidative Metabolism and Ros in Chondrocytes," Biochemical and Biophysical Research Communications 373(2), 224-229 (2008)

[130] Heywood, H. K., Sembi, P. K., Lee, D. A. and Bader, D. L., "Cellular Utilization Determines Viability and Matrix Distribution Profiles in Chondrocyte-Seeded Alginate Constructs," Tissue Engineering 10(9-10), 1467-1479 (2004)

[131] Himmelblau, D. M., "Diffusion of Dissolved Gases in Liquids," Chemical Reviews 64(5), 527-550 (1964)

[132] Hotze, A. C., Bacac, M., Velders, A. H., Jansen, B. A., Kooijman, H., Spek, A. L., Haasnoot, J. G. and Reedijk, J., "New Cytotoxic and Water-Soluble Bis(2-Phenylazopyridine)Ruthenium(Ii) Complexes," Journal of Medicinal Chemistry 46(9), 1743-1750 (2003)

[133] Hulst, A. C., Hens, H. J. H., Buitelaar, R. M. and Tramper, J., "Determination of the Effective Diffusion Coefficient of Oxygen in Gel Materials in Relation to Gel Concentration," Biotechnology Techniques 3(3), 199-204 (1989)

[134] Hunziker, E. B., "Articular Cartilage Repair: Basic Science and Clinical Progress. A Review of the Current Status and Prospects," Osteoarthritis and Cartilage 10(6), 432-463 (2002)

[135] Hunziker, E. B., Quinn, T. M. and Häuselmann, H. J., "Quantitative Structural Organization of Normal Adult Human Articular Cartilage," Osteoarthritis and Cartilage 10(7), 564-572 (2002)

[136] Imhof, H., Sulzbacher, I., Grampp, S., Czerny, C., Youssefzadeh, S. and Kainberger, F., "Subchondral Bone and Cartilage Disease: A Rediscovered Functional Unit," Invest Radiol 35(10), 581-588 (2000)

[137] Itoh, T., Yaegashi, K., Kosaka, T., Kinoshita, T. and Morimoto, T., "In Vivo Visualization of Oxygen Transport in Microvascular Network," Am. J. Physiol. 267(5), H2068-2078 (1994)

[138] Ivano, B., Harry, G. B., Stephen, L. J. and Selverstone, V. J., Bioinorganic Chemistry, University Science Books, Mill Valley, Calif. (1994).

[139] Jain, A., Xu, W., Demas, J. N. and Degraff, B. A., "Binding of Luminescent Ruthenium(Ii) Molecular Probes to Vesicles," Inorg. Chem. 37(8), 1876-1879 (1998)

[140] James, A. M., "A Dictionary of Thermodynamics," pp. 1-262p, The MacMillan Press Ltd, London, New York (1976).

[141] Jebens, E. H. and Monk-Jones, M. E., "On the Viscosity and Ph of Synovial Fluid and the Ph of Blood," J Bone Joint Surg Br 41-B(2), 388-400 (1959)

[142] Ji, J., Rosenzweig, N., Jones, I. and Rosenzweig, Z., "Molecular Oxygen-Sensitive Fluorescent Lipobeads for Intracellular Oxygen Measurements in Murine Macrophages," Analytical Chemistry 73(15), 3521-3527 (2001)

[143] Ji, J., Rosenzweig, N., Jones, I. and Rosenzweig, Z., "Novel Fluorescent Oxygen Indicator for Intracellular Oxygen Measurements," J Biomed Opt 7(3), 404-409 (2002)

[144] Juris, A., Balzani, V., Barigelletti, F., Campagna, S., Belser, P. and Von Zelewsky, A., "Ru(Ii) Polypyridine Complexes: Photophysics, Photochemistry, Eletrochemistry, and Chemiluminescence," Coordination Chemistry Reviews 84(85-277 (1988)

[145] Kadenbach, B., "Intrinsic and Extrinsic Uncoupling of Oxidative Phosphorylation," Biochimica et Biophysica Acta (BBA) - Bioenergetics 1604(2), 77-94 (2003)

[146] Kaiser, W. and Garrett, C. G. B., "Two-Photon Excitation in Ca $F_2$: $Eu^{2+}$," Physical Review Letters 7(6), 229 (1961)

[147] Kammeyer, C. W. and Whitman, D. R., "Quantum Mechanical Calculation of Molecular Radii. I. Hydrides of Elements of Periodic Groups Iv through Vii," The Journal of Chemical Physics 56(9), 4419-4421 (1972)

[148] Karni, Y., Jordens, S., De Belder, G., Schweitzer, G., Hofkens, J., Gensch, T., Maus, M., De Schryver, F. C., Hermann, A. and Müllen, K., "Intramolecular Evolution from a Locally Excited State to an Excimer-Like State in a Multichromophoric Dendrimer Evidenced by a Femtosecond Fluorescence Upconversion Study," Chemical Physics Letters 310(1-2), 73-78 (1999)

[149] Kellner, K., Liebsch, G., Klimant, I., Wolfbeis, O. S., Blunk, T., Schulz, M. B. and Gopferich, A., "Determination of Oxygen Gradients in Engineered Tissue Using a Fluorescent Sensor," Biotechnol Bioeng 80(1), 73-83 (2002)

[150] Keuren, E. V., Littlejohn, D. and Schrof, W., "Three-Dimensional Thermal Imaging Using Two-Photon Microscopy," J Phys. D:Appl. Phys. 37(20), 2938 (2004)

[151] Khan, M., Kwiatkowski, P., Rivera, B. K. and Kuppusamy, P., "Oxygen and Oxygenation in Stem-Cell Therapy for Myocardial Infarction," Life Sciences 87(9-10), 269-274 (2010)

[152] Kimura, S., Matsumoto, K., Mineura, K. and Itoh, T., "A New Technique for the Mapping of Oxygen Tension on the Brain Surface," Journal of the Neurological Sciences 258(1), 60-68 (2007)

[153] Kiviranta, I., "Tissue Engineering and Repair of Articular Cartilage," in **http://www.luotain.uku.fi/terac/research_fields/**, Kuopio, Finland (2003).

[154] Klimant, I. and Wolfbeis, O. S., "Oxygen-Sensitive Luminescent Materials Based on Silicone-Soluble Ruthenium Diimine Complexes," Analytical Chemistry 67(18), 3160-3166 (1995)

[155] Knight, A. and Selinger, B., "Single Photon Decay Spectroscopy," Australian Journal of Chemistry 26(1), 1-27 (1973)

[156] Knight, M. M., "Deformation of Isolated Articular Chondrocytes Cultured in Agarose Constructs," in Medical Engineering, p. 217, Queen Mary, London (1997).

[157] Kodibagkar, V. D., Cui, W., Merritt, M. E. and Mason, R. P., "Novel 1h Nmr Approach to Quantitative Tissue Oximetry Using Hexamethyldisiloxane," Magnetic Resonance in Medicine 55(4), 743-748 (2006)

[158] Konig, K., "Multiphoton Microscopy in Life Sciences," Journal Microscopy 200(Pt 2), 83-104 (2000)

[159] Koning, M., Harmsen, M. C., Van Luyn, M. J. A. and Werker, P. M. N., "Current Opportunities and Challenges in Skeletal Muscle Tissue Engineering," Journal of Tissue Engineering and Regenerative Medicine 3(6), 407-415 (2009)

[160] Koolman, J. and Röhm, K.-H., Color Atlas of Biochemistry, Thieme, Stuttgart, New York (2006).

[161] Korson, L., Drost-Hansen, W. and Millero, F. J., "Viscosity of Water at Various Temperatures," The Journal of Physical Chemistry 73(1), 34-39 (1969)

[162] Kraan, P. M. V. D., Buma, P., Kuppevelt, T. V. and Den Berg, W. B. V., " Interaction of Chondrocytes, Extracellular Matrix and Growth Factors: Relevance for Articular Cartilage Tissue Engineering," Osteoarthritis and Cartilage 10( 8), 631-637 (2002)

[163] Krishna, M. C., English, S., Yamada, K., Yoo, J., Murugesan, R., Devasahayam, N., Cook, J. A., Golman, K., Ardenkjaer-Larsen, J. H., Subramanian, S. and Mitchell, J. B., "Overhauser Enhanced Magnetic Resonance Imaging for Tumor Oximetry: Coregistration of Tumor Anatomy and Tissue Oxygen Concentration," Proceedings of the National Academy of Sciences of the United States of America 99(4), 2216-2221 (2002)

[164] Krohn, K. A., Link, J. M. and Mason, R. P., "Molecular Imaging of Hypoxia," J Nucl Med 49(Suppl_2), 129S-148 (2008)

[165] Kruger, A. and Feru, P., "Getting Pratical: New Materials Such as Yb:Kgw Yield Simpler, More Versatile Femtosecond Systems. ," in SPIE's oemagazine, pp. 23-25 (2004).

[166] Kuang, Y. and Walt, D. R., "Detecting Oxygen Consumption in the Proximity of *Saccharomyces Cerevisiae* Cells Using Self-Assembled Fluorescent Nanosensors," Biotechnology and Bioengineering 96(2), 318-325 (2007)

[167] Kuhl, M., Rickelt, L. F. and Thar, R., "Combined Imaging of Bacteria and Oxygen in Biofilms," Applied and Environmental Microbiology 73(19), 6289-6295 (2007)

[168] Kumar, S., Dunsby, C., De Beule, P. A. A., Owen, D. M., Anand, U., Lanigan, P. M. P., Benninger, R. K. P., Davis, D. M., Neil, M. A. A., Anand, P., Benham, C., Naylor, A. and French, P. M. W., "Multifocal Multiphoton Excitation and Time Correlated Single Photon Counting Detection for 3-D Fluorescence Lifetime Imaging," Optics Express 15(20), 12548-12561 (2007)

[169] Kumelan, J., Kamps, A. P.-S., Urukova, I., Tuma, D. and Maurer, G., "Solubility of Oxygen in the Ionic Liquid [Bmim][Pf6]: Experimental and Molecular Simulation Results," The Journal of Chemical Thermodynamics 37(6), 595-602 (2005)

[170] Lakowicz, J. R., Principles of Fluorescence Spectroscopy, Kluwer Academic/Plenum, New York; London (1999).

[171] Lakowicz, J. R. and Springerlink, Principles of Fluorescence Spectroscopy, Springer, New York (2006).

[172] Lakowicz, J. R. and Weber, G., "Quenching of Fluorescence by Oxygen. A Probe for Structural Fluctuations in Macromolecules," Biochemistry 12(21), 4161-4170 (1973)

[173] Lammerding, J., Kamm, R. D. and Lee, R. T., "Mechanotransduction in Cardiac Myocytes," Annals of the New York Academy of Sciences 1015(1), 53-70 (2004)

[174] Laufer, J., Elwell, C., Delpy, D. and Beard, P., "Spatially Resolved Blood Oxygenation Measurements Using Time-Resolved Photoacoustic Spectroscopy," in Oxygen Transport to Tissue Xxvii, pp. 155-160 (2006).

[175] Lawrence, B. J. and Madihally, S. V., "Cell Colonization in Degradable 3d Porous Matrices," 2(1), 9 - 16 (2008)

[176] Leddy, H. A., Awad, H. A. and Guilak, F., "Molecular Diffusion in Tissue-Engineered Cartilage Constructs: Effects of Scaffold Material, Time, and Culture Conditions," J. Biomed. Mater. Res. Part B: Appl. Biomater 70B(2), 397-406 (2004)

[177] Lee, D. A., Noguchi, T., Knight, M. M., O'donnell, L., Bentley, G. and Bader, D. L., "Response of Chondrocyte Subpopulations Cultured within Unloaded and Loaded Agarose," Journal of Orthopaedic Research 16(6), 726-733 (1998)

[178] Lee, K. C. B., Siegel, J., Webb, S. E. D., Leveque-Fort, S., Cole, M. J., Jones, R., Dowling, K., Lever, M. J. and French, P. M. W., "Application of the Stretched

Exponential Function to Fluorescence Lifetime Imaging," Biophysical Journal 81(3), 1265-1274 (2001)

[179] Lee, R. B. and Urban, J. P., "Evidence for a Negative Pasteur Effect in Articular Cartilage," Biochem J. 321(Pt 1), 95-102. (1997)

[180] Lemercier, G., Bonne, A., Four, M. and Lawson-Daku, L. M., "3mlct Excited States in Ru(Ii) Complexes: Reactivity and Related Two-Photon Absorption Applications in the near-Infrared Spectral Range," Comptes Rendus Chimie In Press, Corrected Proof((2008)

[181] Lentz, T. L., "Cell Fine Structure: An Atlas of Drawings of Whole-Cell Structure," W.B. Saunders company, Philadelphia (1971).

[182] Levick, J. R., "Microvascular Architecture and Exchange in Synovial Joints," Microcirculation 2(3), 217-233 (1995)

[183] Li, X.-M., Ruan, F.-C. and Wong, K.-Y., "Optical Characteristics of a Ruthenium(Ii) Complex Immobilized in a Silicone Rubber Film for Oxygen Measurement," Analyst 118(3), 289-292 (1993)

[184] Liebsch, G., Klimant, I. and Wolfbeis, O. S., "Luminescence Lifetime Temperature Sensing Based on Sol-Gels and Poly(Acrylonitrile)S Dyed with Ruthenium Metal-Ligand Complexes," Advanced Materials 11(15), 1296-1299 (1999)

[185] Lin, Z., Willers, C., Xu, J. and Zheng, M. H., "The Chondrocyte: Biology and Clinical Application," Tissue Engineering 12(7), 1971-1984 (2006)

[186] Linder, B., Thermodynamics and Introductory Statistical Mechanics, John Wiley & Sons, Inc., New Jersey (2004).

[187] Liu, Y. and Wang, S., "3d Inverted Opal Hydrogel Scaffolds with Oxygen Sensing Capability," Colloids and Surfaces B: Biointerfaces 58(1), 8-13 (2007)

[188] Maheswari, P. U., Rajendiran, V., Palaniandavar, M., Thomas, R. and Kulkarni, G. U., "Mixed Ligand Ruthenium(Ii) Complexes of 5,6-Dimethyl-1,10-Phenanthroline: The Role of Ligand Hydrophobicity on DNA Binding of the Complexes," Inorganica Chimica Acta 359(14), 4601-4612 (2006)

[189] Maisch, T., Baier, J., Franz, B., Maier, M., Landthaler, M., Szeimies, R.-M. and Baumler, W., "The Role of Singlet Oxygen and Oxygen Concentration in Photodynamic Inactivation of Bacteria," Proceedings of the National Academy of Sciences 104(17), 7223-7228 (2007)

[190] Malda, J., Martens, D. E., Tramper, J., Van Blitterswijk, C. A. and Riesle, J., "Cartilage Tissue Engineering: Controversy in the Effect of Oxygen," Crit Rev Biotechnol. 23(3), 175-194. (2003)

[191] Mamchaoui, K. and Saumon, G., "A Method for Measuring the Oxygen Consumption of Intact Cell Monolayers," Am J Physiol Lung Cell Mol Physiol 278(4), L858-863 (2000)

[192] Martin, I., Wendt, D. and Heberer, M., "The Role of Bioreactors in Tissue Engineering," Trends in Biotechnology 22(2), 80-86 (2004)

[193] Masters, B. R. and So, P. T. C., "Antecedents of Two-Photon Excitation Laser Scanning Microscopy," Microscopy Research and Technique 63(1), 3-11 (2004)

[194] Matsumoto, S., Hyodo, F., Subramanian, S., Devasahayam, N., Munasinghe, J., Hyodo, E., Gadisetti, C., Cook, J. A., Mitchell, J. B. and Krishna, M. C., "Low-Field Paramagnetic Resonance Imaging of Tumor Oxygenation and Glycolytic Activity in Mice," The Journal of Clinical Investigation 118(5), 1965-1973 (2008)

[195] Matthews, C., Engineers' Data Book, Professional Engineering Publishing, London (2004).

[196] Matthews, D. R., Summers, H. D., Njoh, K., Errington, R. J., Smith, P. J., Barber, P., Ameer-Beg, S. and Vojnovic, B., "Technique for Measurement of Fluorescence Lifetime by Use of Stroboscopic Excitation and Continuous-Wave Detection," Appl. Opt. 45(9), 2115-2123 (2006)

[197] Mcclain, W. M., "Two-Photon Molecular Spectroscopy," Accounts of Chemical Research 7(5), 129-135 (1974)

[198] Mcconnell, G., "Pulsed Lasers and Nonlinear Optics," EMBO course, Plymouth (2010).

[199] Mckibbin, B. and Holdsworth, F. W., "The Nutrition of Immature Joint Cartilage in the Lamb," J Bone Joint Surg Br 48(4), 793-803 (1966)

[200] Mcnaught, A. D. and Wilkinson, A., "Iupac Compendium of Chemical Terminology - Gold Book," IUPAC (1997).

[201] Meeren, P., Vleeschauwer, D. and Debergh, P., "Determination of Oxygen Profiles in Agar-Based Gelled in Vitro Plant Tissue Culture Media," Plant Cell, Tissue and Organ Culture 65(3), 239-245 (2001)

[202] Mehta, G., Mehta, K., Sud, D., Song, J. W., Bersano-Begey, T., Futai, N., Heo, Y. S., Mycek, M. A., Linderman, J. J. and Takayama, S., "Quantitative Measurement and Control of Oxygen Levels in Microfluidic Poly(Dimethylsiloxane) Bioreactors During Cell Culture," Biomed Microdevices (2006)

[203] Meilan, P. F. and Garavaglia, M., "Rayleigh Criterion of Resolution and Light Sources of Different Spectral Composition," in Fifth International Topical Meeting on Education and Training in Optics, pp. 296-303, SPIE, Delft, Netherlands (1997).

[204] Menzel, R., Photonics: Linear and Nonlinear Interactions of Laser Light and Matter, Springer, New York; London (2001).

[205] Meschede, D., Optics, Light and Lasers : A Practical Approach to Modern Aspects of Photonics and Laser Physics, Wiley-VCH, Weinheim; Cambridge (2004).

[206] Miedlar, K. and Das, P. K., "Tris(2,2'-Bipyridine)Ruthenium(Ii)-Sensitized Photooxidation of Phenols. Environmental Effects on Electron Transfer Yields and Kinetics," Journal of the American Chemical Society 104(26), 7462-7469 (1982)

[207] Mik, E. G., Johannes, T., Zuurbier, C. J., Heinen, A., Houben-Weerts, J. H. P. M., Balestra, G. M., Stap, J., Beek, J. F. and Ince, C., "In Vivo Mitochondrial Oxygen Tension Measured by a Delayed Fluorescence Lifetime Technique," Biophysical Journal 95(8), 3977-3990 (2008)

[208] Mik, E. G., Van Leeuwen, T. G., Raat, N. J. and Ince, C., "Quantitative Determination of Localized Tissue Oxygen Concentration in Vivo by Two-Photon Excitation Phosphorescence Lifetime Measurements," J Appl Physiol 97(5), 1962-1969 (2004)

[209] Mills, I., Cvitas, T., Homann, K., Kallay, N. and Kuchitsu, K., "Quantites, Units and Symbols in Physical Chemistry," Iupac, Ed., Blackwell Science Ltd (1993).

[210] Milner, P. I., Fairfax, T. P. A., Browning, J. A., Wilkins, R. J. and Gibson, J. S., "The Effect of Oxygen Tension on Ph Homeostasis in Equine Articular Chondrocytes," Arthritis & Rheumatism 54(11), 3523-3532 (2006)

[211] Molter, T. W., Holl, M. R., Dragavon, J. M., Mcquaide, S. C., Anderson, J. B., Young, A. C., Burgess, L. W., Lidstrom, M. E. and Meldrum, D. R., "A New Approach for Measuring Single-Cell Oxygen Consumption Rates," Automation Science and Engineering, IEEE Transactions on 5(1), 32-42 (2008)

[212] Morris, K. J., Roach, M. S., Xu, W., Demas, J. N. and Degraff, B. A., "Luminescence Lifetime Standards for the Nanosecond to Microsecond Range and Oxygen Quenching of Ruthenium(Ii) Complexes," Analytical Chemistry 79(24), 9310-9314 (2007)

[213] Morton, G. A., "Photon Counting," Appl. Opt. 7(1), 1-10 (1968)

[214] Moseley, R., Waddington, R., Evans, P., Halliwell, B. and Embery, G., "The Chemical Modification of Glycosaminoglycan Structure by Oxygen-Derived Species in Vitro," Biochimica et Biophysica Acta (BBA) - General Subjects 1244(2-3), 245-252 (1995)

[215] Mow, V. C., Ratcliffe, A. and Robin Poole, A., "Cartilage and Diarthrodial Joints as Paradigms for Hierarchical Materials and Structures," Biomaterials 13(2), 67-97 (1992)

[216] Muir, H., "The Chondrocyte, Architect of Cartilage. Biomechanics, Structure, Function and Molecular Biology of Cartilage Matrix Macromolecules," BioEssays 17(12), 1039-1048 (1995)

[217] Mulazzani, Q. G., Sun, H., Hoffman, M. Z., Ford, W. E. and Rodgers, M. A. J., "Quenching of the Excited States of Ruthenium(Ii)-Diimine Complexes by Oxygen," J. Phys. Chem. 98(4), 1145-1150 (1994)

[218] Murphy, C. L. and Sambaniss, A., "Effect of Oxygen Tension on Chondrocyte Extracellular Matrix Accumulation," Connective Tissue Research 42(2), 87-96 (2001)

[219] Nag, A., De, A. K. and Goswami, D., "A Sensitive Technique for Two-Photon Absorption Measurements: Towards Higher Resolution Microscopy," Journal of Physics: Conference Series 80(012034 (2007)

[220] Nell, S. G., Lain, A. M., Tumbull, K. W. and Tremper, K. K., "Measurement of Oxygen by Mass Spectrometry," Canadian Journal of Anesthesia / Journal canadien d'anesthésie 34(1), 56-58 (1987)

[221] Neugebauer, U., Pellegrin, Y., Devocelle, M., Forster, R. J., Signac, W., Moran, N. and Keyes, T. E., "Ruthenium Polypyridyl Peptide Conjugates: Membrane Permeable Probes for Cellular Imaging," Chemical Communications 42), 5307-5309 (2008)

[222] Nicholls, P., "Introduction: The Biology of the Water Molecule," Cellular and Molecular Life Sciences (CMLS) 57(7), 987-992 (2000)

[223] O'connell, J. P. and Prausnitz, J. M., "Thermodynamics of Gas Solubility in Mixed Solvents," Industrial & Engineering Chemistry Fundamentals 3(4), 347-351 (1964)

[224] O'connor, D. V. and Phillips, D., Time-Correlated Single Photon Counting, Academic, London (1984).

[225] O'neal, D. P., Meledeo, M. A., Davis, J. R., Ibey, B. L., Gant, V. A., Pishko, M. V. and Cote, G. L., "Oxygen Sensor Based on the Fluorescence Quenching of a Ruthenium Complex Immobilized in a Biocompatible Poly(Ethylene Glycol) Hydrogel," Sensors Journal, IEEE 4(6), 728-734 (2004)

[226] O'regan, B. and Gratzel, M., "A Low-Cost, High-Efficiency Solar Cell Based on Dye-Sensitized Colloidal Tio2 Films," Nature 353(6346), 737-740 (1991)

[227] Oegema, T. R., Carpenter, R. J., Hofmeister, F. and Thompson, R. C., "The Interaction of the Zone of Calcified Cartilage and Subchondral Bone in Osteoarthritis," Microscopy Research and Technique 37(4), 324-332 (1997)

[228] Ogata, K., Whiteside, L. A. and Lesker, P. A., "Subchondral Route for Nutrition to Articular Cartilage in the Rabbit. Measurement of Diffusion with Hydrogen Gas in Vivo," J Bone Joint Surg Am 60(7), 905-910 (1978)

[229] Oh, J.-T., Li, M.-L., Zhang, H. F., Maslov, K., Stoica, G. and Wang, L. V., "Three-Dimensional Imaging of Skin Melanoma in Vivo by Dual-Wavelength Photoacoustic Microscopy," Journal of Biomedical Optics 11(3), 034032-034034 (2006)

[230] Othmer, D. F. and Thakar, M. S., "Correlating Diffusion Coefficient in Liquids," Ind. Eng. Chem. 45(3), 589-593 (1953)

[231] Oxford_Optronix, "Dissolved Oxygen Tissue Po2 Monitors - Oxylab Po2 and Oxylite," http://www.oxford-optronix.com/pO2monitors.htm (2010).

[232] Palsson, B. O. and Bhatia, S., Tissue Engineering, Pearson Education, Upper Saddle River, N.J. USA (2004).

[233] Paris, J. P. and Brandt, W. W., "Charge Transfer Luminescence of a Ruthenium(Ii) Chelate," Journal of the American Chemical Society 81(18), 5001-5002 (1959)

[234] Paschotta, R., Encyclopedia of Laser Physics and Technology, Wiley-VCH ; [John Wiley, distributor], Weinheim; Chichester (2008).

[235] Patterson, G. H. and Piston, D. W., "Photobleaching in Two-Photon Excitation Microscopy," Biophysical Journal 78(4), 2159-2162 (2000)

[236] Pawley, J. B., Handbook of Biological Confocal Microscopy, Springer, New York, NY (2006).

[237] Pelster, R., "Dielectric Relaxation Spectroscopy in Polymers: Broadband Ac-Spectroscopy and Its Compatibility with Tsdc," in Electrets, 1999. ISE 10. Proceedings. 10th International Symposium on, pp. 437-444 (1999).

[238] Pettersen, E. O., Larsen, L. H., Ramsing, N. B. and Ebbesen, P., "Pericellular Oxygen Depletion During Ordinary Tissue Culturing, Measured with Oxygen Microsensors," Cell Prolif. 38(4), 257-267 (2005)

[239] Pierre, J., Gemmiti, C., Kolambkar, Y., Oddou, C. and Guldberg, R., "Theoretical Analysis of Engineered Cartilage Oxygenation: Influence of Construct Thickness and Media Flow Rate," Biomechanics and Modeling in Mechanobiology 7(6), 497-510 (2008)

[240] Piston, D. W., Fellers, T. J. and Davidson, M. W., "Fundamentals and Applications in Multiphoton Excitation Microscopy," in Fluorescence Mircoscopy, Nikon MircosopyU (Web) (2000-2010).

[241] Plant, R. L. and Burns, D. H., "Quantitative, Depth-Resolved Imaging of Oxygen Concentration by Phosphorescence Lifetime Measurement," Applied Spectroscopy 47(10), 1594-1599 (1993)

[242] Pluen, A., Netti, P. A., Jain, R. K. and Berk, D. A., "Diffusion of Macromolecules in Agarose Gels: Comparison of Linear and Globular Configurations," Biophysical Journal 77(1), 542-552 (1999)

[243] Poole, A. R., Kojima, T., Yasuda, T., Mwale, F., Kobayashi, M. and Laverty, S., "Composition and Structure of Articular Cartilage: A Template for Tissue Repair," Clin Orthop Relat Res Suppl(391), S26-33 (2001)

[244] Poole, C. A., "Review. Articular Cartilage Chondrons: Form, Function and Failure," Journal of Anatomy 191(01), 1-13 (1997)

[245] Poulsen, P. H., Smith, D. F., Østergaard, L., Danielsen, E. H., Gee, A., Hansen, S. B., Astrup, J. and Gjedde, A., "In Vivo Estimation of Cerebral Blood Flow, Oxygen Consumption and Glucose Metabolism in the Pig by [15o]Water Injection, [15o]Oxygen Inhalation and Dual Injections of [18f]Fluorodeoxyglucose," Journal of Neuroscience Methods 77(2), 199-209 (1997)

[246] Presens, "Precision Sensing - Oxygen Microsensors - Sensor Type Pst1 and Tos7," http://www.presens.de (2010).

[247] Pryor, W. A., Houk, K. N., Foote, C. S., Fukuto, J. M., Ignarro, L. J., Squadrito, G. L. and Davies, K. J. A., "Free Radical Biology and Medicine: It's a Gas, Man!," Am J Physiol Regul Integr Comp Physiol 291(3), R491-511 (2006)

[248] Reid, R. C., Prausnitz, J. M. and Poling, B. E., The Properties of Gases and Liquids (1986).

[249] Rendell, D., Fluorescence and Phosphorescence Spectroscopy, Wiley on behalf of ACOL, Chichester (1987).

[250] Rettich, T. R., Battino, R. and Wilhelm, E., "Solubility of Gases in Liquids. 22. High-Precision Determination of Henry's Law Constants of Oxygen in Liquid Water Fromt = 274 K Tot = 328 K," The Journal of Chemical Thermodynamics 32(9), 1145-1156 (2000)

[251] Rharass, T., Vigo, J., Salmon, J.-M. and Ribou, A.-C., "Variation of 1-Pyrenebutyric Acid Fluorescence Lifetime in Single Living Cells Treated with Molecules Increasing or Decreasing Reactive Oxygen Species Levels," Analytical Biochemistry 357(1), 1-8 (2006)

[252] Ribou, A.-C., Vigo, J. and Salmon, J.-M., "Lifetime of Fluorescent Pyrene Butyric Acid Probe in Single Living Cells for Measurement of Oxygen Fluctuation," Photochem and Photobiol 80(2), 274-280 (2004)

[253] Rice, K. M., Uddemarri, S., Desai, D. H., Morrison, R. G., Harris, R., Wright, G. L. and Blough, E. R., "Pgf2[Alpha]-Associated Vascular Smooth Muscle Hypertrophy Is Ros Dependent and Involves the Activation of Mtor, P70s6k, and Pten," Prostaglandins & Other Lipid Mediators 85(1-2), 49-57 (2008)

[254] Rivarola, C. R., Bertolotti, S. G. and Previtali, C. M., "Photoreduction of $[Ru(Bpy)_3]^{2+}$ by Amines in Aqueous Solution. Kinetics Characterization of a Long-Lived Nonemitting Excited States.," Photochemistry and Photobiology 82(1), 213-218 (2006)

[255] Robergs, R. A., Ghiasvand, F. and Parker, D., "Biochemistry of Exercise-Induced Metabolic Acidosis," Am J Physiol Regul Integr Comp Physiol 287(3), R502-516 (2004)

[256] Rosso, L. and Fernicola, V. C., "Time- and Frequency-Domain Analyses of Fluorescence Lifetime for Temperature Sensing," Review of Scientific Instruments 77(3), 034901 (2006)

[257] Rusak, D. A., James, W. H. I., Ferzola, M. J. and Stefanski, M. J., "Investigation of Fluorescence Lifetime Quenching of $[Ru(Bpy)_3]^{2+}$ by Oxygen Using a Pulsed Light-Emitting Diode," J. Chem. Educ. 83(12), (2006)

[258] Saez, M., Abuin, E. A. and Lissi, E. A., "Fluorescence Quenching by Oxygen in Reverse Micellar Solutions," Langmuir 5(4), 942-947 (1989)

[259] Saul, A. and Wagner, W., "International Equations for the Saturation Properties of Ordinary Water Substance," J. Phys. Chem. Ref. Data 16(4), 893-901 (1987)

[260] Schroder, C. R., Polerecky, L. and Klimant, I., "Time-Resolved Ph/Po2 Mapping with Luminescent Hybrid Sensors," Analytical Chemistry 79(1), 60-70 (2007)

[261] Sears, F. W. and Salinger, G. L., Thermodynamics, Kinetic Theory, and Statistical Thermodynamics, Addison-Wesley (1986).

[262] Sengers, B. G., Heywood, H. K., Lee, D. A., Oomens, C. W. J. and Bader, D. L., "Nutrient Utilization by Bovine Articular Chondrocytes: A Combined Experimental and Theoretical Approach," Journal of Biomechanical Engineering 127(5), 758-766 (2005)

[263] Sensi, S. L., Yin, H. Z., Carriedo, S. G., Rao, S. S. and Weiss, J. H., "Preferential Zn2+ Influx through Ca2+-Permeable Ampa/Kainate Channels Triggers Prolonged Mitochondrial Superoxide Production," Proceedings of the National Academy of Sciences of the United States of America 96(5), 2414-2419 (1999)

[264] Sharma, B. and Elisseeff, J. H., "Engineering Structurally Organized Cartilage and Bone Tissues," Annals of Biomedical Engineering 32(1), 148-159 (2004)

[265] Sharman, K. K., Periasamy, A., Ashworth, H., Demas, J. N. and Snow, N., "Error Analysis of the Rapid Lifetime Determination Method for Double-Exponential Decays and New Windowing Schemes," Analytical Chemistry 71(5), 947-952 (1999)

[266] Shchepina, L. A., Pletjushkina, O. Y., Avetisyan, A. V., Bakeeva, L. E., Fetisova, E. K., Izyumov, D. S., Saprunova, V. B., Vyssokikh, M. Y., Chernyak, B. V. and

Skulachev, V. P., "Oligomycin, Inhibitor of the F0 Part of H+-Atp-Synthase, Suppresses the Tnf-Induced Apoptosis," Oncogene 21(53), 8149-8157 (2002)

[267] Shibata, M., Ichioka, S. and Kamiya, A., "Estimating Oxygen Consumption Rates of Arteriolar Walls under Physiological Conditions in Rat Skeletal Muscle," Am J Physiol Heart Circ Physiol 289(1), H295-300 (2005)

[268] Shonat, R. D. and Johnson, P. C., "Oxygen Tension Gradients and Heterogeneity in Venous Microcirculation: A Phosphorescence Quenching Study," Am. J. Physiol. 272(5), H2233-2240 (1997)

[269] Sigma-Aldrich, "Dubecco's Modified Eagle's Medium (Dme) Base," (2007).

[270] Sigma-Aldrich and Fluka, "Tris(4,7-Diphenyl-1,10-Phenanthroline)Ruthenium(Ii) Dichloride Complex " (2008).

[271] Silver, I. A. and Maroudas, A., "Measurement of Ph and Ionic Composition of Pericellular Sites " Philosophical Transactions of the Royal Society of London. Series B, Biological Sciences 271(912), 261-272 (1975)

[272] Slinker, J., Bernards, D., Houston, P. L., Abruna, H. D., Bernhard, S. and Malliaras, G. G., "Solid-State Electroluminescent Devices Based on Transition Metal Complexes," Chemical Communications 19), 2392-2399 (2003)

[273] Smith, F. L. and Harvey, A. H., "Avoid Common Pitfalls When Using Henry's Law," Chemical Engineering Progress 103(9), 33-39 (2007)

[274] So, P. T. C., Dong, C. Y., Masters, B. R. and Berland, K. M., "Two-Photon Excitation Fluorescence Microscopy," Annual Review of Biomedical Engineering 2(1), 399-429 (2000)

[275] Spectra-Physics, "Mai Tai: Broadband, Mode-Locked Ti:Sapphire Laser *User's Manual*," in Part number 0000-327A, Rev. A, Spectra-Physics - Laser & Photonics, Mountain View, CA (2004).

[276] Stockwell, R. A., Biology of Cartilage Cells, Cambridge University Press, Cambridge (1979).

[277] Stucker, M., Schulze, L., Pott, G., Hartmann, P., Lubbers, D. W., Rochling, A. and Altmeyer, P., "Flim of Luminescent Oxygen Sensors: Clinical Applications and Results," Sensors and Actuators B: Chemical 51(1-3), 171-175 (1998)

[278] Sud, D. and Mycek, M.-A., "Calibration and Validation of an Optical Sensor for Intracellular Oxygen Measurements," Journal of Biomedical Optics 14(2), 020506-020503 (2009)

[279] Sud, D., Zhong, W., Beer, D. and Mycek, M.-A., "Measurement of Intracellular Oxygen Levels Using Fluorescence Lifetime Imaging Microscopy (Flim)," Proc. SPIE 5859 (Photon Migration and Diffuse-Light Imaging II), 595907-595901 to -595910 (2005)

[280] Suhling, K., "Fluorescence Lifetime Imaging," in Cell Imaging - Methods Express D. Stephens, Ed., pp. 219-245, Scion, Bloxham, Oxfordshire (2006).

[281] Suhling, K., French, P. M. and Phillips, D., "Time-Resolved Fluorescence Microscopy," Photochem Photobiol Sci 4(1), 13-22 (2005)

[282] Suhling, K., Mcloskey, D. and Birch, D. J. S., "Multiplexed Single-Photon Counting. Ii. The Statistical Theory of Time-Correlated Measurements," Review of Scientific Instruments 67(6), 2238-2246 (1996)

[283] Suhling, K., Sergent, N., Levitt, J. and Green, M., "Rapid Wide-Field Photon Counting Imaging with Microsecond Time Resolution," Opt. Express 18(24), 25292-25298 (2010)

[284] Sytsma, J., Vroom, J. M., Grauw, D. C. J. and Gerritsen, H. C., "Time-Gated Fluorescence Lifetime Imaging and Microvolume Spectroscopy Using Two-Photon Excitation," Journal of Microscopy 191(1), 39-51 (1998)

[285] Tarnovsky, A. N., Gawelda, W., Johnson, M., Bressler, C. and Chergui, M., "Photexcitation of Aqueous Ruthenium(Ii)-Tris-(2,2â€˜-Bipyridine) with High-Intensity Femtosecond Laser Pulses," The Journal of Physical Chemistry B 110(51), 26497-26505 (2006)

[286] Temenoff, J. S. and Mikos, A. G., "Review: Tissue Engineering for Regeneration of Articular Cartilage," Biomaterials 21(5), 431-440 (2000)

[287] Terada, H., "Uncouplers of Oxidative Phosphorylation.," Environ Health Perspect. 87(213-218 (1990)

[288] Thannickal, V. J. and Fanburg, B. L., "Reactive Oxygen Species in Cell Signaling," Am J Physiol Lung Cell Mol Physiol 279(6), L1005-1028 (2000)

[289] Tile, M., "Osteoarthritis," in The Workplace Safety and Insurance Appeals Tribunal (2008).

[290] Treuhaft, P. S. and Mccarty, D. J., "Synovial Fluid Ph, Lactate, Oxygen and Carbon Dioxide Partial Pressure in Various Joint Diseases," Arthritis & Rheumatism 14(4), 475-484 (1971)

[291] Tromans, D., "Temperature and Pressure Dependent Solubility of Oxygen in Water: A Thermodynamic Analysis," Hydrometallurgy 48(3), 327-342 (1998)

[292] Tromans, D., "Modeling Oxygen Solubility in Water and Electrolyte Solutions," Ind. Eng. Chem. Res. 39(3), 805-812 (2000)

[293] Tuli, R., Li, W. J. and Tuan, R. S., "Current State of Cartilage Tissue Engineering," Arthritis Res Ther 5(5), 235-238 (2003)

[294] Ulrich-Vinther, M., Maloney, M. D., Schwarz, E. M., Rosier, R. and O'keefe, R. J., "Articular Cartilage Biology," J Am Acad Orthop Surg 11(6), 421-430 (2003)

[295] Unsense, "Oxygen Sensors," http://www.unisense.com (2010).

[296] Urban, J. P. G., "The Chondrocyte: A Cell under Pressure," British Journal of Rheumatology 33(10), 901-908 (1994)

[297] Urban, J. P. G., Hall, A. C. and Gehl, K. A., "Regulation of Matrix Synthesis Rates by the Ionic and Osmotic Environment of Articular Chondrocytes," Journal of Cellular Physiology 154(2), 262-270 (1993)

[298] Valentin, J. E., Freytes, D. O., Grasman, J. M., Pesyna, C., Freund, J., Gilbert, T. W. and Badylak, S. F., "Oxygen Diffusivity of Biologic and Synthetic Scaffold Materials for Tissue Engineering," Journal of Biomedical Materials Research Part A 91A(4), 1010-1017 (2009)

[299] Van Dyck, S., "The Impact of Singlet Oxygen on Lipid Oxidation," Lipid Technology 19(12), 278-280 (2007)

[300] Van Houten, J. and Watts, R. J., "Temperature Dependence of the Photophysical and Photochemical Properties of the Tris(2,2'-Bipyridyl)Ruthenium(Ii) Ion in Aqueous Solution," Journal of the American Chemical Society 98(16), 4853-4858 (1976)

[301] Vaughn, W. M. and Weber, G., "Oxygen Quenching of Pyrenebutyric Acid Fluorescence in Water. Dynamic Probe of the Microenvironment," Biochemisty 9(3), 464-473 (1970)

[302] Vinogradov, S. A. and Wilson, D. F., "Metallotetrabenzoporphyrins. New Phosphorescent Probes for Oxygen Measurements," J. Chem. Soc., Perkin Trans. 2 1), 103-111 (1995)

[303] Visser, T. D., Oud, J. L. and Brakenhoff, G. J., "Refractive Index and Axial Distance Measurements in 3d Microscopy," Optik 90(1), 17-19 (1992)

[304] Vunjak-Novakovic, G., Martin, I., Obradovic, B., Treppo, S., Grodzinsky, A. J., Langer, R. and Freed, L. E., "Bioreactor Cultivation Conditions Modulate the Composition and Mechanical Properties of Tissue-Engineered Cartilage," Journal of Orthopaedic Research 17(1), 130-138 (1999)

[305] Walker, J., "'O' Rings," in www.jameswalker.co.uk (2005).

[306] Walker, J. G., "Iterative Correction for 'Pile-up' in Single-Photon Lifetime Measurement," Optics Communications 201(4-6), 271-277 (2002)

[307] Wang, D. W., Fermor, B., Gimble, J. M., Awad, H. A. and Guilak, F., "Influence of Oxygen on the Proliferation and Metabolism of Adipose Derived Adult Stem Cells," Journal of Cellular Physiology 204(1), 184-191 (2005)

[308] Wang, W. and Vadgama, P., "O2 Microsensors for Minimally Invasive Tissue Monitoring," Journal of The Royal Society Interface 1(1), 109-117 (2004)

[309] White, J. G., Amos, W. B. and Fordham, M., "An Evaluation of Confocal Versus Conventional Imaging of Biological Structures by Fluorescence Light Microscopy," The Journal of Cell Biology 105(1), 41-48 (1987)

[310] Wieser, M. E., "Atomic Weights of the Elements 2005 (Iupac Technical Report)," Pure and Applied Chemistry 78(11), 2051-2066 (2006)

[311] Wilhelm, E., "Solubility of Gases in Liquids: A Critical Review," Pure Appl. Chem. 57(2), 303-322 (1985)

[312] Wilhelm, E., Battino, R. and Wilcock, R. J., "Low-Pressure Solubility of Gases in Liquid Water," Chemical Reviews 77(2), 219-262 (1977)

[313] Wodnicka, M., Guarino, R. D., Hemperly, J. J., Timmins, M. R., Stitt, D. and Pitner, J. B., "Novel Fluorescent Technology Platform for High Throughput Cytotoxicity and Proliferation Assays," J Biomol Screen 5(3), 141-152 (2000)

[314] Woodruff, T., "Biospherix Specifications," N. Hosny, Ed. (2009).

[315] Xiao, D., Mo, Y. and Choi, M. M. F., "A Hand-Held Optical Sensor for Dissolved Oxygen Measurement," Meas. Sci. Technol. 14(6), 862-867 (2003)

[316] Xie, Z. and Askari, A., "$Na^+/K^+$-Atpase as a Signal Transducer," European Journal of Biochemistry 269(10), 2434-2439 (2002)

[317] Xu, C. and Webb, W. W., "Measurement of Two-Photon Excitation Cross Sections of Molecular Fluorophores with Data from 690 to 1050 Nm," J. Opt. Soc. Am. B 13(3), 481-491 (1996)

[318] Xu, W., Kneas, K. A., Demas, J. N. and Degraff, B. A., "Oxygen Sensors Based on Luminescence Quenching of Metal Complexes: Osmium Complexes Suitable for Laser Diode Excitation," Analytical Chemistry 68(15), 2605-2609 (1996)

[319] Yanez, C., "Two Photon Excitation Vs. Single Photon Excitation," in Zhenli Huang Fluorescein, Ed., University of Central Florida (2006).

[320] Yaseen, M. A., Srinivasan, V. J., Sakad?I, S., Wu, W., Ruvinskaya, S., Vinogradov, S. A. and Boas, D. A., "Optical Monitoring of Oxygen Tension in Cortical Microvessels with Confocal Microscopy," Opt. Express 17(25), 22341-22350 (2009)

[321] Zhang, G., Mcshane, M. J. and Robinson, C. J., "Quenching Properties of a Self-Referenced Fluorescence Oxygen Nanosensor under a Wide-Field Intrinsic Optical Signal Imaging System," in Engineering in Medicine and Biology 27th Annual Conference, Proceedings of the 2005 IEEE, pp. 1438-1441, Shanghai, China (2005).

[322] Zhang, L. and Siepmann, J., "Direct Calculation of Henry's Law Constants from Gibbs Ensemble Monte Carlo Simulations: Nitrogen, Oxygen, Carbon Dioxide and

Methane in Ethanol," Theoretical Chemistry Accounts: Theory, Computation, and Modeling (Theoretica Chimica Acta) 115(5), 391-397 (2006)

[323] Zhao, D., Ran, S., Constantinescu, A., Hahn, E. W. and Mason, R. P., "Tumor Oxygen Dynamics: Correlation of in Vivo Mri with Histological Findings," Neoplasia 5(4), 308-318 (2003)

[324] Zhong, W., Urayama, P. and Mycek, M. A., "Imaging Fluorescence Lifetime Modulation of a Ruthenium-Based Dye in Living Cells: The Potential for Oxygen Sensing," Journal of Physics D: Applied Physics 36(14), 1689-1695 (2003)

[325] Zhou, S., Cui, Z. and Urban, J. P. G., "Factors Influencing the Oxygen Concentration Gradient from the Synovial Surface of Articular Cartilage to the Cartilage-Bone Interface: A Modeling Study," Arthritis & Rheumatism 50(12), 3915-3924 (2004)

[326] Zhou, S., Cui, Z. and Urban, J. P. G., "Nutrient Gradients in Engineered Cartilage: Metabolic Kinetics Measurement and Mass Transfer Modeling," Biotechnology and Bioengineering 101(2), 408-421 (2008)

[327] Zhuang, X., Ha, T., Kim, H. D., Centner, T., Labeit, S. and Chu, S., "Fluorescence Quenching: A Tool for Single-Molecule Protein-Folding Study," Proceedings of the National Academy of Sciences 97(26), 14241-14244 (2000)

[328] Zink, J. I., "Triboluminescence," Accounts of Chemical Research 11(8), 289-295 (1978)

[329] Zipfel, W. R., Williams, R. M., Christie, R., Nikitin, A. Y., Hyman, B. T. and Webb, W. W., "Live Tissue Intrinsic Emission Microscopy Using Multiphoton-Excited Native Fluorescence and Second Harmonic Generation," Proceedings of the National Academy of Sciences 100(12), 7075-7080 (2003)